ABSTRACT

Title of Dissertation:	SYNTHESIS OF MAIN GROUP ELEMENT CLUSTERS OF GROUPS 13 AND 15 FROM DISPROPORTIONATION PATHWAYS AND ZINTL POLYANIONS
	Lauren M. Stevens, Doctor of Philosophy, 2019
Dissertation directed by:	Professor Bryan W. Eichhorn, Department of Chemistry and Biochemistry

This thesis details the synthesis and characterization of main group element clusters of Groups 13 (aluminum) and 15 (phosphorus, arsenic). Aluminum clusters were synthesized from metastable Al(I)X (X = Cl, Br) solutions, which have proven adept at fostering the growth of metalloid clusters of the form Al_nR_m (where n > m). Group 15 – transition metal coordination complexes and ligand-free binary anions are synthesized through the use of Zintl ion precursors, originating from phases K_3Pn_7 (Pn = P, As, Sb).

The novel cluster $[(Bu_2O)_3Li][Li_4Al_5Ph_{12}]$ has been synthesized and characterized, reported here in seven different crystallographic modifications. In addition to being the first low-valent phenyl aluminum cluster, this anion exhibits metastability in both the solid-state and solution, as indicated through ESI-MS, LDI-MS, and solid-state NMR analyses. The Zintl-derived coordination complexes $[(\eta^4\text{-}As_7)Co(\eta^3\text{-}As_3)]^{3-}$, $[(\eta^4\text{-}As_7)Rh(COD)]^{2-}$, and $[(\eta^4\text{-}As_7)Ir(COD)]^{2-}$ are reported as the first As / Group 9 clusters, and are isoelectronic to known coordination species of Zintl anions and transition metal carbonyl fragments. Additionally, the product $[(\eta^4\text{-}As_7)Co(\eta^3\text{-}As_3)]^{3-}$ is the first known

carbon-free binary anion of As / Co. These complexes have been characterized via LDI-MS, NMR, single crystal XRD, and quantum chemical calculations. The doubly substituted coordination complex $[(en)(CO)_3Mo(\eta^1,\eta^4\text{-}P_7)Mo(CO)_3]^{3-}$ completes a series of previously reported Group 6 polyphosphide complexes, and is compared to its W congener, $[(en)(CO)_3W(\eta^1,\eta^4\text{-}P_7)W(CO)_3]^{3-}$. Unlike coordination complexes, which retain the nuclearity of the seven-atom precursors $[Pn_7]^{3-}$, binary intermetalloids $[Mo_2P_{16}]^{4-}$ and $[Rh_3As_{16}]^{3-}$ show extensive reorganization of the original polypnictide cages. These anions feature *cyclo*-$[P_{10}]^{2-}$ and *cyclo*-$[As_5]^{1-}$ subunits, which are the first to be isolated and described in products of Zintl anions. Additionally, these are the first binary systems to be reported for Mo/P and Rh/As, and could potentially be used for the formation of binary phases (i.e. $RhAs_2$) upon oxidation.

SYNTHESIS OF MAIN GROUP ELEMENT CLUSTERS OF GROUPS 13 AND 15 FROM DISPROPORTIONATION PATHWAYS AND ZINTL POLYANIONS

by

Lauren M. Stevens

Dissertation submitted to the Faculty of the Graduate School of the
University of Maryland, College Park, in partial fulfillment
of the requirements for the degree of
Doctor of Philosophy
2019

Advisory Committee:
Professor Bryan Eichhorn, Chair
Professor Efrain Rodriguez
Professor Philip DeShong
Professor Jeffery Davis
Professor Vincent Lee, Dean's representative

Foreword

Perfer et obdura - hic dolor tibi proderit olim.

Persevere and endure - one day, this grief will be useful to you.

- Ovid

Dedication

To my father, Michael J. Stevens, who has stopped at nothing to give me everything.

Table of Contents

List of Tables

List of Figures

Figure 2.3: (a): $[Li_4Al_5]^{11+}$ cluster core of **2.1**. Al-Li interactions are shown only as a guide to illustrate the substituted body-centered heterocubane-like architecture of this portion of the cluster. (b): Bonding environment of a single Li^+ ion. Each Li^+ participates in three η^2 interactions with three adjacent Ph units, each bound to a different Al atom. Aluminum = green, lithium = violet, carbon = black. Hydrogens omitted for clarity.

Figure 2.4: (a): Polymeric dimer of $LiAlPh_4$ showing cation-pi interactions between Li^+ and Ph rings. (b): Stacked chains of $[LiAlPh_4]_n$, linked primarily through edge-to-face π-stacking from Ph rings. Li = violet, Al = green, C = black. Hydrogens omitted for clarity.

Figure 2.5: (a): ^{27}Al MAS NMR spectrum for $[(Bu_2O)_3Li][Li_4Al_5Ph_{12}]$. The spectrum was acquired following a single pulse of length 1 ms with a delay time between scans of 4 s and a spinning speed of 20 kHz. (b): Magnification of the region from 0 – 175 ppm, showing three signals. (c): Further magnification of signal. Peak-fittings, used to determine the signal intensities (integration of signal area) are given in the legend.

Figure 2.6: (a): ^{7}Li MAS NMR spectra for $[(Bu_2O)_3Li][Li_4Al_5Ph_{12}]$ and (b): Peak fits to two lines, determining signal intensities. Spectra acquired following a single pulse of length 1 ms with a wait time between scans of 2 s and a spinning speed of either 10 or 20 kHz.

Figure 2.7: Mass spectra of crystals containing **2.1** (black). Inset shows mass envelope at *m/z* = 1087.44, the mass fragment associated with the parent ion of **2.1**, $[Li_4Al_5Ph_{12}]^{1-}$. Simulated spectrum in red (Mmass Software, version 3).

Figure 2.8: Mass envelopes for four major peaks in the mass spectrum of crystals containing **2.1,** which may arise due to fragmentation of the parent ion. (a): *m/z* = 481.16, $[AlPh_2(C_4H_{10}O)_2]^{1-}$ (b): *m/z* = 611.27, $[Li_2Al_4Ph_3(C_7H_8)_2(C_4H_{10}O)]^{1-}$ (c): *m/z* = 778.35, $[LiAl_3Ph_8(C_4H_{10}O)]^{1-}$(d): *m/z* = 862.40, $[Li_2Al_3Ph_9(C_4H_{10}O)]^{1-}$. Experimental spectra in black, simulated spectra in red (Mmass Software, version 3).

Figure 2.9: (a): Negative mode ESI-MS of crystals containing **2.1** in a diethyl ether solution. Mass envelopes corresponding to (b): $[AlPh_4]^{1-}$, m/z = 335.14, (c): $[LiAl_3Ph_5(Et_2O)(Bu_2O)]^{1-}$, m/z = 677.37, and (d): $[Li_2Al_4Ph_9(Et_2O)(Bu_2O)]^{1-}$, m/z = 1019.52. Masses given in amu.

Figure 2.10: A simplified molecular orbital depiction of the Al-Al bonding in **2.1**. Calculated energy values are shown for the LUMO ($3t_2^*$), HOMO ($3t_2$), and HOMO-1 ($2a_1$), with a HOMO-LUMO gap of 3.2 eV. Apical Al^{2+} ions interact with the central Al^{1-} in a covalent manner, each providing one electron to form each 2c-2e Al-Al bond.

Figure 2.11: Electron density showing the four NNAs between central and apical Al atoms.

Figure 2.12: ELF of **2.1** (left) and the core Al-Al bonds (right). Visualized at the 0.83 isosurface value.

Figure 2.13: (a): Core of **2.1**, oriented to highlight Al-Al bonding (b): Four NNAs reveal four two-center, two-electron bonds between central and apical Al atoms. (c): ELF of core Al-Al bonds, visualized at the 0.83 isosurface value. ELF results also support four Al-Al bonds, with extensive electron delocalization from the central Al to the more electron-deficient apical Al atoms, supporting that the central Al is more electron-rich (lower charge) than the apical Al atoms.

Figure 2.14: Perspective view of Schnockel's $[Al_5Br_6•6(THF)][Al_5Br_8•4(THF)]$ salt, where the tetrahedral arrangement of Al atoms in the cluster core bears resemblance to those in **2.1**.

Figure 2.15: Images of co-crystallites $[(Bu_2O)_3Li][Li_4Al_5Ph_{12}]$]•2(tol) and $LiAlPh_4$, illustrating differences in size, color, and crystal habit of each species. Recorded at the Advanced Photon Source of Argonne National Lab, Dec. 2014.

Figure 3.1: Ball and stick models of Zintl-transition metal coordination complexes (a) $[(\eta^2\text{-}As_7)PtH(PPh_3)]^{2-}$ (b) $[(\eta^4\text{-}P_7)Ni(CO)]^{3-}$ and (c) $[(\eta^4\text{-}As_7)Cr(CO)_3]^{3-}$. Phenyl hydrogens omitted for clarity. P = magenta, Pt = orange, As = red-violet, Ni = dark green, Cr = bright green, C = black, O = red.

Figure 3.2: (a) Ball and stick model of $[(\eta^3\text{-}As_3)Co(\eta^4\text{-}As_7)]^{3-}$. (b) Top down view showing orientation of As_3 relative to As_7. (Co = blue, As = red-violet)

Figure 3.3: (a) Ball and stick model of $[(\eta^4\text{-}As_7)Rh(COD)]^{2-}$. Hydrogens omitted for clarity (b) Top down view of $[(\eta^4\text{-}As_7)Rh(COD)]^{2-}$, showing orientation of COD ligand relative to As_7 cage. Hydrogens omitted for clarity (Rh = yellow, As = red-violet, C = black).

Figure 3.4: (a) Ball and stick model of $[(\eta^4\text{-}As_7)Ir(COD)]^{2-}$ (b) Top down view of $[(\eta^4\text{-}As_7)Ir(COD)]^{2-}$, illustrating the orientation of the COD ligand in relation to the $[As_7]^{3-}$ cage. Hydrogens omitted for clarity (Ir = red, As = red-violet, C = black).

Figure 3.5: Representation of select orbitals in $[(\eta^3\text{-}As_3)Co(\eta^4\text{-}As_7)]^{3-}$ (**3.1**).

Figure 3.6: Qualitative Molecular orbital diagram for C_s $[(\eta^3\text{-}As_3)Co(\eta^4\text{-}As_7)]^{3-}$, comprised of interactions between π-type orbitals of C_{2v} norbornadiene As_7^{3-} and C_{3v} $CoAs_3$ fragments.

Figure 3.7: Aliphatic region of $^{13}C\{^1H\}$ spectrum of $[K(2,2,2\text{-crypt})]_2[(\eta^4\text{-}As_7)Rh(COD)]$. Recorded at 298 K at 400 MHz in d_5-pyridine. Signals corresponding to 2,2,2-cryptand are designated by an asterisk (*).

Figure 3.8: $^{13}C\{^1H\}$ spectrum of $[K(2,2,2\text{-crypt})]_2[(\eta^4\text{-}As_7)Rh(COD)]$, with focus on the region between 68 – 71 ppm. Signals from 2,2,2-cryptand are denoted with an asterisk (*). Recorded at 298 K at 400 MHz in d_5-pyridine.

Figure 5.13: A simplified molecular orbital depiction of the frontier orbitals of **5.2**. Calculated energy values are shown for the LUMO ($3t_2^*$) down to HOMO -4, with a HOMO-LUMO gap of 1.30 eV.

Figure 5.14: Comparisons of (a) $[Mo_2P_{10}]^{2+}$ unit and coordination of a single Mo center as $[MoP_6]^{n+}$ with the crown-like (b) $[MoAs_8]^{2-}$ and (c) $[MoSb_8]^{3-}$ anions.

Figure 5.15: Structural comparisons of intermetalloids $[Rh_3As_{16}]^{3-}$, $[Ni_5Sb_{17}]^{4-}$, $[Pd_7As_{16}]^{4-}$, and $[Sb@Pd_{12}@Sb_{20}]^{3-/4-}$.

List of Abbreviations

Å	Angstrom
Ar	2,6-diisopropylphenyl
bpy	2,2'-bipyridine
COD	1,5-cyclooctadiene, C_8H_{12}
Cp	cyclopentadienyl, C_5H_5
Cp*	pentamethylcyclopentadienyl, $C_{10}H_{15}$
2,2,2-Crypt	4,7,13,16,21,24-hexaoxa-1,10-diazobicyclo[8.8.8]hexacosane
Cy	Cyclohexyl
Dipp	2,6-diisopropylphenyl
DMF	dimethylformamide
e^-	electron
EDX	Energy-Dispersive X-Ray Spectroscopy
EPR	Electron Paramagnetic Resonance
Eq	Equation
ESI-MS	Electrospray Ionization Mass Spectrometry
Et_2O	diethyl ether
HMDS	hexamethyldisilazide, $[N(Si(Me)_3)_2]^-$
Hz	Hertz
^iPr	isopropyl
Mes	1,3,5-mesityl
mg	milligrams
MFC	mass flow controller
MHCR	Metal-Halide Co-Condensation Reactor

MHz	megahertz
min	minutes
mL	milliliter
mmol	millimole
mM	millimolar (mmol / mL)
MS	Mass spectrometry
nm	nanometer
NacNac	([N(2,6-diisopropylphenyl)C(Me)]$_2$CH
Naph	Naphthalene, $C_{10}H_8$
NMR	Nuclear Magnetic Resonance
Ph	phenyl, C_6H_5
ppm	parts per million
^{t}Bu	tert-butyl
THF	tetrahydrofuran
Tol	toluene
XRD	X-Ray diffraction

Chapter 1: Introduction

1.1 Main Group Element Clusters

Upon the discovery of spherically shaped fullerenes (C_{60}, C_{70}, C_{78}, etc.) and their remarkable electronic properties, many physical scientists were inspired to investigate other systems of related "naked" molecular main group element clusters. [1,2] Some of the most prominent findings were related to polyborane (boron hydride, heteroborane, metallaborane) chemistry, which include development of the multiple-center bonding description for deltapolyhedral structures, leading to the Wade-Mingos rules for electron counting in electron-deficient skeletal clusters. [3-5] The chemistry of boron hydrides also laid the groundwork for investigations of 3D aromaticity, more advanced quantum chemical calculations to describe electron delocalization in clusters, and development of structure-property relationships. Eventually, clusters of the heavier Group 13 elements (aluminum, gallium, indium, and thallium) were also studied, and found to have properties that differed quite profoundly to their boron congeners. [5-7] Simultaneously, investigations were ongoing to describe the formation, functionalization, stability, and properties of homo- and heteroatomic molecular clusters of Group 14 (Ge, Sn, Pb) and Group 15 (P, As, Sb, Bi) elements, of which little was known. In particular, clusters comprised of Group 14 or 15 elements combined with transition metals were shown to adopt structures that differed from known intermetallic phases, and therefore exhibit unique electronic properties and reactivities. [8,9] All of these investigations lead to a rapid

expansion of main group element chemistry, which today has applications ranging from energetics, materials science, nanomaterials, and medical technology.

The work described in this thesis focused on the synthesis and characterization of new main group element clusters of groups 13 and 15, synthesized through two separate routes. Low oxidation state ligand-stabilized homoatomic Group 13 clusters of aluminum have been synthesized through a disproportionation method, utilizing a specialized apparatus to gain access to pre-reduced Al(I)X (X = Cl, Br) subhalide solutions. Heteroatomic clusters of Group 15 elements (P, As) and transition metals, both ligated and "naked", have been synthesized using Zintl precursors. Each of these methodologies and the classifications of products obtained are detailed herein.

1.2 Group 13 Elements

The chemistry of the Group 13 elements boron, aluminum, gallium, indium, and thallium is diverse and fascinating. Unlike other families of elements, the Group 13 elements do not display cohesive properties in terms of their elemental electronegativities, oxidation states, and reactivities. Boron, a metalloid, tends to form bonds that are more covalent than other members of the group, and exhibits the largest electronegativity of the Group 13 elements (2.04 on the Pauling scale). It is common for boron to exist in compounds with multiple B-B bonds with an oxidation state of +1. Aluminum and gallium are typically observed in the +3 oxidation state, and most often behave as Lewis acids due to their electron deficiency. Low valent compounds for Al and Ga are far less abundant, while indium and thallium are more commonly found in the +1 oxidation state due to the inert pair effect. Though indium may also be present in its +3 oxidation state, this is not the case for thallium, which almost exclusively exists as +1.[7,10]

Considerable interest has been shown in development of the field of subvalent aluminum and gallium chemistries, which could have applications in organometallic chemistry and energetic materials research, much like their boron congeners. [10-14] One subset of low-valent Group 13 chemistry studies the formation of metalloid clusters of the type E_nR_m (n > m), where the number of metal-metal bonds exceeds the number of metal-ligand bonds. [15,16]

1.2.1 Synthesis and Reactions of Al(I) and Ga(I) halides

Professor Hangeorg Schnöckel, expanding on the work of Dr. Peter Timms, [17,18] pioneered solution-phase low-valent Group 13 chemistry through the development of a synthetic method used to generate metastable AlX and GaX (X = Cl, Br, I) solutions using a novel metal-halide co-condensation reactor (MHCR, Figure 1.1).[15] During operation of the MHCR, HX gas flows over molten aluminum inside of a resistively heated graphite furnace (**B**), initially yielding the trivalent species and hydrogen gas (Equation 1.1). At high temperature and low pressure, comproportionation occurs between the trihalide and two additional equivalents of molten metal to produce the monovalent species (Equation 1.2). Equilibrium of this reaction can be manipulated to favor the monovalent halides, so that at 1000 °C and 10^{-3} mbar, it is possible to synthesize AlX (X = Cl, Br) species in yields exceeding 95%.[19] Examples for the generation of aluminum (I) halide are given below:

$$Al\ (l) + 3HX\ (g) \rightarrow AlX_3\ (g) + 3/2H_2\ (g) \qquad (1.1)$$

$$AlX_3\ (g) + 2Al\ (l) \rightleftharpoons 3AlX\ (g) \qquad (1.2)$$

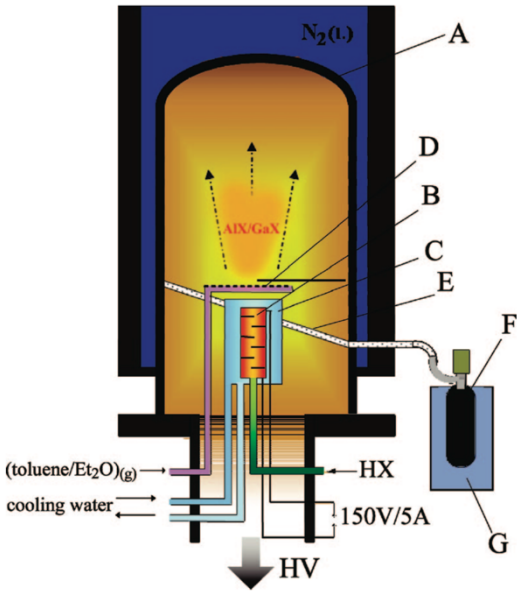

Figure 1.1 Schematic of the metal-halide co-condensation reactor designed by Schnöckel. A = Stainless steel bell jar (30L), B = Al (s) or Ga (s) in resistively heated graphite furnace piece, C = Cooling shield, D = Solvent inlet, E = Drainage trough, F = Schlenk vessel, G = Dewar cooled to -78°C, HX = Hydrogen halide gas (X = Cl, Br), HV = High vacuum (oil diffusion pump). Adapted from [10]

These subvalent aluminum / gallium halide species deposit on the interior surface of the reactor (**A**) at 77K in a solvent mixture of 3:1 toluene: donor solvent (e.g. diethyl ether, triethylamine, or THF). Once the reaction is complete, the solution thaws, draining into an air-free Schlenk type vessel (**F**) cooled to -78ºC (**G**). These solutions are metastable with respect to disproportionation for up to one month when stored at -80 °C.

Upon warming of these solutions, disproportionation will readily occur to produce bulk metal and trihalide (Equation 1.3).

$$3AlX \rightarrow 2Al\ (s) + AlX_3 \qquad (1.3)$$

If anionic ligands are introduced to the solutions before disproportionation begins, the kinetic intermediates that form as the reaction proceeds can be trapped as molecular systems or metalloid clusters. Sterically bulky ligands such as terphenyl, β-diketiminate, and guanidinate have generated low-valent Al or Ga atoms in discrete molecular systems such as those shown in Figure 1.2. [20-23] The terphenyl-derived compound :GaAr (**1.1**, Ar = 2,6-diisopropylphenyl) is a rare example of a neutral organogallium(I) complex. Compounds :Al(^{Ar}NacNac) (**1.2**, ^{Ar}NacNac = [N(Ar)C(Me)]$_2$CH)**)** and :Ga(Ar$_2$N)$_2$CNCy2 (**1.3**, Cy = cyclohexyl) have exhibited interesting behavior, including the ability to behave analogously to N-heterocyclic carbenes and insert into unsaturated C-C bonds.

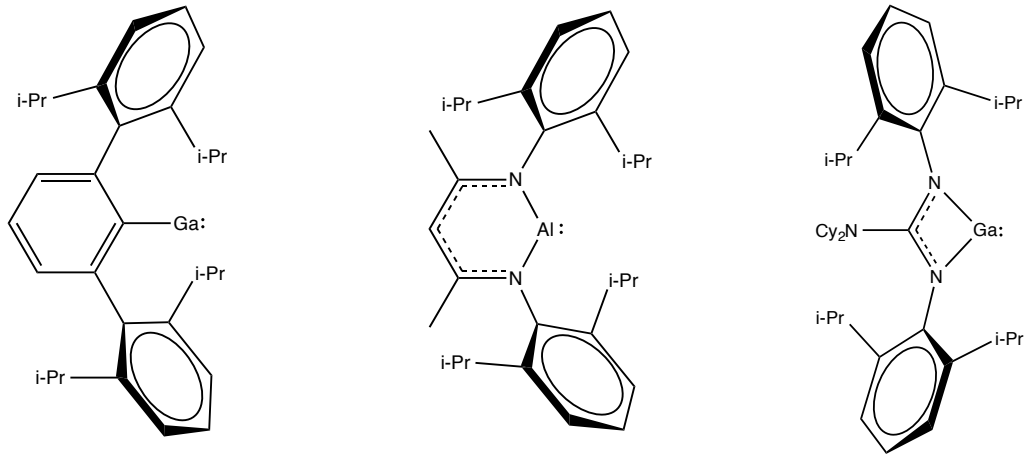

(1.1) **(1.2)** **(1.3)**

Figure 1.2: Structures of :GaAr (1.1, Ar = 2,6-diisopropylphenyl) derived from a terphenyl ligand system, the β –diketiminate derived :Al(^{Ar}NacNac) (1.2, ^{Ar}NacNac = [N(Ar)C(Me)]$_2$CH), and the guanidinate complex :Ga(Ar$_2$N)$_2$CNCy2 (1.3, Cy = cyclohexyl). 1.2 and 1.3 demonstrate characteristics isolobal to 6 and 4-membered N-heterocyclic carbenes.[4]

Silylated amine and methyl derivatives such as hexamethyldisilazide (HMDS, N(SiMe$_3$)$_2^-$), and tris(trimethylsilyl)methyl anion (trisyl, C(SiMe$_3$)$_3^-$), as well as pentamethylcyclopentadienide (Cp*, C$_5$H$_5^-$) ligands, have been observed to promote both molecular and metalloid cluster formation. [24-38] Reaction conditions dictate whether the

molecular or metalloid compounds are formed in each case. Studies performed with the HMDS ligand demonstrated that reaction temperature and precursor solution have profound effects on product formation. When an AlCl precursor solution was reacted with Li(HMDS), the size of the clusters varied directly with reaction temperature. The cluster $Al_7(N(SiMe_3)_2)_6^-$ formed at -7°C, while $Al_{12}(N(SiMe_3)_2)_8^-$ was isolated at room temperature, and ultimately $Al_{69}(N(SiMe_3)_2)_{18}^{3-}$ was isolated after warming the solution to 60°C. [29,31] Performing these same experiments using the less reactive AlI solution yields $Al_{14}(N(SiMe_3)_2)_6I_6^-$ at room temperature, and one of the most notable metalloid clusters, $Al_{77}(N(SiMe_3)_2)_{20}^{2-}$, at 60°C. [7,32,33]

In addition to varying the type of precursor solution and temperature of each reaction to establish synthetic pathways leading to metalloid clusters, molecular species may be used as synthons to grow metalloid clusters, as is demonstrated by the formation of the metalloid cluster $Al_{50}Cp^*_{12}$ from its non-metalloid precursor, $Al_4Cp^*_4$ (Scheme 1). [39]

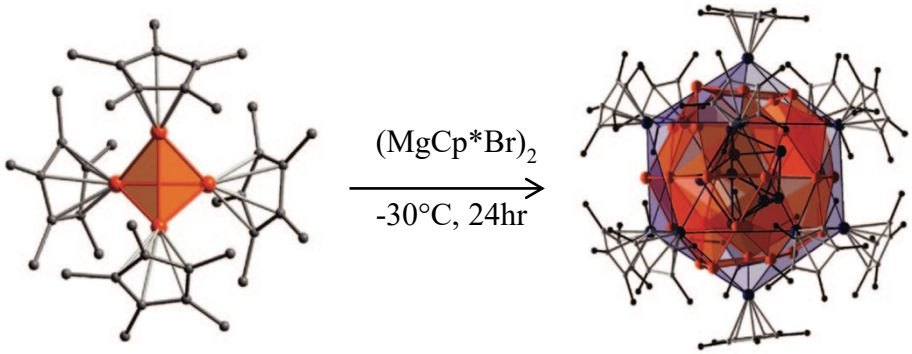

Scheme 1.1 Synthesis of the metalloid cluster $Al_{50}Cp^*_{12}$ from the molecular precursor $Al_4Cp^*_4$. H atoms omitted for clarity. Al = orange, purple C = black. Adapted from [10]

1.2.2 A Closer Look at Metalloid Clusters

Metalloid clusters can be viewed as kinetically trapped intermediates that form as subvalent species disproportionate into the bulk metal and trivalent species. These materials present the interface between large molecular metal clusters and small metallic nanoparticles. Typically, metal atoms in metalloid clusters have average oxidation states in between those of the bulk metal (ox state = 0) and the highest allowable oxidation state ($0 < n_{av} < n_{salt}$). The ligands mainly serve to provide a barrier to further disproportionation, stabilizing the metalloid cluster compounds. The structures of these clusters generally feature motifs that are relatable to the structure of their solid elemental metals (Figure 1.3). The metal atoms in larger clusters are commonly arranged in concentric shells, each becoming progressively less metallic towards the surface of the cluster. Oftentimes, their topologies can be represented as metal-ligand units protecting a metal Zintl-like core. This is seen in the structures of two most notable metalloid clusters, $[Al_{77}\{N(SiMe_3)_2\}_{20}]^{2-}$ and $[Ga_{84}\{N(SiMe_3)_2\}_{20}]^{4-}$ (Figure 1.4).

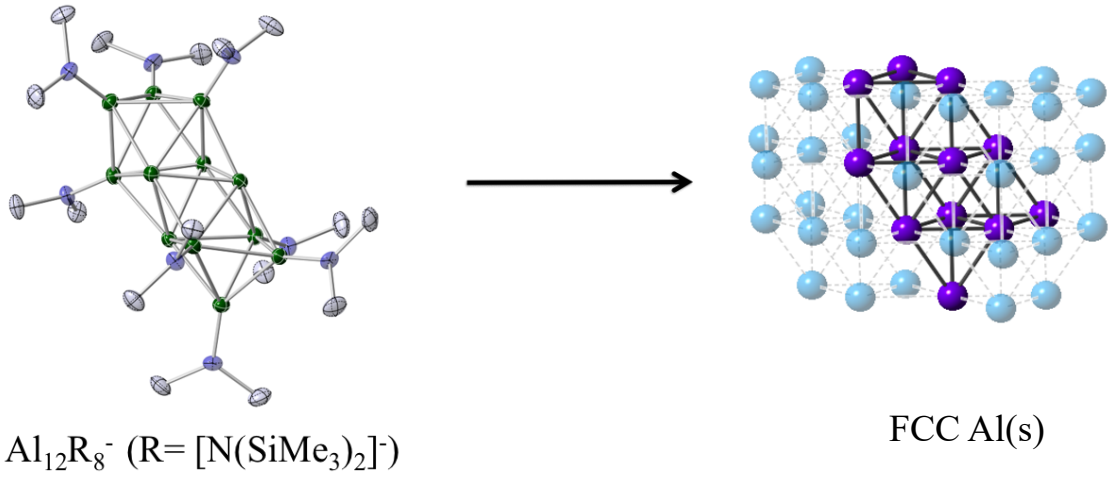

Figure 1.3 Structure of $Al_{12}(N(SiMe_3)_2)_8^-$ and its resemblance to the topology found in metallic Al. Al = green, Si = Gray, N = purple. Carbons and hydrogens omitted for clarity.

The cluster $[Al_{77}\{N(SiMe_3)_2\}_{20}]^{2-}$ contains a central naked Al atom coordinated by a distorted icosahedral shell of 12 Al atoms. The next shell contains 44 Al atoms, followed by a shell of 20 Al-HMDS units. The average Al-Al bond distances within each shell decrease from the icosahedral shell (2.760 Å) to the outer shell (2.688 Å), indicating that the nature of Al-Al bonds is transitioning from metallic to molecular. [33]

The $[Ga_{84}\{N(SiMe_3)_2\}_{20}]^{4-}$ cluster, synthesized from the reaction of $GaBr\cdot(THF)_n$ and $LiN(SiMe_3)_3$, is the largest known Group 13 metalloid cluster. At the center are two Ga atoms, surrounded by a conical construction of 32 Ga atoms with icosahedral caps. A belt of 30 Ga atoms encapsulates the Ga_2Ga_{32} unit, and the entire framework is capped with 20 GaHMDS groups. This cluster has a high pseudosymmetry, and exhibits molecular bonding that is analogous to that found in fullerenes. [40] Additionally, this cluster contains a high degree of mixed-valency Ga atoms, which may also be chemically different. Together, clusters $[Al_{77}\{N(SiMe_3)_2\}_{20}]^{2-}$ and $Ga_{84}\{N(SiMe_3)_2\}_{20}]^{4-}$ represent the canonical examples of metalloid clusters.

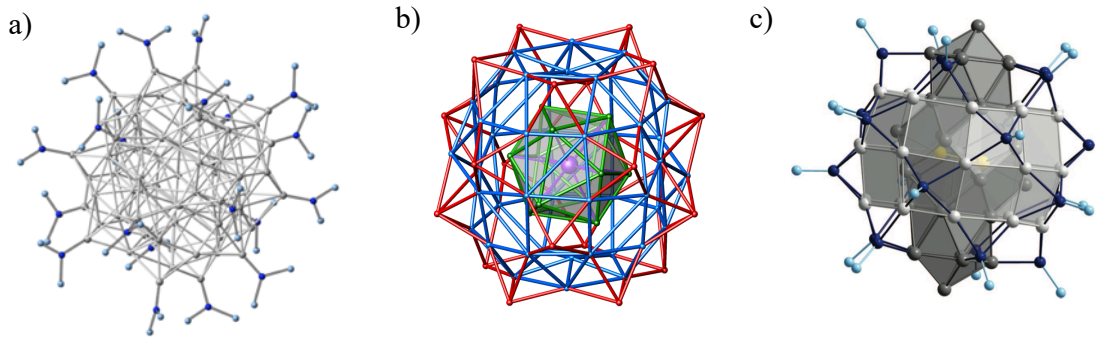

Figure 1.4 Perspective view of $[Al_{77}\{N(SiMe_3)_2\}_{20}]^{2-}$ (a,b) and $Ga_{84}\{N(SiMe_3)_2\}_{20}]^{4-}$ (c). (a) may be viewed as a central Al atom (violet) coordinated to an icosahedral shell of 12 Al atoms (green), followed by a shell of 44 Al atoms (blue), which are capped by 20 Al(HMDS) units (red). Carbon and hydrogen omitted for clarity. (b) highlights the shell arrangement of Al atoms (c) contains two central Ga atoms (yellow), surrounded by a conical tube of 32 Ga atoms (dark gray), surrounded by a belt of 30 Ga atoms (light gray). These shells are capped by 20 Ga-HMDS units (Ga = dark blue, N = light blue). For clarity, silicon, carbon, and hydrogen omitted.

Reactions with the above-mentioned ligands have been well studied and characterized. The research presented in Chapter 2 of this thesis will extend beyond the traditional syntheses by investigating the reactions of aryl ligands, beginning with the phenyl ligand, which has been used to isolate a low oxidation state aluminum cluster in multiple crystallographic modifications.

1.3 Zintl Chemistry

Zintl chemistry is a subclass of main group cluster chemistry focused on investigations of cyclic polyanions of main group elements 13-16. The first mention of main group anions was in 1890 by the French scientist M. Joannis. [41] He observed that when lead metal was dissolved in sodium / liquid ammonia solutions under various conditions, a distinct color change from the characteristic blue of solvated electrons to an intense green occurred. These solutions precipitated Na_xPb_y species (e.g. $NaPb_4 \cdot 2NH_3$, $NaPb_2$), giving the first indication that main group elements could exist in an anionic

state. In 1907, electrochemical studies by Kraus *et al.* confirmed that these solutions did contain plumbides, which behaved as electrolytes, dissociating like salts to give Na^+ and Pb_x^- (x = 2, 4). Through subsequent electrochemical experiments on Na/Pb and Na/Sb solutions, scientists Smyth and Peck, *et al.*, determined the stoichiometry of dissolved anions to be 2.25 Pb : 1.0 Na and 2.33 Sb: 1.0 Na. [42] The molecular formulas were determined to be $Na_4Pb{\cdot}(Pb_8)$ and $Na_3Sb{\cdot}(Sb_6)$, corresponding to solution-phase anions Pb_9^{4-} and Sb_7^{3-}, which are now well-known and studied. [43]

Building on these results, Eduard Zintl performed potentiometric titrations of normal-valent main group element salts such as PbI_2 in metallic sodium solutions of liquid ammonia to elucidate the stoichiometry of numerous solutions-phase polyatomic anions of main groups elements 14 and 15 (Equation 1.4) [8,44]

$$(4 + 2x)Na + xPbI_2 \rightarrow Na_4Pb_x + 2xNaI \qquad (1.4)$$

Potentiometric titration allowed for determination of both metal and sodium oxidation states in solution. These studies revealed that electrochemical methods could be used to prepare homoatomic polyanions of tetrels and pnictides of the forms E_9^{4-} (E = tetrel, Pb, Sn), Pn_7^{3-} (Pn = pnictide, Sb, Bi), Pn_5^{3-} (Pn = As, Bi), Pn_3^{3-} (Pn = As, Sb, Bi) in solution, and established a link between the solid-state and solution phases. [45,46] To honor his groundbreaking contributions to the field of main group chemistry, main group element polyanions of this form and their solid-state precursors were posthumously named "Zintl anions," and "Zintl phases", respectively.

The formula and structure of proposed Zintl anions were not verified until almost 45+ years later, when the crystal structure $[Na_4(en)_7][Sn_9]$, containing the polycyclic anion Sn_9^{4-}, verified the proposed cage structure of Zintl anions. Structural elucidation of multiple tetrel and pnictide cages was further made possible by Corbett *et al.*, who used

chelating agents such as 2,2,2-cryptand to sequester cations. [47] Sequestering agents promote crystallization by effectively enhancing the size of the cations relative to anions, allowing for more efficient packing in the crystal lattice. Additionally, use of cation sequestering agents is also crucial to enhance reactivity of the polycyclic cages by interrupting the strong ion pairing between K^+ and the anion.

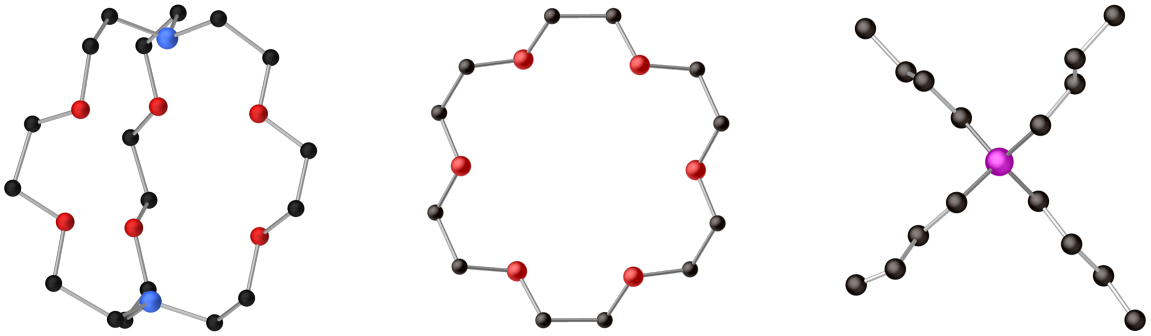

2,2,2-cryptand 18-crown-6 $[(n\text{-Bu})_4P]^+$

Figure 1.5 Common cation sequestering agents or cations used to aid in reactivity and crystallization of products from Zintl reactions. $[(n\text{-Bu})_4P]^+$ originates from the salt $[(n\text{-Bu})_4P]Br$, added to reaction solutions to both sequester K^+ and serve as a cation.

Polyanions of Groups 14 and 15 assume very different structures and therefore exhibit completely different reactivity. Group 14 (tetrel) polyanions tend to adopt polyhedral borane-like geometries, while Group 15 (pnictogen) cages have localized two-center two-electron (2c-2e) bonds, and are electron precise. Emphasis will be placed on describing the structure, bonding, and reactivity of Group 15 Zintl anions, though derivatives of Group 14 polyanions will be presented, primarily for comparison.

1.3.1 Homoatomic Clusters of Group 15 Zintl Anions

Group 15 elements exhibit a wide range of structural variability when forming homoatomic polyanionic chains, rings, and clusters. Group 15 elements tend to form electron-precise structures containing two-center, two-electron bonds, reminiscent of

organic species. Select homoatomic polyanions isolated from Zintl phases both in solid state and using solution methods shown in Figure 1.6. [48-60]

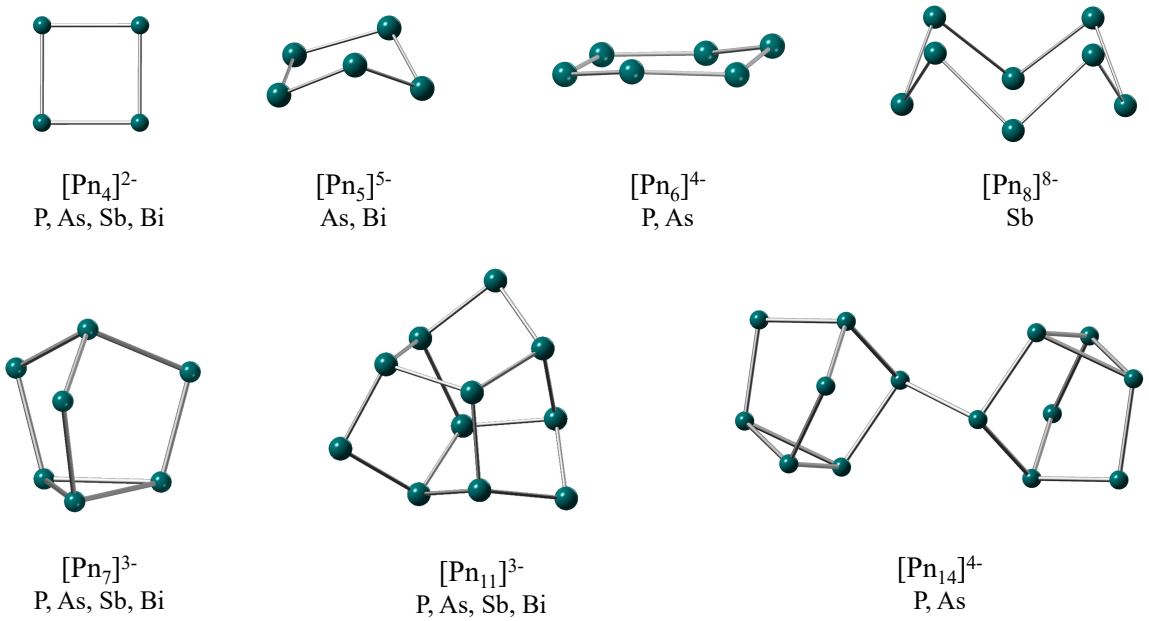

Figure 1.6 Select structures of homoatomic Group 15 clusters isolated from either solid state or solution-phase methods.

1.3.2 Derivatives of $[Pn_7]^{3-}$ Zintl Ions

The Zintl anion $[Pn_7]^{3-}$ can be obtained from the phases A_3Pn_7 (A = Li, Na, K, Rb, Cs; Pn = P, As, Sb) and Ae_3Pn_{14} (Ae = Sr, Ba; E = P, As). The most commonly used precursor is the phase of nominal composition K_3Pn_7 (Pn = P, As, Sb), formed from a fusion of corresponding elements in the solid state. When these solid state Zintl ion precursors are extracted into a polar aprotic solvent such as ethylenediamine (en), pyridine (py), N,N'-dimethylformamide (DMF), or liquid ammonia (NH_3), the solutions contain polycyclic $[Pn_7]^{3-}$. Use of appropriate sequestering agents such as 2,2,2-cryptand or 18-crown-6 prevents extensive ion pairing between the polyanion and free K^+, thus enhancing reactivity. [60]

These C_{3v}-symmetric cages are electron-precise, comprised of two-center, two-electron Pn-Pn bonds, and isolobal to the carbon species nortricyclane (C_7H_{10}), where a neutral Pn ≅ CH and anionic Pn^{1-} ≅ CH_2 . Within the structure, each atom of a basal triangle (Pn5, Pn6, Pn7) is linked by three vertex atoms (Pn2, Pn3, Pn4) to an apical atom (Pn1) (Figure 1.7), resulting in a structure comprised of three fused cyclo-Pn_5 faces. Each two-coordinate bridging pnictide vertex is formally 1^- , and isolobal to a CH_2 unit, yielding an overall charge of 3^- for the anion. The longest bonds in each heptapnicanortricyclane trianion occur in the basal triangle (C), while the vertex atoms (B) exhibit the shortest Pn-Pn bonding.

These clusters react in a variety of ways, owing to their nucleophilicity, basicity, high reductive potential, and relative instability of the nortricyclane-like geometry. [43,60,62] Broadly, products of reaction with these cages can be categorized by those that retain the parent nuclearity and approximate cage geometry, and those where significant activation of the parent cage has occurred.

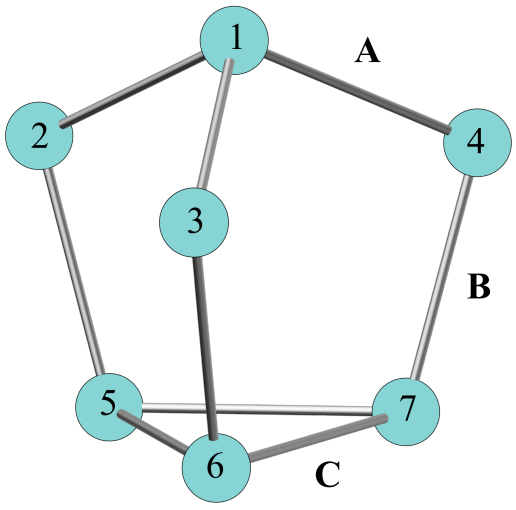

Figure 1.7 Structure of the $[Pn_7]^{3-}$ anion (Pn = P, As, Sb, Bi), with atoms and unique bond groups labeled. Distances given in Table 1.2. Adapted from [60]

Table 1.2: Mean bond lengths [Å] in the $[Pn_7]^{3-}$ series of Zintl anions. Labeling of bond groups consistent with Figure 1.6.

Bond	$[P_7]^{3-}$	$[As_7]^{3-}$	$[Sb_7]^{3-}$	$[Bi_7]^{3-}$
A	2.20	2.43	2.78	2.94
B	2.15	2.40	2.70	2.90
C	2.26	2.50	2.86	3.07

Cages $[Pn_7]^{3-}$ can coordinate to ligands primarily in either η^1, η^2, or η^4 coordination modes, where pnictide vertices behave as two-, four-, and six-electron donors, respectively. [63-65]

In the cage of η^4 coordination, cages undergo a structural rearrangement. Homolytic cleavage of a bond in the basal triangle gives rise to a norbornadiene-like geometry. The identity of the main group element and the transition metal fragment both influence the degree of cage activation. The extent of this activation is reflected in Pn4-Pn5 and Pn6-Pn7 bond distances, which should be equal if complete bond cleavage has occurred.

The $[(CO)_3Cr(\eta^4\text{-}As_7)]^{3-}$ anion was the first structurally characterized Zintl anion / transition-metal coordination complex to highlight this norbornadiene – nortricyclane cage interconversion. [63] Soon after, the Sb/Mo analogue $[(CO)_3Mo(\eta^4\text{-}Sb_7)]^{3-}$ was reported, along with the isostructural series $[(CO)_3M(\eta^4\text{-}Pn_7)]^{3-}$ anions (M = Cr, Mo, W; Pn = P, As, Sb). Subsequent functionalization of the $[(CO)_3M(\eta^4\text{-}Pn_7)]^{3-}$ anions through protonation, alkylation, and metalation indicated that the apical pnictide atom Pn1 of the norbornadiene cage was the most reactive site (Scheme 1.2) during electrophilic addition. The norbornadiene cage and η^4 - ligation to the original $M(CO)_3$ fragment was unchanged during these reactions. Nucleophilic addition showed metal-based reactivity, with an equivalent of CO adding to the transition metal, causing an η^4: η^2 shift in coordination

mode of the Pn_7 ligand, with the cage returning to a nortricyclane-like geometry. These transformations are summarized in Scheme 1.2. [66-70]

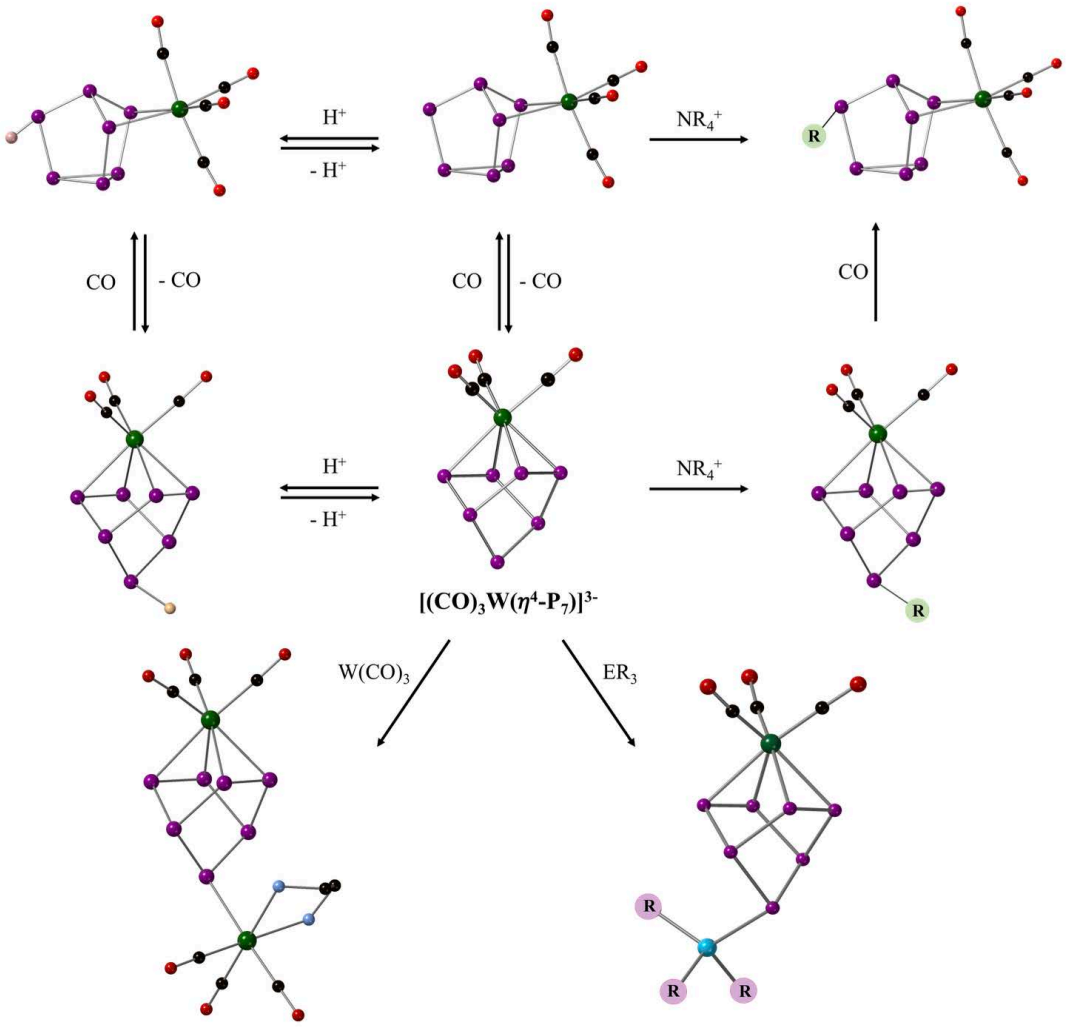

Scheme 1.2: Transformations available for the $[(CO)_3W(\eta^4\text{-}P_7)]^{3-}$ ion.

1.3.3 Heteroatomic and Intermetalloid Clusters

Reactions of transition metal complexes with different $[Pn_7]^{3-}$ do not always yield the same product type. In certain instances, the $[Pn_7]^{3-}$ structure undergoes extensive reorganization, forming subunits that are no longer directly relatable to the parent ion in arrangement or nuclearity. For example, reaction of $[P_7]^{3-}$ with $Ni(CO)_2(PPh_3)_2$ gives the

coordination complex $[(CO)Ni(\eta^4\text{-}HP_7)]^{3-}$, in which the polyphosphide cage is structured in a norbornadiene-type arrangement, as discussed in the previous section. [71] Reaction of this same $Ni(CO)_2(PPh_3)_2$ complex with $[Sb_7]^{3-}$ resulted formation of the ion $[(CO)_3Ni_3Sb_7]^{3-}$, which exhibits a 10 atom nido-$[Ni_3Sb_7]$ core (Figure 1.7), one in which the arrangement of the seven antimony atoms no longer bore resemblance to either nortricyclane- or norbornadiene-$[Sb_7]^{3-}$. This unique structural arrangement is more directly relatable to the deltahedral structures known for the tetrel Zintl complexes, and, more importantly, was the first product of this kind, where transition metals were incorporated into the core of the cluster. [72]

Since this initial discovery, several other anions, both ligand-stabilized and carbon-free (binary) anions of Group 15 – transition metal systems have been isolated, exhibiting extensive activation of the Zintl precursor (Figure 1.8, Table 1.2). Binary anions have been successfully isolated by employing transition metal complexes with particularly labile ligands during syntheses. This strategy was used by Eichhorn *et al* to isolated the crown-like $[MoAs_8]^{2-}$ anion using the highly labile $Mo(naphthalene)_2$ precursor. Currently, the series of $[MPn_8]^{n-}$ (M = Cr, Mo, Nb ; Pn = As, Sb ; n = 2, 3) have been isolated, in addition to the chain polymer $^1{}_\infty[(KCrAs_8)^{2-}]$.[73-75] Isolation of the remarkable electron-precise $[As@Ni_{12}@As_{20}]^{3-}$ was the first structural instance of a Zintl ion bearing electronic resemblance to a fullerene species. The cluster, in which atoms are arranged in "onion-skin" type layers, is constructed of an $[(\mu^{12}\text{-}As)Ni_{12}]^{3-}$ icosahedron encapsulated in a nearly undistorted fullerene-like As_{20} dodecahedron. This cluster exhibits near perfect I_h symmetry, giving access to potentially eight oxidation states in solution. [76] Access to multiple oxidation states was later shown through isolation and characterization of $[Sb@Pd_{12}@Sb_{20}]^{3/4-}$, where clusters of varying charges were

characterized in gas-phase LDI studies, and in the solid-state. [77]. Other binary anions, such as $[Ni_5Sb_{17}]^{4-}$ and $[Pd_7As_{16}]^{4-}$ contain completely unique pnictide moieties. [78,79]

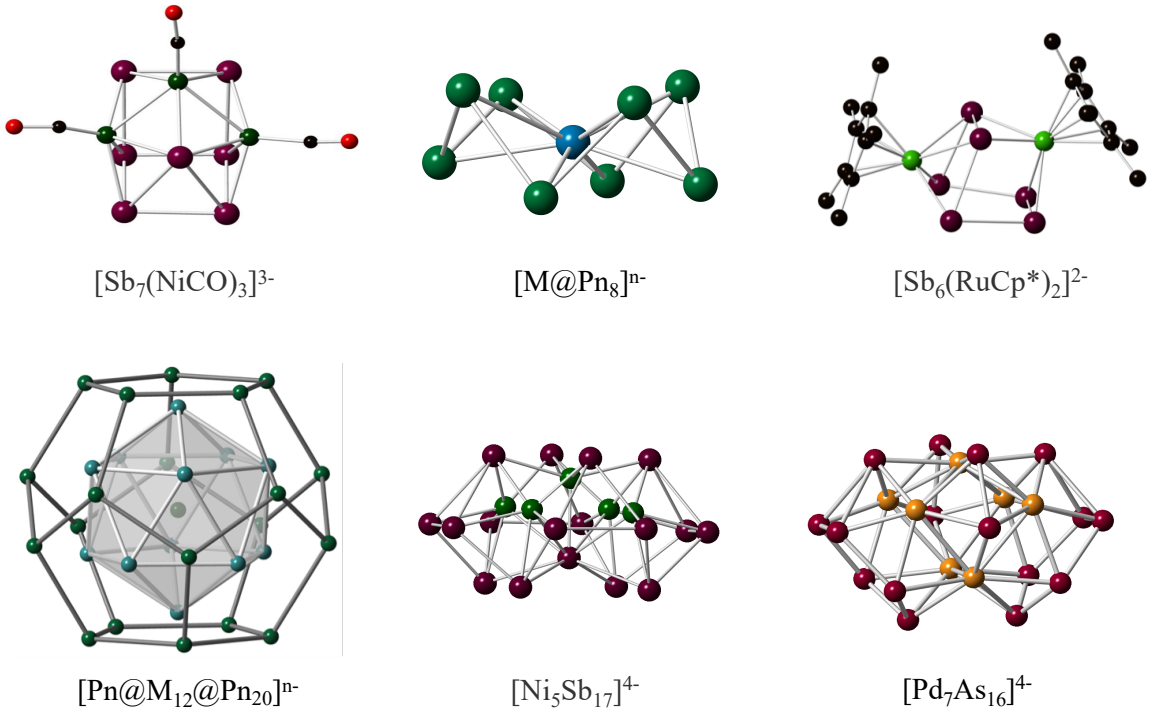

Figure 1.8 Select intermetalloid and binary anions of transition-metal Group 15 systems.

Table 1.2: Select ligand-stabilized and naked intermetalloid clusters.

Cluster	Ref.
Ligand-Stabilized	
$[Sb_7Ni_3(CO)_3]^{3-}$	80
$[Sb_8Co_6(CO)_6]^{3-}$	*
$[As_8Co_6(CO)_6]^{3-}$	*
$[Sb_6Ru_2Cp^*_2]^{3-}$	81
Binary Anions	
$[Ni_5Sb_{17}]^{4-}$	78
$[Pd_7As_{16}]^{4-}$	79
$[Rh_3As_{16}]^{3-}$	*
$[Mo_2P_{16}]^{4-}$	*
$[Ru_4As_{16}]^{3-}$	*
$[As_3CoAs_7]^{3-}$	*
$[RuSb_{13}]^{3-}$	*
$[M@As_8]^{n-}$ (M = Cr, Nb,	82
$[M@Sb_8]^{n-}$ (M = Nb, Mo)	83
$[As@Ni_{12}@As_{20}]^{3-}$	76
$[Sb@Ni_{12}@Sb_{20}]^{3-}$	77
$[Sb@Pd_{12}@Sb_{20}]^{3-/4-}$	77

*Unpublished results, found in this thesis or elsewhere.

1.4 Overview of the thesis

This thesis will present the synthesis and characterization of products obtained from both disproportionation methods of Al(I)X, and those obtained from reactions between transition metal complexes and pnictide Zintl precursors. Chapter 2 focuses on the synthesis and characterization of the mixed-valent, metastable aluminum cluster $[(Bu_2O)_3Li][Li_4Al_5Ph_{12}]$. Chapter 3 focuses on the synthesis and isolation of three As / Group 9 coordination complexes, $[(\eta^4\text{-}As_7)Co(\eta^3\text{-}As_3)]^{3-}$, $[(\eta^4\text{-}As_7)Rh(COD)]^{2-}$, and $[(\eta^4\text{-}As_7)Ir(COD)]^{2-}$. Chapter 4 discusses further reaction of the product type presented in Chapter 3 by highlighting features of the coordination complex $[(en)(CO)_3Mo(\eta^4\text{-}$

P_7)$Mo(CO)_3]^{3-}$. Chaper 5 focuses on synthesis and bonding descriptions of novel $[Pn_x]$ subunits exhibited in the binary anions $[Mo_2P_{16}]^{4-}$ and $[Rh_3As_{16}]^{3-}$.

Chapter 2: $[Li_4Al_5Ph_{12}]^{1-}$: A Metastable Low Oxidation State Aluminum-Lithium Cluster

2.1 Introduction

Clusters containing low oxidation state aluminum atoms (0 < ox. state < +3) have been of interest for over 40 years due to unusual structures, reactivity, and untapped energetic potential.[7,16] Reduction of organo-aluminum(III) halides (R_2AlX; R = alkyl, aryl, silyl) with alkali metals is the most common method of producing low-oxidation state aluminum clusters containing Al-Al bonds.[16] However, reductive methods typically employ sterically demanding ligands (terphenyl, NacNac, NON) to stabilize aluminum atoms in thermodynamically unfavorable oxidation states and protect from subsequent oxidation. The use of these ligands also restricts nuclearity of product clusters, where the number of Al atoms is limited to four or fewer, with the exception of the icosahedral $[Al_{12}{}^{i}Bu_{12}]^{2-}$, reported by Klinkhammer in 1991.[84] Aluminum monohalide precursor solutions [AlX•D (X= Cl, Br ; D = THF, Et_2O, or NEt_3)], containing pre-reduced aluminum in an average oxidation state of +1, are metastable at low temperature (-78 °C) with respect to disproportionation of the aluminum species (see Chapter 1, Equation 1.3).[25] These solutions provide access to far more complex species that are inaccessible through traditional reductive methods, specifically higher nuclearity clusters with extensive Al-Al bonding. Salt metathesis reactions between AlX•D solutions and organolithium salts, LiR (where R = organic ligand), promotes the formation of discrete molecular species such as the tetrameric $Al_4Cp^*_4$, where aluminum retains a formal 1^+ oxidation state. Salt metathesis reactions followed by disproportionation of Al^{1+} species has led to the isolation of metalloid clusters of the form Al_nR_m (where n>m), which exhibit rich structural diversity.[16] The arrangement of aluminum atoms in metalloid

clusters is topologically similar to the fcc arrangement of aluminum in Al metal. Therefore, metalloid clusters are oftentimes described as ligand-stabilized aluminum nanoparticles, kinetically trapped during disproportionation. Metalloid clusters $Al_{50}Cp^*_{12}$ and $[Al_{77}(N(SiMe_3)_2)_{20}]^{2-}$ have received attention for their potential applications in organometallic chemistry and energetic materials research, much akin to their boron congeners. Recent publications indicate that non-metalloid Al(I) species such as $[AlBr(NEt_3)]_4$ and $Al_4Cp^*_4$ are also effective dopants for hydrocarbon fuels, exhibiting a significant burn rate enhancement when compared to non-doped fuels.[85-87] To expand the scope of low-oxidation state Al species, both metalloid and non-metalloid, new ligand sets need to be considered.

While numerous low-oxidation state Al clusters have been stabilized through interactions with ligands such as $[C_5(CH_3)_5]^{1-}$ (Cp*), $[N(SiMe_3)_2]^{1-}$ (HMDS), and silyl derivatives $[SiMe_3]^{1-}$ $[Si^tBu_3]^{1-}$, $[Si(SiMe_3)_3]^{1-}$ (Hyp), examples of species containing σ-type subvalent aluminum-aryl bonds remain scarce. [7] Molecular species featuring Al(III)-Ph σ-bonds, such as di-μ-phenyl-bis(diphenylaluminum) (Al_2Ph_6), trimeric diphenyl aluminum hydride ($Al_3H_3Ph_6$), and the discrete molecule $AlPh_3•OEt_2$, have been reported extensively. [88] Power *et al*. investigated the reduction of the Al-terphenyl complexes Ar'AlI_2 (Ar' = C_6H_3-2,6-(C_6H_3-2,6-^{i}Pr$_2$)$_2$) and Ar"AlI_2 (Ar" = C_6H_3-2,6-(C_6H_2-2,4,6-Me_3)$_2$) with Na(s), yielding the low-valent dialuminyne, Na_2[Ar'AlAlAr'], and cyclotrialuminene, Na_2[(AlAr")$_3$], species, respectively (Figure 2.1). [89] These di- and trinuclear species demonstrated the ability of σ-donating aryl ligands to stabilize low oxidation state Al atoms and Al-Al bonds, making this class of ligands enticing candidates for reaction with AlX•D solutions.

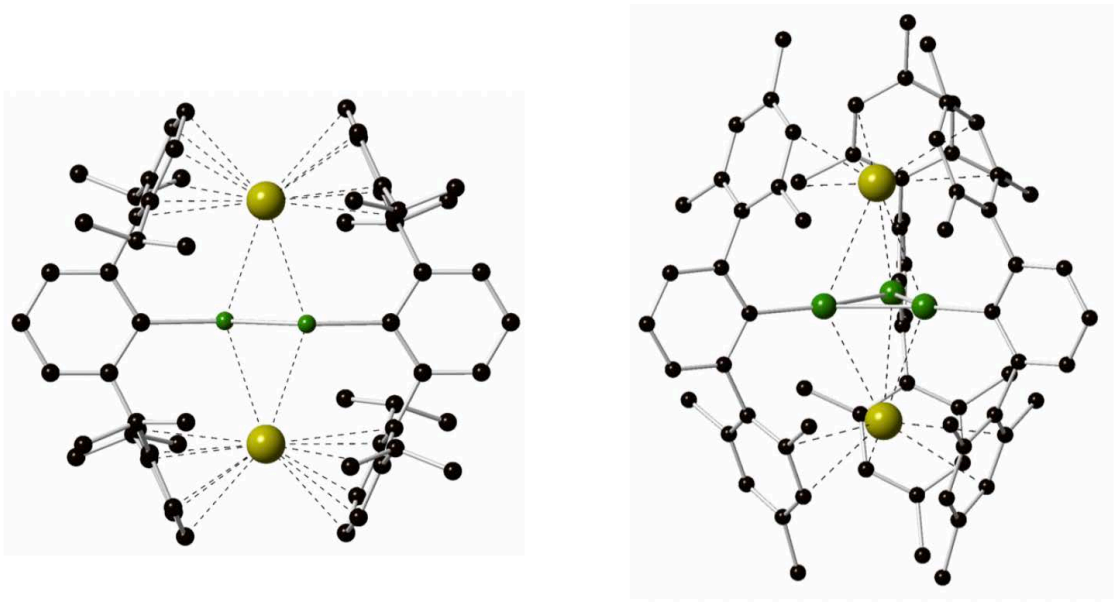

Figure 2.1: Perspective views of dialuminyne, $Na_2[Ar'AlAlAr']$ (left, Ar' = C_6H_3-2,6-2,4,6-$Me_3)_2$). Hydrogens omitted for clarity. Al = green, Na = yellow, C = black.

The sterically inhibiting nature of the terphenyl ligand, combined with incorporation of Na^+ into the cluster core undoubtedly restrict cluster nuclearity to two and three Al atoms. We selected the phenyl anion ($C_6H_5^-$, Ph) for initial study due to its decreased steric bulk, lack of reactive β-hydrogens, and hard, non-polarizable nature, properties similar to those of $[N(SiMe_3)_2]^-$ and $[C(SiMe_3)_3]^-$ ligands, which are known to stabilize metalloid clusters. Additionally, the phenyl anion is readily modifiable by a variety of substituents, allowing for alterations which may promote crystallization, tune electronic properties of products, or provide additional protection against subsequent oxidation.

We report here the synthesis and characterization of $[Li_4Al_5Ph_{12}]^{1-}$, which features a low oxidation-state, five-atom Al core stabilized by twelve σ-bound phenyl ligands and four Li^+ cations. The $[Li_4Al_5Ph_{12}]^{1-}$ anion forms reproducibly from a variety of synthetic routes and has been structurally characterized in the solid-state in several different

crystallographic modifications. The electronic structure, solid-state NMR properties, and mass spectral characterizations are also reported.

2.2 Results

2.2.1 Synthesis

Red-brown toluene / diethyl ether (tol / Et_2O) solutions of aluminum subhalides react with dibutyl ether (Bu_2O) solutions of phenyllithium (PhLi) at -78 °C to afford two new organoaluminum-lithium complexes. Metastable $AlBr\cdot(Et_2O)_n$ and $AlCl\cdot(Et_2O)_n$ solutions react with varying stoichiometric equivalents of PhLi (between 0.5 – 2) to produce the anion $[Li_4Al_5Ph_{12}]^{1-}$ (**2.1**) and the tetrahedral Al^{3+} complex, $LiAlPh_4$ (**2.2**) (Figures 2.2, 2.3). Attempts to optimize crystalline yields by tuning various reaction conditions resulted in the isolation of **2.1** in five distinct crystallographic modifications. For the sake of clarity, the first crystallographically characterized modification of the **2.1**, $[(Bu_2O)_3Li][Li_4Al_5Ph_{12}]\bullet 2(tol)$, isolated from the reaction of $AlBr\cdot(Et_2O)_n$ and 2 equivalents of PhLi, will be used as a representative model for discussion and bonding considerations. A summarization of reaction conditions used to isolate each modification of **2.1** is given in Table 2.1. Complete synthetic methodologies and details are given in the Experimental Section (2.4) of this chapter.

Complex **2.1** readily and reproducibly crystallizes from solution as a $[(Bu_2O)_3Li]^+$ salt with the polymeric co-product **2.2** (Equation 2.1). The presence of $LiBr_{(s)}$ and $Al_{(s)}$ by-products were confirmed through powder X-ray diffraction (pXRD) analyses.

$$10\ AlBr\bullet(Et_2O)_n + 16\ PhLi\bullet(Bu_2O)_n \longrightarrow [(Bu_2O)_3Li][Li_4Al_5Ph_{12}] + LiAlPh_4 + 10\ LiBr_{(s)} + 4\ Al_{(s)} \quad (2.1)$$

Table 2.1: A summary of reaction conditions used to isolate the distinct crystalline modifications of salts containing the $[Li_4Al_5Ph_{12}]^{1-}$ anion.

Product ID	Reaction	Product Formula	Space Group
UMAPS-14-12-LS	$AlBr{\cdot}(Et_2O)$ + 2 PhLi, -78°C →25°C or 25°C	$[(Bu_2O)_3Li][Li_4Al_5Ph_{12}]{\cdot}2(tol)$	*Pnna*
UM2671	$AlBr{\cdot}(Et_2O)$ + 1.5 PhLi -78°C →25°C	$[(Bu_2O)_3Li][Li_4Al_5Ph_{12}]{\cdot}2(tol)$	*Pnna*
UM2736	$AlCl{\cdot}(Et_2O)$ + 0.5PhLi -78°C →25°C	$[(Bu_2O)_x(Et_2O)_{3-x}Li]$ $[Li_4Al_5Ph_{12}]{\bullet}1.5(tol)$	*P-1*
UM2746	$AlBr{\cdot}(Et_2O)$ + 2 PhLi -78°C →55°C, TMEDA	$[(TMEDA)_nLi][Li_4Al_5Ph_{12}]{\cdot}2(tol)$	*R-3*
UM2789*	$AlCl{\cdot}(Et_2O)$ + PhLi -78°C →25°C or 55°C	$[(Et_2O)_3Li][Li_4Al_5Ph_{12}]{\cdot}2.5(tol)$	*C2/c*
UM2790*	$AlCl{\cdot}(Et_2O)$ + PhLi -78°C →25°C or 55°C	$[(Solvent)_xLi][Li_4Al_5Ph_{12}]$	*P-1*

*UM2789 and UM2790 co-crystallized from the same reaction solution. UM2789 was more abundant, crystallizing in a higher yield as dark brown needles, and exhibited less disorder than UM2790.

The salt $[(Bu_2O)_3Li][Li_4Al_5Ph_{12}]$ forms as dark brown microcrystalline blocks in low yield (~13%). The crystals are air and moisture sensitive, degrade in solutions of THF, CH_3CN, Et_2O, and are insoluble in toluene, benzene, and hexane, though the compound will slowly degrade when suspended in these solvents. The polymeric $LiAlPh_4$ co-crystallizes as aggregates of light yellow rods from the reaction mixture in higher yield (c.a. 40%), and has similar solubilities as **2.1**. Both complexes have been characterized by single-crystal X-ray diffraction (XRD), ^{27}Al solid-state NMR (SS-NMR), ^{7}Li SS-NMR, Electrospray Ionization Mass Spectrometry (ESI-MS), and Laser Desorption/Ionization time-of-flight Mass Spectrometry (LDI-TOF MS). The electronic structures were investigated by density functional theory (DFT) and electron localization function (ELF) quantum calculations.

2.2.2 Solid State Structures

2.2.2.1 $[(Bu_2O)_3Li][Li_4Al_5Ph_{12}]\bullet 2(tol)$

Crystals of the $[(Bu_2O)_3Li][Li_4Al_5Ph_{12}]\bullet 2(tol)$ salt are orthorhombic, space group *Pnna*, and contain one $[(Bu_2O)_3Li]^+$ cation, the $[Li_4Al_5Ph_{12}]^{1-}$ (**2.1**) cluster (Figure 2.2), and two toluene solvate molecules in the crystal lattice. The central Al of the $[Li_4Al_5Ph_{12}]^{1-}$ cluster resides on a crystallographic twofold rotation axis, with other atoms occupying general positions. Disorder is present in the dibutyl ether tails and the Li^+ ions of the $[(Bu_2O)_3Li]^+$ cation, as well as within the toluene solvate molecules, but was successfully modeled. Selected bond distances are reported in Table 2.2., and a summary of the crystallographic data is given in Table 2.3.

The $[Li_4Al_5Ph_{12}]^{1-}$ cluster (**2.1**) can be viewed as a mixed-valent complex containing a central Al^{1-} atom coordinated by four $(AlPh_3)^{1-}$ units (Al^{2+} + 3 Ph^{1-}), which are charge-balanced in part by four Li^+ ions (Figure 2.2). Apical Al^{2+} and Li^+ ions alternate, giving rise to a substituted body centered heterocubane-type architecture for the $[Li_4Al_5]^{11+}$ subunit of the structure (Figure 2.3a). Lithium ions are coordinated by neighboring Ph ligands through three η^2 cation-π interactions, with Li-C interactions ranging from 2.435(7) – 2.746(8) Å (see Figure 2.3b). Interactions between Li^+ ions and apical Al2 /Al3 atoms are very weak or non-existent, as suggested by long interatomic distances (3.000 - 3.238(1) Å). The distance between the central Al1 and each Li^+ ion is shorter, averaging 2.741(3) Å, which does not immediately suggest interactions. Contact between Al1-Li is highly dependent on the electron density available at the central aluminum atom, and were investigated through quantum chemical calculations on the $[Li_4Al_5]^{11+}$ core (discussed in Section 2.2.5).

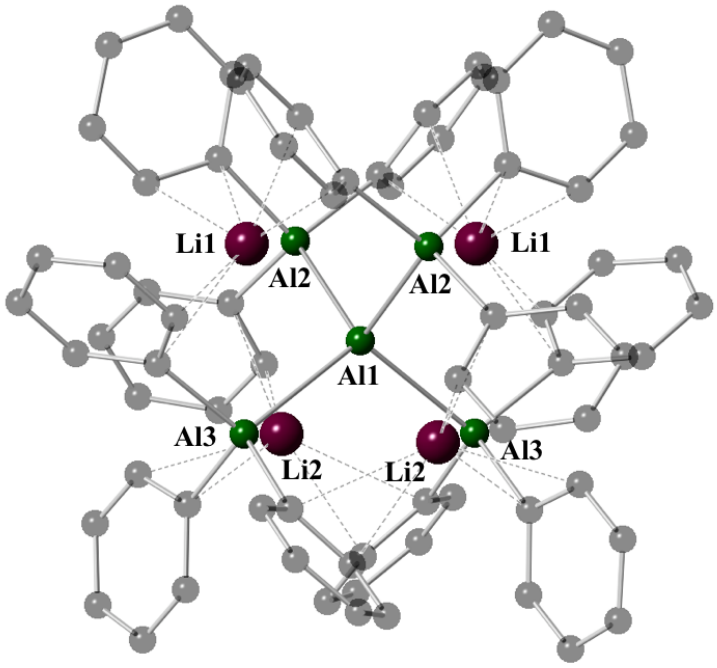

Figure 2.2: Ball and stick model of **2.1**, with Al and Li atoms labeled as symmetry equivalents based on the solid-state structure. Aluminum = green, lithium = violet, carbon = translucent black. Hydrogens omitted for clarity.

The $[Al_5]^{7+}$ metallic core of the $[Al_5Ph_{12}]^{5-}$ portion of the cluster forms a slightly distorted tetrahedron and exhibits virtual T_d point symmetry. The central Al displays near tetrahedral geometry, with Al-Al-Al bond angles ranging from 106.963(3) – 110.545(3)°, average 109.46(7)°. The Al1-Al2 and Al1-Al3 bond distances are 2.657(1) Å and 2.675(1) Å, respectively. These bonds are shorter than those found in fcc aluminum metal (2.86(1) Å), and are slightly longer than those reported for mixed-valent Al^0 -Al^{2+} clusters (2.53(3) – 2.55(2) Å). The bond distances fall on the continuum of low-oxidation state Al-Al bonds, existing within the range of other Al^{2+} -Al^{2+} (2.58(1) – 2.66(3) Å and Al^I-Al^I (2.64(1) – 2.77(1) Å) single bonds, such as those found in the tetrameric Al^I complex, $Al_4Cp^*_4$.

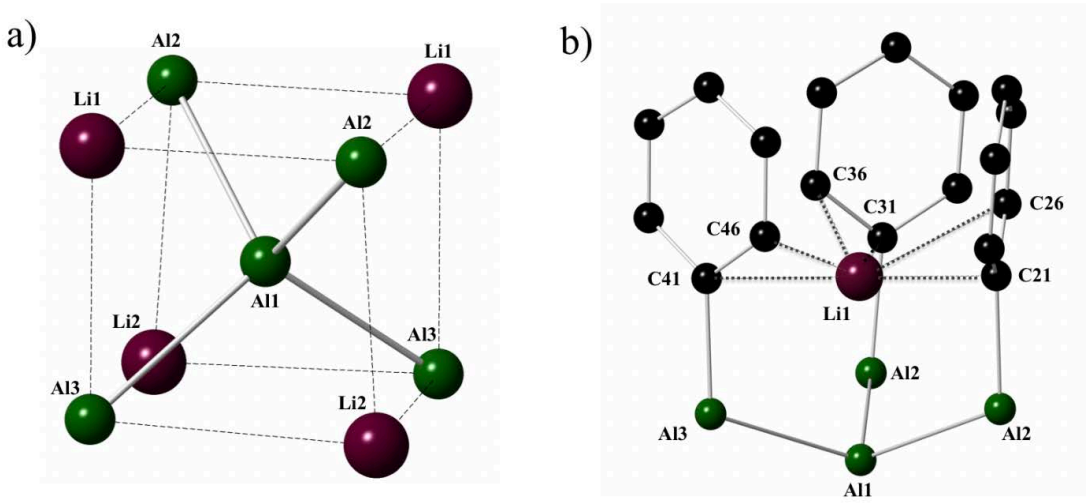

Figure 2.3: (a): $[Li_4Al_5]^{11+}$ cluster core of **2.1**. Al-Li interactions are shown only as a guide to illustrate the substituted body-centered heterocubane-like architecture of this portion of the cluster. (b): Bonding environment of a single Li^+ ion. Each Li^+ participates in three η^2 interactions with three adjacent Ph units, each bound to a different Al atom. Aluminum = green, lithium = violet, carbon = black. Hydrogens omitted for clarity.

The apical Al^{2+} atoms adopt distorted tetrahedral geometries with respect to the phenyl ligands and central aluminum atom, with C-Al-C bond angles ranging from 106.81(3) – 107.26(3)°. The Al-C_{ipso} bond distances in **2.1** are in the range 2.015-2.033(1) Å, which are similar to other subvalent Al-aryl bonds in the reported dialuminyne and cyclotrialuminene complexes. As expected, these Al-C_{ipso} bonds are slightly longer than those reported in other complexes containing Al^{3+}-C_{ipso} aryl bonds (1.943(2)-1.960(4) Å), due to the larger ionic radius of Al^{2+} as compared to Al^{3+}. Calculation of variance (σ^2) in bond lengths and angles between morphologies (see Table 2.4) indicates that there is no significant statistical difference in the bonding of the anionic cluster $[Li_4Al_5Ph_{12}]^{1-}$ of each solid-state structure.

Table 2.2: Select Bond Lengths [Å] and angles (°) for the $[Li_4Al_5Ph_{12}]^{1-}$ ion

Bond Lengths [Å]					
Al1-Al2	2.657(1)	Al1-Al3	2.675(1)	Al1-Li1	2.751(6)
Al1-Li2	2.731(6)	Al2-Li1	3.182(5)	Al2-Li2	3.186(7)
Al3-Li1	3.107(5)	Al3-Li2	3.235(7)	Al2-C11	2.025(4)
Al2-C21	2.034(4)	Al2-C31	2.031(3)	Al3-C41	2.021(4)
Al3-C51	2.017(4)	Al3-C61	2.015(4)	Li-$C_{centroid}$	2.672(1)
Li2-C11	2.656(8)	Li2-C16	2.435(7)	Li1-C21	2.531(7)
Li1-C26	2.525(7)	Li1-C31	2.657(7)	Li1-C36	2.498(7)
Li1-C41	2.531(7)	Li1-C46	2.487(7)	Li2C-C51	2.746(8)
Li2-C56	2.485(8)	Li2-C61	2.490(7)	Li2-C66	2.502(8)
Angles (°)					
Al2-Al-Al3	109.70(3)	C-Al-C	107.15(7)	Al-Li-Al	89.19(6)

2.2.2.2 Crystallographic Modifications of $[(Sol)_nLi][Li_4Al_5Ph_{12}]\bullet X$

All crystallographic modifications containing the anion **2.1** and select bond distances are listed in Table 2.4. Each modification, with the exception of UM2789 and UM2790, was synthesized using a different set of reaction conditions, which are detailed in the experimental section. Crystal environments are most likely determined by the inclusion and orientation of toluene solvate and the solvent coordinated to the Li^+ counter-cation. In some cases, disorder in the cation solvent shell could not be fully modeled, and excess electron density was accommodated using a SQUEEZE command, with all atoms modeled as C of varying occupancies.

Table 2.3: Select Crystallographic Collection and Refinement Data for $[(Bu_2O)_3Li][Li_4Al_5Ph_{12}]$•2(tol) (UMAPS-14-12-LS) and $LiAlPh_4$.

	$[(Bu_2O)_3Li][Li_4Al_5Ph_{12}]$•2(tol)[a]	$LiAlPh_4$[a]
Empirical formula	$C_{110}H_{130}Al_5Li_5O_3$	$C_{24}H_{20}AlLi$
Formula weight	1669.73	342.32
Temperature/K	150(2)	150(2)
Crystal system	Orthorhombic	Tetragonal
Space group	*Pnna*	$P\text{-}42_1/c$
a/Å	23.1070(7)	11.952(2)
b/Å	25.3897(8)	11.952(2)
c/Å	16.6714(5)	6.2757(11)
α/°	90	90
β/°	90	90
γ/°	90	90
Volume/Å^3	9780.8(5)	896.56
Z	4	2
ρ_{cal} cg/cm^3	1.134	1.268
μ/mm-1	0.054	0.059
F(000)	3576.0	360.0
Crystal size/mm^3	0.02 × 0.02 × 0.03	0.01 × 0.02 × 0.005
Radiation	Synchrotron (λ = 0.5180)	Synchrotron (λ = 0.5180)
2*θ* range for data collection/°	2.488 to 34.998	3.512 to 38.866
Index ranges	$-20 \le h \le 26$, $-29 \le k \le 28$, $-18 \le l \le 19$	$-11 \le h \le 15$, $-15 \le k \le 9$, $-5 \le l \le 7$
Reflections collected	70354	4052
Independent reflections	7977 [R_{int} = 0.0604, R_{sig} = 0.0395]	834 [R_{int} = 0.0747, R_{sig} = 0.0742]
Data/restraints/parameters	7977/595/684	834/0/64
Goodness-of-fit on F^2	1.091	1.000
R_1/wR_2 [$I>=2\sigma(I)$]	0.0795, 0.1577	0.0388, 0.0692
R_1/wR_2 [all data]	0.1004, 0.1678	0.0529, 0.0724

[a] See the Crystallographic Studies Section for details on the refinement.

Table 2.4: Average bond distances [Å], range [Å], and variance (σ^2) for Al-Al and Al-C_{ispo} interactions in $[Li_4Al_5Ph_{12}]^{1-}$ anion (**2.1**), reported for each distinct crystallographic modification and calculated for all modifications containing **2.1**.

Product ID	Space Group	Al-Al distances			Al-C_{ipso} distances		
		Average (Å)	Range (Å)	Variance[a] σ^2 x 10^{-3}	Average (Å)	Range (Å)	Variance[a] σ^2 x 10^{-3}
UMAPS-14-12-LS	*Pnna*	2.666(8)	0.017	0.096	2.022(24)	0.021	0.061
UM2671	*Pnna*	2.679(6)	0.013	0.056	2.030(17)	0.015	0.026
UM2736	*P-1*	2.671(7)	0.020	0.073	2.040(80)	0.079	0.61
UM2746	*R-3*	2.656(16)	0.036	0.324	2.029(35)	0.026	0.12
UM2789*	*C2/c*	2.664(1)	0.001	0.00033	2.026(19)	0.015	0.033
UM2790*	*P-1*	2.664(2)	0.010	0.0074	2.026(58)	0.052	0.31
All structures	**----**	**2.666(3)**	**0.035**	**1.4 x 10^{-5}**	**2.029(15)**	**0.018**	**5.2 x 10^{-5}**

[a]Variance (σ^2) $= \left[\Sigma_{i=1}^{N}(x_i - \bar{x})^2\right]/(N-1)$.

Table 2.5: Select Bond Distances [Å] and Angles (º) for clusters and molecules containing Al-Ar bonds through a σ-C_{ipso} bond. [88,89]

Na_2[Ar'AlAlAr']	**Na_2[(AlAr")$_3$]**	**Al_2Ph_6**
d(Al-Al): 2.428(1)	d_{av}(Al-Al): 2.520(2)	d(Al-Al): 2.701(2)
d(Al-C_{ipso}): 2.043(2)	d(Al-C_{ipso}): 2.021(3)	d(Al-C_{term}): 1.958(5)
d(Al-Na): 3.152(1)	d(Al-Na): 3.285(2)	d(Al-$C_{bridg.}$): 2.181(5)
d_{av}(Na-C_{centr}): 2.991(2)	d_{av}(Na-C_{centr}): 3.177(2)	C_{term}-Al-C'$_{term}$: 103.5(0.2)
Al-Al-C_{ipso}: 131.71(7)	Al-Al-Al: 60.0	C_{term}-Al-$C_{bridg.}$: 108.4(0.2)
$AlPh_3$•OEt_2	**$Al_3H_3Ph_6$**	
d(Al-C_{ipso}): 1.978-1.985(2)	d(Al-H): 1.62(3)-1.76(3)	
d(Al-O): 1.920(1)	Al-H-Al: 142(2)-145(2)	
O-Al-C: 103.6	H-Al-H: 96(1)-97(1)	
C-Al-C: 114.6	C-Al-C: 129.3(1)-132.4(1)	

2.2.2.3 [$LiAlPh_4$]

Crystals of [$LiAlPh_4$] are tetragonal, space group *P-42$_1$/c*, and contains one Al^{3+}, one Li^+, and one Ph ring (Figure 2.4). This structure is similar to that reported by Goel *et al*, but is solvent-free and forms one-dimensional chains.[88,90] The central Al^{3+} resides on a crystallographic fourfold inversion rotation axis. Two Li^+ cations are located on a crystallographic four-fold axis, with *ipso* and *para* carbon atoms occupying positions along two-fold rotation axes. Al is coordinated by four Ph rings via σ-bonded ipso carbons. Phenyl rings interact with the Li^+ cation via four η^2 cation-π interactions, linking neighboring $[AlPh_4]^-$ moieties (Figure 2.4a). The formula unit $LiAlPh_4$ is repeated in a polymeric fashion, with layers of chains interacting via edge-to-face *π-π* stacking interactions between phenyl rings of neighboring chains (Figure 2.4b).
The Al-C_{ipso} bond distance (2.009(2) Å) is shorter than those found in **2.1**, and slightly longer compared to other Al^{III}-C_{ipso} aryl bonds (1.943(2)-1.960(4) Å), which can be due to crystal packing influences rather than oxidation state considerations. A long interatomic distance between Al-Li (3.1378(6) Å) indicates no Al-Li bond. Li-C bond distances, ranging from 2.479(2) – 2.558(3) Å, are on the same order of magnitude as those found in the anion **2.1**. The Al and Li atoms are each in virtual tetrahedral coordination environments.

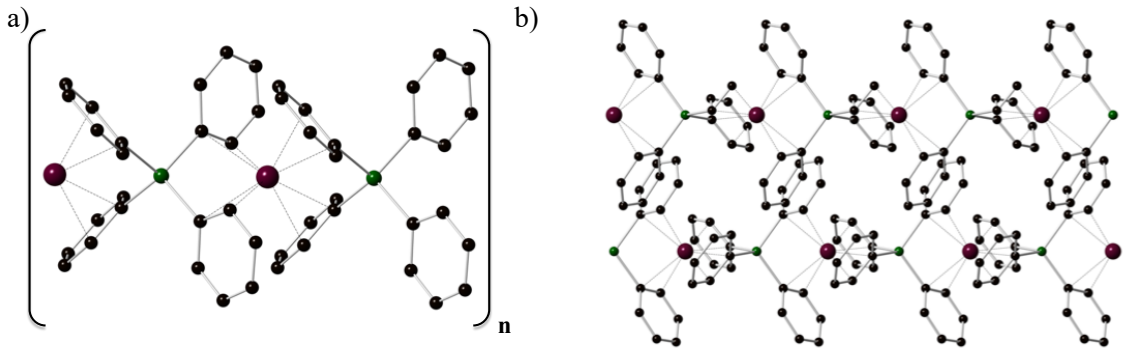

Figure 2.4: (a): Polymeric dimer of $LiAlPh_4$ showing cation-pi interactions between Li^+ and Ph rings. (b): Stacked chains of $[LiAlPh_4]_n$, linked primarily through edge-to-face π-stacking from Ph rings. Li = violet, Al = green, C = black. Hydrogens omitted for clarity.

2.2.3 Solid State NMR – Experimental and Theoretical Data

2.2.3.1 Experimental Data

Due to co-crystallization of 2.1 and 2.2, ^{27}Al and ^{7}Li SS-NMR spectra were collected on solids containing both complexes (in collaboration with Dr. Christopher Klug at the Naval Research Laboratory). Given the small crystallite size of both products and their co-crystallization, physical separation of the complexes was not possible (See Crystallographic Studies, Section 2.4.3, Figure 2.12).

The three distinct peaks in the ^{27}Al spectrum (Figure 2.5) correspond to the apical Al^{2+} ions in **2.1** (149.0 ppm), the central Al^{1-} of **2.1** (14.2 ppm), and the Al present in the co-crystallite **2.2** (132.2 ppm). Peak assignments were made through the use of an $LiAlPh_4$ standard (synthesized via reductive methods from $AlCl_3$ and PhLi), calculated chemical shifts (see below), and integrated peak ratios. The integration ratios for the Al^{2+}/Al^{1-} peaks (2.77:1) is less than expected (4:1), which could be due to the difference in relaxation times of the two nuclei. The peak at 132.2 ppm ($LiAlPh_4$, Al^{3+}) is the most

prominent peak in the spectrum, with integration ratios Al^{3+}/Al^{1-} (51.2:1) and Al^{3+}/Al^{2+} (18.6:1).

The intensity of the peak at 132.2 ppm intensifies over time, while the peak at 149.0 ppm diminishes. Ruling out oxidation of the sample, this conversion process could indicate decomposition of **2.1** into Al(s) and $LiAlPh_4$, as proposed in Equation 2.2. This proposed fluxional process, as indicated through changing peak intensities, is indication of the metastability of **2.1** in the solid-state.

$$[Li_4Al_5Ph_{12}]^{1-} \longrightarrow Al + n\ LiAlPh_4 \qquad \text{(Eq. 2.2)}$$

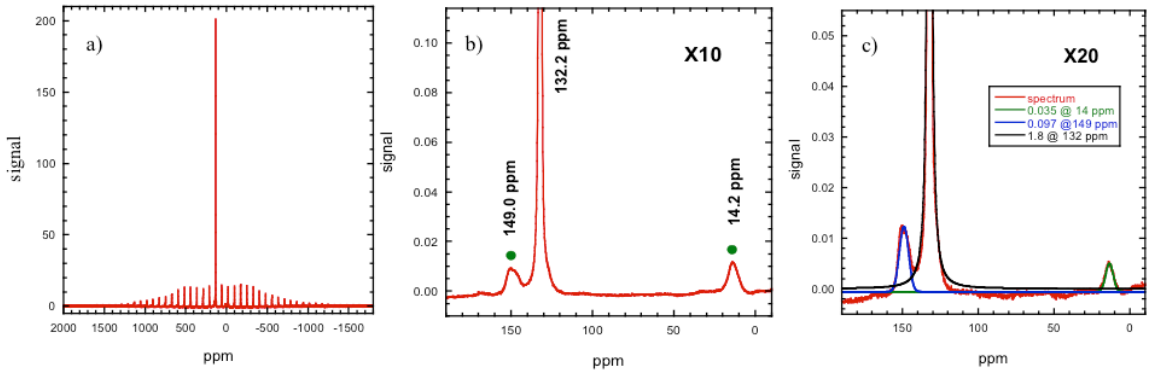

Figure 2.5: (a): ^{27}Al MAS NMR spectrum for $[(Bu_2O)_3Li][Li_4Al_5Ph_{12}]$. The spectrum was acquired following a single pulse of length 1 ms with a delay time between scans of 4 s and a spinning speed of 20 kHz. (b): Magnification of the region from 0 – 175 ppm, showing three signals. (c): Further magnification of signal. Peak-fittings, used to determine the signal intensities (integration of signal area) are given in the legend.

The spin-lattice relaxation time, T_1, for the peak at 14.2 ppm is nearly an order of magnitude longer than for the other peaks, indicating a different chemical environment for this Al signal, relative to the other two. Additionally, a ^1H to ^{27}Al cross-polarization experiment yielded signals for the two low-field peaks, but not the Al giving rise to the signal at 14.2 ppm, which is consistent with its assignment as the central Al^{1-} of **2.1**, given its coordination solely to other Al atoms. Lastly, ^{27}Al nutation experiments show that the two low-field peaks have similar quadrupolar couplings, another indication that

the Al atoms giving rise to the low-field signals are in very similar chemical environments.

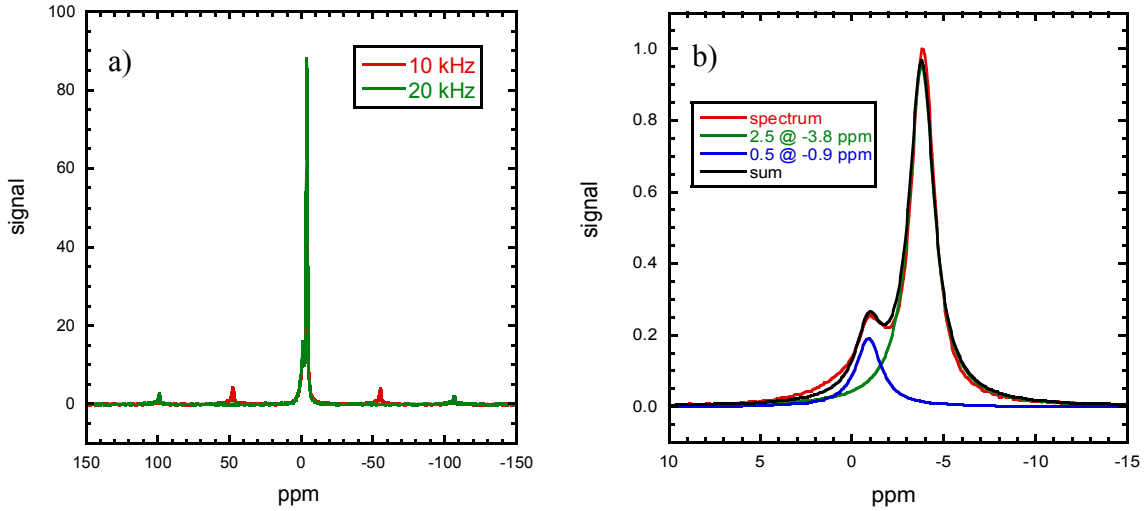

Figure 2.6: (a): ^{7}Li MAS NMR spectra for $[(Bu_2O)_3Li][Li_4Al_5Ph_{12}]$ and (b): Peak fits to two lines, determining signal intensities. Spectra acquired following a single pulse of length 1 ms with a wait time between scans of 2 s and a spinning speed of either 10 or 20 kHz.

^{7}Li MAS NMR spectra show two distinct Li^+ environments (Figure 2.6). Integration of the peaks gives a 5:1 signal for the chemical shifts at -3.8 ppm and -0.9 ppm respectively. The signal at -3.8 ppm is a combination of 4 Li^+ in the cluster core and that from $LiAlPh_4$, which are expected to have similar chemical shift values due to similar bonding environments. The signal at -0.9 ppm is attributed to the Li^+ ion of the $[(Bu_2O)_3Li]^+$ cation, which may be shifted further upfield due to coordination by Bu_2O.

2.2.3.1. SS-NMR Theoretical Calculations

Calculations were performed by Dr. Brett Dunlap at the Naval Research Laboratory. Full descriptions of theoretical methods and treatments are given in the experimental details section.

The calculated and experimental NMR parameters for ^{27}Al and ^{7}Li nuclei in $LiAlPh_4$ are shown in Table 2.6. The calculated quadrupolar coupling constants Cq agree with experiment (note that the sign of η is not determined experimentally). The experimental chemical shifts and theoretical shielding generally cannot be compared unless the theoretical shielding for a reference standard is also calculated, which was not done in this case, although trends can be informative.

Table 2.6: Calculated and experimental solid-state NMR parameters for ^{27}Al and ^{7}Li in $LiAlPh_4$

Nucleus	Experimental		Calculated	
	C_q (MHz)	σ (ppm)	C_q (MHz)	σ (ppm)
^{27}Al	0.82 ± 0.1	132.0 ± 0.5	-0.703	422.4
^{7}Li	0.028 ± 0.002		0.0374	93.4

The calculated chemical shieldings and experimental chemical shifts for ^{13}C in $LiAlPh_4$ are shown in Table 2.7. The shielding decreases with distance from the Al atom, perhaps due to inductive effects. The total range of calculated chemical shieldings is 21.7 ppm, while the total range of experimental chemical shifts is 21.3 ppm. The chemical shieldings given in Table 2.7 were calculated using the equation $\sigma = 169.9 - \delta$, where the chemical shift value, δ, was determined from experimental SS-NMR data (collected at Naval Research Laboratory by Dr. Christopher Klug).

As J-coupling calculations are not yet available for crystals, we performed gas-phase Gaussian09 calculations on the $Li_2AlPh_4^+$ ion. We used the nmr = spinspin and the 6-311G+(d,p) basis set and obtained 78 Hz for the Al-C1 *J* coupling constant. The experimentally determined J-coupling is 94 ± 2 Hz, in agreement with the calculation.

Table 2.7: Calculated and experimental chemical shifts for ^{13}C in $LiAlPh_4$. Chemical shield was calculated using the equation $\sigma = 169.9 - \delta$.

	Calculated	Experimental	
Site	**σ (ppm)**	**σ (ppm)**	**δ (ppm)**
C1	19.0	19.4 ± 0.2	150.5 ± 0.2
C2	25.9	27.0 ± 0.2	142.9 ± 0.2
C3	40.7	40.7 ± 0.2	129.2 ± 0.2
C4	41.0	40.7 ± 0.2	129.2 ± 0.2
C5	36.7	37.5 ± 0.2	132.4 ± 0.2
C6	39.0	37.5 ± 0.2	132.4 ± 0.2

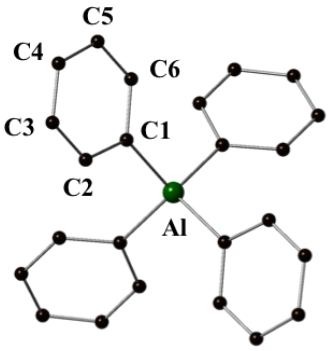

The NMR parameters calculated for ^{27}Al and ^{7}Li within the $[Li_4Al_5Ph_{12}]^{1-}$ anion are given in Table 2.8. Note that while the apical Al nuclei are not all equivalent by symmetry, as indicated by the solid-state structure, they have very similar shieldings. Thus, a mixture of products **2.1** and **2.2** might be expected to exhibit three ^{27}Al chemical shifts with the middle shift belonging to atoms in $LiAlPh_4$. The predicted difference between the ^{27}Al values for $LiAlPh_4$ and the apical Al^{2+} atoms in **2.1** is 6-9 ppm, while the difference in shift for the central ^{27}Al environments within the anion of **2.1** is predicted to be greater than 140 ppm. These calculations support the assignments given in the previous section.

Table 2.8: Calculated solid-state NMR parameters for ^{27}Al and ^{7}Li in $[(Bu_2O)_3Li][Li_4Al_5Ph_{12}]$.

Nucleus	Position	σ (ppm)
^{27}Al	Central Al1	557.6
	Vertex Al2	416.6
	Vertex Al3	413.2
^{7}Li	Vertex Li1	90.2
	Vertex Li2	90.1
	Counter-cation	92.0

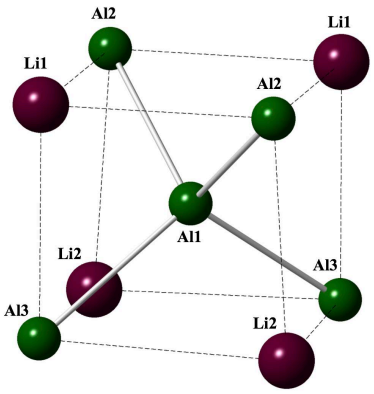

2.2.4 Mass Spectrometry Studies

2.2.4.1 Laser Desorption/Ionization Mass Spectrometry (LDI-MS)

Laser Desorption/Ionization time-of-flight mass spectra (LDI-TOF MS, Bruker Autoflex) were collected in negative ion mode with a nitrogen pulsed laser. Crystals of $[(Bu_2O)_3Li][Li_4Al_5Ph_{12}]$•2(tol) were loaded onto the sample holder via carbon tape with no matrix. Direct desorption from the crystalline samples at high laser pulse energies gave peaks for the parent ion, along with numerous fragments (Figure 2.7). High laser pulse energies also resulted in mass shifts of the ions to higher *m/z* due to distorted electric fields. Lowering the laser pulse energies decreased the signal intensity for the parent ion ($[Li_4Al_5Ph_{12}]^-$, m/z = 1087.4) but decreased the mass shift. The spectrum is complex, and not all higher mass fragments were identified, indicating facile formation of larger nuclearity species (*m/z* > 2000 amu) in the gas phase, where molecules / atoms in the crystal lattice fragment and recombine.

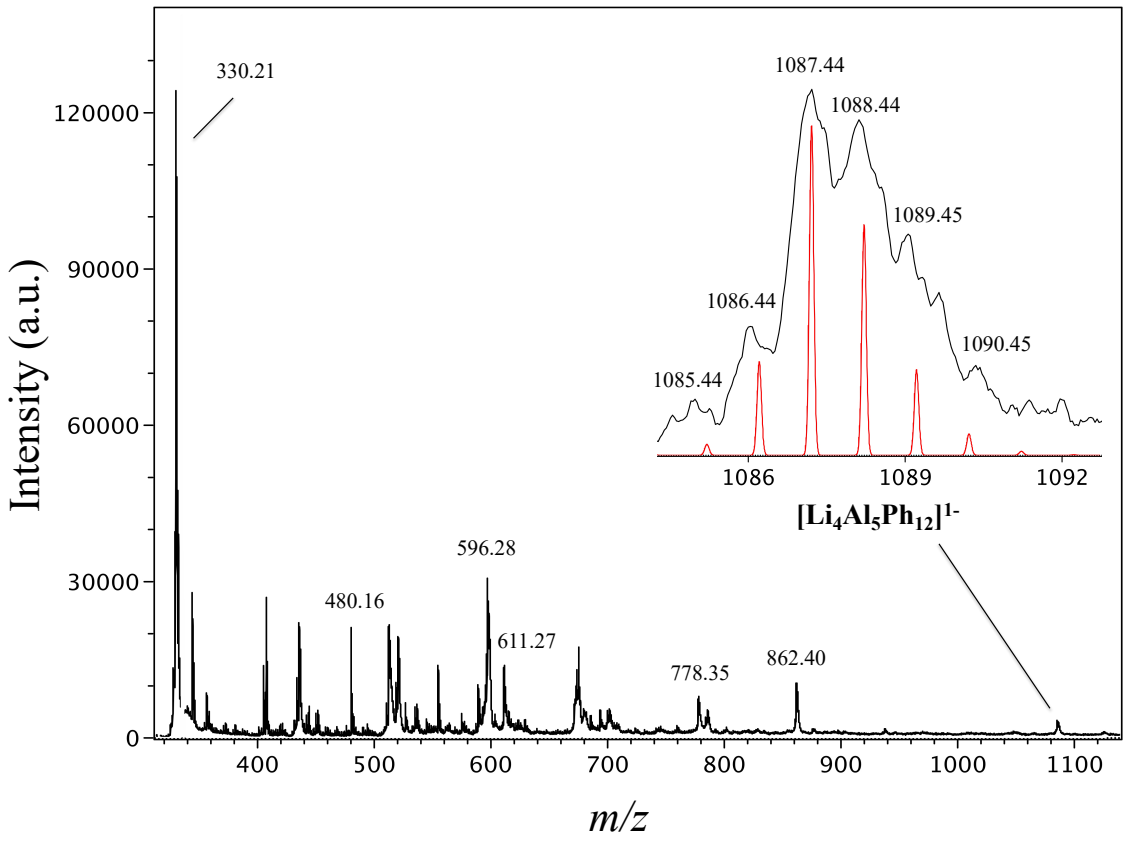

Figure 2.7: Mass spectra of crystals containing **2.1** (black). Inset shows mass envelope at *m/z* = 1087.44, the mass fragment associated with the parent ion of **2.1**, $[Li_4Al_5Ph_{12}]^{1-}$. Simulated spectrum in red (Mmass Software, version 3).

The most intense peak is at *m/z* = 330.21, corresponding to $AlPh_2(Et_2O)_2$. Deconvolution of isotopic envelopes for other peaks allowed for the tentative identification of their composition, such as $[Al_3Ph_4(C_7H_8)]^-$ (*m/z* = 480.16), $[Li_2Al_4Ph_4(C_7H_8)(C_4H_{10}O)]^-$ (*m/z* = 597.26), $[Li_2Al_4Ph_3(C_7H_8)_2(C_4H_{10}O)]^-$ (*m/z* = 611.27), $[LiAl_3Ph_8(C_4H_{10}O)]^-$ (*m/z* = 778.35), and $[Li_2Al_3Ph_9(C_4H_{10}O)]^-$ (*m/z* = 862.40), where C_7H_8 (toluene) and $C_4H_{10}O$ (Et_2O) originate from the crystal lattice (Figure 2.8(a)-(d)).

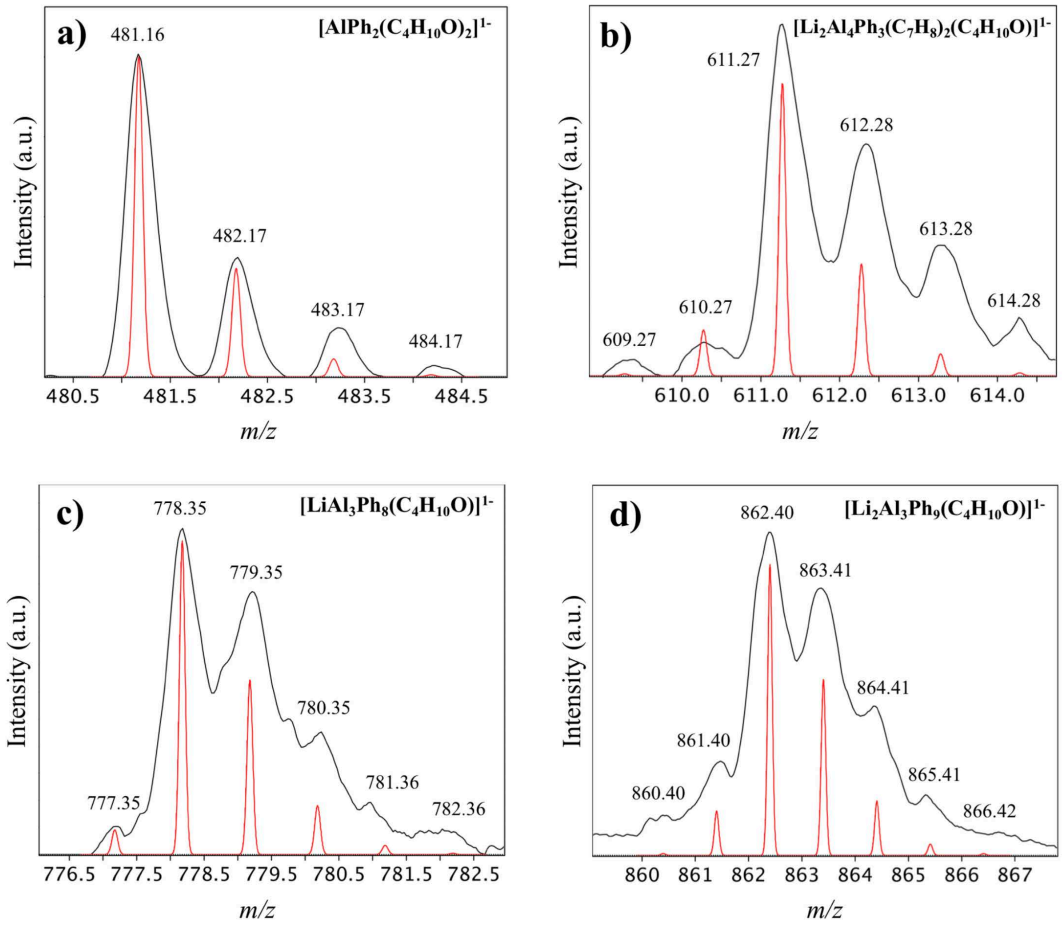

Figure 2.8: Mass envelopes for four major peaks in the mass spectrum of crystals containing **2.1,** which may arise due to fragmentation of the parent ion. (a): *m/z* = 481.16, $[AlPh_2(C_4H_{10}O)_2]^{1-}$ (b): *m/z* = 611.27, $[Li_2Al_4Ph_3(C_7H_8)_2(C_4H_{10}O)]^{1-}$ (c): *m/z* = 778.35, $[LiAl_3Ph_8(C_4H_{10}O)]^{1-}$(d): *m/z* = 862.40, $[Li_2Al_3Ph_9(C_4H_{10}O)]^{1-}$.
Experimental spectra in black, simulated spectra in red (Mmass Software, version 3).

Mass fragments $[LiAl_3Ph_8(C_4H_{10}O)]^-$ (*m/z* = 778.35), and $[Li_2Al_3Ph_9(C_4H_{10}O)]^-$ (*m/z* = 862.40), related by the loss of PhLi, each contain aluminum in a formally reduced 2^+ oxidation state (based on oxidation state assignments of Li = +1, Ph = -1, $(C_4H_{10}O)$ = 0). This is further indication that these fragments may have formed from direct decomposition of the parent ion $[Li_4Al_5Ph_{12}]^{1-}$.

2.2.4.2 Electrospray Ionization Mass Spectrometry (ESI-MS)

Electrospray mass spectra of solvated crystals containing **2.1** (THF and Et_2O solutions) were collected on an ACCUTOF ESI-MS operating at -2500 V (Negative Ion Mode), introduced via air-tight syringe through an air-tight ESI-MS inlet. The highest intensity mass fragment in all spectra corresponds to $AlPh_4^-$ (*m/z* = 335.14), with lower intensity fragments belonging to the assumed degradation products of **2.1**, such as $[LiAl_3Ph_5(Et_2O)(Bu_2O)]^{1-}$, where the average oxidation state of aluminum is reduced (Figure 2.9), indicating that this fragment most likely originated from a source containing low oxidation state aluminum atoms, such as **2.1**.

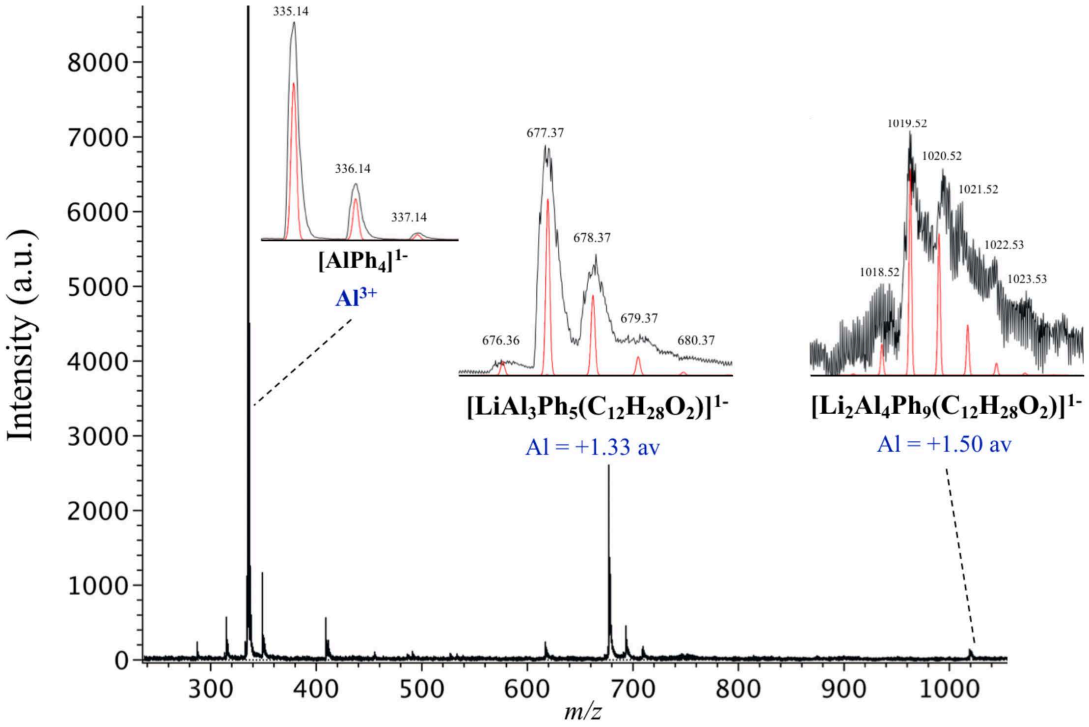

Figure 2.9: (a): Negative mode ESI-MS of crystals containing **2.1** in a diethyl ether solution. Mass envelopes corresponding to (b): $[AlPh_4]^{1-}$, m/z = 335.14, (c): $[LiAl_3Ph_5(Et_2O)(Bu_2O)]^{1-}$, m/z = 677.37, and (d): $[Li_2Al_4Ph_9(Et_2O)(Bu_2O)]^{1-}$, m/z = 1019.52. Masses given in amu.

2.2.5 Quantum Chemical Calculations

DFT calculations of **2.1** were performed on the Gaussian G16.A03 software at the M06-2X/6-31G* level of theory (Figure 2.10). Bond critical points were determined using the DGrid software. ELF analysis was done using the TopMoD software. Numerical integrations for population and localization/delocalization indexes were performed with Multiwfn software. All calculations were performed on DOD HPC computer clusters by Warren Tomlinson and Dr. Joseph Hooper of the Naval Postgraduate School.

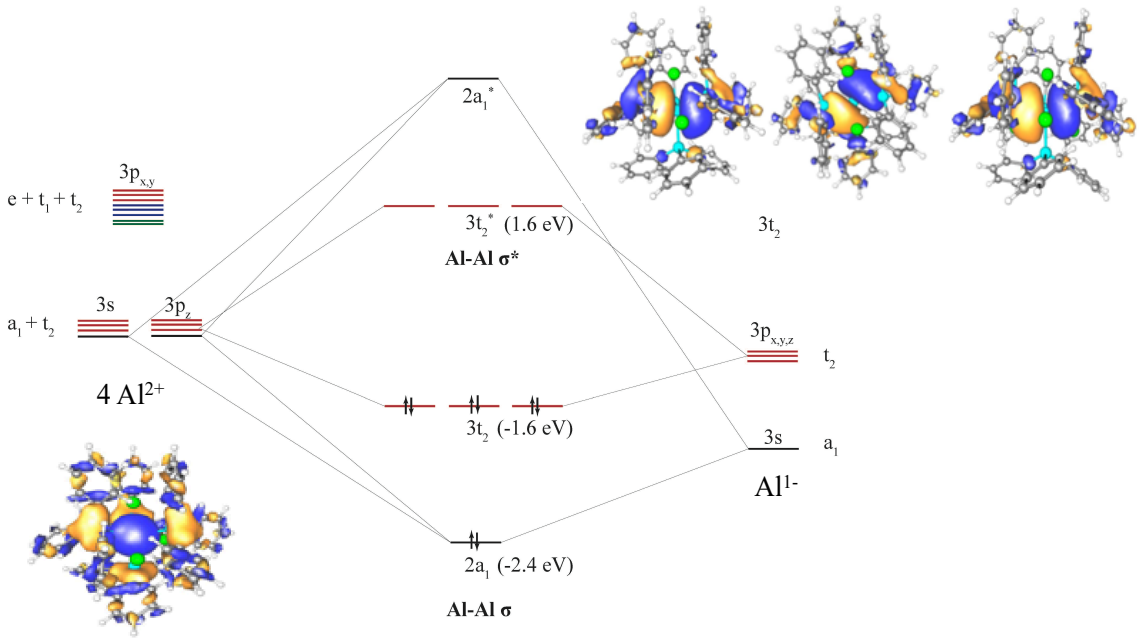

Figure 2.10: A simplified molecular orbital depiction of the Al-Al bonding in **2.1**. Calculated energy values are shown for the LUMO ($3t_2^*$), HOMO ($3t_2$), and HOMO-1 ($2a_1$), with a HOMO-LUMO gap of 3.2 eV. Apical Al^{2+} ions interact with the central Al^{1-} in a covalent manner, each providing one electron to form each 2c-2e Al-Al bond.

Analysis of $[Li_4Al_5Ph_{12}]^{1-}$ via the Quantum Theory of Atoms in Molecules (QTAIM) and the Electron Localization Function (ELF) indicates an oxidation scheme which is consistent with a negatively charged central Al and four apical Al^{2+} atoms. Bond

order between the central and apical Al atoms is approximately one, and electron density from Li ions is shared between both types of aluminum equally. This scheme is consistent with four Al-Al bonds, and very weakly interacting Li ions.

Figure 2.11 shows an isosurface of the electron density that clearly reveals four non-nuclear attractors (NNAs) between the central and outer Al atoms. The NNAs between Al atoms have a positive Laplacian, which can be associated with a non-covalent bond; however, the energy density is less than zero, which is a stronger indicator of covalency, supporting a model of two-center two-electron bonds between Al atoms.

This is consistent with the ELF depiction of both the entire cluster and the core (Figure 2.12, Figure 2.13). Core basins in the ELF are shown in cyan, valance basins are in green and protonated valence basins are in red. Valence basins in the ELF between the central and apical Al are symmetric. Integration of the core ELF basins of the Li gives a population close to $2e^-$ (Table 2.10), consistent with the ionic interactions of Li with the Ph rings, and, to a lesser extent, the Al atoms. While there are bond critical points between the central Al and the Li, indicative of bonding interactions, they have a very low electron density consistent with very weak, closed shell bonding.

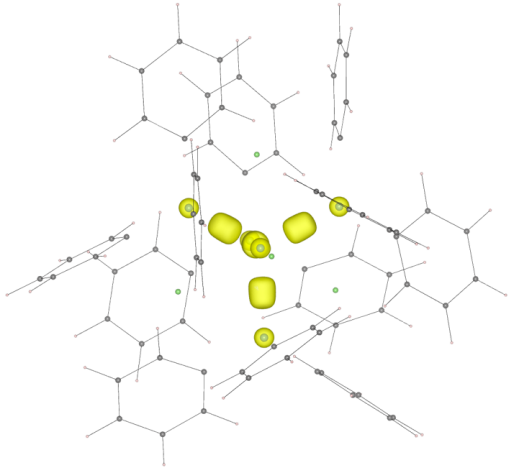

Figure 2.11: Electron density showing the four NNAs between central and apical Al atoms.

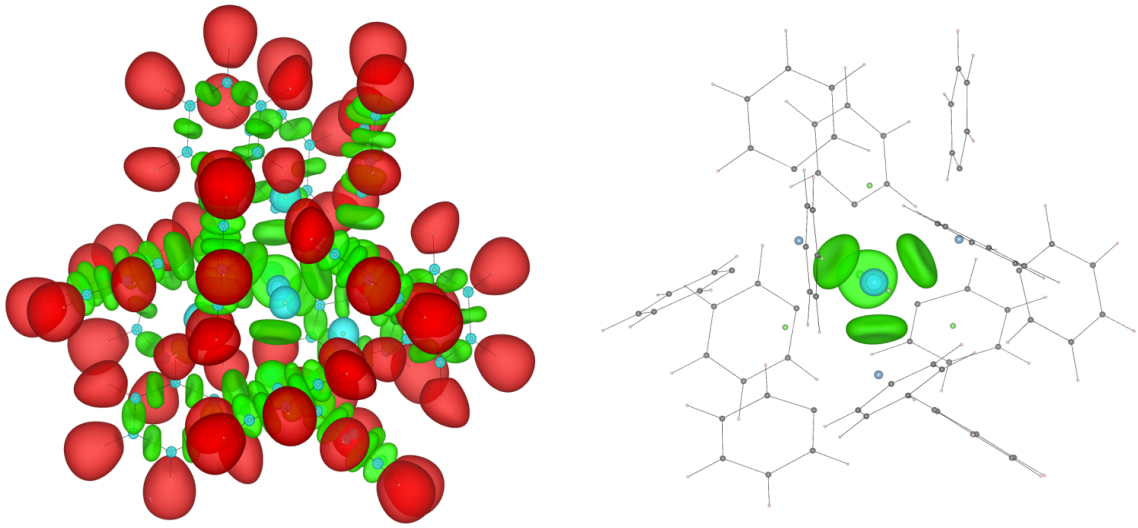

Figure 2.12: ELF of **2.1** (left) and the core Al-Al bonds (right). Visualized at the 0.83 isosurface value.

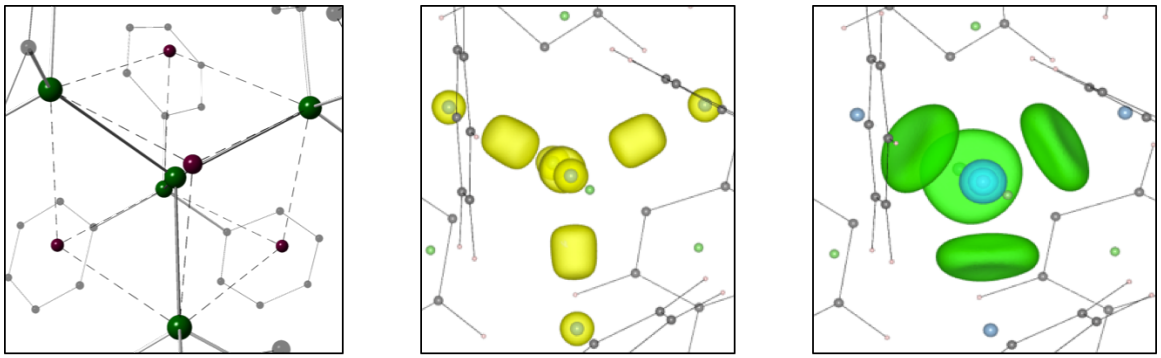

Figure 2.13: (a): Core of **2.1**, oriented to highlight Al-Al bonding (b): Four NNAs reveal four two-center, two-electron bonds between central and apical Al atoms. (c): ELF of core Al-Al bonds, visualized at the 0.83 isosurface value. ELF results also support four Al-Al bonds, with extensive electron delocalization from the central Al to the more electron-deficient apical Al atoms, supporting that the central Al is more electron-rich (lower charge) than the apical Al atoms.

Table 2.9: AIM metrics for the central and apical Al. Al* indicates the central aluminum. All numbers are in atomic units.

Atom	N(A)	λ(A)	Pair	δ(A, B)
Al*	12.74	10.93	(Al*, Al)	0.246
NNAs	0.676	0.149	(Al*, NNA)	0.412
Al	10.95	10.08	(Al, NNA)	0.221
Al	10.95	10.09	(Al, C)	0.323
Al	10.95	10.08		
Al	11.02	10.23		

Table 2.9 shows the AIM electron populations N(A) along with the localization index λ(A) and delocalization index δ(A, B). The delocalization indices are averages. The apical Al have populations very close to $11e^-$, consistent with an Al^{2+} oxidation state. The collective population of the four NNAs and the central aluminum atom is approximately $15.5e^-$, indicating significant delocalized charge within the cluster core. If the NNAs and central aluminum atom are considered as a group, the collective localization index is approximately 11.5e, indicating four shared electrons. This is consistent with the collective delocalization index of the three pairs (δ(Al*, NNA), δ(Al, NNA) and δ(Al, NNA) where Al* is the central aluminum) of 0.879 on average. In a manner similar to Platts et. al., we use this collective delocalization index to suggest a bond order of approximately one between the central and apical aluminum. While the central aluminum has an AIM population of 12.74e, there is significant nearby electron density delocalized in the NNAs. This, along with a calculated Mulliken partial charge of -0.738 on the central Al, is consistent with a central -1 ion.

Table 2.10: AIM and ELF parameters for the Li. All numbers are in atomic units

Atom	ρ	N(A)	λ(A)	Pair	δ(A, B)
Li	2.03	2.11	1.98	(Li, Al*)	0.032
Li	2.03	2.11	1.98	(Li, Al)	0.021
Li	2.03	2.11	1.98		
Li	2.03	2.11	1.98		

2.3 Discussion

Traditionally, low-valent Al complexes have been prepared by employing reductive methods on trivalent alkyl aluminum halides. These methods have been utilized to synthesize the dialuminyne and cyclotrialuminene complexes, both of which have sodium ions incorporated into the solid-state structures and exhibit Al-Al multiple bonds. These systems brought attention to the σ-aryl systems, bonding directly through negatively charged ipso carbons, as a new ligand set for stabilization of low-valent aluminum.

The chemistry of low-valent aluminum with an unsubstituted aryl ligand, the phenyl anion, was further investigated here through reactions with Al(I)X precursor solutions, producing two new compounds. These products are rare examples of aluminum-lithium compounds with high Li:Al ratios and σ Al-aryl bonds. The salt form of **2.1** exists in multiple crystallographic modifications and can be used as a precursor for further reactions. The formation of complex **2.1** may be dependent on formation of the co-product, $LiAlPh_4$, as it has never been isolated without this co-crystallite, even in reactions where stoichiometric equivalents of PhLi were varied to maximize yield of **2.1**. Isolation of **2.1** and **2.2** is highly reproducible across a wide range of reaction conditions,

including syntheses performed with $AlCl\cdot(Et_2O)_n$ instead of $AlBr\cdot(Et_2O)_n$, changes in reactant ratios, temperature, and addition of Li chelation agents such as TMEDA. The different crystallographic modifications, contain identical $[Li_4Al_5Ph_{12}]^-$ anions , as indicated by the statistical bond variance (σ^2) for Al-Al (1.4×10^{-5}) and Al-C_{ipso} (5.2×10^{-5}) interatomic distances. These variance values are negligible, indicating that the anions isolated in different crystallographic morphologies are statistically identical. While anion **2.1** readily crystallizes from reaction solution, its facile decomposition in solution and solid-state, as indicated by ESI-MS, solution-phase NMR, and SS-NMR studies, reveal the metastable nature of this Al cluster.

Oxidation state assignments of four apical Al^{2+} bound to a central Al^{1-}, while merely a formalism, are corroborated by SS-NMR and ELF calculations, and support a covalent-type model of Al-Al bonding, containing four 2c-2e bonds. Complex **2.1** forms through a disproportionation pathway, as evidenced by the byproducts KBr and Al(s), and the central Al^{1-} in the cluster (Eq. 2.1). The $[Li_4Al_5Ph_{12}]^{1-}$ framework is reminiscent of the salt $[Al_5Br_6\bullet 6THF][Al_5Br_8\bullet 4THF]$, isolated directly from solutions of Al(I)Br. [91] The complex contains two mixed-valent Al-centered clusters, with bonding descriptions similar to **2.1**, but without the presence of alkali metal cations (Figure 2.14). Oxidation states of the Al atoms are described as 0, +1, and +2 for cationic $[Al_5Br_6\bullet 6THF]^+$, and 0, +2 for the anion $[Al_5Br_8\bullet 4THF]^-$. As described in **2.1**, central aluminum atoms have a lower oxidation state than apical Al atoms, and form four 2c-2e Al-Al bonds, arranged in a tetrahedral fashion. The Al-Al bond distances in $[Al_5Br_6\bullet 6THF]^+$ (2.532 Å) and $[Al_5Br_8\bullet 4THF]^-$ (2.543 Å) are similar, but shorter than the average Al-Al distances in **2.1** (2.667 Å). Bond distances in these Al_5 units are not only reflective of Al oxidation state, but are also

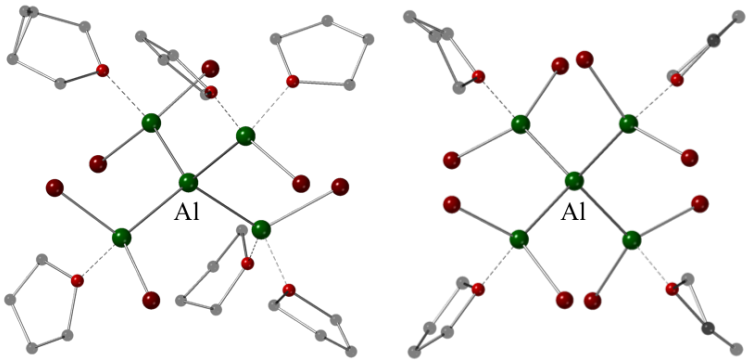

Figure 2.14: Perspective view of Schnockel's $[Al_5Br_6•6(THF)][Al_5Br_8•4(THF)]$ salt, where the tetrahedral arrangement of Al atoms in the cluster core bears resemblance to those in **2.1**.

influenced by Coulombic interactions and steric effects of ligands within the molecule. Undoubtedly, the presence of Li^+ in the cluster core affects Al-Al bond distances and constrains geometry of the cluster, as ELF calculations reveal that weak interactions between Li^+ are present between apical and central Al atoms. The formation mechanism of **2.1** may be similar to the formation mechanism proposed for $[Al_5Br_6•6THF][Al_5Br_8•4THF]$ by Schnöckel, whereby formation of the salt occurs primarily via an Al(III) seed through reaction with Al(I)Br. Based on the co-crystallization of $LiAlPh_4$ in each reaction, we propose that successive insertion of AlPh units and PhLi into this co-product ultimately yields the Al_5 cluster framework (Scheme 2.1). This tetrahedral arrangement of "E_5" units (E = Al, Ga) can also be seen in the numerous Ga structures, $Ga_5Cl_7L_5$ (L = Et_2O, $NHEt_2$), $Ga_5Br_7L_5$ (L = THF, $NHEt_2$), and $Ga_5Cl_7L_4$ (L = NEt_3).

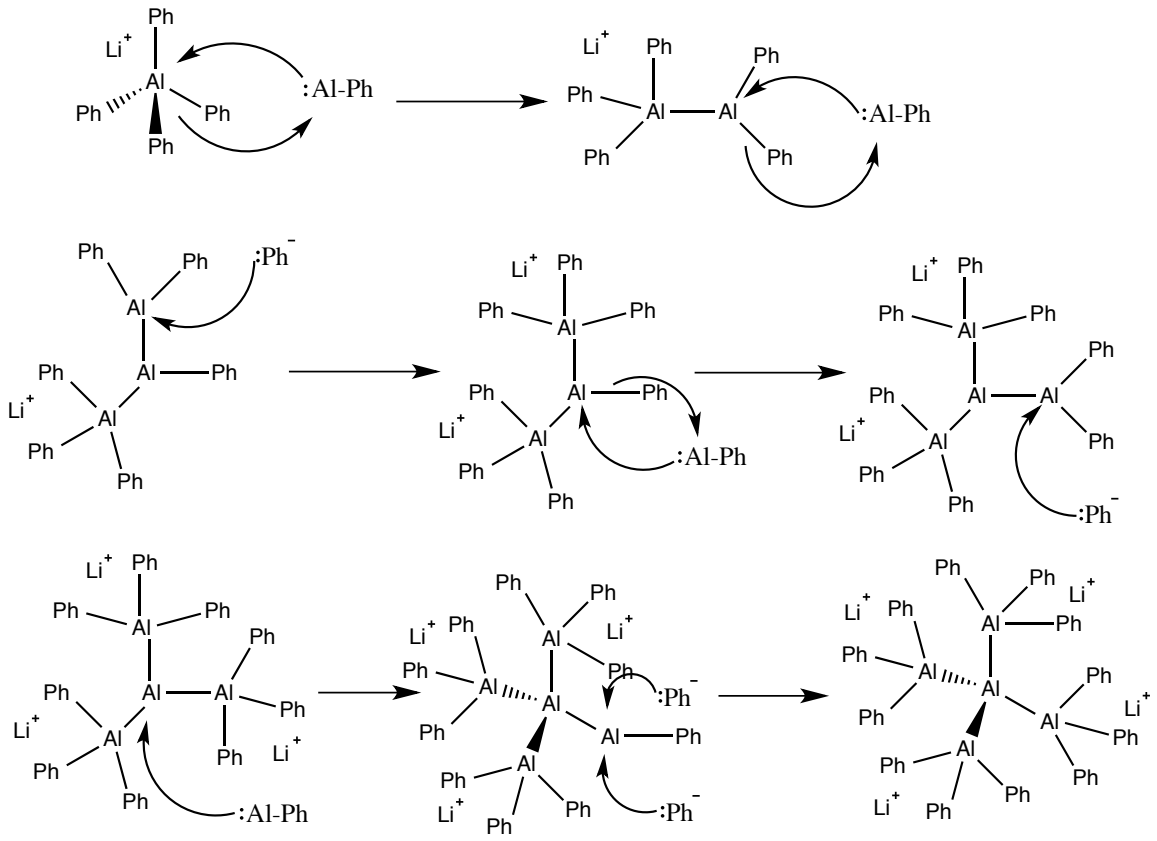

Scheme 2.1: Proposed formation mechanism of 2.1 beginning from the co-crystallite $LiAlPh_4$. This reaction scheme is a modification of that that proposed in Ref [91] for the formation of the "Al_5 salt" $[Al_5Br_6•6THF][Al_5Br_8•4THF]$.

LDI-MS analysis showed the parent ion of **2.1**, $[Li_4Al_5Ph_{12}]^{1-}$, at *m/z* = 1087.44 from direct ablation of crystals, with the isotopic envelope supporting the elemental assignments made in the solid-state structures. The $[Al_5]$ framework of **2.1**, while stable in the solid state and gas phase, undergoes degradation in donor solvents such as THF and Et_2O, as demonstrated by ESI-MS spectra. The most prevalent ion detected in THF or Et_2O solutions of **2.1** is *m/z* = 335.14, corresponding to $[AlPh_4]^{1-}$. The instability of **2.1** in solution is attributed to weak Al-Al bonds, and the ability of donor solvents to remove Li^+ from the core of the cluster, exposing oxophilic aluminum atoms. It is well known that low oxidation-state aluminum atoms readily undergo disproportionation to form more favorable Al^{3+} and Al^0 species. Degradation of the Al_5 framework of **2.1** into Al^{3+}

and Al^0 is consistent with disproportionation. In addition to being subject to ready disproportionation in solution, the cluster also undergoes a decompositional process in the solid-state, as indicated by SS-NMR, where the intensity of the signal associated with the central and apical Al atoms decrease, while the peak assigned to the Al^{3+} species $LiAlPh_4$ grows over time.

2.4 Experimental Section

2.4.1 General Considerations

All reactions were performed under an inert atmosphere of dry nitrogen or argon in a dry box (Vacuum Atmosphere Co) or using standard Schlenk techniques. All solvents were purified by distillation from sodium benzophenone ketyl under a dinitrogen atmosphere and stored over 3 Å molecular sieves in an inert atmosphere. Phenyllithium was purchased from Sigma-Aldrich and used as received. $AlCl{\cdot}(Et_2O)_n$ and $AlBr{\cdot}(Et_2O)_n$ were prepared via a modified Timms/Schnöckel metal-halide co-condensation apparatus according to standard procedures, which are described elsewhere (Ref). The halide contents of the AlX solutions were determined by a Mohr titration.

Laser Desorption/Ionization time-of-flight mass spectra (LDI-TOF MS, Bruker Autoflex) were collected in negative ion mode with a nitrogen pulsed laser, wavelength 337 nm, frequency 10 Hz, and pulse power of 130 μJ. Crystals of $[(Bu_2O)_3Li][Li_4Al_5Ph_{12}]{\bullet}2(tol)$ were loaded onto the sample holder via carbon tape with no matrix. Direct desorption from the crystalline samples at high laser pulse energies resulted in mass shifts of the ions to higher m/z due to distorted electric fields. Lowering the laser pulse energies decreased the signal intensity for the parent ion (m/z = 1033.1) but decreased the mass shift (Figure S2). The shifts were corrected in the reported spectra. The mass envelopes were fit by using the Gauss Model in OriginPro 9. The peak position and full width at half maximum

(FWHM) values were fixed before the simulation and were calculated by Mmass Software Version 3.

2.4.2 Synthesis of AlX and GaX solutions

All aluminum and gallium monohalide solutions are prepared using similar protocols, modified based on the type of halide and donor solvent used. A sample synthesis for AlBr•Et_2O is presented below.

2.4.2.1 Synthesis of AlBr•Et_2O

The following data were collected during a reaction of molten aluminum with HBr (g), utilizing a 3:1 mixture of toluene: diethyl ether (total volume = 120 mL) as the solvent system (LMS1-29). Aluminum metal was loaded into graphite furnace crucibles and assembled into the furnace piece. The entire furnace piece (66.2933 g) was placed into the silica furnace tube. The HX inlet tubing was attached to the mass flow controller (MFC) leading to the HBr lecture bottle via a three-way valve. The resistance across the entire furnace assembly was measured using a Fluka multimeter (R = 6.3Ω). The 30-L stainless steel bell jar was lowered onto the furnace assembly and affixed with 12 bolts. A 250 mL collection Schlenk flask, equipped with a J. Young valve, was attached to the drain spout of the bell jar.

A 3:1 solvent mixture of toluene: diethyl ether (120 mL) was prepared in a 350 mL solvent addition flask, cooled to -78°C, and degassed. Upon warming to room temperature, the flask was inverted and attached to the reactor assembly via a 2-neck round bottom flask, leading to the solvent inlet.

Once all glassware and tubing was attached, the MFC and HX line were filled with ultrapure Ar and purged three times utilizing an external vacuum trap. The entire

reactor assembly was evacuated with a mechanical pump overnight (16 hours), reaching a pressure of 32 mTorr.

Once the apparatus was degassed, the diffusion pump and cooling water were started. After 45 minutes, the valve leading from the reaction chamber to the mechanical pump was closed, and the butterfly valve leading to the diffusion pump was opened. The outgas pressure increased from 32 to 51 mTorr. An ion gauge was used to degas the system for a period of 20 minutes, after which time the outgas pressure decreased to 40 mTorr and the chamber pressure reached 7.6×10^{-6} Torr. At this time, the solvent heating mantle and belt-warmer were turned on. Following this, voltage was applied to the resistive furnace, and slowly increased from 0 to 175 V. Over a period of 30 minutes, the outgas pressure increased to 70 mTorr and the chamber pressure increased to 3.5×10^{-5} Torr. The system was degassed multiple times using the ion gauge until the outgas pressure reached 51 mTorr and the chamber pressure was 1.2×10^{-5} Torr.

The outer portion of the bell jar was filled with liquid nitrogen, decreasing the outgas pressure to 40 mTorr and the chamber pressure to 3.4×10^{-6} Torr. Once the nitrogen fill was complete, solvent was slowly introduced to the system dropwise in gaseous form. After 10 minutes of solvent addition, which deposits a "base layer" of solvent matrix to the interior of the bell jar, HBr was slowly added to the system, increasing the delivery steadily from 15% of the MFC maximum. During this addition, the pressures increased, indicating the formation of H_2 (g). As the reaction proceeded, the outgas pressure was maintained between 50 – 60 mTorr and the chamber pressure was steadily maintained around 10^{-5} Torr. Nitrogen was added to the bell jar as needed throughout the duration of the reaction.

After 2 hours, the reaction was ended and HBr flow was stopped. The remaining solvent (approximately 10 mL) was condensed on the reactor walls. Once solvent addition was complete, the butterfly valve was closed, closing the diffusion pump off from the system. The voltage was shut off and the liquid nitrogen in the bell jar was drained through an external side arm. The reaction chamber and MFC were back-filled with ultrapure argon. The collection flask was cooled to -78°C with a dry ice container. After approximately 3 hours, the solution had thawed and drained into the collection flask. The Schlenk was sealed and transferred to a -80 °C freezer for storage. The reactor was disassembled and cleaned with washes of acetone and dilute nitric acid. The furnace piece was weighed (65.8791 g) to determine that 0.4142 g (15.3 mmol) of Al reacted, giving an aluminum concentration of 95.9 mM in solution.

Three 1 mL aliquots of the solution were titrated by the Mohr method to determine the average bromide concentration (147 mM). The concentration ratio of aluminum to bromide was determined to be 1: 1.5 (nominal formula $AlBr_{1.5}$)

2.4.3 Synthesis of Crystalline Modifications of $[Li_4Al_5Ph_{12}]^{1-}$ and $LiAlPh_4$

2.4.3.1 $[(Bu_2O)_3Li][Li_4Al_5Ph_{12}]\cdot 2(tol)$ (UMAPS-14-12-LS)

A solution of PhLi (1.9 M, 0.004 mol, 2.2 mL) was added dropwise to a solution of $AlBr\cdot(Et_2O)_n$ (0.07 M, 0.002 mol, 20.8 mL) at -78 ºC with vigorous stirring. The solution gradually changed color from deep red brown to black over a period of 15 minutes. The reaction slowly warmed to room temperature with stirring for 20 hours, maintaining its black color. Noticeable tan precipitate formed along the solvent line. The solution was concentrated to 10 mL, and the supernatant was filtered from the off-white

solid. After storing the filtered solution at room temperature for ~10 hours, small block-like brown-orange crystals of $[(Bu_2O)_3Li][Li_4(AlPh_3)_4Al]\cdot 2(tol)$ formed on the walls of the vessel. (~20 mg, ca 13% yield). Microcrystalline material of $LiAlPh_4$ formed simultaneously and remained suspended in solution (ca 40% yield). See Figure 2.15 for images of crystals. Structures were determined via synchrotron X-ray synchrotron diffraction at Argonne National Lab with the assistance of Dr. Yu-Sheng Chen (UMAPS-14-12-LS) and solved by Lauren Stevens under the guidance of Dr. Peter Zavalij (UMD).

2.4.3.2 $[(Bu_2O)_3Li][Li_4Al_5Ph_{12}]\cdot 2(tol)$ (UM2671)

A solution of PhLi (1.9 M, 0.004 mol, 2.2 mL) was added dropwise to a solution of $AlBr\cdot(Et_2O)_n$ (0.07 M, 0.002 mol, 20.8 mL) at -78 ºC with vigorous stirring. The solution gradually changed color from deep red brown to black over a period of 15 minutes. The reaction slowly warmed to room temperature with stirring for 20 hours, maintaining its black color. Noticeable tan precipitate formed along the solvent line. The solution was concentrated to 10 mL, and the supernatant was filtered from the off-white solid. After storing the filtered solution at room temperature for ~10 hours, small block-like brown-orange crystals of $[(Bu_2O)_3Li][Li_4(AlPh_3)_4Al]\cdot 2(tol)$ formed on the walls of the vessel. (~20 mg, ca 13% yield). Microcrystalline material of $LiAlPh_4$ formed simultaneously and remained suspended in solution (ca 40% yield). Structures were solved by Lauren Stevens under the guidance of Dr. Peter Zavalij (UMD).

2.4.3.3 $[(Bu_2O)_x(Et_2O)_{3-x}Li][Li_4Al_5Ph_{12}]\cdot 1.5(tol)$ (UM2736)

A solution of PhLi (1.9 M, 0.001 mol, 0.5 mL) was added dropwise to a solution of $AlCl\cdot(Et_2O)_n$ (0.120 M, 0.002 mol, 16.7 mL) at -78 ºC with vigorous stirring. The

solution slowly changed color from deep red brown to black over a period of several hours, while warming to 25 ºC. The reaction stirred at room temperature for an additional 20 hours, maintaining its dark color. Noticeable tan precipitate formed along the solvent line and bottom of the Schlenk vessel. The solution was concentrated to 8 mL, and the supernatant was filtered from the off-white solid. After storing the filtered solution at room temperature for four days, dark brown plates of $[(Bu_2O)_x(Et_2O)_{3-x}Li][Li_4Al_5Ph_{12}]\cdot 1.5(tol)$ formed on the walls and bottom of the Schlenk vessel. (~45 mg, ca 31% yield, assuming x = 1, y = 2). Microcrystalline $LiAlPh_4$ formed simultaneously and remained suspended in solution (ca 35% yield). Structures were collected and refined by Dr. Peter Zavalij (UMD).

2.4.3.4 $[(TMEDA)_nLi][Li_4Al_5Ph_{12}]\cdot 2(tol)$ (UM2746)

A solution of PhLi (1.8 M, 0.004 mol, 2.2 mL) was added dropwise to a solution of $AlBr\cdot(Et_2O)_n$ (0.0959 M, 0.002 mol, 20.8 mL) at -78 ºC with vigorous stirring. The solution rapidly changed color from deep red brown to black over several minutes, while warming to 25 ºC. The reaction was then slowly heated in increments of 5 ºC / 10 min until it reached an internal temperature of 55 ºC. The reaction stirred at 55 ºC for 4.0 hours, when a noticeable darkening of the supernatant occurred, along with concomitant formation of a tan precipitate and black semi-solid near the solvent line. The reaction was slowly cooled to room temperature without stirring, to allow the precipitate to settle. The reaction was filtered via Teflon cannula into a clean Schlenk tube and stored at room temperature in a dark cabinet. After 10 days with no crystal formation, a 2.0 mL aliquot of the reaction was layered with 1.0 mL of a toluene / TMEDA solution (0.1 molar equivalent TMEDA: Al). After ~7 days, dark brown prisms of

$[(TMEDA)_nLi][Li_4Al_5Ph_{12}]\cdot 2(tol)$ formed near the solvent line. (~5.0 mg, theoretical yield not determinable). Microcrystalline $LiAlPh_4$ was not detected. Structure was collected and refined by Dr. Peter Zavalij (UMD).

2.4.3.5 $[(Et_2O)_3Li][Li_4Al_5Ph_{12}]\cdot 2.5(tol)$ (UM2789) and $[(Solvent)_xLi][Li_4Al_5Ph_{12}]$ (UM2790)

The crystallographic modifications $[(Et_2O)_3Li][Li_4Al_5Ph_{12}]\cdot 2.5(tol)$ (UM2789) and $[(Solvent)_xLi][Li_4Al_5Ph_{12}]$ (UM2790) were isolated as co-crystallites, in addition to $LiAlPh_4$, using two synthetic methods detailed below.

Synthesis 1: At -78 ºC, a solution of PhLi (1.9 M in dibutyl ether, 0.005 mol, 2.6 mL) was added dropwise to a solution of $AlCl\cdot(Et_2O)_n$ (89.7 mM, 0.005 mol, 60.1 mL) with vigorous stirring. Almost immediately, the solution color changed from a red-brown to deep brown. The reaction stirred at -78 ºC for 30 min, and was then warmed to room temperature with stirring over a period of 1.5 hours. The reaction was stirred under Ar for an additional 11 hours at room temperature. Noticeable tan precipitate formed along the solvent line. The solution was concentrated to 20 mL in vacuo, and the supernatant was filtered from the precipitate into a 50 mL Schlenk tube, and stored in a dark cabinet for crystallization. After several days, dark brown needles of UM2789 (~30 mg, ca 24% yield) and dark yellow needles of UM2790 (~10 mg, yield cannot be estimated due to unknown identity of solvate in counter-cation shell) formed in the bottom of the Schlenk vessel. Small crystals of $LiAlPh_4$ formed (~20 mg, ca 11% yield), remaining suspended in solution. Structural data was collected and refined by Dr. Peter Zavalij (UMD).

Synthesis 2: At -78 ºC, a solution of PhLi (1.9 M in dibutyl ether, 0.005 mol, 2.6 mL) was added dropwise to a solution of $AlCl\cdot(Et_2O)_n$ (89.7 mM, 0.005 mol, 60.1 mL) with vigorous stirring. Almost immediately, the solution color changed from a red-brown

to deep brown. The reaction was then slowly heated in increments of 5 ºC / 10 min until it reached an internal temperature of 55 ºC. The reaction stirred at 55 ºC for 2.5 hours, when a noticeable darkening of the supernatant occurred, along with concomitant formation of a tan precipitate. The reaction was slowly cooled to room temperature without stirring, to allow the precipitate to settle. The reaction was filtered via Teflon cannula into a clean Schlenk tube and stored at room temperature for 12 hours. Crystals of UM2789 and UM2790 formed in the bottom of the Schlenk vessel, with only a few noticeable crystals of $LiAlPh_4$. The identity of each species was confirmed by collecting the unit cells by single-crystal X-ray diffraction. Full structures were not collected, and yields were not determined.

2.4.4 Crystallographic Studies

Single crystal data collections were performed at ChemMatCARS Sector 15 of the Advanced Photon Source (APS) and at UMD. At APS, a suitable single crystal of $C_{110}H_{130}Al_5Li_5O_3$ (UMAPS-14-12-LS) was analyzed using a Huber three-circle diffractometer (κ-angle offset of 60º) equipped with a Dectris PILATUS3X CdTe 1M detector. The crystal was kept at 150(2) K during data collection, and the distance between the crystal and detector was 130 mm. A custom-designed software was used for data collection, and frames were converted to Bruker-compatible format for data processing in *APEX II*. At UMD, suitable single crystals of $C_{110}H_{130}Al_5Li_5O_3$ (UM2671, UM2736, UM2746, UM2789, UM2790) were selected and measured on a Bruker Smart Apex2 CCD diffractometer. The crystals were kept at 120(2) K during data collection.

In all cases, integral intensity data were corrected for absorption using the multi-scan method of SADABS software. The structures were solved with the ShelXT-2014 program and refined with the ShelXL-2015 program and least-square minimization using ShelX software package. In all crystal morphologies, dibutyl or diethyl ether molecules present as part of the Li-cation and toluene solvate molecules were disordered in multiple alternative positions. The heavily disordered hydrocarbon tails were refined with geometry restrained to be similar and atomic displacement parameters to correspond to rigid body motions.

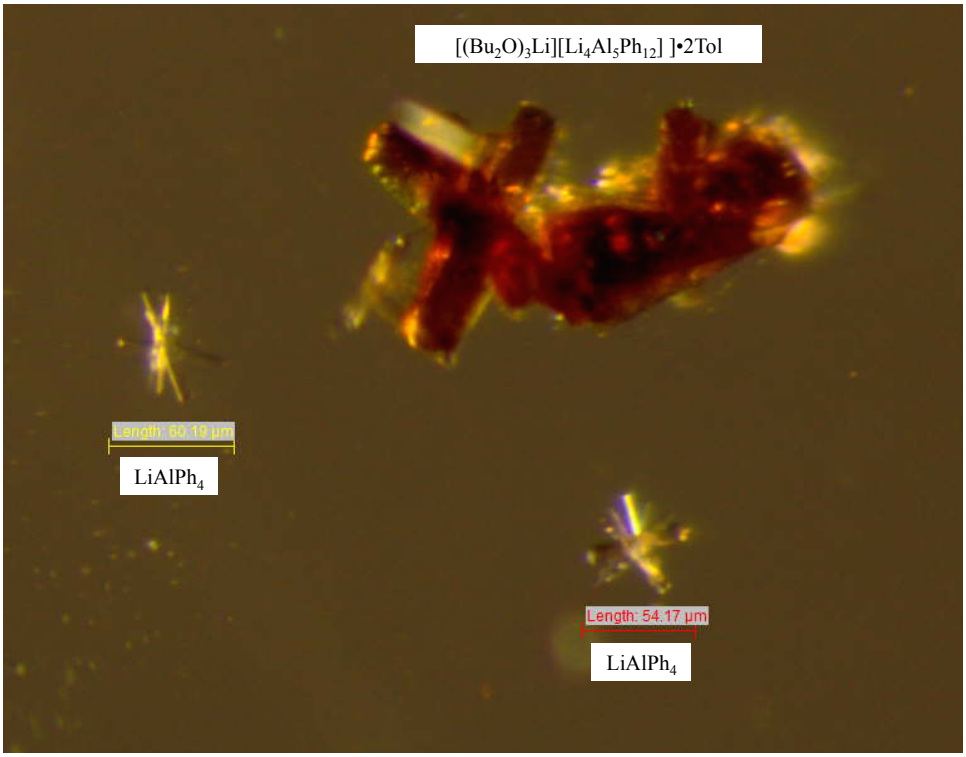

Figure 2.15: Images of co-crystallites $[(Bu_2O)_3Li][Li_4Al_5Ph_{12}]$]•2(tol) and $LiAlPh_4$, illustrating differences in size, color, and crystal habit of each species. Recorded at the Advanced Photon Source of Argonne National Lab, Dec. 2014.

Table 2.11: Crystallographic Collection and Refinement Data for Distinct Crystallographic Modifications Containing **2.1**[a]

UM Identifier	**UM2671** $[(Bu_2O)_3Li][Li_4Al_5Ph_{12}]$•2(tol)	**UM2736*** $[(Bu_2O)_x(Et_2O)_{3-x}Li][Li_4Al_5Ph_{12}]$•1.5(tol)	**UM2746*** $[(TMEDA)_xLi][Li_4Al_5Ph_{12}]$
Empirical formula	$C_{110}H_{130}Al_5Li_5O_3$	$C_{99.35}H_{72}Al_5Li_5O_{0.75}$	$C_{82.8}H_{60}Al_5Li_{4.27}$
Formula weight	1669.73	1447.37	1219.42
Temperature/K	150(2)	120(2)	150(2)
Crystal system	Orthorhombic	Triclinic	Trigonal
Space group	Pnna	P-1	R-3
a/Å	23.1837(10)	15.9768(16)	15.767(2)
b/Å	25.5173(11)	16.0341(16)	15.767(2)
c/Å	16.8014(7)	18.6621(19)	51.984(7)
α/°	90	89.833(2)	90
β/°	90	79.489(2)	90
γ/°	90	68.191(2)	120
Volume/Å^3	9939.5(7)	4353.1(8)	11192(2)
Z	4	2	6
ρ_{cal} cg/cm^3	1.116	1.104	1.086
μ/mm-1	0.105	0.109	0.115
F(000)	3576.0	1508.0	3808.0
Crystal size/mm^3	0.24 × 0.17 × 0.08	0.40 × 0.06 × 0.05	0.095 × 0.09 × 0.09
Radiation	Mo*Kα* (λ = 0.71073)	Mo*Kα*	Mo*Kα*
2*θ* range	3.514 to 46.654	3.406 to 50	3.37 to 44.97
Reflections	63495	42257	33697
Independent reflections	7197 [R_{int} = 0.0484, R_{sig} = 0.0247]	15343 [R_{int} = 0.0771, R_{sig} = 0.1065]	3243 [R_{int} = 0.0776, R_{sig} = 0.0355]
Data/restraints/parameters	7197/582/683	15343/258/1036	3243/0/310
Goodness-of-fit	1.024	1.050	1.320
R_1/wR_2 [$I>=2\sigma(I)$]	0.0625, 0.1197	0.0832, 0.1460	0.0787, 0.1631
R_1/wR_2 [all data]	0.0828, 0.1299	0.1747, 0.1790	0.1138, 0.1796

[a]See the Crystallographic Studies Section for details on the refinement.
*Very heavy disorder present in solvent coordinated to Li countercations. Heavy disorder for all atoms, regardless of type, was modeled as C atoms of varying occupancies.

Table 2.11, Continued: Crystallographic Collection and Refinement Data for Distinct Crystallographic Modifications Containing **2.1**[a]

UM Identifier	**UM2789** $[(Et_2O)_3Li][Li_4Al_5Ph_{12}]\bullet 2.5$ (tol)	**UM2790*** $[(Solvent)_xLi][Li_4Al_5Ph_{12}]$
Empirical formula	$C_{101.5}H_{110}Al_5Li_5O_3$	$C_{90.93}H_{60}Al_5Li_5$
Formula weight	1547.49	1322.09
Temperature/K	150(2)	150(2)
Crystal system	Monoclinic	Triclinic
Space group	C2/c	P-1
a/Å	21.4440(14)	15.9031(14)
b/Å	18.2834(12)	16.0211(14)
c/Å	24.8432(16)	18.6443(16)
α/°	90	89.6350(10)
β/°	109.7590(10)	79.7280(10)
γ/°	90	67.7980(10)
Volume/Å^3	9166.8(1)	4317.9(7)
Z	4	2
ρ_{cal} cg/cm^3	1.121	1.017
μ/mm-1	0.109	0.104
F(000)	3292.0	1371.0
Crystal size/mm^3	0.28 × 0.17 × 0.12	0.56 × 0.18 × 0.11
Radiation	Mo*Kα* (λ = 0.71073)	Mo*Kα* (λ = 0.71073)
2*θ* range	3.8 to 47	3.908 to 49.996
Reflections collected	42415	46239
Independent reflections	6788 [R_{int} = 0.0492, R_{sig} = 0.0354]	15158 [R_{int} = 0.0288, R_{sig} = 0.0357]
Data/restraints/param.	6788/1296/686	15158/0/962
Goodness-of-fit on F^2	1.072	1.037
R_1/wR_2 [$I>=2\sigma(I)$]	0.0710, 0.01457	0.0978, 0.1889
R_1/wR_2 [all data]	0.1033, 0.1611	0.1402, 0.2098

[a]See the Crystallographic Studies Section for details on the refinement.
*Heavy disorder prevented identification of solvent. All heavily disordered atoms were modeled as C atoms of varying occupancies.

2.4.5 Experimental and Theoretical SS-NMR

2.4.5.1 SS-NMR

Solid State ^{27}Al and ^{7}Li NMR spectra were obtained using a Varian NMR500 spectrometer using two magnetic fields (11.7 T and 2.35 T). A 3 mm triple-resonance MAS NMR probe was used with both superconducting magnets. All samples were loaded into 3 mm rotors under an inert atmosphere.

Studies of a standard of $LiAlPh_4$ (synthesized via reductive methods from $AlCl_3$ and PhLi) aided in assignment of the ^{27}Al chemical shift for this species.

2.4.5.2 Pseudo-planewave Calculations

Planewave pseudopotential calculations were performed using the Quantum Espresso (QE) 5.4.0 computer code constrained by the experimental space-groups and lattice constants for $LiAlPh_4$ and $[(Bu_2O)_3Li][Li_4Al_5Ph_{12}]$. Of central importance for the NMR calculations is the reconstruction of the all-electron wavefunction from the pseudopotential using the gauge-including projector-augmented wave (GIPAW) method. Calculation of an all-electron wavefunction from the pseudopotential using the gauge-including projector-augmented wave (GIPAW) method requires the use of GIPAW pseudopotentials. We chose Troullier-Martins norm-conserving potentials that were generated by D. Ceresoli: Al.pbe-tm-gipaw-dc.UPF; C.pbe-tm-new-gipaw-dc.UPF; Li.pbe-tm-gipaw-dc.UPF; H.pbe-tm-new-gipaw-dc.UPF that are available online.
The computed $LiAlPh_4$ band gap is 3.8 eV and occurs at the gamma point, and the Li_4Al_5 metalloid gap is 2.1 eV, consistent with the difference in the colors of the crystals (yellow and brown, respectively). The Li_4Al_5 core is nearly cubic. In the crystal it has a two-fold rotational axis through one of its faces. The calculated face-diagonals of the cube caused by second-neighbor Al-Al bonds range from 4.22 to 4.42 Å and those due to Li-Li bonds range from 4.38 to 4.45 Å. The crystal has rotational symmetry perpendicular to a pair of these bonds, and thus only 3 distinct Li and Al atoms. The HOMO-LUMO DFT gap for molecular $Li_4Al_5^-$ in S_4 symmetry is 0.5 eV, which is large for a negatively charge metal cluster in DFT. In the molecular anion, the face diagonals are 4.15 and 4.16 Å, respectively.

Chapter 3: Synthesis and Characterization of Coordination Complexes $[(\eta^4\text{-As}_7)\text{M(L)}]^{n-}$, where M = Co, L = $(\eta^3\text{-As}_3)$, n = 3 ; M = Rh, Ir, L = 1,5-cyclooctadiene, n = 2.

3.1 Introduction

The solid-state structure of the coordination anion $[(\eta^4\text{-As}_7)\text{Cr(CO)}_3]^{3-}$, reported by Eichhorn *et al*. in 1989, contained the first direct evidence of a group 15 Zintl polyanion bound to a transition metal fragment (Figure 3.1c).[63] This anion also featured the first instance of an inorganic nortricyclane-to-norbornadiene structural rearrangement of the $[\text{As}_7]^{3-}$ polypnictide cage. Proof of the ability of Zintl anions to serve as polyatomic ligands in transition metal complexes, coupled with polypnictide cage activation, founded an expansive subdivision of Zintl research. Results from subsequent investigations indicated that Zintl anions could undergo transformations similar to tetrahedral polypnictides Pn_4 (Pn = P, As) and their carbon-based analogues, allowing for parallel comparisons of structure and bonding. [43,61,92-94]

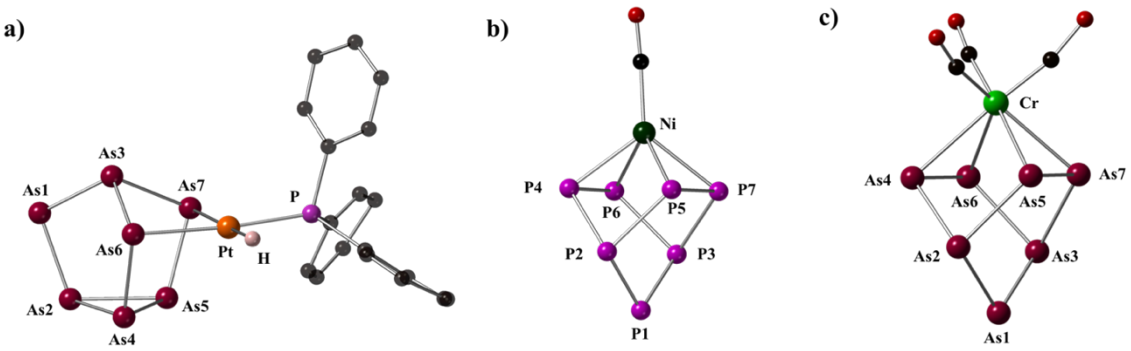

Figure 3.1: Ball and stick models of Zintl-transition metal coordination complexes (a) $[(\eta^2\text{-As}_7)\text{PtH(PPh}_3)]^{2-}$ (b) $[(\eta^4\text{-P}_7)\text{Ni(CO)}]^{3-}$ and (c) $[(\eta^4\text{-As}_7)\text{Cr(CO)}_3]^{3-}$. Phenyl hydrogens omitted for clarity. P = magenta, Pt = orange, As = red-violet, Ni = dark green, Cr = bright green, C = black, O = red.

Many coordination complexes featuring Zintl polyanions are formed through displacement of a weakly coordinating ligand in a transition metal complex by the $[Pn_7]^{3-}$ moiety (Pn = P, As, Sb). For example, pnictide complexes $[(\eta^4\text{-}Pn_7)M(CO)_3]^{3-}$ (Pn = P, As, Sb; M = Cr, Mo, W) [63,95] are formed methodically through reactions of solvated $[Pn_7]^{3-}$ ions with stoichiometric equivalents of transition metal carbonyl complexes $LM(CO)_3$ (M = Cr, W, L = mesitylene ; M = Mo, L = cycloheptatriene) in the presence of 2,2,2,-cryptand, as given in Eq. 3.1.

$$K_3Pn_7 + 3(2,2,2\text{-crypt}) + LM(CO)_3 \longrightarrow [K(2,2,2\text{-crypt})]_3[Pn_7M(CO)_3] + L \quad (3.1)$$

Select examples of $[Pn_7]^{3-}$ (Pn = P, As, Sb) Zintl polyanions behaving as ligands to transition metal fragments in multiple coordination modes are presented in Table 3.1. The atom numbering of the $[(\eta^4\text{-}Pn_7)]^{3-}$ ligands in Figure 3.1 will be ascribed to all norbornadiene-type $[(\eta^4\text{-}Pn_7)]^{3-}$ cages (Pn = P, As, Sb) to allow for direct comparison of bond metrics both within and across transition metal series.

Table 3.1: Group 15 Zintl ion-transition metal coordination clusters containing (η^2-Pn_7) or (η^4-Pn_7) moieties (Pn = P, As, Sb), and their precursors. Binary anions, clusters comprised solely of two elements (TM/MGE or MGE/MGE), and lacking organic components, are listed separately.

Precursor	TM reagent	Product	Reference
	Coordination Clusters with $[Pn_7]^{3-}$ Ligands		
K_3P_7	$LM(CO)_3$ (M = Cr, Mo, W)	$[(\eta^4\text{-}P_7)M(CO)_3]^{3-}$	96
K_3P_7	$Ni(CO)_2(PPh_3)_2$	$[(\eta^4\text{-}P_7)Ni(CO)]^{3-}$	64
K_3P_7	$Pt(PPh_3)_2(C_2H_4)_2$	$[(\eta^2\text{-}P_7)PtH(PPh_3)]^{2-}$	64
K_3As_7	$LM(CO)_3$ (M = Cr, Mo, W)	$[(\eta^4\text{-}As_7)M(CO)_3]^{3-}$	63,96
K_3As_7	$Pt(PPh_3)_2(C_2H_4)_2$	$[(\eta^2\text{-}As_7)PtH(PPh_3)]^{2-}$	97
K_3As_7	$In(C_6H_5)_3$	$[(\eta^2\text{-}As_7)In(C_6H_5)_2]^{2-}$	98
K_3Sb_7	$LM(CO)_3$ (M = Cr, Mo, W)	$[(\eta^4\text{-}Sb_7)M(CO)_3]^{3-}$	96
Na_3Sb_7	$Mo(bipy)(CO)_4$	$[(\eta^4\text{-}Sb_7)Mo(CO)_3]^{3-}$	99
	Binary Anions With [Pn7]3- Moieties		
K_3P_7	$M(C_6H_5)_2$ (M = Zn, Cd)	$[M(\eta^2\text{-}P_7)_2]^{4-}$	100
K_3P_7	$InCl_3$	$[In(\eta^2\text{-}P_7)_2]^{3-}$	101
K_3P_7	TlCl	$[Tl(\eta^2\text{-}P_7)]^{2-}$	101
K_3P_7	$Cu_5(Mes)_5$	$[Cu_2(\mu,\eta^{1:3}\text{-}P_7)_2]^{4-}$	100
K_3P_7	EI_2 (E = Sn, Pb)	$[EP(\mu,\eta^{1:1}\text{-}P_7)_2]^{3-}$	101
K_3As_7	$Zn(C_6H_5)_2$	$[Zn(\eta^2\text{-}As_7)_2]^{4-}$	100,101
K_3As_7	Cd(cyclohexanebutyrate)$_2$	$[Cd(\eta^2\text{-}As_7)_2]^{4-}$	102
K_3As_7	TlCl	$[Tl(\eta^2\text{-}As_7)]^{2-}$	101
K_3As_7	$InCl_3$	$[In(\eta^2\text{-}As_7)_2]^{3-}$	101
K_3As_7	In(I)(OTf)	$[In(\eta^2\text{-}As_7)_2]^{3-}$	*
K_3As_7	$Hg(C_6H_5)_2$	$[Hg_2(\eta^2\text{-}As_7)_2]^{4-}$	102,103
K_3As_7	0.5 $Hg(C_6H_5)_2$	$[HgAs(\mu,\eta^{1:1}\text{-}As_7)_2]^{4-}$	102
K_3As_7	$Pd(PCy_3)_2$	$[Pd_2(\mu,\eta^{2:2}\text{-}As_7)_2]^{4-}$	104
K_3As_7	$Cu_5(Mes)_5$	$[Cu_2(\mu,\eta^{1:3}\text{-}As_7)_2]^{4-}$	100
K_3As_7	EI_2 (E = Sn, Pb)	$[EP(\mu,\eta^{1:1}\text{-}As_7)_2]^{3-}$	101
A_3As_7 (A = K, Rb, Cs)	$AuP(C_6H_5)_3Cl$	$[Au_2(\mu,\eta^{1:1}\text{-}As_7)_2]^{4-}$	105

For $LM(CO)_3$, L = 1,3,5-mesitylene (Mes) when M = Cr, W; L = cycloheptatriene when M = Mo. COD = 1,5-cyclooctadiene. Cy = Cyclohexyl. $(OTf)^{1-} = (CF_3SO_3)^{1-}$

*Stevens,L; Zavalij, P.; Eichhorn, B.W. unpublished results.

Formation of Zintl ion-transition metal complexes and binary anions have been most successful utilizing electron-rich, low oxidation state Groups 6, 10, 11, and 12 transition metal precursors containing at least one labile ligand (e.g. 2,2'-bipyridine, 1,3,5-mesitylene, phenyl, cycloheptatriene). Products of pnictide polyanions with Groups 7, 8, and 9 transition metals, especially of second and third row species, remain underrepresented. Interest in isolating and studying pnictide – Group 9 clusters stems from the catalytic properties of Group 9 transition metals, and their similarities to other elements of the platinum-group metals (PGMs). Group 14 – Group 9 complexes have been described, including coordination species $[(\eta^4\text{-}E_9)M(COD)]^{3-}$ (M = Rh, E = Pb; M = Ir, E = Sn, Pb ; COD = 1,5-cyclooctadiene) and binary anions $[Co@Ge_{10}]^{3-}$, $[Co@Sn_9]^{5-}$, $[Co_2@Sn_{17}]^{5-}$, $[Rh@Sn_{10}]^{3-}$, $[Rh@Pb_{12}]^{3-}$, and $[Ir@Sn_{12}]^{3-}$.[106-111] Analogous Group 15-Group 9 complexes, in particular those of the form $[(\eta^4\text{-}Pn_7)M(COD)]^{n-}$ (Pn = P, As, Sb ; M = Rh, Ir) have not yet been reported.

This Chapter details the reactions of Zintl ion $[As_7]^{3-}$ with Group 9 transition metal complexes $[Co(PPh_3)_2Cl_2]$ and $[M(COD)Cl]_2$ (M = Rh, Ir ; COD = 1,5-cyclooctadiene). The synthesis, structure, and properties of products $[(\eta^4\text{-}As_7)M(COD)]^{2-}$ (M = Rh, Ir) and the carbon-free binary anion $[(\eta^3\text{-}As_3)Co(\eta^4\text{-}As_7)]^{3-}$ are presented. These three complexes are the first to exhibit $[(\eta^4\text{-}As_7)]^{3-}$ serving as a polyatomic ligand to the Group 9 transition metals. Additionally, the cluster $[(\eta^3\text{-}As_3)Co(\eta^4\text{-}As_7)]^{3-}$ is the only known binary anion of Co and As, and represents a new combination of these elements. This structure type is unprecedented among previously reported binary anions obtained from reaction of pnictogen Zintl ions with transition metals complexes.

3.2 Results

3.2.1 Syntheses

3.2.1.1 Synthesis of [K(2,2,2-crypt)]$_3$[(η^3-As$_3$)Co(η^4-As$_7$)]·(en)

Ethylenediamine (en) solutions of a melt of nominal composition "K_3As_7" react with toluene solutions of [Co(PPh$_3$)$_2$Cl$_2$] in the presence of 2,2,2-cryptand to yield [K(2,2,2-crypt)]$_3$[(η^3-As$_3$)Co(η^4-As$_7$)] as the major product (Eq. 3.2).

$$1.4\ K_3As_7 + 3\ (2,2,2\text{-crypt}) + Co(PPh_3)_2Cl_2 \longrightarrow [K(2,2,2\text{-crypt})]_3[(\eta^3\text{-}As_3)Co(\eta^4\text{-}As_7)] + 2\ KCl + 2\ PPh_3 \quad (3.2)$$

After approximately 10 days, dark brown crystals of [K(2,2,2-crypt)]$_3$[(η^3-As$_3$)Co(η^4-As$_7$)] form in high yield (73%) as aggregates of plates. The crystals are highly air and moisture sensitive, sparingly soluble in THF, pyridine (py), and en, soluble in CH_3CN and DMF, and partially dissolve in crystallographic immersion oil. The cluster has been characterized by single-crystal XRD and laser desorption/ionization time-of-flight mass spectrometry (LDI-TOF MS). The electronic structure was further investigated through quantum chemical calculations.

3.2.1.2 Synthesis of [K(2,2,2-crypt)]$_2$[(η^4-As$_7$)M(COD)] (M = Rh, Ir)

Ethylenediamine (en) solutions of a melt of nominal composition "K_3As_7" react with toluene solutions of [M(COD)Cl]$_2$ (M = Rh, Ir) in the presence of 2,2,2-cryptand to afford coordination complexes [K(2,2,2-crypt)]$_2$[(η^4-As$_7$)Rh(COD)], and [K(2,2,2-crypt)]$_2$[(η^4-As$_7$)Ir(COD)], according to Equation 3.3.

$$K_3As_7 + 3(2,2,2\text{-crypt}) + 0.5[M(COD)Cl]_2 \longrightarrow [K(2,2,2\text{-crypt})]_2[(\eta^4\text{-}As_7)M(COD)] + KCl \quad (3.3)$$

where M = Rh, Ir

The product $[K(2,2,2\text{-crypt})]_2[(\eta^4\text{-}As_7)Rh(COD)]$ crystallizes as red-orange needles in reasonably high yield (61-78%). The crystals are air and moisture sensitive, soluble in pyridine (py), en, and DMF. Red plates of $[K(2,2,2\text{-crypt})]_2[(\eta^4\text{-}As_7)Ir(COD)]$ form in high yield (~82%) after approximately one week. The crystals are air and moisture sensitive, and soluble in py, en, and DMF. Both complexes have been characterized by single-crystal XRD, ^{1}H-NMR, ^{13}C-NMR, energy-dispersive X-ray analysis (EDX), and laser desorption/ionization time-of-flight mass spectrometry (LDI-TOF MS).

3.2.2 Solid State Structures

3.2.2.1 Solid State Structure of $[K(2,2,2\text{-crypt})]_3[(\eta^3\text{-}As_3)Co(\eta^4\text{-}As_7)]\cdot(en)$

Crystals of $[K(2,2,2\text{-crypt})]_3[(\eta^3\text{-}As_3)Co(\eta^4\text{-}As_7)]$ are triclinic, space group P-1, and contain the $[(\eta^3\text{-}As_3)Co(\eta^4\text{-}As_7)]^{3-}$ cluster (**3.1**), three $[K(2,2,2\text{-crypt})]^+$ cations, and one ethylenediamine solvate. Disorder in the cryptand and ethylenediamine were successfully modeled. Select bond distances and angles are reported in Table 3.2, and crystallographic data / refinement parameters are shown in Table 3.3.

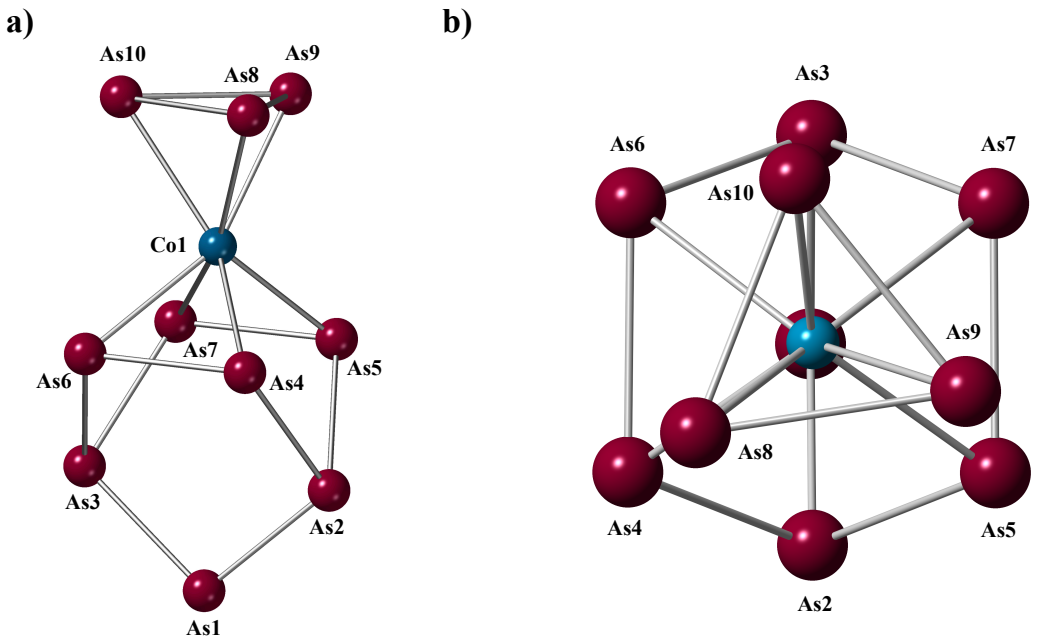

Figure 3.2: (a) Ball and stick model of $[(\eta^3\text{-As}_3)\text{Co}(\eta^4\text{-As}_7)]^{3-}$. (b) Top down view showing orientation of As_3 relative to As_7. (Co = blue, As = red-violet)

The anion **3.1** has 62 valence electrons [($5e^-$ x 10 As) + ($9e^-$ x 1 Co) + ($3e^-$ charge) = 62 e^-] and is predicted to be diamagnetic. In the solid-state structure, a D_{3h} cyclo-As_3 unit and a C_{2v} norbornadiene-type As_7 cage are bridged by a single Co atom (Figure 3.2). The As_7 ligand, ligated to Co in an η^4 – fashion, is reminiscent of the η^4-As_7 ligand described in the $[(\eta^4\text{-As}_7)\text{M(CO)}_3]^{3-}$ (M = Cr, Mo, W) series of anions, with an overall 3^- charge. These η^4-As_7 ligands coordinate to transition metals through four As atoms through six shared electrons. [63,96,112] Previously described cyclo-As_3 fragments have been assigned an overall charge of 3^-, and coordinate as six electron donors, satisfying Hückel's [4n+2]π electron rule for aromaticity. [113-117] In order to balance the charges to yield an overall 3^- charge on the cluster, Co is assigned an oxidation state of 3^+. The structural parameters of **3.1**, such as bond distances and angles (described below), support a description of its subunits as cyclo-As_3^{3-}, Co^{3+}, and $[As_7]^{3-}$. For electron

accounting purposes, both As_3^{3-} and As_7^{3-} are considered six electron donors to $Co^{3+}(d^6)$, resulting in an 18-electron complex.

Within the cyclo-As_3 unit, As-As bond distances of 2.382(1) – 2.386(1) Å are between As-As single (2.42 Å) and double bonds (2.28 Å), suggestive of some electron delocalization in the ring and partial multiple bond character. Endocyclic As-As-As angles average 60.0˚. These structural metrics are similar to those of other Co-bound cyclo-As_3 fragments, such those seen in [(η^3-As_3)$Co(CO)_3$] [$d(As\text{-}As)_{av}$ = 2.372(5) Å, ∠As-As-As = 58.2 (1)-60.0(-)˚], and [(η^3-As_3)$Co\{\eta^4\text{-}As_4(mes)_2\}]^{2-}$ [(Mes) = 2,4,6-trimethylphenyl; $d(As\text{-}As)_{av}$ = 2.381(1) Å, ∠As-As-As = 59.74(4)-60.26(5)˚].[113,118,119] The η^3 – coordination of cyclo-As_3 to cobalt forms a nearly undistorted [$CoAs_3$] tetrahedron, with Co-{As_3} bond distances between 2.393(1) – 2.405(1) Å, As-Co-As angles averaging 59.6˚, and As-As-Co angles of 60.2˚.

The η^4-As_7 ligand exhibits a norbornadiene-type conformation of seven As atoms. Structural transformation of C_{3v} nortricyclane $[As_7]^{3-}$ precursors to η^4-ligated C_{2v} norbornadiene-type $[As_7]^{3-}$ through insertion into one As-As bond has been reported, most notably in the first structurally characterized complex of this class, [(η^4-As_7)$Cr(CO)_3$]$^{3-}$.[61,63,65,101,112,120] Nonbonding interactions As4···As5 (3.209(1) Å) and As6···As7 (3.170(1) Å) indicate a nearly complete nortricyclane-norbornadiene transformation, and are far too long for primary As-As bonding interactions. Within the As_7 ligand, As-As bond distances [2.343(1) – 2.487(1) Å] and As-As-As angles [89.2(3)˚ – 104.75(3)˚] are comparable to those seen in the [(η^4-As_7)$M(CO)_3]^{3-}$ series of anions (M = Cr, Mo, W). Coordination of the As_7 subunit to Co through [As4, As5, As6, As7] is reminiscent of a square-based pyramidal geometry, with As-As-As angles averaging 90.1(3)˚, and As-As bond distances of 2.351(1) Å (As4-As5) and 2.353(1) Å (As5-As7).

These distances are similar to those of the cyclo-As_3 subunit, and also are indicative of As-As multiple bond character (bond order greater than 1). The Co-{As_7} [2.396(1) – 2.431(1) Å] distances are comparable to those of Co-{As_3} [2.393(1) – 2.405(1) Å] and Co(III)-As bonding interactions in $[(\eta^3\text{-}As_3)Co(\eta^4\text{-}As_4(mes)_2)]^{2-}$ [2.364(1) – 2.467(1) Å] and $[(\eta^3\text{-}As_3)Co(CO)_3)]$ [2.351(4) – 2.412(4) Å]. [113,121] A narrow range of Co-{As_7} distances [2.396(1) – 2.431(1) Å] indicates minimal influence of Co-{As_3} interactions on the length of Co-{As_7} bond distances through either cooperative or synergistic effects.

Table 3.2: Selected Bond Lengths [Å] and angles (°) for the $[(\eta^3\text{-}As_3)Co(\eta^4\text{-}As_7)]^{3-}$ anion

Distances [Å]			
As1-As2	2.3427(7)	As8-As10	2.3821(9)
As1-As3	2.3723(8)	As9-As10	2.3848(7)
As2-As4	2.4803(11)	As4-Co1	2.4119(9)
As2-As5	2.4757(10)	As5-Co1	2.3957(12)
As3-As6	2.4762(10)	As6-Co1	2.4311(10)
As3-As7	2.4867(11)	As7-Co1	2.4195(8)
As4-As6	2.3506(9)	As8-Co1	2.3930(9)
As5-As7	2.3535(9)	As9-Co1	2.3979(10)
As8-As9	2.3858(7)	As10-Co1	2.4051(7)
Angles (°)			
As5-Co1-As7	58.52(4)	As10-Co1-As8	59.53(2)
As4-Co1-As5	83.75(4)	As4-Co1-As6	58.07(4)
As10-Co1-As7	101.47(6)	As3-As4-As5	97.33(7)
As10-Co1-As6	96.38(5)	As5-As7-As6	90.40(3)
As8-Co1-As5	127.82(7)	As8-As9-As10	59.97(6)
As8-Co1-As7	157.23(7)	As9-As8-As10	60.01(3)
As9-Co-As6	155.87(5)	As8-As10-As9	60.07(3)
As9-Co1-As4	139.15(6)	As2-As4-As6	104.75(3)
As4-Co1-As8	92.53(3)	As3-As7-As6	103.92(4)
As9-Co1-As5	90.73(5)	As4-As2-As5	80.91(4)
As9-Co1-As7	100.79(6)	As7-As3-As6	79.39(5)
As6-Co1-As7	81.96(5)	As2-As1-As3	98.69(6)
As8-Co1-As9	59.73(3)		
As9-Co1-As10	59.53(4)		

Table 3.3: Selected Crystallographic, Data Collection, and Refinement Data for **3.1**

	[K(2,2,2-crypt]$_3$(**3.1**)•en
Empirical formula	$C_{56}H_{116}As_{10}CoK_3N_8O_{18}$
Formula weight	2114.99
Temperature/K	150(2)
Crystal system	Triclinic
Space group	P-1
a/Å	13.7699(5)
b/Å	14.0382(5)
c/Å	22.7111(9)
α/°	94.8566(6)
β/°	101.4088(6)
γ/°	103.3492(6)
Volume/Å^3	4147.9(3)
Z	2
ρ_{cal} cg/cm^3	1.693
μ/mm-1	4.379
F(000)	2132.0
Crystal size/mm^3	0.22 x 0.20 x 0.04
Radiation	Mo Kα (λ = 0.71073)
2*θ* range for data collection/°	3.120 to 54.994
Index ranges	-17 ≤ h ≤ 17, -18 ≤ k ≤ 18, -29 ≤ l ≤ 29
Reflections collected	59689
Independent reflections	19023 [R_{int} = 0.0346, R_{sig} = 0.0441]
Data/restraints/parameters	19023/335/941
Goodness-of-fit on F^2	1.168
R_1/wR_2 [$I>=2\sigma(I)$]	0.0365, 0.0684
R_1/wR_2 [all data]	0.0604, 0.0729

3.2.2.2 Solid State Structure of [K(2,2,2-crypt)]$_2$[(η^4-As$_7$)Rh(COD)]

Crystals of [K(2,2,2-crypt)]$_2$[(η^4-As$_7$)Rh(COD)] are monoclinic, space group $P2_1$. The asymmetric unit contains two [K(2,2,2-crypt)]$^+$ cations and the dianionic complex [(η^4-As$_7$)Rh(COD)]$^{2-}$ (**3.2**, Figure 3.3). The structure was refined as a two-component inversion twin, yielding Flack parameter x = 0.011(5). Crystallographic data are summarized in Table 3.6, and a list of bond distances and angles is given in Table 3.4.

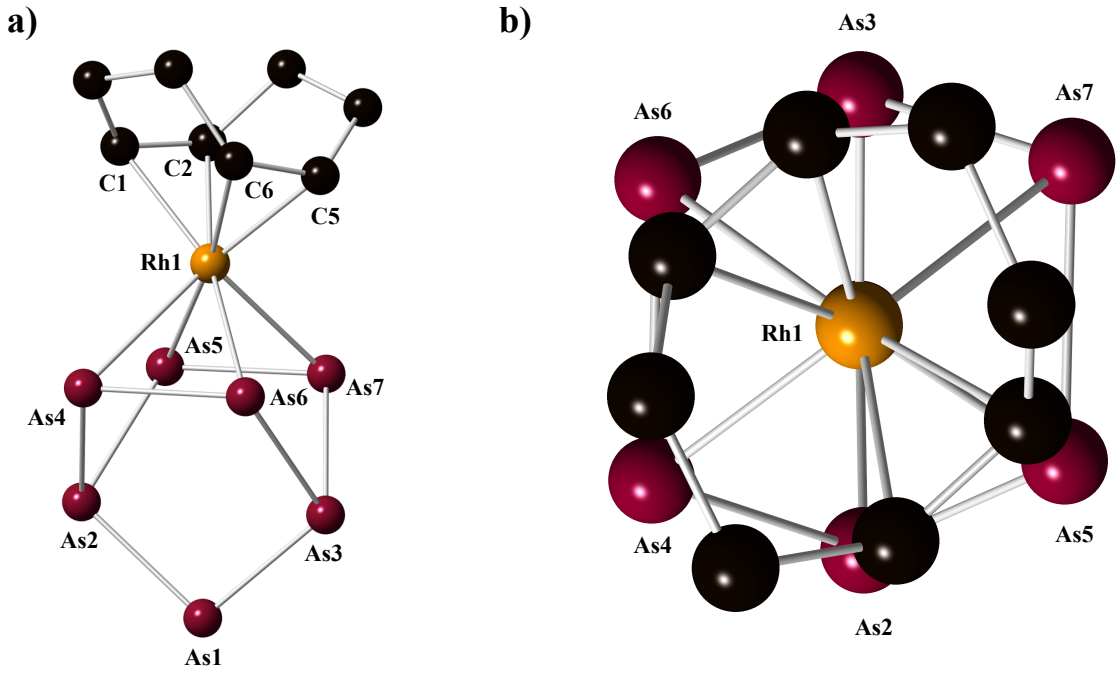

Figure 3.3: (a) Ball and stick model of $[(\eta^4\text{-}As_7)Rh(COD)]^{2-}$. Hydrogens omitted for clarity (b) Top down view of $[(\eta^4\text{-}As_7)Rh(COD)]^{2-}$, showing orientation of COD ligand relative to As_7 cage. Hydrogens omitted for clarity (Rh = yellow, As = red-violet, C = black).

Cluster **3.2** is a 50 electron complex [($5e^-$ x 7 As) + ($9e^-$ x 1Rh) + ($2e^-$ x 2(C=C)) + $2e^-$ overall charge], predicted diamagnetic. The structure is comprised of a nearly C_{2v} norbornadiene-like $[As_7]^{3-}$ ligand coordinated in an η^4- fashion to a C_{2v} $[Rh(COD)]^{1+}$ fragment. Due to asymmetry between the COD ligand and $[As_7]^{3-}$ cage (see Figure 3.3b), the symmetry of the resultant ion is lowered to C_s. The $[As_7]^{3-}$ ligand has been described previously as a six-electron donor, coordinating to transition metal fragments primarily through π-type orbitals. [95] A more complete discussion of this $[As_7]^{3-}$ bonding model is given alongside the results of quantum chemical calculations in Section 3.2.3. Rhodium is coordinated to eight atoms, arranged in a distorted square anti-prismatic geometry. The formal oxidation state of Rh is assigned as +1, resulting in a diamagnetic 18-electron complex ($Rh^{1+}(d^8)$: 8 e^-, $[As_7]^{3-}$: 6 e^-, COD: 4 e^-).

As-As distances are between 2.3360(8) – 2.4845(9) Å, similar to those found in the $[As_7M(CO)_3]^{3-}$ ion series (M = Cr, Mo, W). [63,95] As with previously described nortricyclane-norbornadiene structural transitions, the extent of activation of the As_7 unit can be inferred from As4···As5 and As6···As7 contacts, which are equal in idealized norbornadiene geometry. Nonbonding contacts in **3.2** are 3.215(6) Å (As4···As5) and 3.225(7) Å (As6···As7), indicting almost complete structural activation. Distances between bonded pairs As4-As6 (2.3421(8) Å) and As5-As7 (2.3360(8) Å) are longer than As-As double bonds (2.28 Å), shorter than As-As single bonds (2.42 Å) [100], and contracted compared to As-As bonds in the parent nortricyclane-like $[As_7]^{3-}$ ion (2.399 – 2.498 Å). Bonds between apex As1 and neighboring As2 and As3 atoms [2.3435(9) - 2.3563(6) Å] are similarly shorter, suggesting multiple bond character. Remaining As-As distances [2.4622(8) -2.4845(9) Å] are in the appropriate range for As-As single bonds.

As-Rh interactions [2.5228(6) – 2.6552(7) Å] are slightly longer than other As-Rh interactions, such as those in the dinuclear cation $[(triphos)Rh(As_2S)Rh(triphos)]^{2+}$ [d(As-As) = 2.410(4) – 2.582(3) Å]. [122] Of the As-Rh interactions in **3.2**, As5-Rh1 and As6-Rh1 are longer, at 2.6552(7) Å and 2.5977(6) Å. A relative lengthening of certain Pn-M distances in $[Pn_7M(CO)_3]^{3-}$ ions (Pn = P, As, Sb) were rationalized to be the result of a high *trans* influence of CO ligands on pnictide atoms, as mediated through the metal center (average C-M-Pn angle = 175°). In the case of **3.2**, *trans* influence is ruled out, as As-Rh-C angles are closest to linear for As4-Rh1-C1 (169.57(4)°) and As7-Rh1-C5 (172.23(8)°), yet the As4-Rh1 / As7-Rh1 bond lengths are the shortest [av. 2.532(9) Å].

Rh-C bond lengths (2.1594(32) – 2.1786(36) Å) and C-C distances (av. 1.403(67) Å) are elongated compared to other olefin-Rh and alkene bond lengths (1.337 Å in free ethylene), indicating π-backbonding between the transition metal and alkene. The

synergistic effects between transition metals and coordinated alkenes are described qualitatively using the Dewar-Chatt-Duncanson model. M-C σ bonding occurs through a filled alkene π-orbital, donating electrons to an empty metal d-orbital. In electron-rich transition metals, extensive back-donation of electron density from a filled metal d-orbital to an empty π^* antibonding orbital of the alkene can occur. Donation of electron density to alkene antibonding orbitals weakens C=C bonding, and may cause rehybridization of carbon orbitals from sp^2 to sp^3, resulting in a lengthening of the alkene bond distance and narrowing C-R and C-H angles. Given the average C-C bond distance of 1.403(67) Å in **3.2**, bonding may be more accurately described by a metallocyclopropane resonance, as opposed to purely M-L complexation through a single σ interaction.

Table 3.4: Selected Bond Lengths [Å] and angles (°) for $[(\eta^4\text{-}As_7)Rh(COD)]^{2-}$ (**3.2**)

Distances [Å]			
As1-As2	2.3563(6)	As5-Rh1	2.6552(7)
As1-As3	2.3435(9)	As6-Rh1	2.5977(6)
As2-As4	2.4622(8)	As7-Rh1	2.5228(6)
As2-As5	2.4845(9)	Rh1-C1	2.1636(44)
As3-As6	2.4841(7)	Rh1-C2	2.1561(40)
As3-As7	2.4652(6)	Rh1-C5	2.1786(36)
As4-As6	2.3421(8)	Rh1-C6	2.1495(32)
As5-As7	2.3360(8)	C1-C2	1.4008(71)
As4-Rh1	2.5489(12)	C5-C6	1.4061(61)
Angles (°)			
As4-Rh1-As6	54.128(14)	As2-As1-As3	98.75(21)
As6-Rh1-As7	77.756(15)	C1-Rh1-C2	37.84(15)
As5-As7-As6	93.989(18)	Rh1-C1-C2	70.78(20)
As6-As3-As7	81.004(16)	C1-C2-C3	124.70(40)
As1-As2-As4	104.753(20)		

3.2.2.4 Solid-State Structure of [K(2,2,2-crypt)]$_2$[(η^4-As$_7$)Ir(COD)]

Crystals of [K(2,2,2-crypt)]$_2$[(η^4-As$_7$)Ir(COD)] are monoclinic, space group *C2/c*, and contain the [(η^4-As$_7$)Ir(COD)]$^{2-}$ anion (**3.3**) and two [K(2,2,2-crypt)]$^+$ cations. The Ir resides on a crystallographic two-fold axis, with other atoms occupying general positions. Crystallographic data are summarized in Table 3.6, and a list of bond distances and angles is given in Table 3.5.

The geometric and electronic structures of this cluster are nearly identical to **3.2**, with some subtle differences. This cluster is isoelectronic to **3.2**, with a total electron count of 50e$^-$ [(5e$^-$ x 7 As) + (9e$^-$ x 1 Ir) + (2e$^-$ x 2(C=C)) + 2e$^-$ overall charge], and is also predicted to be diamagnetic. A C_{2v} norbornadiene-type As$_7^{3-}$ cage is ligated in an η^4-fashion to a C_{2v}-symmetric [Ir(COD)]$^{1+}$ fragment. The resulting anion possesses C_{2v} symmetry, which is crystallographically imposed by a C_2-rotational axis bisecting the cluster (Figure 3.4). The d^8- Ir^{1+} center is coordinated to eight atoms, and has a molecular geometry reminiscent of a distorted square antiprism. Considering [As$_7$]$^{3-}$ a six-electron donor and the COD ligand a four-electron donor, the total electron count at Ir is 18 e$^-$.

As-As bond distances [2.3448(8) - 2.4846(7) Å] are similar to reported values, and those found in **3.1** and **3.2**. [95] As previously mentioned, the extent of nortricyclane – norbornadiene transition for [As$_7$]$^{3-}$, is noted by the nonbonding separation distance between As3···As4' and As4···As3' (analogous to As4···As5 and As6···As7 contacts in **3.1** and **3.2**). In **3.3**, these distances are equal (3.229(8) Å) due to crystallographic symmetry, and indicate minimal bonding interactions between these As atoms. The shorter As-As bonds, As3-As4 and As3'-As4' [2.3448(8) Å], are assumed to have multiple bond character. Bonds between As1-As2 [2.3568(5) Å] are also in the same

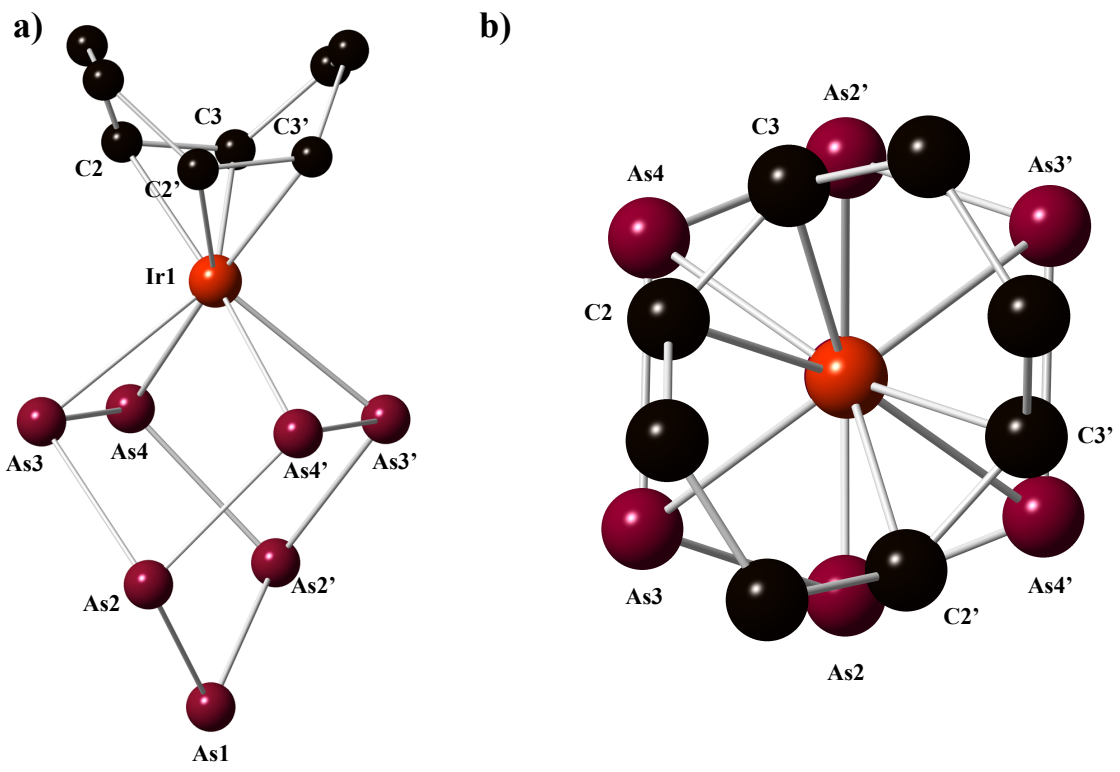

Figure 3.4: (a) Ball and stick model of $[(\eta^4\text{-}As_7)Ir(COD)]^{2-}$ (b) Top down view of $[(\eta^4\text{-}As_7)Ir(COD)]^{2-}$, illustrating the orientation of the COD ligand in relation to the $[As_7]^{3-}$ cage. Hydrogens omitted for clarity (Ir = red, As = red-violet, C = black).

range as those of the Rh congener, with remaining As-As distances [2.4727(5) -2.4846(7) Å] on the order of single bonds.

The As-Ir bonds [2.5369(8)– 2.6114(5) Å] are slightly elongated compared to other As-Ir interactions, with As3-Ir1 (2.6114(5) Å) longer than As4-Ir1 (2.5369(8) Å). The As4-Ir-C2 bond angle is the closest to linear, at 166.3(7)°, with remaining As-Ir-C angles <140°. The Ir-C bond lengths [2.1408(22) – 2.1475(19) Å] and an elongated C=C bond distance [COD, 1.438(3) Å] are comparable to other Ir-olefin complexes, such as the precursor $[Ir(COD)Cl]_2$, and longer than typical alkene bond lengths (1.337 Å in free ethylene). This indicates a highly activated olefin bond, resulting from extensive backdonation of electron density from a filled Ir d orbital to the C=C π* antibonding orbital, which reduces the formal C-C bond order. Simultaneously, π-backdonation

strengthens metal-carbon bonding, leading to a contraction of M-C bond distances. The Ir-C distances in **3.3** are similar to other Ir-olefin interactions, many of which are described as exhibiting electron backdonation. Therefore, olefin complexation to Ir in **3.3** is most suitably described by a metallocyclopropane resonance structure, which is not unexpected for row 3 transition metal-olefin complexes.

Table 3.5: Bond Lengths [Å] and angles (°) in $[(\eta^4\text{-}As_7)Ir(COD)]^{2-}$ (**3.3**)

Distances [Å]			
As1-As2	2.3568(5)	Ir1-C2	2.1475(19)
As2-As3	2.4846(7)	Ir1-C3	2.1408(22)
As2-As4	2.4727(5)	C2-C3	1.4380(33)
As3-As4	2.3448(8)		
As3-Ir1	2.6114(5)		
As4-Ir1	2.5369(8)		
Angles (°)			
As1-As2-As3	107.943(11)	As3-Ir1-As4	77.674(7)
As4-As2'-As1	106.065(10)	C2-Ir1-C3	39.19(8)
C2-Ir1-As3	139.42(11)	As3-As2-As4'	81.290(9)
C2-C3-C4	123.25(19)		
C2-C3-Ir1	70.66(10)		

Table 3.6: Select Crystallographic, Data Collection, and Refinement Data for **3.2** and **3.3**.

	[K(2,2,2-crypt)]$_2$(**3.2**)	[K(2,2,2-crypt)]$_2$(**3.3**)
Empirical formula	$C_{44}H_{84}As_7K_2N_4O_{12}Rh$	$C_{44}H_{84}As_7IrK_2N_4O_{12}$
Formula weight	1566.70	1655.99
Temperature/K	120(2)	120(2)
Crystal system	Monoclinic	Monoclinic
Space group	$P2_1$	C2/c
a/Å	11.6336(5)	25.5878(11)
b/Å	21.3723(10)	19.3867(8)
c/Å	12.9618(6)	12.8793(6)
α/°	90	90
β/°	111.9859(7)	108.1941(6)
γ/°	90	90
Volume/Å^3	2988.4(2)	6069.5(5)
Z	2	4
ρ_{cal} cg/cm^3	1.741	1.812
μ/mm-1	4.327	6.180
F(000)	1572.0	3272.0
Crystal size/mm^3	0.27 x 0.25 x 0.025	0.30 × 0.17 × 0.15
Radiation	Mo Kα (λ = 0.71073)	Mo Kα (λ = 0.71073)
2θ range for data collection/°	3.388 to 59.998	3.85 to 61.996
Index ranges	-16 ≤ h ≤ 16, -30 ≤ k ≤ 30, -18 ≤ l ≤ 18	-36 ≤ h ≤ 36, -28 ≤ k ≤ 28, -18 ≤ l ≤ 18
Reflections collected	44734	52345
Independent reflections	16887 [R_{int} = 0.0311, R_{sig} = 0.0421]	9661 [R_{int} = 0.0338, R_{sig} = 0.0277]
Data/restraints/parameters	16887/1/652	9661/0/329
Goodness-of-fit on F^2	1.000	1.230
R_1/wR_2 [$I>=2\sigma$ (I)]	0.0253, 0.0468	0.0227, 0.0423
R_1/wR_2 [all data]	0.0315, 0.0480	0.0298, 0.0434

See the Crystallographic Studies Section for details on the refinement.

3.2.3 Density Functional Theory Analyses

Quantum calculations were performed on [(η^3-As$_3$)Co(η^4-As$_7$)]$^{3-}$ (**3.1**) by Dr. Mark Palenik at the Naval Research Laboratory. Density functional theory (DFT) calculations used to generate molecular orbital surfaces were performed with a Def2-TZVP basis set in Gaussian 09, using the solid-state structural data with optimized C_s symmetry as an initial model. Wiberg Bond Index (WBI) calculations were performed in

Gaussian 09 (results are given in Table 3.7). Preliminary charge densities used for Bader Charge Analyses were generated in Gaussian 09 and compiled using Bader Charge Analysis Code from the Henkelman group (results given in Table 3.8).

Calculated molecular orbitals of **3.1** are shown in Figures 3.5 and 3.6. The LUMO is largely comprised of As_3 based σ antibonding orbitals, and dictates that this as one potential center of reactivity for the molecule. The HOMO and lower lying orbitals consist mainly of As lone pair orbitals. HOMO-4 shows heavy electron localization on the As_3 ring, potentially of lone pair electrons. There are also bonding interactions between As p orbitals and the Co atom. Two orthogonal lone pairs are indicated for two-coordinate As1, with significant As-p_y orbital character in HOMO and HOMO-1, and As-p_z orbital character in HOMO-2 and HOMO -3. Many of the bonding interactions are delocalized over the As_3 ring, the Co ion, and the four Co-bound As atoms of the As_7 moiety. Interactions of this type have previously been described as main group interactions mediated by a transition metal.

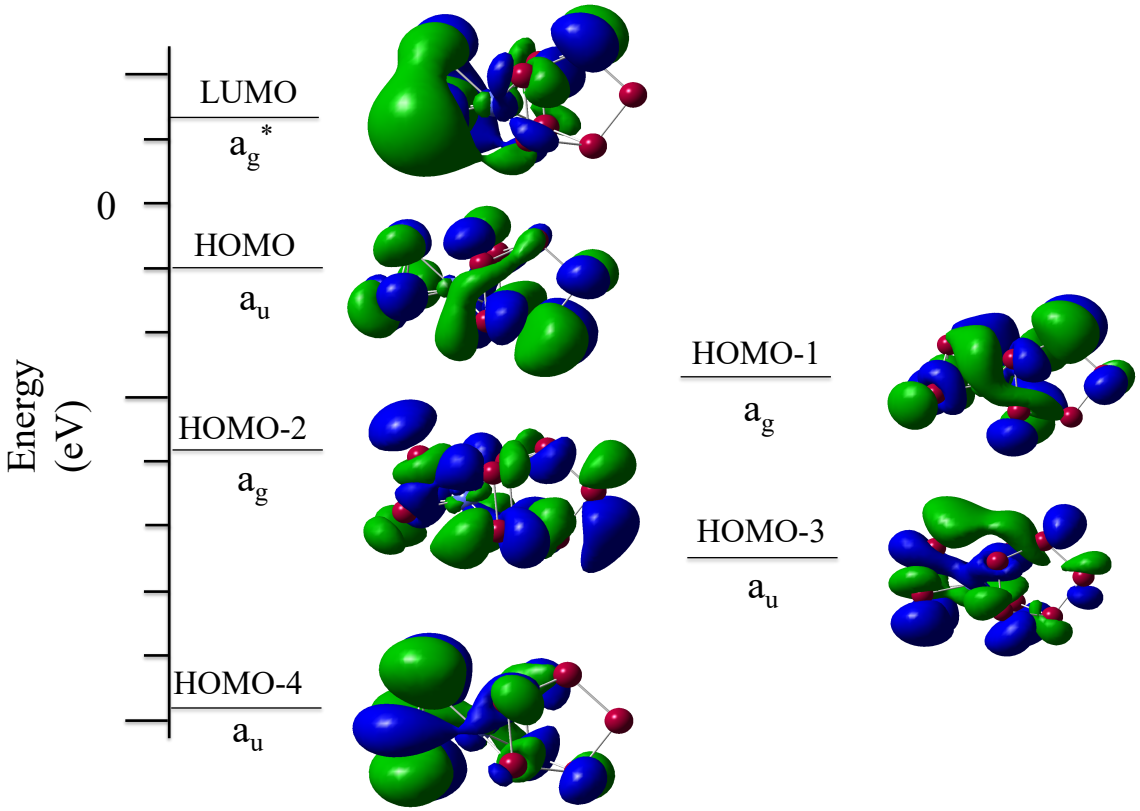

Figure 3.5: Representation of select orbitals in $[(\eta^3\text{-}As_3)Co(\eta^4\text{-}As_7)]^{3-}$ **(3.1)**.

A qualitative molecular orbital diagram constructed using fragment orbital approach is shown in Figure 3.6, where the symmetry adapted linear combination (SALCs) of π-type orbitals in $[As_7]^{3-}$ are adapted from [Ref]. The initial description of $[As_7]^{3-}$ molecular orbitals, constructed from Fenske-Hall Molecular Orbital calculations on C_{2v} $[As_7]^{3-}$, are in good agreement with current DFT analyses. In the qualitative depiction of $[As_3CoAs_7]^{3-}$, a norbornadiene-like $[As_7]^{3-}$ ligand with idealized C_{2v} geometry combines with a $CoAs_3$ tetrahedron of C_{3v} symmetry to yield the cluster **3.1**, with overall C_s symmetry. The four Co-ligated As atoms of $[As_7]^{3-}$ share a delocalized 2^- charge in predominantly π-type orbitals, and are isoelectronic to a cyclobutadiene fragment. The HOMO of **3.1** is primarily nonbonding, derived from the lone pair (b2 character) of the two-coordinate As1 site.

Wiberg bond indices and Bader partial charges for each atom of **3.1** are given in Table 3.7. Calculated Bader charges are in excellent agreement with the expectations of the simple bonding scheme described previously. In this model, there is an isolated -1 charge on the two-coordinate As1 atom, and a -2 charge delocalized over As4-As6 and As5-As7 bond pairs. Furthermore, the As_3^{3-} ligand has a formal -1 charge on each As, balanced by the positive charge on the Co^{3+} ion.

Table 3.7: Results from Wiberg Bond Index calculations and Bader charge analyses on **3.1**.

Site	Wiberg Index	Bader Partial Charges
Co1	4.4547	0.2375
As1	3.1214	-0.4977
As2	3.1626	-0.2561
As3	3.1627	-0.2443
As4	3.1215	-0.3155
As5	3.1861	-0.3144
As6	3.1219	-0.3029
As7	3.1628	-0.3040
As8	3.1628	-0.3574
As9	3.1219	-0.3525
As10	3.1863	-0.2885
	Total	-2.9958

Calculated bond indices of As atoms are similar (~3.15), indicating a similar number of bond order for each As. As expected, As1 carries the greatest charge (-0.50), with As2 and As3, bound directly to As1, bearing the smallest charges. Partial charges from other As atoms are mitigated by donation to the Co(III) ion, resulting in a reduction of their Bader charges (i.e., charges of As2 – As10 are lower than that of As1). Similarly, the positive partial charge on the cobalt (+0.24) is reduced compared to a qualitative description, but still supports the suggested model.

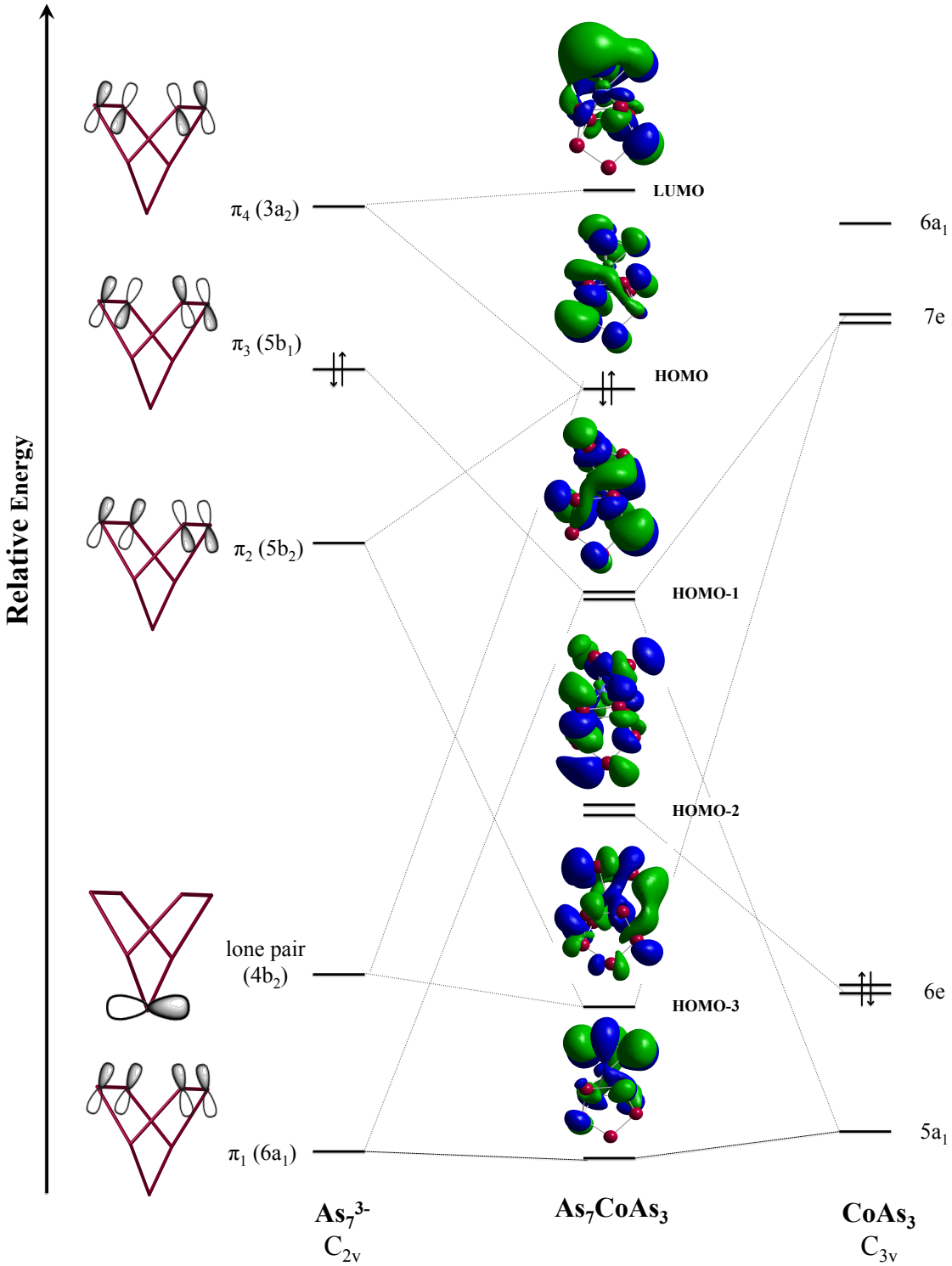

Figure 3.6: Qualitative Molecular orbital diagram for C_s $[(\eta^3\text{-}As_3)Co(\eta^4\text{-}As_7)]^{3-}$, comprised of interactions between π-type orbitals of C_{2v} norbornadiene As_7^{3-} and C_{3v} $CoAs_3$ fragments.

3.2.4 NMR Spectroscopy

The $^{13}C\{^{1}H\}$ NMR spectrum of $[(\eta^4\text{-}As_7)Rh(COD)]^{2-}$ **(3.2)** shows resonances of 2,2,2-cryptand (δ = 54.4, 68.2, 70.9 ppm), residual toluene (δ = 21.7, 126.1, 129.0, 129.8 ppm), and the COD ligand (δ = 35.2, 70.3, 70.4 ppm) (Figure 3.7). The COD signal at δ = 35.2 ppm is assigned to the methylene carbons (B), while the doublet signals at 70.3 and 70.4 originate from olefin carbon resonances. The methylene resonances are deshielded relative to the precursor, $[Rh(COD)Cl]_2$ (δ = 31.3 ppm), while the olefin resonances are shifted upfield (δ = 78.8, 78.9 ppm).

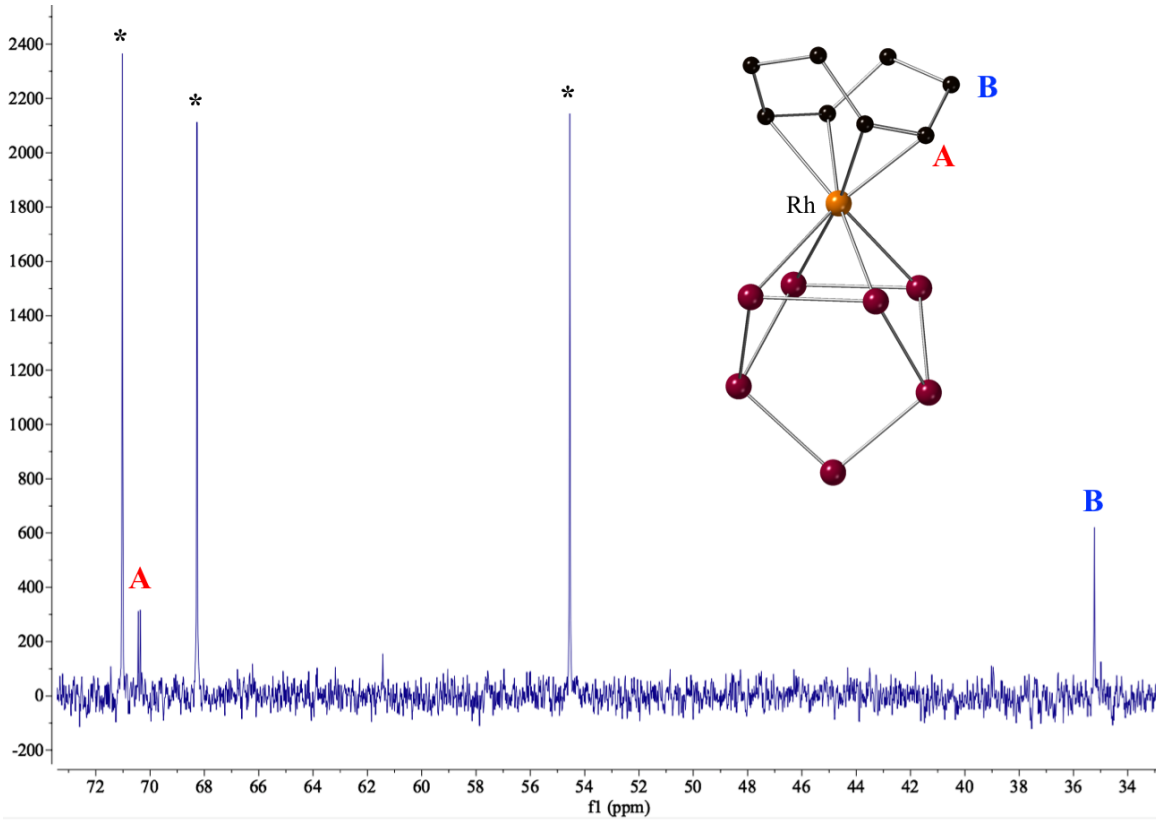

Figure 3.7: Aliphatic region of $^{13}C\{^{1}H\}$ spectrum of $[K(2,2,2\text{-crypt})]_2[(\eta^4\text{-}As_7)Rh(COD)]$. Recorded at 298 K at 400 MHz in d_5-pyridine. Signals corresponding to 2,2,2-cryptand are designated by an asterisk (*).

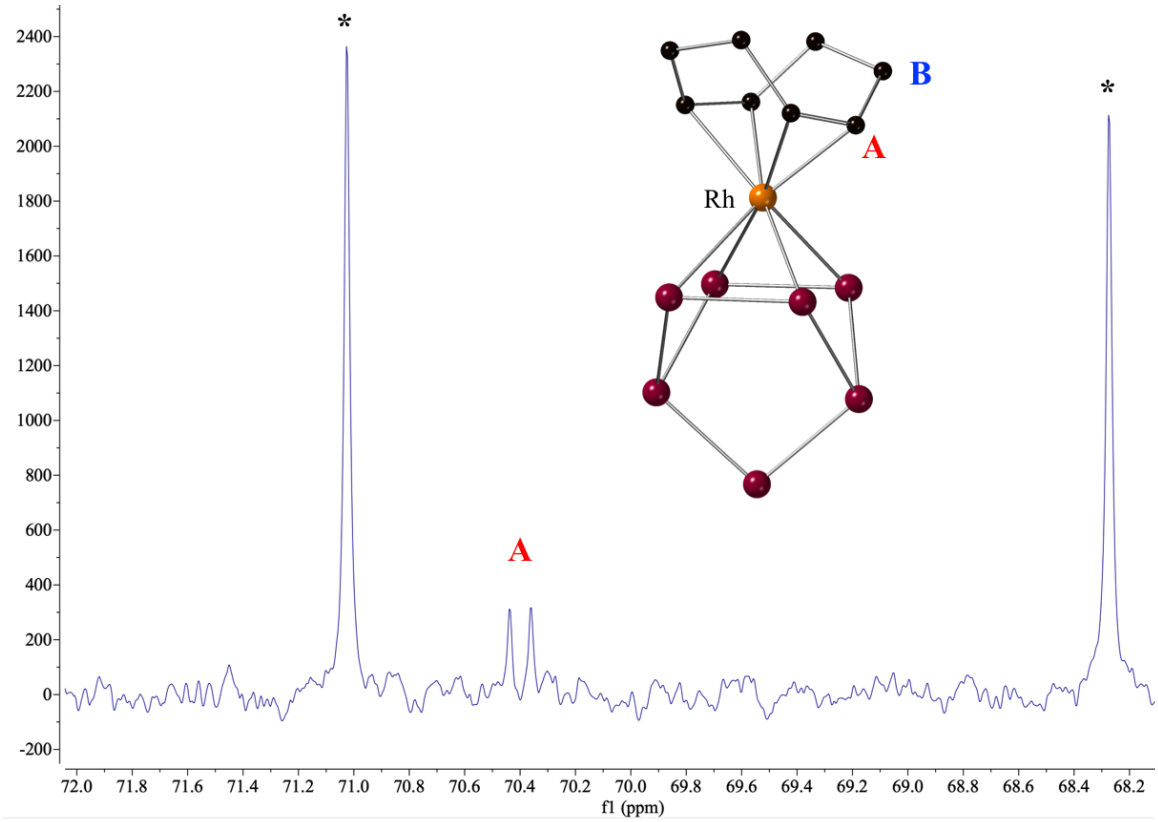

Figure 3.8: $^{13}C\{^{1}H\}$ spectrum of $[K(2,2,2\text{-crypt})]_2[(\eta^4\text{-}As_7)Rh(COD)]$, with focus on the region between 68 – 71 ppm. Signals from 2,2,2-cryptand are denoted with an asterisk (*). Recorded at 298 K at 400 MHz in d_5-pyridine.

The $^{13}C\{^{1}H\}$ NMR spectrum of the $[K(2,2,2\text{-crypt})]^+$ salt of $[(\eta^4\text{-}As_7)Ir(COD)]^{2-}$ (**3.3**, Figure 3.9) exhibits resonances of 2,2,2-cryptand (δ = 54.4, 68.2, 70.9 ppm), a toluene impurity (δ = 21.7, 126.2, 129.1, 129.8 ppm), and the COD ligand (δ = 36.6 ppm). The COD signal at δ = 36.6 ppm is assigned to the methylene carbons (B), and is deshielded relative to those of the precursor, $[Ir(COD)Cl]_2$ (δ = 32.3). The olefin carbon signal (A) is not observed, and is likely obscured by 2,2,2-cryptand signal ($^{13}C\{^{1}H\}$

[Ir(COD)Cl]$_2$: δ = 62.2 ppm). This signal was also absent in the $^{13}C\{^1H\}$ NMR spectrum of the analogous group 14 anion [(η^4-Sn$_9$)Ir(COD)]$^{3-}$, indicating similar chemical shifts, and therefore chemical environments, for olefin carbons in these clusters. [106,107]

The ^{1}H-NMR spectra show three signals for the COD ligand of each cluster, as expected. The olefin protons of [(η^4-As$_7$)Rh(COD)]$^{2-}$ have a chemical shift of δ = 4.71 ppm. The methylene protons are diastereotopic, with resonances δ = 2.35 and 2.69 ppm. Proton resonances for the COD ligand of [(η^4-As$_7$)Ir(COD)]$^{2-}$, observed at δ = 4.25 ppm (CH) and δ = 2.28 and 2.55 ppm (CH$_2$), are shifted upfield relative to [(η^4-As$_7$)Rh(COD)]$^{2-}$. These resonances are similar to those of group 14-Ir coordination complexes [(η^4-Sn$_9$)Ir(COD)]$^{3-}$ and [(η^4-Pb$_9$)Ir(COD)]$^{3-}$.[107,123] The broad signals hint

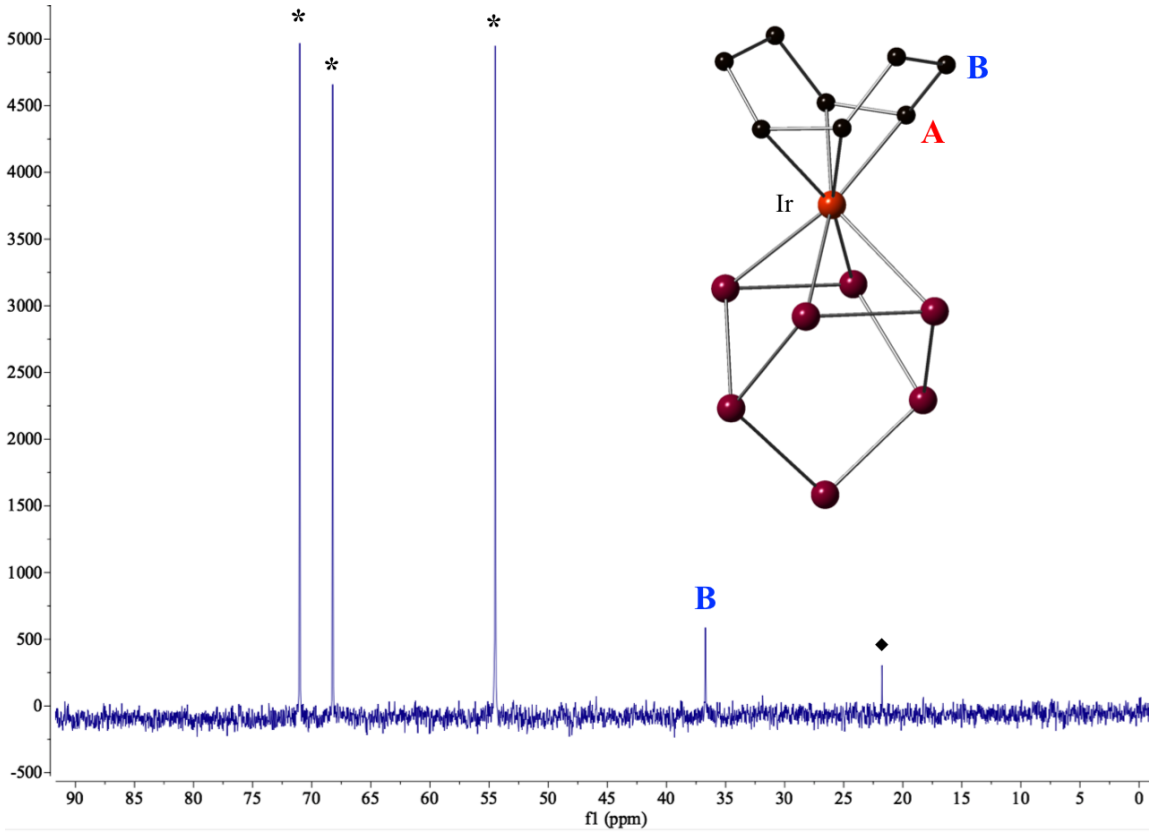

Figure 3.9: $^{13}C\{^1H\}$ spectrum of [K(2,2,2-crypt)]$_2$[(η^4-As$_7$)Ir(COD)]. Signals from 2,2,2-cryptand are denoted with an asterisk (*). Recorded at 298 K at 500 MHz in d$_5$-pyridine.

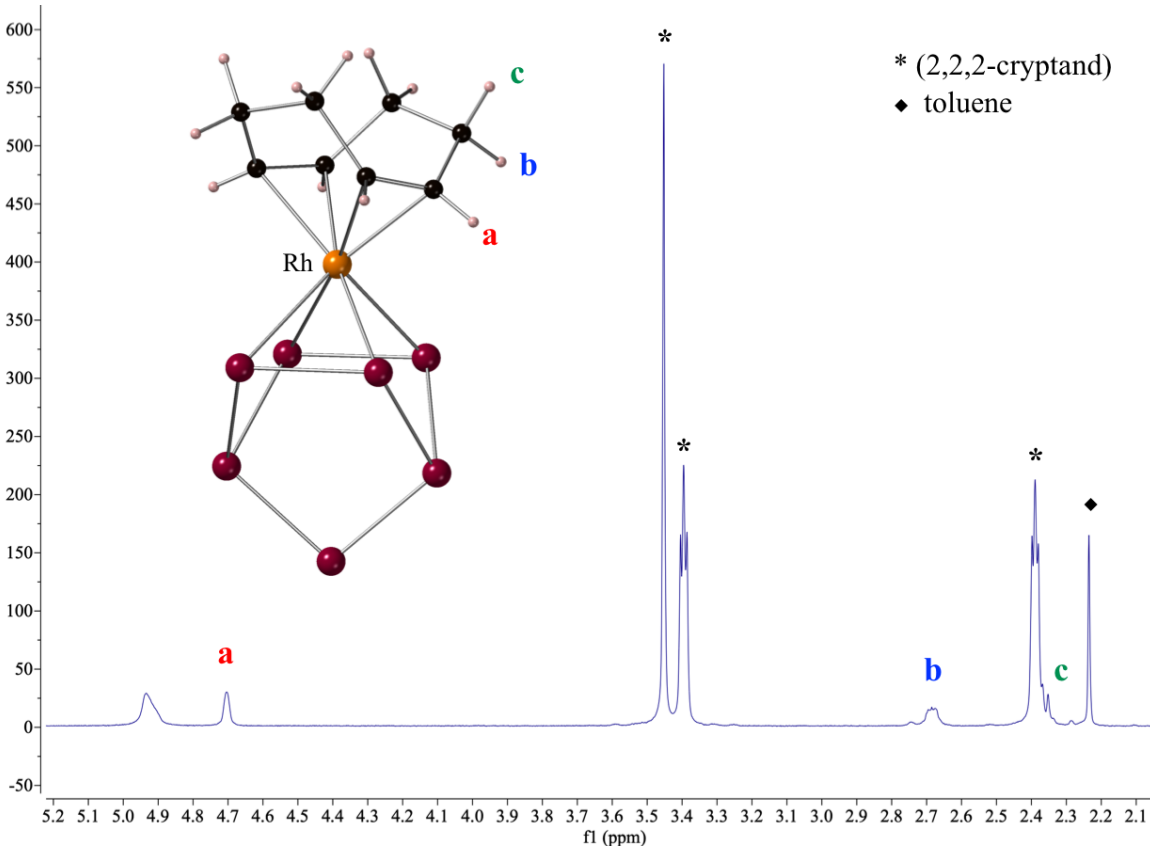

Figure 3.10: $^{1}H\{^{13}C\}$ spectrum of $[K(2,2,2\text{-crypt})]_2[(\eta^4\text{-}As_7)Rh(COD)]$. Signals from 2,2,2-cryptand and toluene are denoted with an asterisk (*) and diamond (◆), respectively. Recorded at 298 K at 400 MHz in d_5-pyridine.

towards a possible dynamic or fluxional process occurring for each cluster in solution, though the exact nature of these exchanges cannot be further investigated due to a lack of other spin-active nuclei.

When coupled with bond distances from the solid-state structures, the ^{13}C chemical shift values can be used to determine the extent of metal to ligand charge transfer (i.e. π -backbonding). When electrons from filled Ir d-orbitals populate the ligand C=C π* antibonding orbital, the bond order of the alkene decreases. In the solid-state, this is reflected by longer C=C interatomic distances, and accompanied by and downfield shift in the ^{13}C NMR signal relative to other transition-metal COD complexes

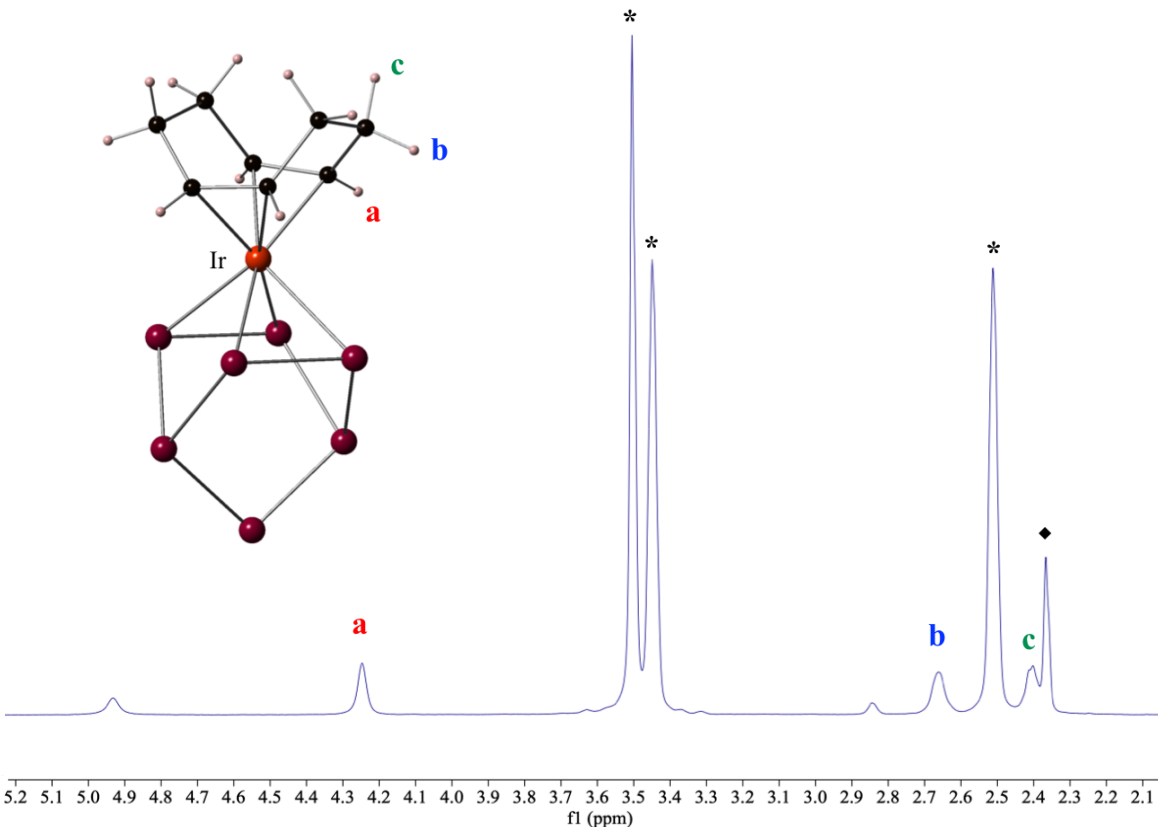

Figure 3.11: $^{1}H\{^{13}C\}$ spectrum of $[K(2,2,2\text{-crypt})]_2[(\eta^4\text{-}As_7)Ir(COD)]$. Signals from 2,2,2-cryptand and toluene are denoted with an asterisk (*) and diamond (◆), respectively. Recorded at 298 K at 500 MHz in d_5-pyridine.

(Table 3.8). In the case of **3.3**, data suggest significant charge transfer from the Ir to the COD ligands, denoting a highly activated C=C bond. This electronic structure is not mirrored by the Rh congener, which stems from a lower propensity for metal-olefin backbonding of the row 2 transition metals relative to row 3.

Table 3.8: Bond lengths [Å] and ^{13}C-NMR Chemical Shift values for select Rh(I) and Ir(I)-COD complexes.

	Distance [Å]			δ COD (ppm)		Reference
	Rh-C	**C=C**	**C-C**	**CH**	**CH_2**	
$[As_7Rh(COD)]^{2-}$	2.162	1.403	1.523	[70.3,	35.2	This work
$[Rh(COD)Cl]_2$	2.10	1.39	1.52	[78.8,	31.3	[124]
	Distance [Å]			**δ COD (ppm)**		
	Ir-C	**C=C**	**C-C**	**CH**	**CH_2**	
$[As_7Ir(COD)]^{2-}$	2.143	1.438	1.525	---	36.6	This work
$[Sn_9Ir(COD)]^{3-}$	2.150	1.423	1.520	---	34.7	[107,123]
$[Pb_9Ir(COD)]^{3-}$	---	---	---	70.6	34.6	[107]
[(hfac)Ir(COD)]	2.101	1.409	1.511	62.0	30.9	[125]
$[Ir(COD)Cl]_2$	2.06	1.42	1.54	62.2	32.3	[126]

3.2.5 Laser Desorption / Ionization Time-of-flight Mass Spectrometry

Laser Desorption Ionization time-of-flight mass spectrometry (LDI-TOF MS) analyses were performed in negative ion mode on crystalline salts containing the clusters **3.1 – 3.3**. The parent ion of **3.1** was observed as $[CoAs_{10}]^{1-}$, *m/z* = 808.15 (Figure 3.12 and 3.13). Several fragments corresponding to lower molecular mass Co/As anions are the most predominant mass fragments in the spectrum, though larger mass fragments formed in the gas phase were also detected.

The monoanionic parent masses of **3.2** and **3.3**, $[As_7Rh(C_8H_{12})]^{1-}$ and $[As_7Ir(C_8H_{12})]^{1-}$ were not observed in the gas phase (Figures 3.14 -3.18), but several fragments corresponding to Rh/As and Ir/As systems are observed as the predominant mass fragments in the spectra (See Figures 3.15 and 3.18). Use of bis(1,8-dimethylamino)naphthalene in a ACN:THF solution (75:25 v:v) as a matrix aided in

increasing intensity of fragments, but also enhanced number and intensity of protonated species and ion-paired potassium salts observed, leading to complex spectra.

Certain mass fragments, such as $[MAs_5]^{1-}$, $[MAs_6]^{1-}$, $[MAs_7]^{1-}$, $[MAs_8]^{1-}$ were common to all spectra, indicating their stability in the gas phase (Table 3.9). These lower molecular weight species may have originated from fragmentation of the parent ion. Heavier fragments, such as $[M_2As_{10}]^{1-}$ and $[M_2As_{11}]^{1-}$, were formed in the gas phase and were observed in the LDI-TOF MS spectra of all three clusters.

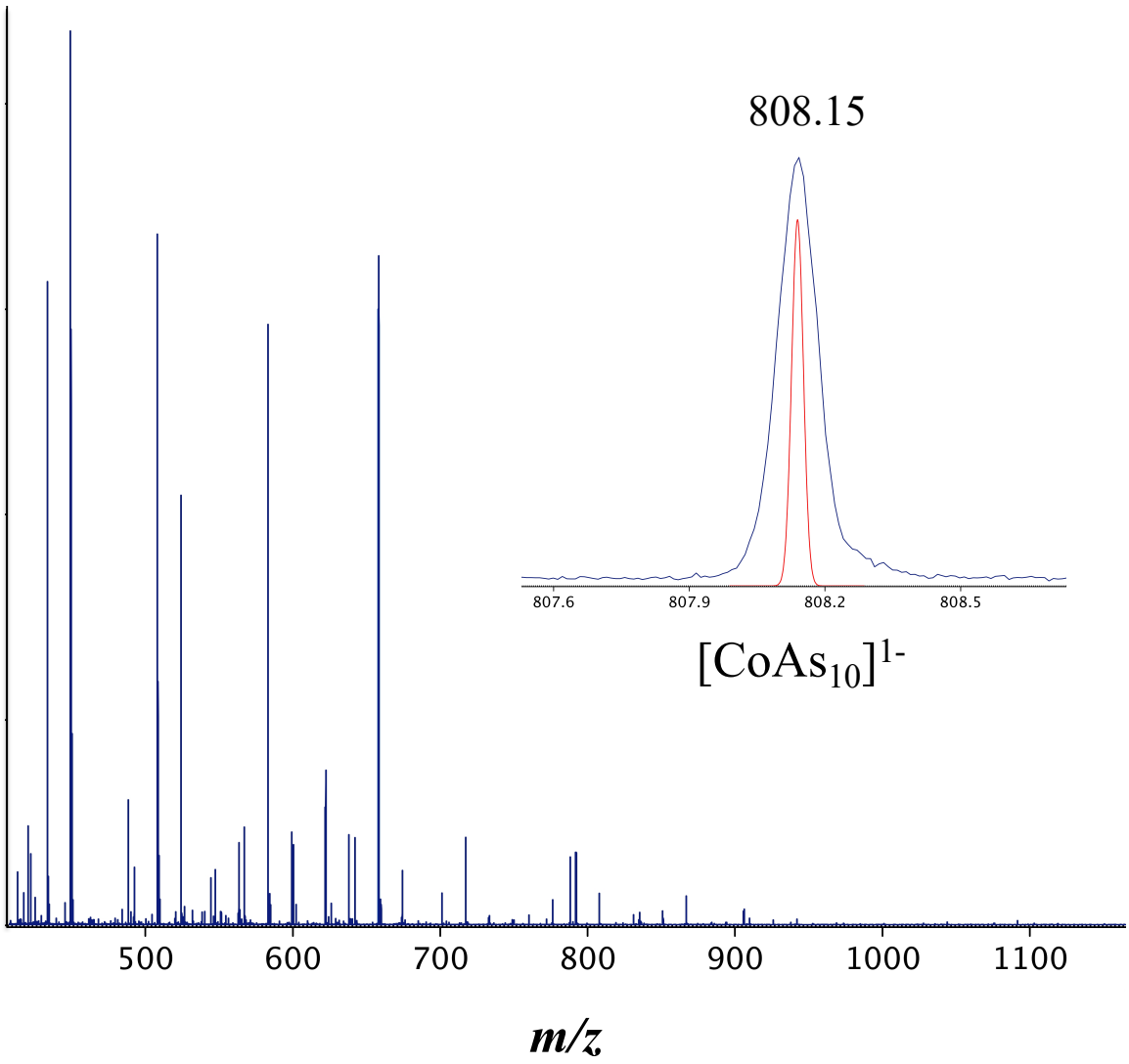

Figure 3.12: Laser desorption/ionization mass spectrum of $[K(2,2,2\text{-crypt})]_3[(\eta^3\text{-}As_3)Co(\eta^4\text{-}As_7)]$ in negative mode. Spectrum was collected from direct ablation of crystals adhered to the target plate with carbon tape. Inset shows mass envelope corresponding to $[CoAs_{10}]^{1-}$, the parent mass of cluster **3.1**.

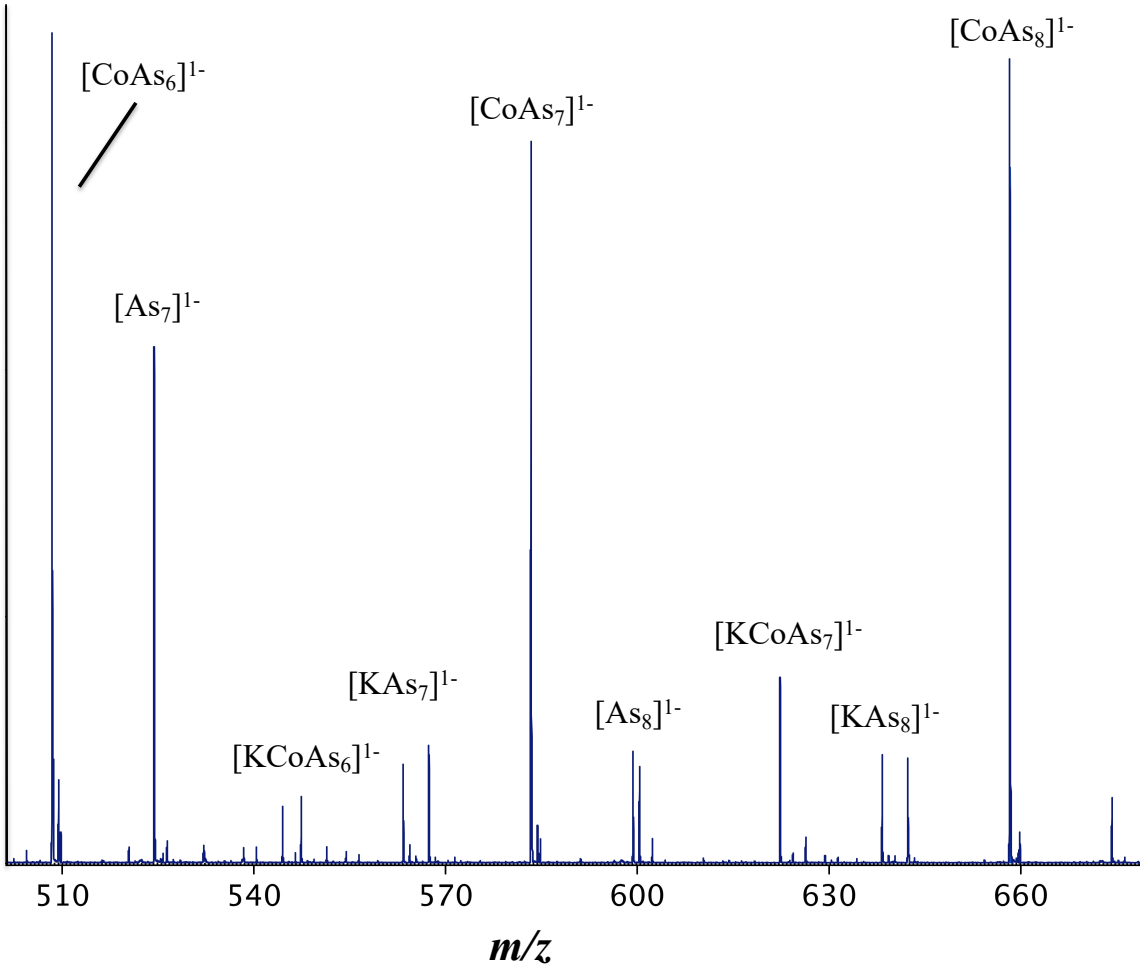

Figure 3.13: Laser desorption/ionization mass spectrum of $[K(2,2,2\text{-crypt})]_3[(\eta^3\text{-}As_3)Co(\eta^4\text{-}As_7$in negative mode, focusing on the region of 510 – 680 *m/z*.

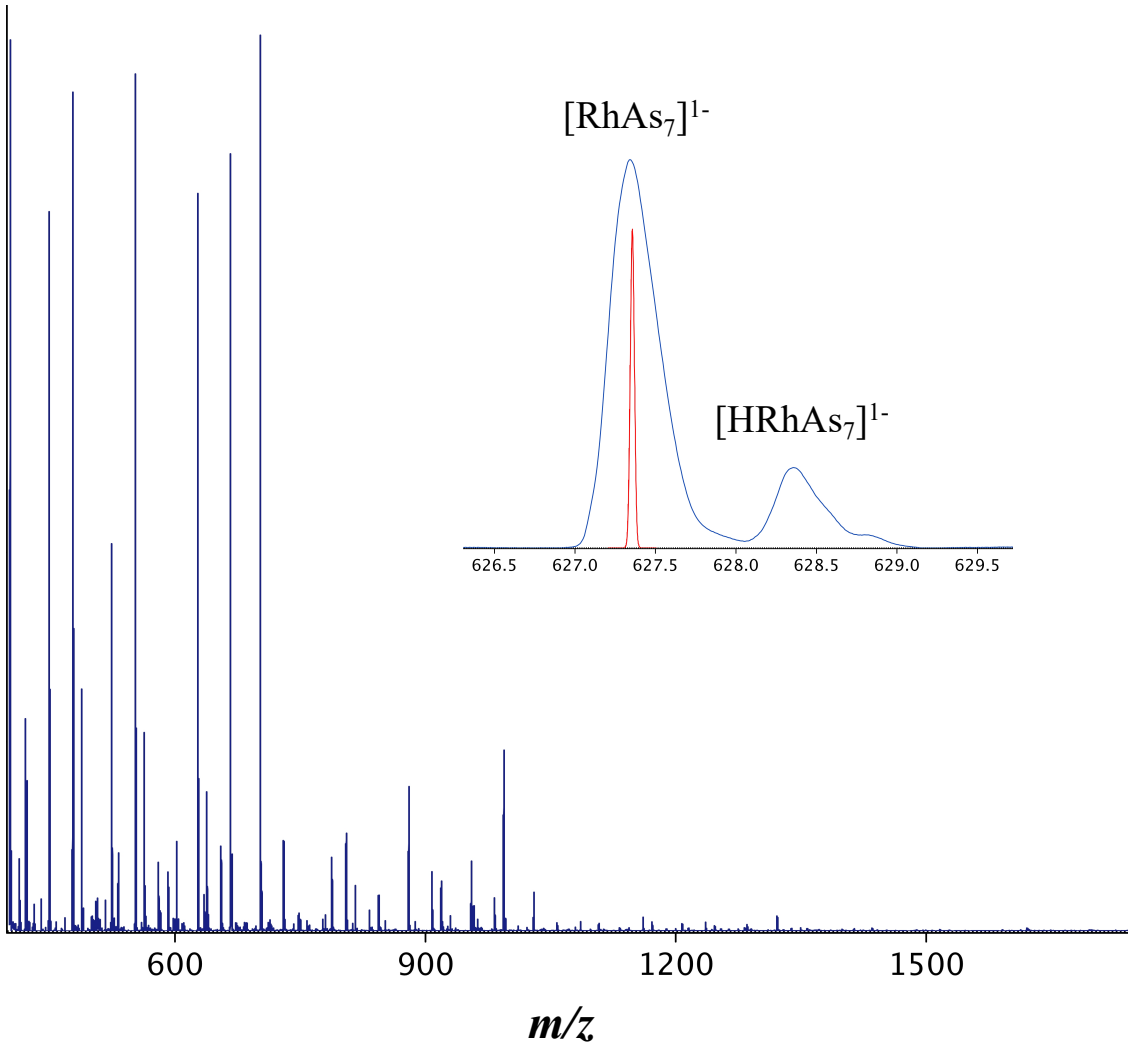

Figure 3.14: Laser desorption/ionization mass spectrum of $[K(2,2,2\text{-crypt})]_2[(\eta^4\text{-}As_7)Rh(COD)]$ in negative mode. Spectrum was collected from direct ablation of crystals adhered to the target plate with carbon tape. Inset shows the peaks of $[RhAs_7]^{1-}$ and $[RhAs_7H]^{1-}$.

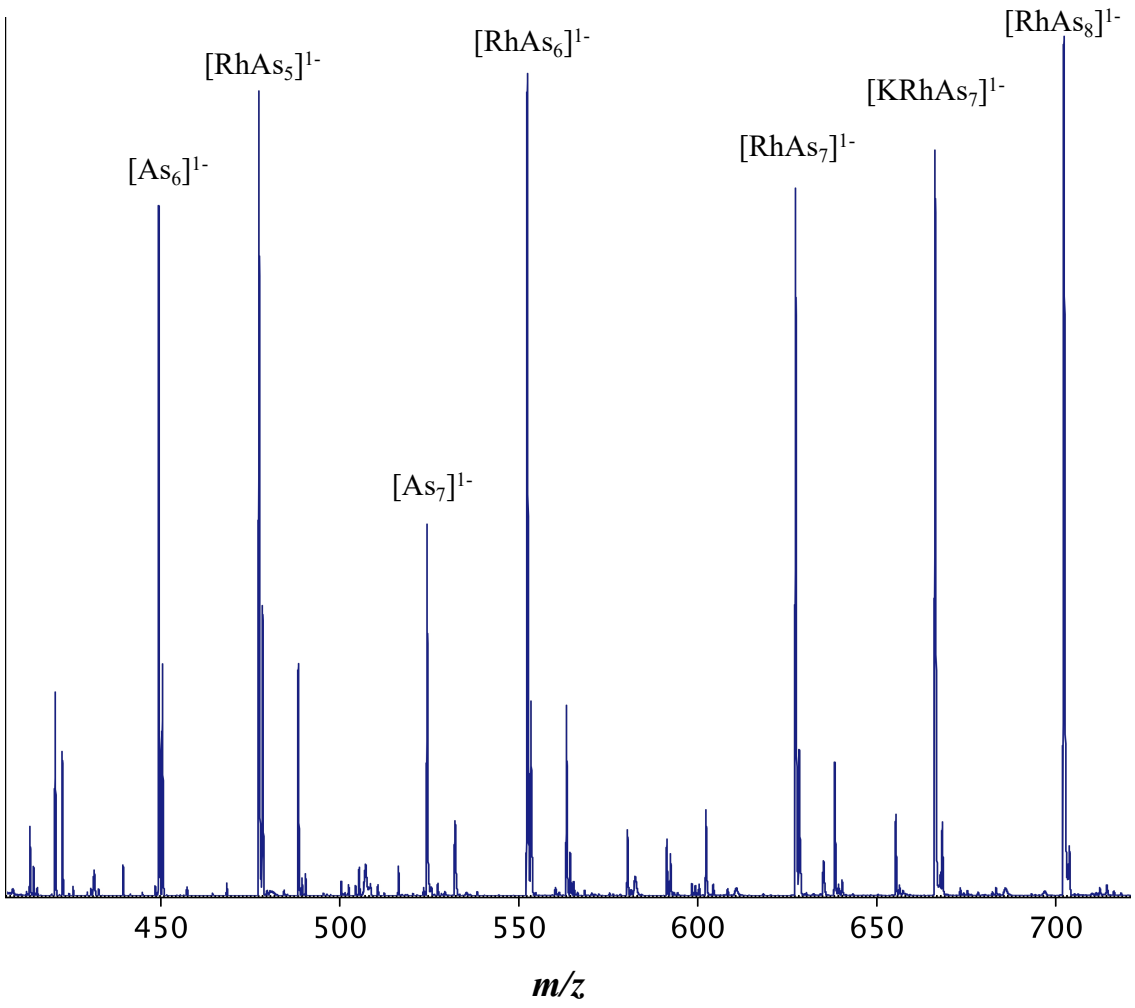

Figure 3.15: LDI-MS of $[K(2,2,2\text{-crypt})]_2[(\eta^4\text{-}As_7)Rh(COD)]$ in negative mode, with focus on the region from 425-700 *m/z*. Major fragments are labeled.

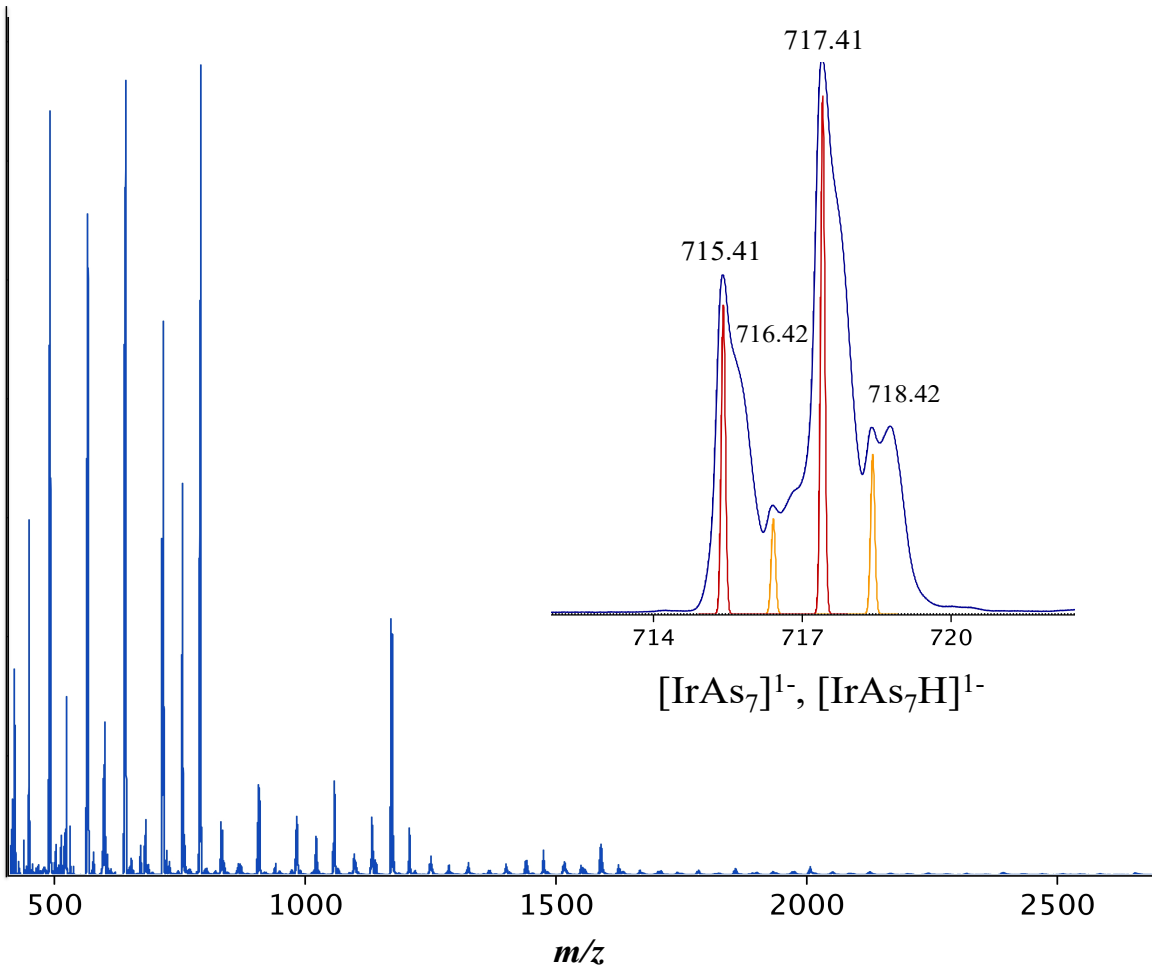

Figure 3.16: Laser desorption/ionization mass spectrum of $[K(2,2,2\text{-crypt})]_2[(\eta^4\text{-}As_7)Ir(COD)]$ in negative mode. Spectrum was collected from direct ablation of crystals adhered to the target plate with carbon tape. Insets show mass envelopes corresponding to $[IrAs_7]^{1-}$ and protonated $[IrAs_7H]^{1-}$

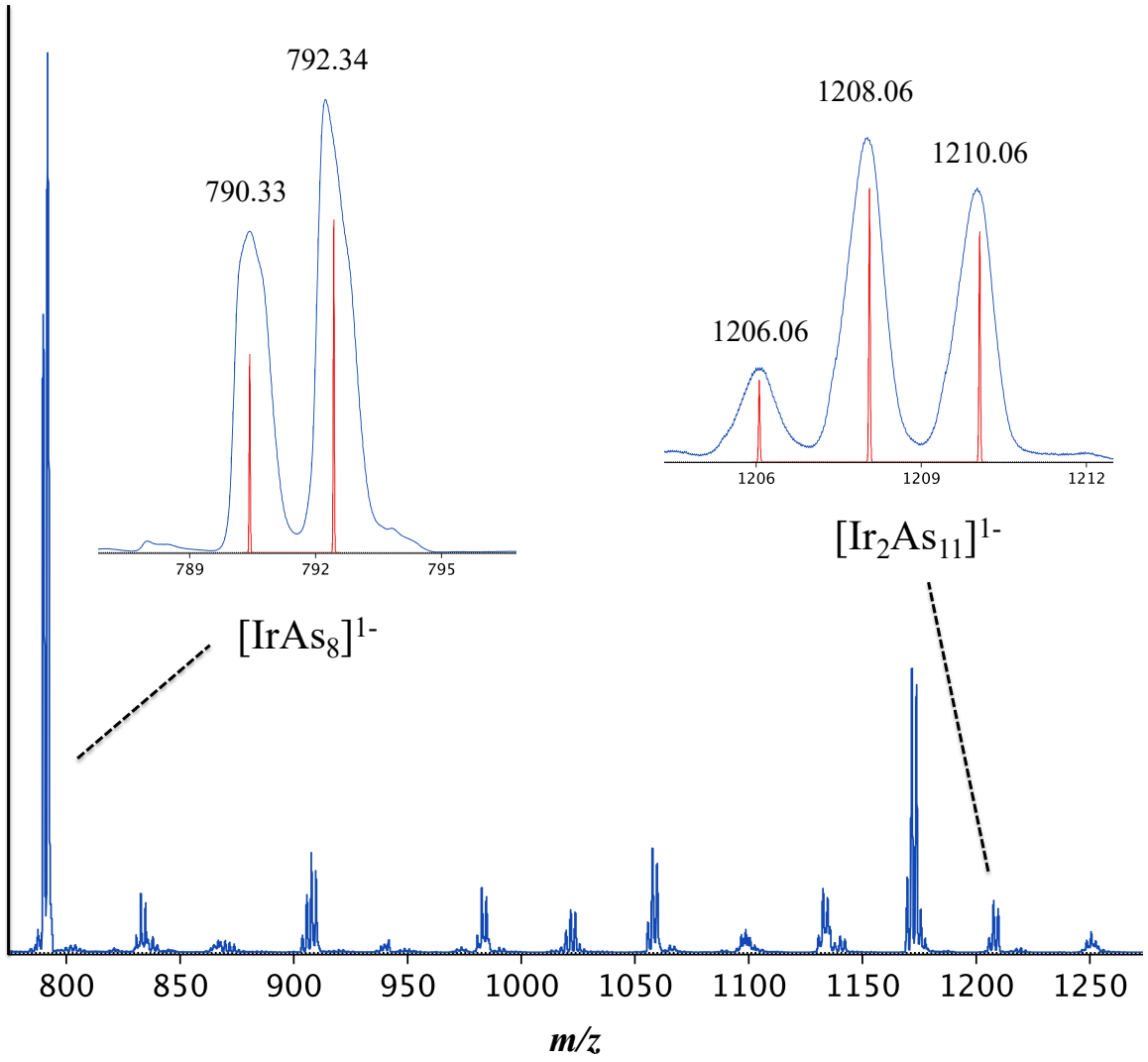

Figure 3.17: Laser desorption/ionization mass spectrum of $[K(2,2,2\text{-crypt})]_2[(\eta^4\text{-}As_7)Ir(COD)]$ in negative mode (blue). Insets show mass envelopes corresponding to $[IrAs_8]^{1-}$ and $[Ir_2As_{11}]^{1-}$ and corresponding calculated mass envelopes (red).

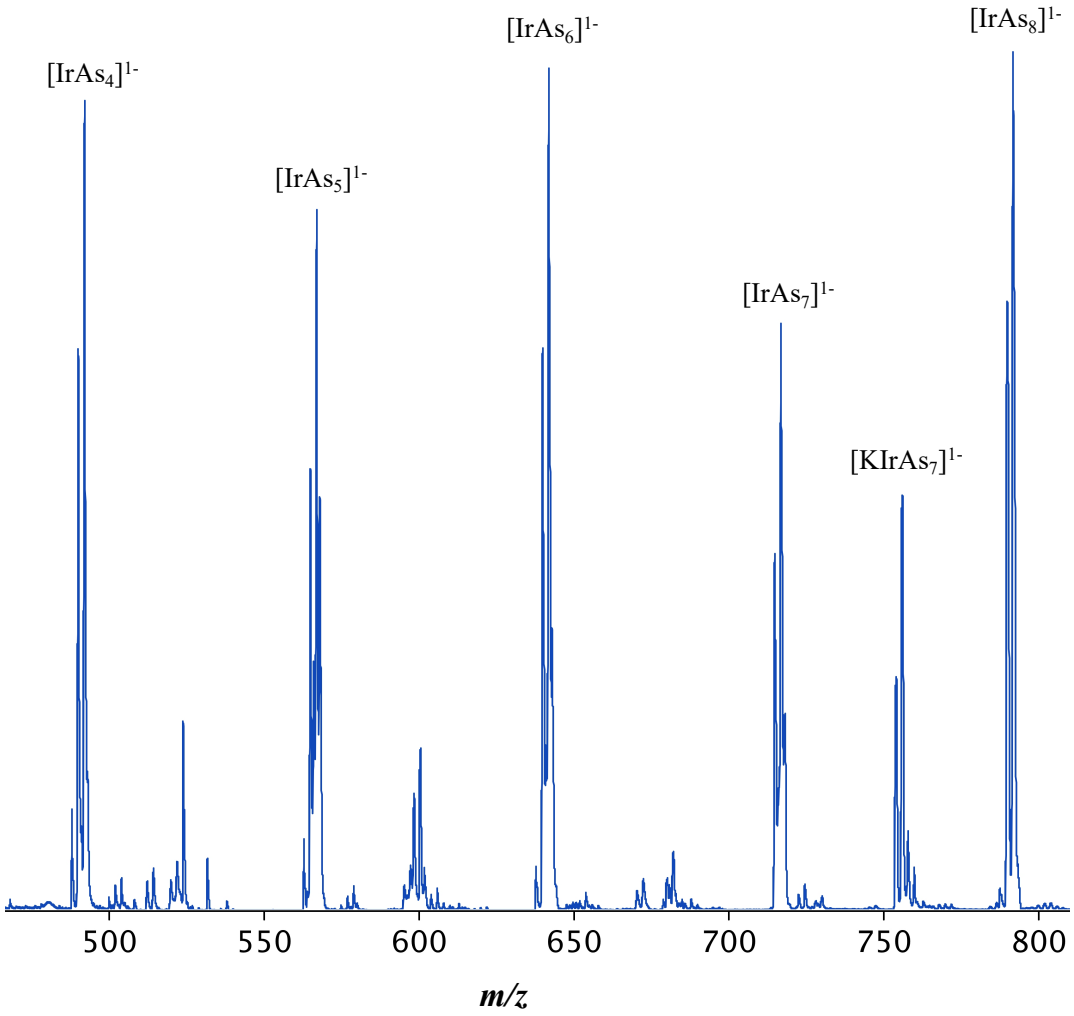

Figure 3.18: LDI-TOF MS of $[K(2,2,2\text{-crypt})]_2[(\eta^4\text{-}As_7)Ir(COD)]$ in negative ion mode, with focus on the region from 450-800 *m/z*. Major mass fragments are labeled.

Table 3.9: Common $[M_xAs_y]^{1-}$ fragments identified in the LDI-TOF MS spectra of crystals containing **3.1**, **3.2**, and **3.3**. For species with multiple isotopes, the mass (in amu) of the predominant peak is listed.

Species	Co (3.1)	Rh (3.2)	Ir (3.3)
$[MAs_4]^{1-}$	358.62	402.59	492.69
$[MAs_5]^{1-}$	433.54	477.51	567.57
$[MAs_6]^{1-}$	508.46	552.44	642.49
$[MAs_7]^{1-}$	583.38	627.36	717.41
$[MAs_8]^{1-}$	658.30	702.28	792.34
$[M_2As_{10}]^{1-}$	867.08	955.03	1133.12
$[K_3M_2As_9]^{1-}$	909.05	997.00	1177.01
$[M_2As_{11}]^{1-}$	942.002	1029.952	1208.06

3.2.6 Electron Dispersive X-Ray Spectroscopy (EDX) Analysis

Elemental analyses via electron dispersive X-ray spectroscopy (EDX) confirmed the presence of Rh, As, and K in the $[K(2,2,2\text{-crypt})]^+$ salts of **3.2** (Figure 3.19). The calculated ratio of these elements [1.0 Rh : 8.1 As : 2.3 K] is agreement with the relative amounts of these elements expected from the solid-state structure [1.0 Rh : 7.0 As : 2.0 K]. In addition to corroborating the composition of the anion, these values indicate the expected charge of 2^- for the cluster anion (assuming all K is in the form of $[K(2,2,2\text{-crypt})]^+$ counter-cations). Elemental analysis of crystals containing **3.3** confirmed the presence of elements Ir, As, and K [1.0 Ir : 7.1 As : 2.2 K], in excellent agreement with the expected atomic ratios [1.0 Ir : 7.0 As: 2.0 K] (Figure 3.20), and a 2^- charge per anion.

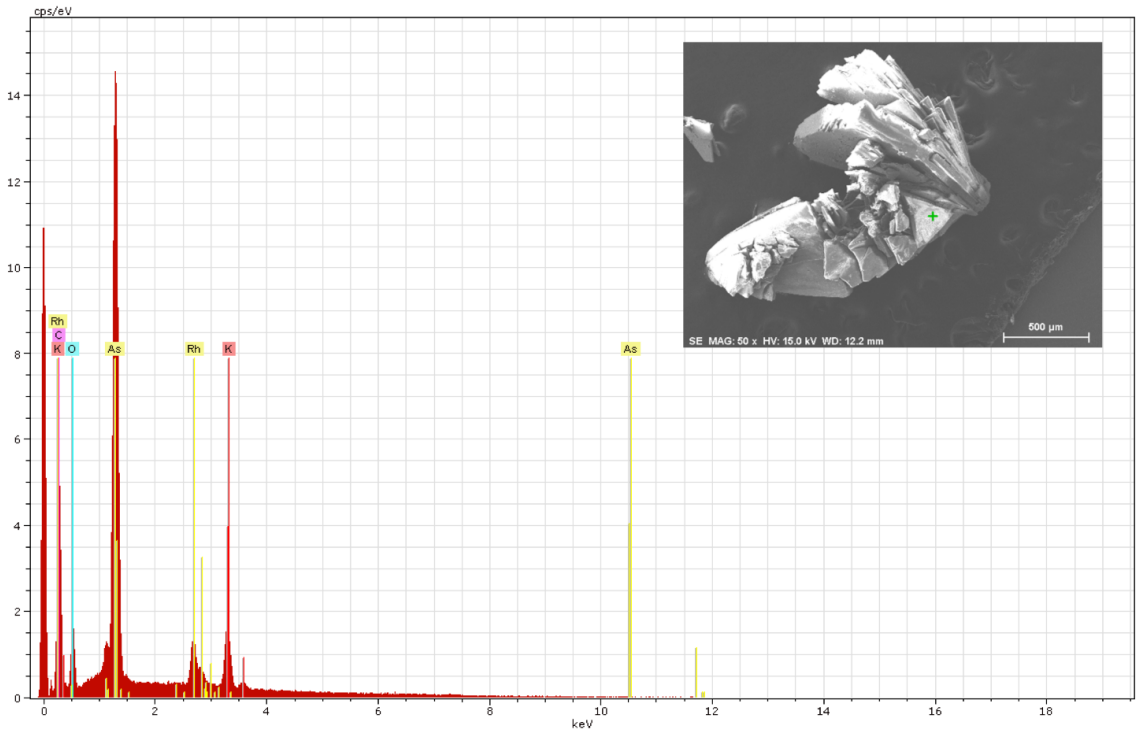

Figure 3.19: Elemental point scan of $[K(2,2,2\text{-crypt})]_2[(\eta^4\text{-}As_7)Rh(COD)]$

Table 3.10: Atom percentages in $[K(2,2,2\text{-crypt})]_2[(\eta^4\text{-}As_7)Rh(COD)]$

Element	AN	Series	[wt%]	[norm wt%]	[norm atom %]	Error [%]
As	33	L-series	45.03	61.29	32.06	2.4
Rh	45	L-series	7.58	10.32	3.93	0.3
O	8	K-series	7.35	10.00	24.50	0.9
K	19	K-series	6.67	9.08	9.10	0.2
C	6	K-series	6.85	9.32	30.40	0.8
		Sum:	73.48	100	100	

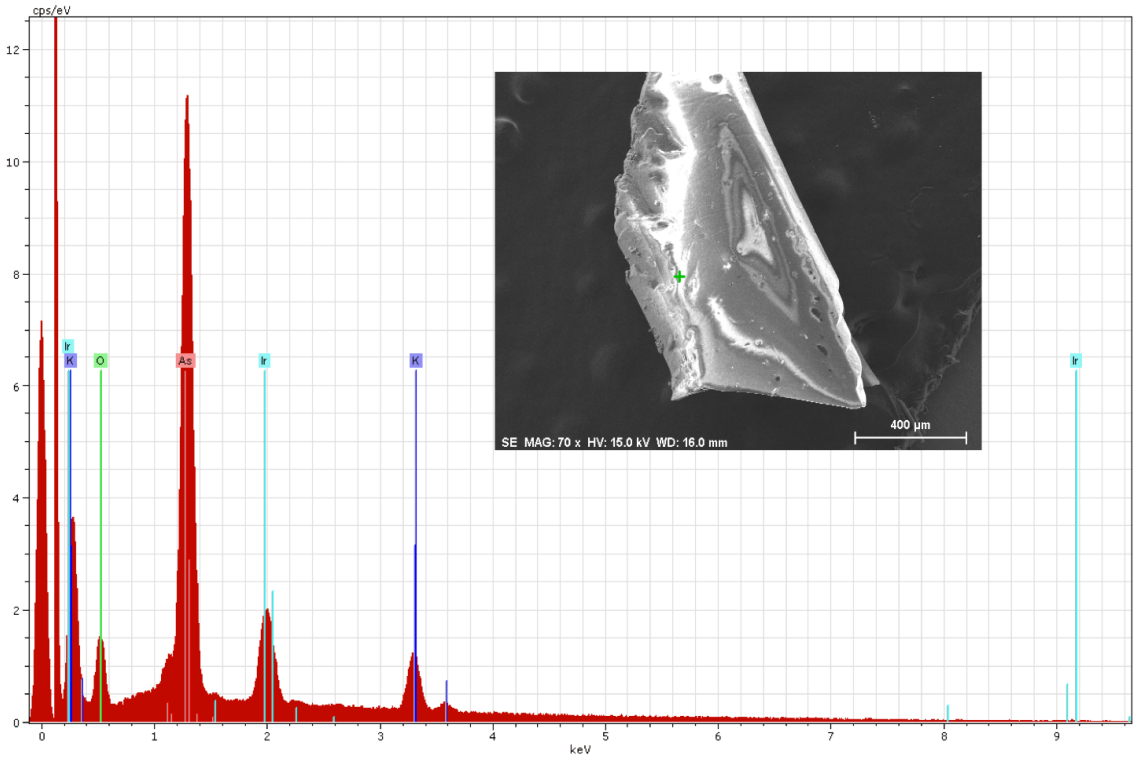

Figure 3.20: Elemental point scan of crystals of $[K(2,2,2\text{-crypt})]_2[(\eta^4\text{-}As_7)Ir(COD)]$.

Table 3.11: Atom percentages in $[K(2,2,2\text{-crypt})]_2[(\eta^4\text{-}As_7)Ir(COD)]$

	AN	Series	[wt%]	[norm wt#]	[norm atom %]	Error [%]
As	33	L-series	34.65	54.05	33.51	1.8
Ir	77	M-series	12.52	19.53	4.72	0.5
O	8	K-series	11.35	17.71	51.43	1.3
K	19	K-series	5.58	8.70	10.34	0.2
		Sum:	64.11	100	100	

3.3 Discussion

The coordination complexes $[(\eta^4\text{-}As_7)Rh(COD)]^{2-}$ **(3.2)**, $[(\eta^4\text{-}As_7)Ir(COD)]^{2-}$ **(3.3)**, and the binary intermetalloid $[(\eta^3\text{-}As_3)Co(\eta^4\text{-}As_7)]^{3-}$ **(3.1)** are new examples of Group 9 / As complexes, isolated through reactions of Zintl anions with transition metal complexes. The structure of **3.1** can be described as a hybrid of a coordination complex and a binary anion. Additionally, it is the first Co-As binary anion.

Each cluster contains a norbornadiene-like $\eta^4\text{-}As_7$ moiety coordinated to a transition metal center. Structural rearrangement from nortricyclane-type to norbornadiene-like $[Pn_7]^{3-}$ cages is common, and the degree of bond insertion is dependent on the identity of the transition metal fragment and the pnictide cage. The extent of this transition is reflected in the Pn4···Pn5 and Pn6···Pn7 separations, which are equal in idealized norbornadiene geometry. When comparing to the isoelectronic $[Pn_7M(CO)_3]^{3-}$ complexes (see Table 3.1), the difference in these separations ($\Delta(d)_{Pn\text{-}Pn}$ = 0.20 – 0.35 Å) reveals a slight asymmetry, which in turn determines C_{2v} or C_s symmetry for the cage. [60,127] These distances are most similar ($\Delta(d)_{As4/5\text{-}As6/7}$ = 0.20 Å) for $[(\eta^4\text{-}As_7)Cr(CO)_3]^{3-}$, which has been attributed to optimal orbital overlap between As and Cr. These same quantities in **3.1** ($\Delta(d)$ = 0.015 Å), **3.2** ($\Delta(d)$ = 0.021 Å), and **3.3** ($\Delta(d)$ = 0 Å) are much lower, and may be due to an even greater overlap between orbitals of Group 9-As, and may be affected by synergistic electronic effects attributed to the cyclo-As_3^{3-} and COD ligands (see Table 3.12). In the case of **3.3**, the As···As nonbonding contacts are crystallographically imposed by a C_2 axis, and may not be the most accurate indicator of asymmetry in the norbornadiene cage.

Table 3.12: Comparison of select bond lengths [Å] and angles (˚) in $[(\eta^3\text{-}As_3)Co(\eta^4\text{-}As_7)]^{3-}$ (**3.1**), $[(\eta^4\text{-}As_7)Rh(COD)]^{2-}$ (**3.2**), $[(\eta^4\text{-}As_7)Ir(COD)]^{2-}$ (**3.3**).

	3.1 (Co)	**3.2 (Rh)**	**3.3 (Ir)***
As4-M1	2.4119(9)	2.5489(12)	2.6114(5)
As5-M1	2.3957(12)	2.6552(7)	2.5369(8)
As6-M1	2.4311(10)	2.5977(6)	2.6114(5)
As7-M1	2.4195(8)	2.5228(6)	2.5369(8)
As4-As6	2.3506(9)	2.3421(8)	2.3448(8)
As5-As7	2.3535(9)	2.3360(8)	2.3448(8)
As4···As5	3.209(1)	3.225(7)	3.229(8)
As6···As7	3.170(1)	3.215(6)	3.229(8)
As4-M-As6	58.07(4)	54.11(4)	54.11(3)
As6-M-As7	81.96(5)	53.58(5)	54.11(3)
As4-M-Ligand	92.53(3) (As8)	87.38(7) (C5)	97.40(4) (C2)

*For the purposes of discussion, atom labels of **3.3** have been adjusted to match the numbering scheme in Figure 3.1.

When describing the electronic structure, a formal charge of 3^- is typically ascribed to the As_7 cage, and complete oxidation of the transition metal is assumed using a Zintl-Klemm bonding formalism. However, studies on $[(\eta^4\text{-}Pn_7)M(CO)_3]^{3-}$ series revealed the extensive electron donation from the cage into the transition metal fragment, as evidenced by C-O stretching frequencies and NMR chemical shift values. The increasingly diffuse nature of p orbitals down Group 15 also lends to a description of TM-Pn bonding that has less π character, and is reflected in the nortricyclane-norbornadiene structural activation, and the ease of complete activation of heavier cages [As_7] and [Sb_7] to form products with nuclearities and geometries that are unrelated to the parent ion. Additionally, the electronegativity values for As and Group 9 elements are very similar, leading to highly covalent cluster bonds, instead of the ionic model assumed for the Zintl-Klemm concept. Despite this, the Zintl-Klemm formalism remains a useful

first order approximation for describing the electronic structures of novel clusters, as evidenced by quantum calculations. Investigation of reactions between new combinations of transition-metal Zintl-ion systems provides crucial data to continue refinement of electronic structure descriptions, and properties that begin to bridge the gap between structure-property relationships for such species.

3.4 Experimental Section

3.4.1 General Considerations. All reactions were performed under an inert atmosphere of dry nitrogen or argon in a dry box (Vacuum Atmospheres Co) or using standard Schlenk techniques. Melts of a Zintl phase of nominal composition K_3As_7 were prepared by fusion (~1100 °C) of stoichiometric ratios of the corresponding elements. *Caution!* Synthesis of Zintl phases is highly exothermic. Full personal protective equipment and blast shields should be used at all times! Ethylenediamine was purified via long-path distillation over K_4Sn_9. Other solvents were purified by distillation from sodium benzophenone ketyl radical under a dinitrogen atmosphere and stored over 3 Å molecular sieves. $[RhCODCl]_2$ (98%, Strem Chemicals) and $[IrCODCl]_2$ (99%, Strem Chemicals) were purchased as microcrystalline powders and used without further purification. KO^tBu (99.97%, Sigma Aldrich) and 4,7,13,16,21,24-hexaoxa-1,10-diazobicyclo[8.8.8]hexacosane (2,2,2-crypt, >98%, TCI America) were dried under vacuum for 24 hours prior to use.

3.4.2 Synthesis of $[K(2,2,2\text{-crypt})]_3[(\eta^3\text{-}As_3)Co(\eta^4\text{-}As_7)]$

In a 10 mL glass scintillation vial, a solution of $Co(PPh_3)_2Cl_2$ and KO^tBu was prepared in toluene at room temperature by first dissolving $Co(PPh_3)_2Cl_2$ (68.0 mg, 0.101 mmol) in 1.5 mL toluene, then adding KO^tBu (22.1 mg, 0.200 mmol) as a solid. This mixture was stirred for 30 min, during which time a noticeable color change from cerulean to electric blue occurred, with noticeable formation of a grainy white precipitate, confirmed via powder X-ray diffraction to be KCl.

In a separate glass vial, K_3As_7 (135.3 mg, 0.211 mmol) and 2,2,2-crypt (238.3 mg, 0.633 mmol) were dissolved in 3 mL of ethylenediamine and stirred for 15 min at 25 °C. The precipitate from the Co-solution was removed via glass wool filter pipet, and the subsequent bright blue solution was added dropwise to the solution of $[As_7]^{3-}$ with vigorous stirring. The reaction stirred at room temperature for six hours, followed by heating at 55 °C for 45 minutes. During this time, the solution darkened to a matte brown and gradually became more opaque. Directly following heating, the reaction was hot filtered through tightly packed glass wool and allowed to cool slowly overnight. After 14 hours, the solution was filtered a second time and layered with 2 mL toluene. After eight days, large, irregular red plates of $[K(2,2,2\text{-crypt})]_3[(\eta^3\text{-}As_3)Co(\eta^4\text{-}As_7)]$ formed. (~100 mg, 82 %).

3.4.3 Synthesis of $[K(2,2,2\text{-crypt})_2[(\eta^4\text{-}As_7)Rh(COD)]$

In a 10 mL scintillation vial, K_3As_7 (243.1 mg, 0.380 mmol) and 2,2,2-crypt (381.3 mg, 1.01 mmol) were dissolved in 5 mL of ethylenediamine, and stirred for 10 min at 55 °C. In a separate vial, $[RhCODCl]_2$ (50.0 mg, 0.101 mmol) was dissolved in 3 mL toluene and stirred for 5 min at 55 °C. To the $[RhCODCl]_2$ / Tol mixture, KO^tBu (15 mg, 0.135 mmol) was added as a solid. The mixture stirred for an additional 10 min at 55

°C and was then filtered through glass wool and added dropwise to the $[As_7]^{3-}$ solution. A slight darkening of the red-orange solution was noticed. The reaction mixture was heated at 55 °C for 45 min with stirring, followed by 15 min at 80 °C, when a color change to orange-brown was noticed and the solution became opaque. The reaction was hot filtered through 1 cm tightly packed glass wool into a clean test tube and cooled slowly. After 12 hours, the solution was filtered a second time and layered with toluene. After four days, fine needle-like clusters of $[K(2,2,2\text{-crypt})]_2[(\eta^4\text{-}As_7)Rh(COD)]$ formed. (Yield: 464.4 mg, 78 %) ^{1}H-NMR (py-d_5) δ (ppm): 2.21 (*s*, Tol-CH_3), 2.35 (*s*, 4H, COD-CH_2), 2.38 (*t*, 24H, cryptand), 2.69 (*br*, 4H, COD-CH_2), 3.39 (*t*, 24H, cryptand), 3.45 (*t*, 24H, cryptand), 4.71 (*br*, 4H, COD-olefin), 4.93 (*br*, 8H, COD-CH), 7.22 (*s*, tol-aromatic). $^{13}C\{^1H\}$-NMR (py-d_5) δ (ppm): 35.2 (*s,*COD-CH_2), 54.4 (*s*, cryptand), 68.2 (*s*, cryptand), 70.3, 70.4 (*d*, COD-CH), 70.9 (*s*, cryptand) ;
EDX: Rh : As : K = 1.0 : 8.1 : 2.3 ; LDI-MS (*m/z*) = 627.36, $[RhAs_7]^{1-}$

3.4.4 Synthesis of $[K(2,2,2\text{-crypt})]_2[(\eta^4\text{-}As_7)Ir(COD)]$

In a glass vial, a solution of $[IrCODCl]_2$ / Tol / KO^{t}Bu was prepared at room temperature by first dissolving $[IrCODCl]_2$ (68.0 mg, 0.101 mmol) in 1.5 mL toluene, then adding KO^{t}Bu (22.1 mg, 0.200 mmol) as a solid. This mixture was stirred for 30 min, during which time a noticeable color change of red orange to ruby red occurred, with noticeable formation of precipitate. In a separate glass vial, K_3As_7 (135.3 mg, 0.211 mmol) and 2,2,2-crypt (238.3 mg, 0.633 mmol) were dissolved in 3 mL of ethylenediamine and stirred for 15 min at 25 °C. The precipitate from the Ir-solution was removed via glass wool filter pipet, and the subsequent deep red solution was added dropwise to the solution of As_7. The reaction solution was kept at room temperature for 22 hours with vigorous stirring, followed by heating at 55 °C for two hours, during which

time the solution darkened. The solution was hot filtered through tightly packed glass wool and allowed to cool slowly overnight. After 14 hours, the solution was filtered a second time and layered with toluene. After eight days, large, irregular red plates of [K(2,2,2-crypt)]$_2$[(η^4-As$_7$)Ir(COD)] formed. (Yield: ~276 mg, 82 %) ^{1}H-NMR (py-d$_5$) δ (ppm): 2.32 (*s*, tol-CH$_3$), 2.27 (*br*, 4H, COD-CH$_2$), 2.39 (*m*, 24H, cryptand), 2.55 (*br*, 4H, COD-CH$_2$), 3.40 (*s*, 24H, cryptand), 3.45 (*s*, 24H, cryptand), 4.25 (*br*, 4H, COD-olefin), 7.22 (*s*, tol-aromatic). ^{13}C{^{1}H}-NMR (py-d$_5$) δ (ppm): 36.6 (*s,* COD-CH$_2$), 54.4 (*s*, cryptand), 68.2 (*s*, cryptand), 70.9 (*s*, cryptand) ; EDX: Ir:As:K = 1.0 : 7.1 : 2.2 ; LDI-MS (*m/z*) = 717.41, [IrAs$_7$]$^{1-}$

3.4.5 Crystallographic Studies

Single crystal data collections were performed at ChemMatCARS Sector 15 of the Advanced Photon Source (APS) and at UMD. At APS, a suitable single crystal of C$_{44}$H$_{84}$As$_7$IrK$_2$N$_4$O$_{12}$ (UMAPS-74-1-LS) was analyzed using a Huber three-circle diffractometer (κ-angle offset of 60º) equipped with a Dectris PILATUS3X CdTe 1M detector. The crystal was kept at 150(2) K during data collection, and the distance between the crystal and detector was 130 mm. A custom-designed software was used for data collection, and frames were converted to Bruker-compatible format for data processing in *APEX II*. The unit cell parameters a = 12.227 Å, b = 21.378 Å c = 12.708 Å, α = 90˚, β = 116.75˚, γ = 90˚, V = 2966.2 Å^3 are isomorphic to the solid state structure of the Rh congener, but pervasive whole-molecule disorder prevented complete refinement of the structure. At UMD, suitable single crystals of C$_{44}$H$_{84}$As$_7$K$_2$N$_4$O$_{12}$Rh (UM3046), C$_{44}$H$_{84}$As$_7$IrK$_2$N$_4$O$_{12}$ (UM3043), C$_{56}$H$_{117}$As$_{10}$CoK$_3$N$_8$O$_{18}$ (UM3074), and C$_{56}$H$_{116}$As$_{10}$CoK$_3$N$_8$O$_{18}$ (UM3191) were selected and measured on a Bruker Smart Apex2 CCD diffractometer. The crystals were kept at 120(2) K during data collection.

In all cases, integral intensity data were corrected for absorption using the multi-scan method of SADABS software. The structures were solved with the ShelXT-2014 program and refined with the ShelXL-2015 program and least-square minimization using ShelX software package.

Chapter 4: Synthesis of the Di-Substituted P-Mo Complex $[Mo(CO)_3(\eta^1,\eta^4\text{-}P_7)Mo(CO)_3(en)]^{3-}$

4.1 Introduction

Chapter 3 introduced Zintl anion – transition metal coordination complexes, wherein $[Pn_7]^{3-}$ (Pn = P, As, Sb) ions serve as polydentate ligands, engaging in either η^2 or η^4 coordination modes, and exhibiting nortricyclane or norbornadiene-like $[Pn_7]^{3-}$ topologies, respectively. Among these complexes are the isostructural homologous series of $[(\eta^4\text{-}Pn_7)M(CO)_3]^{3-}$ ions (M = Cr, Mo, W ; Pn = P, As, Sb), first reported in the 1990's by Eichhorn *et al.* [64,128] These anions are formed through rational synthetic methods, as described in Equation 4.1.

$$K_3Pn_7 + 3(2,2,2\text{-crypt}) + LM(CO)_3 \longrightarrow [K(2,2,2\text{-crypt})]_3[(\eta^4\text{-}Pn_7)M(CO)_3] + L \quad (4.1)$$

where Pn = P, As, Sb
L = 1,3,5-mesitylene for M = Cr, W
L = cycloheptatriene for M = Mo

In addition to descriptions of solid-state and electronic structures of $[(\eta^4\text{-}Pn_7)M(CO)_3]^3$, the reactivity of these species was further investigated through subsequent electrophilic and nucleophilic addition reactions. Select transformations of $[(\eta^4\text{-}P_7)W(CO)_3]^{3-}$ are summarized pictorially in Scheme 4.1, with a complete list given in Table 4.1. The atom numbering of the $[(\eta^4\text{-}P_7)]^{3-}$ ligand in Scheme 4.1 will be applied to all norbornadiene-type $[(\eta^4\text{-}Pn_7)]^{3-}$ cages (Pn = P, As, Sb) to allow for direct comparison of bond metrics in homologous ions.

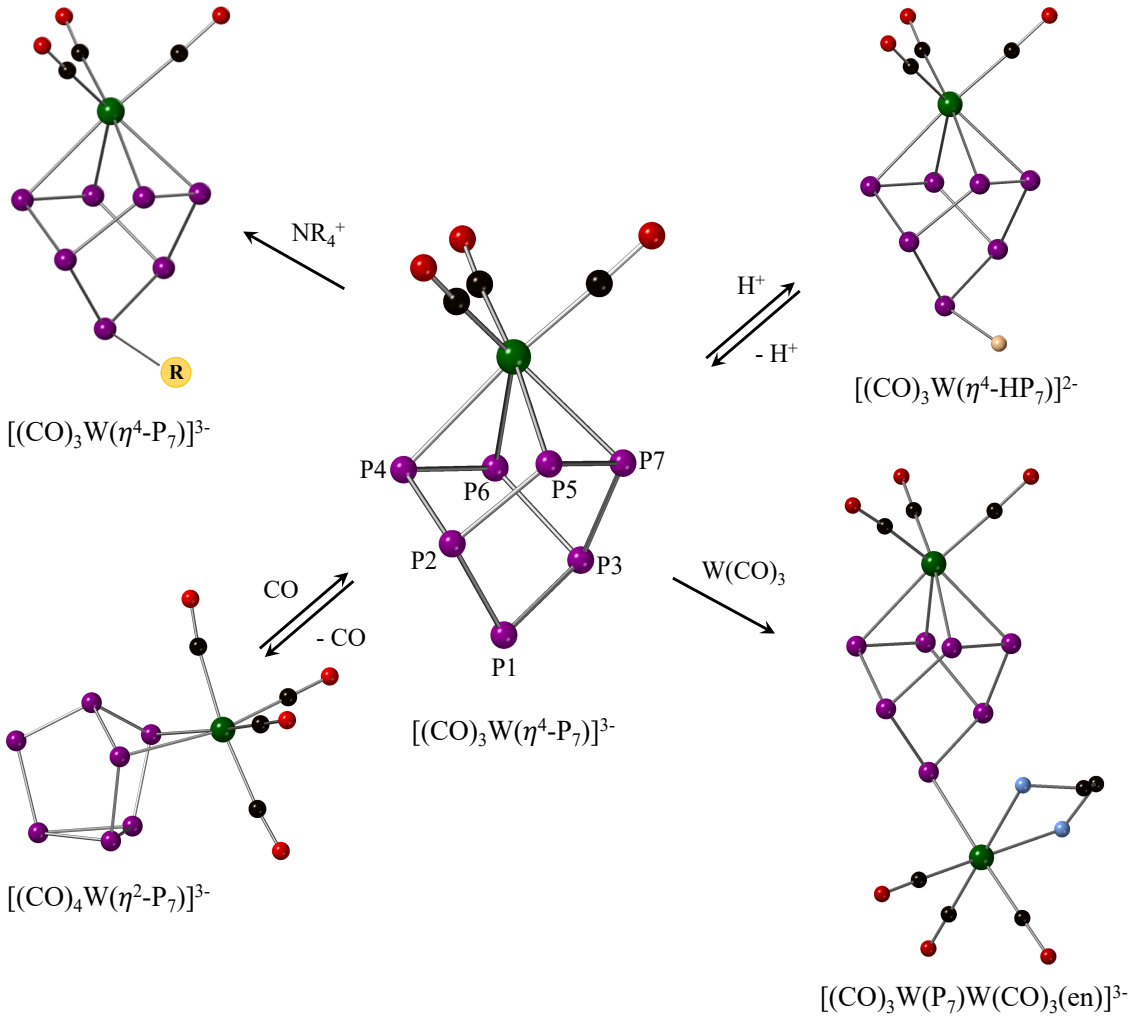

Scheme 4.1: Reactivity of $[P_7W(CO)_3]^{3-}$ through protonation, alkylation, carbonylation, and addition of a second $W(CO)_3$ fragment. Reversible reactions indicated where appropriate. The norbornadiene-$[P_7]$ atom labels are kept consistent throughout this

Reaction of $[(\eta^4\text{-}Pn_7)M(CO)_3]^{3-}$ with the nucleophile CO is transition-metal based, yielding ions $[(\eta^2\text{-}P_7)M(CO)_4]^{3-}$. Electrophilic addition [H^+, R (alkyl, aryl), ER_3 (E = Group 14 element); see Table 4.1] occurs at the two-coordinate Pn1 atom (see Scheme 4.1), which has lone pair electrons occupying high-lying molecular orbitals, allowing for dative bond formation (η^1 coordination mode) to electron-deficient species. When electrophilic addition of $LW(CO)_3$ to $[(\eta^4\text{-}Pn_7)M(CO)_3]^{3-}$ (M = Cr, W; L = 1,3,5-mesitylene) occurs, (η^1-Pn1)-M bond formation occurs through the lone pair of P1,

yielding the doubly substituted $[M(CO)_3(\eta^1, \eta^4\text{-}P_7)W(CO)_3(en)]^{3-}$ ions (M = Cr. W). While systems of Cr / W and W / W were studied, the Mo / W analogue and Mo / Mo analogues were not reported. [129]

Reaction of the $[P_7]^{3-}$ anion with the unsaturated complex $LMo(CO)_3$ (L = cycloheptatriene) has been investigated, yielding the di-substituted $[(en)Mo(CO)_3P_7Mo(CO)_3]^{3-}$ complex (**4.1**). This anion is isostructural and isoelectronic to the reported $[Cr(CO)_3P_7W(CO)_3(en)]^{3-}$ and $[W(CO)_3P_7W(CO)_3(en)]^{3-}$ ions, and is the first structurally characterized Mo analogue in this series of coordination complexes.

Table 4.1: Select reactions of the $[(\eta^4\text{-}P_7)M(CO)_3]^{3-}$ series of anions.

Reaction	**Product Cluster**	**Ref.**
$[(\eta^4\text{-}P_7)M(CO)_3]^{3-} + H^+$ (M = Cr, W) [a]	$[H(\eta^4\text{-}P_7)M(CO)_3]^{2-}$	66
$[(\eta^4\text{-}P_7)M(CO)_3]^{3-} + CO$ (M = Mo, W)	$[(\eta^2\text{-}P_7)M(CO)_4]^{3-}$	130
$[(\eta^2\text{-}P_7)M(CO)_4]^{3-} + MeOH$ (M = Mo, W)	$[H(\eta^2\text{-}P_7)M(CO)_4]^{2-}$	130
$[(\eta^4\text{-}P_7)W(CO)_3]^{3-} + [NR_4]^+$	$[R(\eta^4\text{-}P_7)M(CO)_3]^{2-}$	131
$[(\eta^4\text{-}P_7)W(CO)_3]^{3-} + R_3EX$ [b]	$[(R)_3E(\eta^4\text{-}P_7)W(CO)_3]^{2-}$	129,132
$[(\eta^4\text{-}P_7)W(CO)_3]^{3-} + R_3EX$ [c]	$[(R)_3E(\eta^4\text{-}P_7)W(CO)_3]^{2-}$	132
$[(\eta^4\text{-}P_7)M(CO)_3]^{3-} + (mes)W(CO)_3$ (M = Cr, W)	$[(en)(CO)_3W(\eta^1, \eta^4\text{-}P_7)M(CO)_3]^{2-}$	129

[a] H^+ source is a weak acid such as 9-phenylfluorene
[b] (R_3E = Ph_3Pb, Bu_3Sn, Ph_3Sn, Cy_3Sn, Et_3Sn, Ph_3Ge, Et_3Ge)
[c] (R_3E = Ph_3Si, Me_3Si, $(^nhex)_3Si$, Bu_3Si)

4.2 Results

4.2.1 Synthesis

Ethylenediamine solutions of a phosphorus Zintl phase with nominal composition K_3P_7 react with toluene solutions of $LMo(CO)_3$ (L = cycloheptatriene) in the presence of three equivalents of 2,2,2-cryptand to afford the complex $[K(2,2,2\text{-crypt})]_3[(en)(CO)_3Mo(\eta^1, \eta^4\text{-}P_7)Mo(CO)_3]\cdot 2en$, as shown in Equation 4.2.

$$K_3P_7 + 3(2,2,2\text{-crypt}) + 2\ LMo(CO)_3 \longrightarrow [K(2,2,2\text{-crypt})]_3[(en)(CO)_3Mo(\eta^1, \eta^4\text{-}P_7)Mo(CO)_3] + 2\ L \qquad (4.2)$$

where L = cycloheptatriene, and ethylenediamine (en) originates from the reaction solvent. Crystals of $[K(2,2,2\text{-crypt})]_3[(en)(CO)_3Mo(\eta^1, \eta^4\text{-}P_7)Mo(CO)_3]\cdot 2en$ are brilliant red prisms, formed in almost quantitative yield (96%) after five days. The crystals show mild air and moisture sensitivity, partial solubility in THF and py, and full solubility in en, CH_3CN and DMF. The cluster has been characterized by single crystal XRD, energy-dispersive X-ray analysis (EDX), ^{1}H-NMR, and ^{31}P-NMR analyses. Laser desorption/ionization time-of-flight mass spectrometry (LDI-TOF-MS) analyses were also performed by direct ablation of crystals, adhered to the target plate with carbon tape. Though the intensities of resultant peaks were on the order of 10^7 and the spectra were reproduceable, ablation of this sample generated numerous gas-phase species that are protonated, solvated, partially oxidized, and ion-paired with K^+. As a result, the spectra contained multiple overlapping peaks, which could not be unambiguously assigned to a single mass fragment, or, in some instances, deconvoluted. Therefore, LDI-TOF-MS results are not presented here. Attempts to observe the anion **4.1** in solution will be done through ESI-MS analysis.

4.2.2 Solid State Structure

$[K(2,2,2\text{-crypt})]_3[(en)(CO)_3Mo(\eta^1,\eta^4\text{-}P_7)Mo(CO)_3]\cdot 2en$

Crystals of $[K(2,2,2\text{-crypt})]_3[(en)(CO)_3Mo(\eta^1,\eta^4\text{-}P_7)Mo(CO)_3]\cdot 2en$ are triclinic, space group P-1, and contain the $[(en)(CO)_3Mo(\eta^1,\eta^4\text{-}P_7)Mo(CO)_3]^{3-}$ cluster (**4.1**), three $[K(2,2,2\text{-crypt})]^+$ cations, and two ethylenediamine solvate molecules. Disorder in two cryptands and ethylenediamine were successfully modeled. This anion is isostructural to the previously reported W analogue, $[(en)(CO)_3W(\eta^1,\eta^4\text{-}P_7)W(CO)_3]^{3-}$ (**4.2)**, with near identical unit cell parameters. Complete crystallographic data are given in Table 4.2, with select bond distances and angles listed in Table 4.3.

The anion **4.1** is isoelectronic to **4.2**, with a total electron count of 66 e^- [(5 e^- x 7 P) + (6 e^- x 2 Mo) + (2 e^- x 6 CO) + (4 e^- x 1 en) + (3 e^- overall charge) = 66 e^-], and is predicted to be diamagnetic. The complex is comprised of a C_s norbornadiene-type $[P_7]^{3-}$ polyanion ligated to two neutral molybdenum carbonyl fragments via distinct binding modes. The first C_{3v}-symmetric $Mo(CO)_3$ fragment is bound in an η^4-fashion to four phosphorus atoms [P4, P5, P6, P7] of the $[P_7]^{3-}$ cage. The second $[Mo(CO)_3(en)]$ fragment is bound to the apex phosphide, P1, in an η^1-mode. The P1 site exhibits pyramidal geometry, indicating that only one phosphorus lone pair is involved in σ bonding between P1-Mo2 (Figure 4.1). The coordination sphere of Mo2 is filled by bidentate chelation of an ethylenediamine solvent molecule. The overall anion **4.1** possesses C_s symmetry, with a mirror plane containing C1, Mo1, P1, Mo2, and C4 bisecting the cluster.The Mo1-P (av. 2.671(3) Å) bond distances are virtually identical to those observed in **4.2** [$d(W1\text{-}P)_{av}$ = 2.634(3) Å], and shorter than Mo-P distances in the complex $[HP_7Mo(CO)_4]^{2-}$ [$d(Mo1\text{-}P)_{av}$ = 2.719(6) Å], where P_7 is η^2-bound to a neutral $[Mo(CO)_4]$ fragment. The Mo1-P contacts in **4.1** can be grouped into two shorter

distances [Mo1-P7 = 2.633(2), Mo1-P6 = 2.639(3) Å] and two longer distances [Mo1-P4 = 2.708(3) Å, Mo1-P5 =2.704(3) Å]. This bond asymmetry results from substantial *trans*-influence of CO ligands on Mo-P distances in *trans* positions relative to carbon monoxide [P4-Mo1-C1 = 174.2(6)°, P5-Mo1-C3 = 172.6(2)°]. Electron back-donation occurs from a filled Mo d-orbital to an empty CO π^*-antibonding orbital, contracting Mo-C distances [av. 1.952(9) Å], while lengthening C-O distances [1.187(12) -1.203(16) Å] in relation to non-*trans* CO ligands.

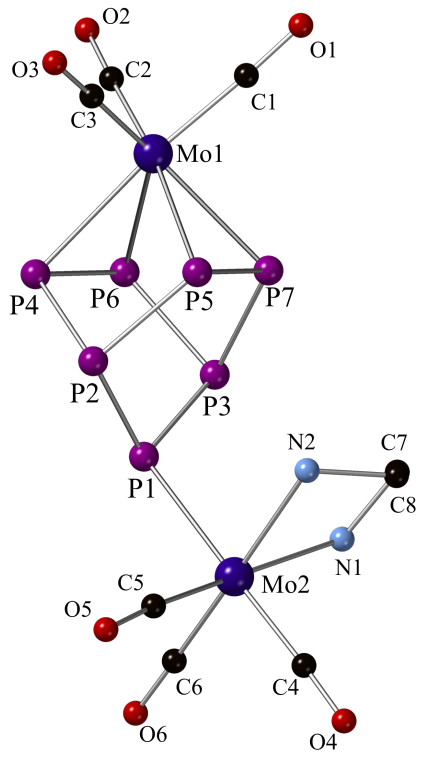

(4.1)

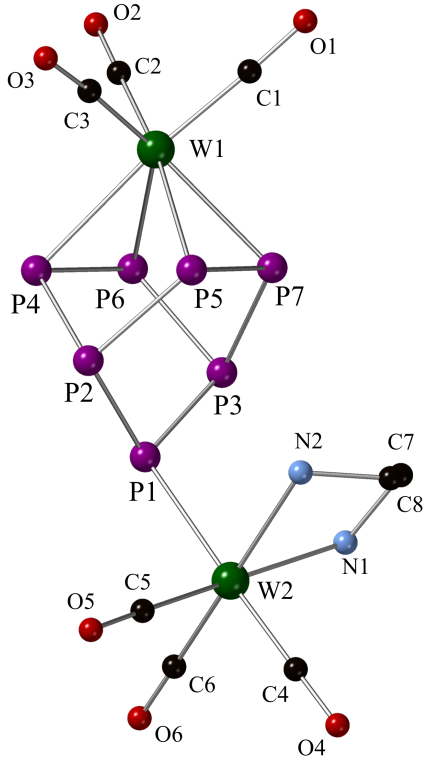

(4.2)

Figure 4.1: Ball and stick models of isostructural Group 6 polyphosphide anions **4.1** and **4.2**. Hydrogens omitted for clarity. P = magenta, Mo = dark blue, W = dark green, C = black, O = red, N = light blue.

The local geometry at P1 is pyramidal, suggesting that one P1 lone pair is used to form an η^1 interaction to Mo2 [P2-P1-Mo2 = 114.33(9)°, P3-P1-Mo2 = 116.90(8)°, and P2-P1-P3 = 97.38(9)°]. The Mo2 atom, bound to three carbonyl ligands, one ethylenediamine chelate, and the (η^1-P_7) ligand, displays a local octahedral molecular geometry. The *trans*-effect of CO ligands influences bond distances at Mo2 [P1-Mo2-C4 = 177.11(9)°], where the Mo2-P1 distance of 2.674(2) Å is close to the average Mo1-P distance (2.671(3) Å). This distance is shorter than Mo-P contacts in $[HP_7Mo(CO)_4]^{2-}$, but elongated when compared to typical Mo-P single bonds [d(Mo-P) = 2.577 Å for $Mo(CO)_4(PPh_3)_6$; 2.552 Å in $Mo(CO)_4(^nBu_3)_6$]. Additionally, CO ligands *trans* to Mo2-N bonds exhibit long Mo2-C contacts [Mo2-C5 = 1.953(9) Å, Mo2-C6 = 1.951(6) Å]. The average Mo2-N distance of 2.339 Å is similar to other Mo-N bonding interactions *trans* to CO ligands [e.g., $d(Mo\text{-}N)_{av}$ = 2.345 Å in *cis*-$Mo(CO)_4(pip)_2$ (pip = piperidine, $C_5H_{11}N$)].

The P-P distances [2.153(3) – 2.255(3) Å] are comparable to those observed in other complexes of this series, where multiple bond character is implicated for the shorter P1-P2, P1-P3, P4-P6, and P5-P7 contacts. As discussed in Chapter 3, the extent of $[Pn_7]^{3-}$ nortricyclane-norbornadiene transformation is discerned by the separation distances of nonbonding pairs P4···P5 and P6···P7. In **4.1**, these nonbonding contacts are asymmetric [P4···P5 = 2.886(3) Å, P6···P7 = 3.244(3) Å], with the difference in interaction length [$\Delta(d)_{P4/5\text{-}P6/7}$ = 0.338(3) Å] indicating a slightly more distorted norbornadiene $[P_7]^{3-}$ cage compared to that of the W analogue **4.2** [$\Delta(d)_{P4/5\text{-}P6/7}$ = 0.319(5) Å]. In both **4.1** and **4.2**, the distortion lowers symmetry of the $[P_7]^{3-}$ ligands from an idealized C_{2v} to C_s.

The d^6- Mo1 atom is pentacoordinate, and has a total electron count of 18 (Mo(d^6): 6 e^-, η^4-$[P_7]^{3-}$: 6 e^- , 3 CO: 6 e^-). Mo2 is also coordinatively saturated, with an electron count of 18 (Mo(d^6): 6 e^-, η^1-$[P_7]^{3-}$: 2 e^- , 3 CO: 6 e^-, 2(-NH_2R): 4 e^-).

Table 4.2: Selected Crystallographic, Data Collection, and Refinement Data for **4.1**.

	[K(2,2,2-crypt)]$_3$(**4.1**)·2en
Empirical formula	$C_{60}H_{128}K_3Mo_2N_{10}O_{18}P_7$
Formula weight	1804.46
Temperature/K	150(2)
Crystal system	Triclinic
Space group	*P-1*
a/Å	14.3290(22)
b/Å	17.6804(9)
c/Å	20.4804(6)
α/°	82.701
β/°	76.823
γ/°	69.075
Volume/Å^3	4712.8(5)
Z	2
ρ_{cal} cg/cm^3	1.3977
μ/mm-1	6.180
F(000)	3272.0
Crystal size/mm^3	0.20 × 0.31 × 0.16
Radiation	sync (λ = 0.44280)
2*θ* range for data collection/°	3.85 to 61.996
Index ranges	-36 ≤ h ≤ 36, -28 ≤ k ≤ 28, -18 ≤ l ≤ 18
Reflections collected	52345
Independent reflections	9661 [R_{int} = 0.0338, R_{sig} = 0.0277]
Data/restraints/parameters	9661/148/329
Goodness-of-fit on F^2	1.03
R_1/wR_2 [$I>=2\sigma$ (I)]	0.1027, 0.1123
R_1/wR_2 [all data]	0.0898, 0.0934

See Crystallographic Section for full refinement details.

Table 4.3: Selected Bond Lengths [Å] and angles (°) in $[(en)(CO)_3Mo(\eta^1,\eta^4\text{-}P_7)Mo(CO)_3]^{3-}$

Distances [Å]			
P1-P2	2.170(3)	Mo1-C1	1.954(9)
P1-P3	2.172(3)	Mo1-C2	1.963(9)
P2-P4	2.239(4)	Mo1-C3	1.951(9)
P2-P5	2.245(3)	Mo2-C4	1.964(9)
P3-P6	2.246(3)	Mo2-C5	1.953(9)
P3-P7	2.255(3)	Mo2-C6	1.951(6)
P4-P6	2.153(4)	C1-O1	1.187(12)
P5-P7	2.153(4)	C2-O2	1.157(12)
Mo1-P4	2.708(3)	C3-O3	1.203(16)
Mo1-P5	2.704(3)	C4-O4	1.184(12)
Mo1-P6	2.639(3)	C5-O5	1.184(13)
Mo1-P7	2.633(2)	C6-O6	1.186(8)
Mo2-P1	2.674(2)	C6-O6	1.186(8)
Mo2-N1	2.337(7)		
Mo2-N2	2.341(8)		
Angles (°)			
P2-P1-P3	97.38(9)	C1-Mo1-P5	103.11(8)
P6-P3-P7	79.76(8)	C2-Mo1-P5	89.08(8)
P4-P2-P5	92.69(8)	P1-Mo2-C5	82.85(8)
P2-P5-P7	103.14(8)	P1-Mo2-C4	177.11(8)
P5-P7-P3	104.82(8)	P1-Mo2-C6	90.36(8)
P3-P6-P4	104.62(8)	P1-Mo2-N2	86.86(8)
P6-P4-P2	103.43(8)	P1-Mo2-N1	87.01(8)
P4-Mo1-P6	47.46(8)	C6-Mo2-N2	102.50(8)
P5-Mo1-P7	47.57(8)	C4-Mo2-C6	88.89(8)
P4-Mo1-P5	73.64(8)	C8-N1-Mo2	106.64(8)
P6-Mo1-P7	66.37(8)	C6-Mo2-N1	176.31(8)
C1-Mo1-P7	85.55(8)	C4-Mo2-C5	88.81(8)
C2-Mo1-P6	137.67(8)	C6-Mo2-C5	82.85(8)
C3-Mo1-P4	99.17(8)	C5-Mo2-N1	100.03(8)
C2-Mo1-P4	91.75(8)	C4-Mo2-N2	90.57(8)
C2-Mo1-P7	134.34(8)	C5-Mo2-N2	173.50(8)
C3-Mo1-P6	84.79(8)	N1-Mo2-C4	93.61(8)
C3-Mo1-P5	172.62(8)	N1-Mo2-N2	74.78(8)
C1-Mo1-P4	174.26(8)	Mo2-N2-C7	111.93(8)
Mo1-C1-O1	176.67(8)	C7-C8-N1	108.59(8)
Mo1-C2-O2	179.06(8)	N2-C7-C8	110.73(8)
Mo1-C3-O3	177.45(8)		

4.2.3 Electron Dispersive X-Ray Spectroscopy (EDX) Analysis

The presence of elements P, Mo, and K in crystals containing the cluster **4.1** was verified through EDX analysis. Measured ratios of these elements [3.5 P : 1.0 Mo : 1.9 K], are in excellent agreement with expected values [3.5 P : 1.0 Mo: 1.5 K] (Table 4.4, Figure 4.2).

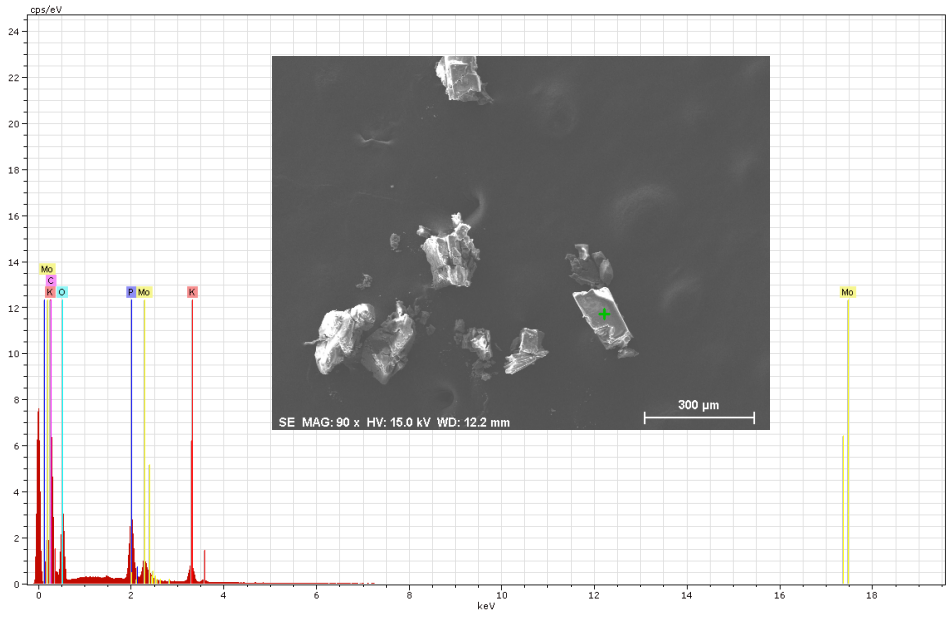

Figure 4.2: EDX analysis of $[(en)(CO)_3Mo(\eta^1,\eta^4\text{-}P_7)Mo(CO)_3]^{3-}$ on carbon tape. P :Mo :K = 3.5 : 1.0 : 1.9.

Table 4.4: Normalized atom % for elements detected in crystals of $[(en)(CO)_3Mo(\eta^1,\eta^4\text{-}P_7)Mo(CO)_3]^{3-}$ through EDX analysis.

Element	AN	Series	[wt%]	[norm wt#]	[norm atom %]	Error [%]
P	15	K-series	5.71	5.71	2.89	0.2
Mo	42	L-series	5.03	5.03	0.82	0.2
O	8	K-series	51.02	51.02	49.99	15.8
K	19	K-series	3.99	3.99	1.60	0.1
C	6	K-series	34.25	34.25	44.70	10.8
		Sum:	100.00	100.00	100.00	

4.3 Discussion

The bimetallic di-substituted cluster anion $[(en)(CO)_3Mo(\eta^1,\eta^4\text{-}P_7)Mo(CO)_3]^{3-}$ (**4.1**) is an addition to the series of Group 6 – polyphosphide structures, previously reported by Eichhorn *et al*. This species crystallizes directly from solution, but it is reasonable to purport that its formation occurs through similar stepwise coordination processes used to isolate Cr/W and W/W (**4.2**) analogues. Formation of **4.2** in solution was monitored by time-lapsed ^{31}P-NMR of crude reaction mixtures of $[P_7W(CO)_3]^{3-}$ with one equivalent of $LW(CO)_3$ (L = 1,3,5-mesitylene) indicated that an $[(en)(CO)_3Mo]$ fragment, formed *in situ* via displacement of the arene ligand by ethylenediamine solvent, coordinated to the pnictide vertex P1 atom of a norbornadiene-like $[P_7]$ cage. The structure and bonding descriptions of **4.1** and **4.2** are similar, with the Mo-P distances of **4.1** being slightly elongated compared to the W-P distances of **4.2**. Difference in the separation distances of P4/P5 and P6/P7 are within the range of those observed in the monosubstituted series, in addition to **3.1**, **3.2**, and **3.3** [$\Delta(d)_{Pn4/5\text{-}Pn6/7}$ = 0.00 – 0.35 Å].

In comparison to norbornadiene-like $[As_7]$ and $[Sb_7]$ structures, those of $[P_7]$ show a greater asymmetry. This could be due to a number of factors, including considerations of atomic radii, which control optimal orbital overlap between main-group and transition-metal fragments, electronegativity of corresponding main group elements, and electronic effects of transition-metal bound ligands. The latter has been discussed earlier in the elongation of M-P (M = Mo, W) bonds due to a heavy *trans*-effect from CO ligands. Previous accounts of ^{31}P-NMR on solutions containing **4.2** show that the η^4-ligated [P4, P5, P6, P7] atoms are rendered equivalent on an NMR timescale due to two intramolecular processes. The first is an intramolecular wagging process, which generates a virtual mirror plane that bisects P4-P6 / P5-P7 bonds, rendering P4 and P5

chemically equivalent to P6 and P7, respectively. Atoms [P4, P5] and [P6, P7] are chemically equivalent through a pyramidal inversion of the $W(CO)_3$(en) ligand at P1. This inversion creates a second virtual mirror plane bisecting P4···P6 and P5···P7 separations and causing equivalency of these atoms. It is assumed that similar intramolecular processes also occur in solution for corresponding analogues $[(en)(CO)_3W(\eta^1,\eta^4\text{-}P_7)Cr(CO)_3]^{3-}$ and $[(en)(CO)_3Mo(\eta^1,\eta^4\text{-}P_7)Mo(CO)_3]^{3-}$ (**4.1**).

Bond distances and geometries indicate that $[P_7]$ interactions to Mo1 are mainly π-type interactions between two pnictyl and two pnictide vertices of four metal-bound P atoms, which are isolobal to a cyclobutadiene fragment (description given in Chapter 3). The Mo-P distances in the solid-state structure of **4.1** are, on average, slightly longer than corresponding W-P interactions. This disparity is not crystallographically imposed, as the two structures are isomorphic, with similar structure factors. Contraction of W-P distances could be due to a higher propensity for π-backbonding to CO ligands, while Mo and W atomic radii are essentially identical (190 pm).

Table 4.5: Comparison of bond lengths [Å] and angles (˚) in $[H(\eta^2\text{-}P_7)Mo(CO)_4]^{2-}$, $[(en)(CO)_3Mo(\eta^1,\eta^4\text{-}P_7)Mo(CO)_3]^{3-}$ (**4.1**), and $[(en)(CO)_3W(\eta^1,\eta^4\text{-}P_7)W(CO)_3]^{3-}$ (**4.2**).

	$[HP_7Mo(CO)_4]^{2-}$	(4.1)	(4.2)
P4-M1	2.722(6)	2.708(3)	2.670(3)
P5-M1	2.717(6)	2.704(3)	2.675(3)
P6-M1	----	2.639(3)	2.601(3)
P7-M1	----	2.633(2)	2.591(3)
P4-P6	2.175(7)	2.153(4)	2.136(5)
P5-P7	2.169(7)	2.153(4)	2.135(5)
P4···P5	3.268(8)	3.244(3)	3.192(5)
P6···P7	2.195(7)	2.886(3)	2.873(5)
P1-P2	2.15(2)	2.170(3)	2.144(4)
P1-P3	2.190(12)	2.172(3)	2.149(4)
P1-M2	----	2.674(2)	2.643(3)
P2-P1-P3	103.7(12)	97.38(9)	97.3(2)
P2-P1-M2	----	114.33(9)	115.0(2)
P3-P1-M2	2.601(3)	116.90(8)	116.9(2)
M1-P1-M2	2.591(3)	134.87(8)	135.5(4)

4.4 Experimental Section

4.4.1 General Considerations

All reactions were performed under an inert atmosphere of dry nitrogen or argon in a dry box (Vacuum Atmospheres Co) or using standard Schlenk techniques. Melts of a Zintl phase of nominal composition K_3P_7 were prepared by fusion (~1100 °C) of stoichiometric ratios of the corresponding elements. *Caution!* Synthesis of Zintl phases is highly exothermic. Full personal protective equipment and blast shields should be used at all times! Ethylenediamine was purified via long-path distillation over K_4Sn_9. Other solvents were purified by distillation from sodium benzophenone ketyl radical under a dinitrogen atmosphere and stored over 3 Å molecular sieves. Complex (cycloheptatriene)$Mo(CO)_3$ was purchased from Strem and used as received. 4,7,13,16,21,24-hexaoxa-1,10-diazobicyclo[8.8.8]hexacosane (2,2,2-crypt, >98%, TCI America) were dried under vacuum for 24 hours prior to use.

4.4.2 Synthesis of $[Mo(CO)_3(\eta^1,\eta^4\text{-}P_7)Mo(CO)_3(en)]^{3-}$

In a 10 mL scintillation vial, K_3P_7 (33.4 mg, 0.100 mmol) and 2,2,2-crypt (113.0 mg, 0.300 mmol) were dissolved in 2 mL of ethylenediamine, and stirred for 10 min at 25 °C, yielding a yellow-brown solution. In a separate vial, (cycloheptatriene)$Mo(CO)_3$ (54.44 mg, 0.200 mmol) was dissolved in 1.5 mL toluene and stirred for 5 min at 25 °C, producing an orange-red solution. The (cycloheptatriene)$Mo(CO)_3$ / tol solution was added dropwise to the K_3P_7 solution with vigorous stirring. The mixture stirred for an additional 4 hours at 25 °C and was then gently heated at 50°C for 30 minutes, during which time the solution darkened to a deep red. The reaction was hot-filtered through glass wool into a clean test tube and cooled slowly before carefully layering with 2 mL of

toluene. After approximately 5 days, red block-like clusters of $[Mo(CO)_3(\eta^1,\eta^4\text{-}P_7)Mo(CO)_3(en)]^{3-}$ formed. (yield (based on K_3P_7): 61.3 mg, 96.2 %)

4.4.3 Crystallographic Studies

Single crystal data collections were performed at ChemMatCARS Sector 15 of the Advanced Photon Source (APS). A suitable single crystal of $C_{56}H_{112}K_3Mo_2N_6O_{18}P_7$ (UMAPS-57-2-LS) was analyzed using a Huber three-circle diffractometer (κ-angle offset of 60º) equipped with a Dectris PILATUS3X CdTe 1M detector. The crystal was kept at 150(2) K during data collection, and the distance between the crystal and detector was 130 mm. A custom-designed software was used for data collection, and frames were converted to Bruker-compatible format for data processing in *APEX II*.

Integral intensity data were corrected for absorption using the multi-scan method of SADABS software. Crystals showed significant radiation damage during the second run of each data collection, but data completeness allowed for structure refinement with only the first 720 frames. The structure was solved with the ShelXT-2014 program and refined with the ShelXL-2015 program and least-square minimization using ShelX software package.

4.4.4 Energy Dispersive X-Ray Spectroscopy

EDX analysis on crystals containing **4.1** was performed on a Hitachi SU-70 SEM, operated at an acceleration voltage of 15 kV. Data acquisition was performed with accumulation intervals of 120 s.

Chapter 5: $[Mo_2P_{16}]^{4-}$ and $[Rh_3As_{16}]^{3-}$ - The First Group 6 Binary Polyphosphide and Group 9 Binary Polyarsenide

5.1 Introduction

Melts of nominal composition "A_3Pn_7" (A = alkali metal = Na, K, Rb ; Pn = pnictogen = P, As, Sb), formed through a high temperature fusion of these elements, serve as precursors to the $[Pn_7]^{3-}$ Zintl polyanions. [60,62,133] Extraction of "A_3Pn_7" with polar aprotic solvents (i.e., ethylenediamine, pyridine, dimethylformamide) in the presence of appropriate cation chelation agents (i.e. [2.2.2-cryptand], 15-crown-5, 18-crown-6, tetrabutylphosphonium bromide), produces solutions containing the homoatomic Zintl anions $[Pn_7]^{3-}$ (Pn = P, As, Sb), where atoms comprising the polycyclic cages adopt a heptapnicanortricyclane-like geometry. The $[Pn_7]^{3-}$ anion is considered the precursor of solution-phase Zintl reactions with Group 15 elements, and, in the case of Pn = As, Sb, readily undergoes functionalization, transfer, oxidative coupling, and activation reactions to form a variety of product types, many of which are inaccessible through reactions with alternative sources of homoatomic pnictogen species (i.e. Pn_4).

In the simplest reactions, $[Pn_7]^{3-}$ anions are functionalized at pnictide vertices by organic ligands, transferred from organohalides (RX ; R = H, alkyl, aryl, or ML_n where M = main group element and L = ligand ; X = Cl, Br, I) or tetraalkylammonium salts ($[NR_4][X]$; R = alkyl ; X = Cl, Br). Products of such reactions, $[(R)_xPn_7]^{(-3+x)}$, retain the nortricyclane-like geometry of the parent $[Pn_7]^{3-}$ cage. When reacted with transition metal complexes $[ML_xR_y]^{n-}$ (M = transition metal ; L = labile ligand ; R = organic ligand), $[Pn_7]^{3-}$ cages can displace weakly bound labile ligands (L), serving as a polyatomic ligand to the transition metal center, coordinated in either η^2 or η^4 modes. Coordination in an η^4 – fashion, the most commonly observed binding mode, results due

to a nortricyclane-to-norbornadiene transformation of the seven-atom cage geometry (see Chapters 3 and 4 for detailed discussion). Oxidative coupling of $[Pn_7]^{3-}$ units gives access to higher nuclearity homoatomic polyanions (i.e. $[P_{14}]^{4-}$, $[As_{22}]^{4-}$) (Figure 5.1).

Products of oxidative coupling, functionalization, and coordination reactions exhibit a clear stoichiometric relationship to the Zintl polyanion precursor. While the $[Pn_7]^{3-}$ cages undergo a mild nortricyclane – norbornadiene structural transition in some cases, the nuclearity of the parent ion is retained. During other reactions, however, $[Pn_7]^{3-}$ cages can undergo facile rearrangement, resulting in the formation of ligand -free intermetalloid species, where the structural arrangement of main group elements is no longer directly related to the parent ions. The propensity of heavier Group 15 (Pn =As, Sb, Bi) polyanions to lend to intermetalloid formation makes them attractive as precursors for isolating ligand-free binary pnictide / transition metal clusters, which exhibit unique Pn-Pn architectures, incorporating transition metals into the structure. [97,99,100]

Syntheses of binary anions traditionally exploit electron rich low-valent transition metal or post-transition metal complexes containing labile ligands, to aid in the isolation of carbon-free anions. This strategy has been successfully employed to isolate crown-like $[MPn_8]^{n-}$ (M = Cr, Nb, Mo ; Pn = As ; n = 3, 2. M = Nb, Mo ; Pn = Sb, n = 3) anions and fullerene-like $As@Ni_{12}@As_{20}^{3-}$ and $Sb@Pd_{12}@Sb_{20}^{3-/4-}$ intermetalloids (See Figure 5.1). [134,135] The arrangement of atoms in ligand-free binary clusters oftentimes differ from known molecular or intermetallic phases, exhibit novel $[Pn_x]^{n-}$ moieties that adopt previously unseen coordination modes, possess high symmetry, and properties inherent to the crossover regime between molecular clusters and extended solids. [78,79] Since heterometallic clusters provide means in which to probe the transition from molecular

clusters to bulk intermetallic phases and can serve as unique precursors to metastable binary phases synthesis and highly ordered phases such as assembled cluster materials (ACMs), the characterization of new species is a rapidly-expanding topic in current Zintl research. [76,136,137]

The synthesis and properties of transition metal complexes with bare polyphosphide ligands has been an area of interest for over 50 years. The majority of polyphosphorus compounds are synthesized through the reaction of unstable white phosphorus (P_4) precursors, which are converted to PCl_3 for industrial chemical purposes. [61,138-141] In efforts to circumvent the use of PCl_3, research has been focused on activation of white phosphorus under mild conditions, specifically by early-transition-metal (ETM)

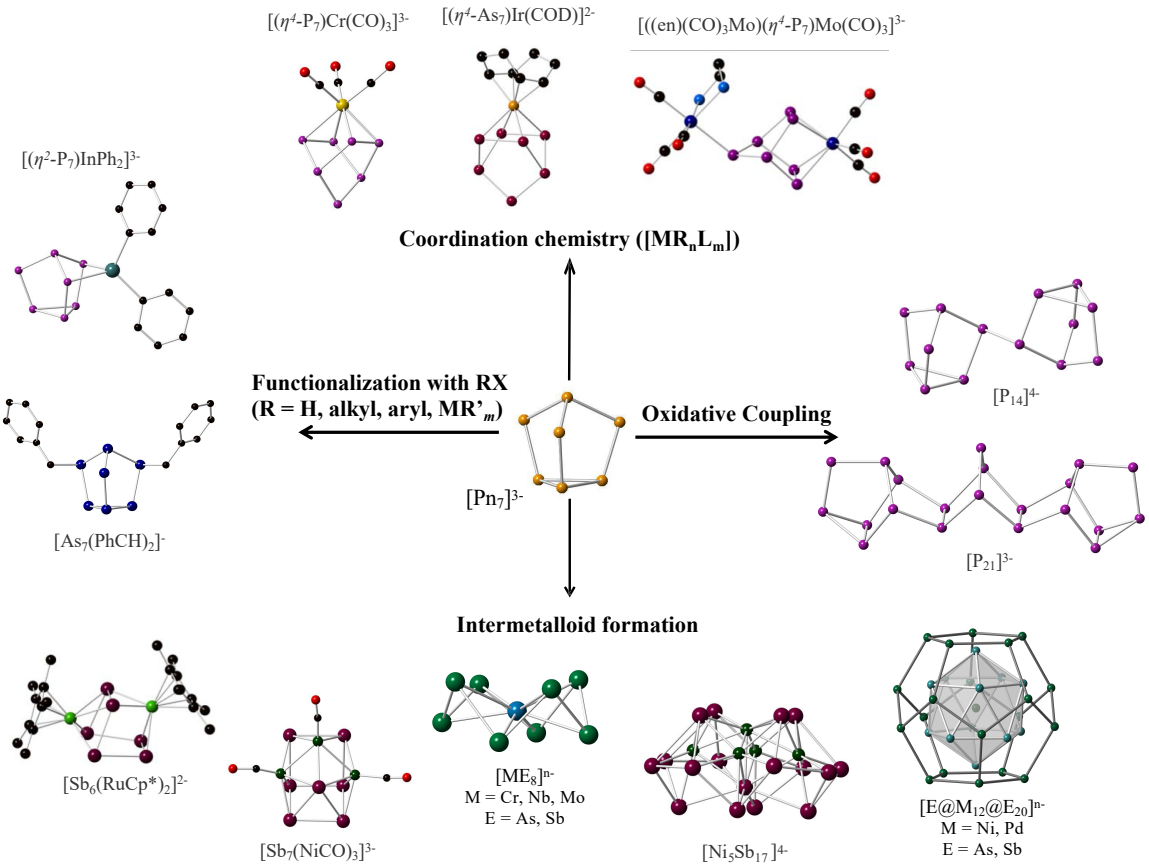

Figure 5.1: Select reactions of pnictogen Zintl polyanions. (M= transition metal, E = main group element, L = organic ligand, R = organic or inorganic ligand)

complexes, which reductively activate a wide variety of small molecule substrates. [138,140] In theory, the polycyclic Zintl anion $[P_7]^{3-}$, which can be viewed as a P_4 tetrahedron with three adjacent P^- vertices inserted, should participate in the same transformations as white phosphorus. Zintl precursors are indeed a viable class of polyphosphorus precursors and have been used to isolate a variety of polyphosphide-containing structures in the solid state. Despite the growing interest and renewed investigations of Zintl pnictide reactions, products synthesized from phosphorus-based systems remains low from a lower propensity of polyphosphide cages to reorganize during reaction. [43,60] Heterometallic clusters of (post-) transition metal-phosphorus systems retain P_7 nuclearity of the parent anion, with many indicating mild cage activation from a nortricyclane-like $[Pn_7]^{3-}$ cage to a norbornadiene-like $[Pn_7]^{3-}$ cage. [100] Isolation of binary anions with larger polyphosphides in other new structural arrangements have yet to be reported using Zintl precursors.

Similarly, the number of pnictogen-Group 9 (Co, Rh, Ir) systems is limited. Species comprised of Group 14 / Group 9 elements have been commonly reported, including the coordination complexes $[(cod)Ir(\eta^4\text{-}E_9)]^{3-}$ (E = Sn, Pb ; cod = 1,5-cyclooctadiene) and endohedral intermetalloids $[Co@Sn_9]^{5-}$, $[Co@Ge_{10}]^{3-}$, $[Rh@Pb_{12}]^{3-}$, and $[Ir@Sn_{12}]^{3-}$.[123,142] No analogous structures from reaction of Group 15 Zintl Phases and Group 9 elements have been previously described in literature. Ligand-capped Rh frameworks with Group 15 / 16 elements in polyhedral cavities ($[Rh_9P(CO)_{21}]^{2-}$, $[Rh_{17}S_2(CO)_{32}]^{3-}$, $[Rh_{10}As(CO)_{22}]^{3-}$) suggest that P / Rh and As / Rh systems may be capable of accommodating the coordination numbers and geometries required to produce endohedral binary anions of Group 15 / 9, heightening interest in the investigation of these systems. [143-145]

A retrosynthetic approach to heterometallic anion formation is not yet realizable, as relationships between precursors and intermetalloids with highly transformed structures remains unclear. Moreover, formation mechanisms cannot be easily investigated, either due to the air and moisture sensitive nature of the reactions, or due to the lack of a suitable spectroscopic handle. To date, commonalities are drawn between the solid-state structures of various intermetalloids or crystallized intermediates, in attempt to surmise the mechanistic pathways involved in the building-up of cluster fragments. [62,146] Thus, deeper understanding of solution dynamics and their relationship to solid-state species is required to further develop hypotheses for structure formation. With the limitations imposed by the systems, this synthetic strategy continues to rely on the isolation and description of novel pnictogen-transition metal intermetalloid species and their subunits, to expand the boundaries of Zintl chemistry and perpetually redefine the types of reactions that are possible, and the types of main group element subunits that form.

Reported herein are the two novel intermetalloids derived from pnictogen Zintl precursors. The first, a binary anion of composition $[Mo_2P_{16}]^{4-}$, is the only early transition metal- phosphorus intermetalloid to be isolated from reaction of a Zintl precursor. This product is the largest binary polyphosphide system and is constructed from moieties that have been isolated in previous work with white phosphorus (P_4) activation. A second binary anion with formula $[Rh_3As_{16}]^{3-}$ is the only Rh-As binary intermetalloid, and contains the first instance of an envelope configuration *cyclo*-As_5^{1-} moiety.

5.2 Results

5.2.1 Syntheses

5.2.1.1 Synthesis of [K(2,2,2-crypt)]$_4$[Mo$_2$P$_{16}$]•0.5(en)

Ethylenediamine (en) solutions of a melt of nominal composition "K_3P_7" react with benzene solutions of Mo(naph)$_2$ (naph = naphthalene) at 25 °C in the presence of 2,2,2-cryptand to yield dark crystals of [K(2,2,2-crypt)]$_4$[Mo$_2$P$_{16}$]•0.5(en), containing the anionic cluster [Mo$_2$P$_{16}$]$^{4-}$ (**5.1**, Figure 5.2). The product [K(2,2,2-crypt)]$_4$[Mo$_2$P$_{16}$]•0.5(en) forms as dark brown / black rhombohedral crystals in ~38% yield after 14 days (Equation 5.1).

2.3 K_3P_7 + 3(2,2,2-crypt) + 2 Mo(naph)$_2$ ⟶ [K(2,2,2-crypt)]$_4$[Mo$_2$P$_{16}$]•0.5(en) (5.1)

Crystals of **5.1** are extremely air and moisture sensitive as a solid and in solutions of CH_3CN and DMF. This anion has been characterized by single crystal X-ray diffraction (XRD), energy dispersive X-ray spectroscopy (EDX), laser desorption/ionization time-of-flight mass spectrometry (LDI-TOF MS) and quantum chemical calculations, including density functional theory (DFT) analyses, Bader charge analyses, and Wiberg Bond Index (WBI) calculations.

5.2.1.2 Synthesis of [K(2,2,2-crypt)]$_3$[Rh$_3$As(As$_5$)$_3$]•0.5(tol)

Melts of nominal composition "K_3As_7" in ethylenediamine react with toluene (tol) solutions of [Rh(COD)Cl]$_2$ at high temperature in the presence of 2,2,2-cryptand to yield violet prismatic crystals of intermetalloid [K(2,2,2-crypt)]$_3$[Rh$_3$As(As$_5$)$_3$]•0.5(tol). The mechanisms of intermetalloid formation, and therefore reagent stoichiometries, are unclear, but a simplified reaction equation can be proposed (Equation 5.2)

$$2.3\ K_3As_7 + 3(2,2,2\text{-crypt}) + 1.5\ [Rh(COD)Cl]_2 \longrightarrow$$

$$[K(2,2,2\text{-crypt})]_3[Rh_3As(As_5)_3]\bullet 0.5(tol) \quad (5.2)$$

The salt $[K(2,2,2\text{-crypt})]_3[Rh_3As(As_5)_3]\bullet 0.5(tol)$ forms as dichromic violet / green prismatic crystals in ~43% yield (based on Rh) after 7 days. The crystals are air and moisture sensitive and partially soluble in CH_3CN and DMF. This cluster has been characterized by single-crystal X-ray diffraction (XRD), EDX, matrix absorption laser desorption ionization- time of flight (MALDI-TOF) and density functional theory (DFT) analyses.

5.2.2 Solid State Structures

5.2.2.1 Solid-State Structure of $[K(2,2,2\text{-crypt})]_4[Mo_2P_{16}]\bullet 0.5(en)$

The $[K(2,2,2\text{-crypt})]_4[Mo_2P_{16}]\bullet 0.5(en)$ salt is monoclinic, space group $P2_1/n$. The asymmetric unit contains the $[Mo_2P_{16}]^{4-}$ anion **(5.1)**, 4 $[K(2,2,2\text{-crypt})]^+$ cations, and 0.5 ethylenediamine solvate molecules. Arrangement of the $[K(2,2,2\text{-crypt})]^+$ cations and **5.1** is highly ordered, with K^+ forming puckered fused hexagonal sheets both above and below the anionic clusters, in a modified A1B2-type lattice arrangement (Figure 5.2). Anions of **5.1** alternate in orientation by roughly 180˚ rotation along the crystallographic a axis from neighboring clusters. Presumably, this packing arrangement of **5.1** is an effect of crystallization, perhaps due to the non-spheroidal nature of the anion. Stacked layers are offset from one another, resulting in an ABAB-type layered lattice.

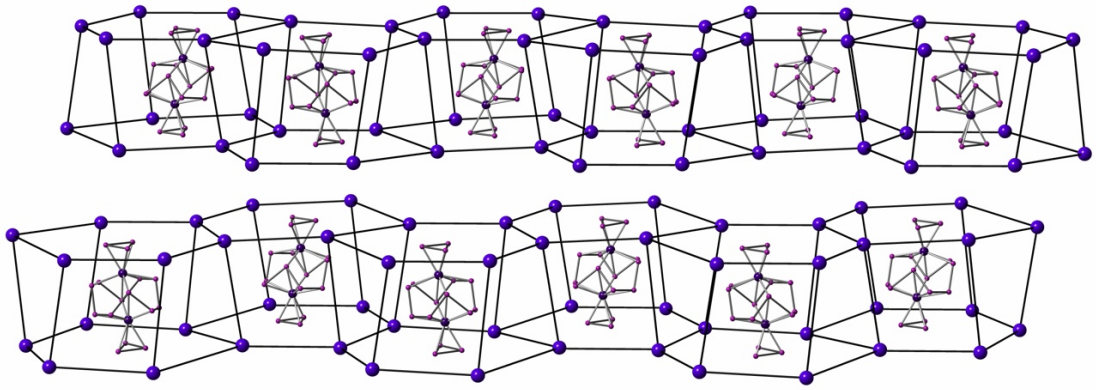

Figure 5.2: Lattice arrangement of anion **5.1** and the K^+ cations (2,2,2-cryptand and en solvate omitted for clarity). Lines joining K^+ are a guide to the eye to illustrate the hexagonal network. Molybdenum = dark blue, P = magenta, Mo = dark blue, K = violet.

The cluster **5.1** possesses virtual C_{2h} point symmetry (Figure 5.3 (a, b)), with a C_2 rotation axis through the center of the cluster, and a perpendicular σ_h mirror plane bisecting the cluster through P1, Mo1, P4, P9, Mo2, P14. The total electron count of the cluster is 96 e^- [(5 e^- x 16 P) + (6 e^- x 2 Mo) + 4 e^- overall charge)], and therefore is predicted to be diamagnetic. The structure contains two *cyclo*-P_3 moieties, two Mo centers, and a *cyclo*-[P_{10}] ring. Each Mo atom is coordinated to six P atoms of the [P_{10}] ligand and capped by an η^3-P_3 unit. The long interatomic Mo-Mo distance (3.603(3) Å) indicates no interactions between the two molybdenum atoms.

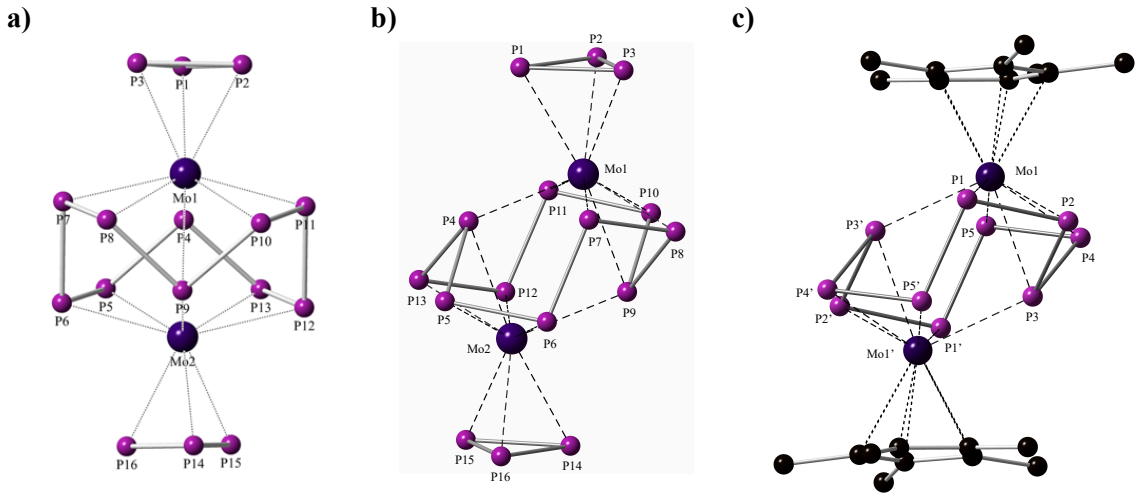

Figure 5.3: (a) Ball and stick model of **5.1**. (b) Projection of **5.1**, showing planarity of *cyclo*-P_3 moieties, geometry of the *cyclo*-P_{10} ring, and the central "Mo_2P_2" unit (c) Ball and stick model of $[Mo_2P_{10}Cp^*_2]$ complex, illustrating geometric and coordinative similarities of the *cyclo*-P_{10}^{2-} ligand to that in **5.1**. Hydrogens of Cp* rings omitted for clarity. P = magenta, Mo = dark blue, C = black.

To assign charges on the polyphosphorous ligands, the Zintl-Klemm pseudoelement concept is invoked, where the group 15 elements are isolobal / isoelectronic to neutral group 14 species ($P \cong CH$, $P^- \cong CH_2$), and complete electron transfer from the transition metal to the main group element is assumed. [46] While this pseudoelement concept has definite limitations, it is useful for a first approximation of structure and bonding to describe the polyphosphide ligands in **5.1**.

The *cyclo*-P_3 ligand has been reported in other transition metal-polyphosphide structures and are structurally similar to the As_3^{3-} ligand of **3.1**, detailed in Chapter 3. [60,138,147-149] Previous η^3-P_3 cycles have been described as having an overall charge of 3^-, and are six electron donors, which satisfies Hückel's [2n+4] rule for aromaticity. Bond distances, angles, and coordination of cyclo-P_3 in **5.1** are consistent with these descriptions. The *cyclo*-P_{10} ligand has been previously reported in the neutral organometallic molybdenum phosphide complex $[Mo_2P_{10}Cp^*_2]$ (Cp^* =

pentamethylcyclopentadienyl, Figure 5.3(c)), and is nearly identical to the configuration seen in **5.1**. [150] With eight three-coordinate P atoms and two two-coordinate phosphorus atoms, an overall 2^- charge ascribed to the $[P_{10}]^{2-}$ moiety. This *cyclo*-decaphosphatetraenediide dianion, $[P_{10}]^{2-}$, is isolobal to the olefin *cyclo*-1,3,6,8-decatetraene ($C_{10}H_{12}$) via the Zintl-Klemm pseudoelement concept. In order to obtain an overall 4^- charge on **5.1**, the molybdenum centers must be formally in the +2 oxidation state, analogous to the Cp* complex shown in Figure 5.3. The bond distances, angles, and coordination geometry for each unit is consistent with its corresponding charge description.

Each Mo of **5.1** is coordinated to 9 P atoms, which can be grouped as follows: three (η^3-P_3), two (η^2-P=P), and two (μ_2:$\eta^{1:1}$-P^{1-}) interactions. Bond angles between {P_3}-Mo-{P_{10}} ligands (79.9˚-86.4˚) and coordination around the Mo from P_{10} interactions (∠ P-Mo-P ~ 50.8˚ - 91.0˚, average 78.3˚) suggests that geometry at Mo centers is arranged in a three-legged piano stool molecular geometry. Mo-P bond distances range from 2.460(5) – 2.565(5) Å, with shorter interactions stemming from P=P bonds, and longer interactions from formally negative P atoms in the P_3 and P_{10} units. Electron donation from $[P_3]^{3-}$ (12 e-), cyclo-$[P_{10}]^{2-}$ (16 e-) to Mo^{II}-d^4 atoms leads to a total electron count of 36 electrons / cluster, or 18 electrons per Mo.

Within the *cyclo*-P_3 ligands, each P vertex is two-coordinate, and therefore is formally negative. The P_3 unit is η^3-coordinated to Mo in a symmetrical fashion. The P-P bond distances range from 2.137(6) – 2.154(6) Å, with endocyclic bond angles averaging ~60.0˚. These distances are between true P-P single (2.21 Å in P_4) and double bond values (av. 2.05 in diphosphenes), and comparable to those described in other [(η^3-P_3)-Mo$(L)_3$] systems (L = organic ligand), where multiple bond character was also

presumed. [147,149] The η^3- coordination of P_3 to Mo results in an $[MoP_3]^{1-}$ tetrahedron, with Mo-P bond distances between 2.500(6) – 2.565(5) Å, and P-Mo-P angles averaging 49.4˚, with P-P-Mo angles of 63.5˚, consistent with reported values for similar compounds.

The ring is highly contorted, exhibiting four shorter bonds (2.146(6) – 2.165(6) Å) between P5-P6, P7-P8, P10-P11, P12-P13, and bond angles from 94.8˚ – 101.5˚ at these atoms, suggestive of P-P multiple bond character. Other P-P bond distances are longer, ranging from 2.211(7) – 2.237(6) Å, and within the range of single bonds. Bicoordinate atoms P4 and P9 exhibit more acute ∠P-P-P angles (89.7˚ – 90.0˚), possibly indicating a different hybridization for these P atoms. These atoms are out-of-plane (where a plane is defined by adjacent (η^2-P=P) units) with torsion angles γ(P6-P12-P13-P4) = 42.39˚ and γ(P7-P11-P10-P9) = 42.86˚, further demonstrating that P4 and P9 may be best described as sp^3 hybridized atoms. Therefore, P4 and P9, are negatively charged, and isolobal to a CH_2 unit, supporting the initial assignment of an overall 2^- charge on the P_{10} ring. Coordination of P4 and P9 to Mo in a (μ_2:$\eta^{1:1}$) mode through orthogonal lone pairs creates a square planar P_2Mo_2 feature in the center of the cluster with P-Mo-P angles averaging 90.0˚ (Figure 5.3). Additionally, each Mo center is coordinated by two P-P double bonds of *cyclo*-$[P_{10}]^{2-}$ in an (η^2:η^2) fashion.

Table 5.1: Selected Bond Lengths [Å] and angles (°) for the $[Mo_2P_{16}]^{4-}$ anion[a]

Distances [Å]			
P1-Mo1	2.559(6)	P1-P2	2.154(6)
P2-Mo1	2.526(5)	P1-P3	2.152(6)
P3-Mo1	2.517(5)	P2-P3	2.140(7)
P4-Mo1	2.509(4)	P4-P5	2.237(6)
P7-Mo1	2.564(5)	P4-P13	2.219(6)
P8-Mo1	2.460(5)	P5-P6	2.146(6)
P10-Mo1	2.492(5)	P6-P7	2.218(7)
P11-Mo1	2.547(5)	P7-P8	2.159(7)
P9-Mo1	2.559(5)	P8-P9	2.211(7)
P9-Mo2	2.516(5)	P9-P10	2.230(6)
P4-Mo2	2.554(5)	P10-P11	2.165(6)
P5-Mo2	2.486(5)	P11-P12	2.219(6)
P6-Mo2	2.560(5)	P12-P13	2.154(6)
P12-Mo2	2.557(5)	P14-P15	2.136(6)
P13-Mo2	2.477(5)	P14-P16	2.146
P14-Mo2	2.565(5)	P15-P16	2.142(7)
P15-Mo2	2.500(6)	Mo1···Mo2	3.603(3)
P16-Mo2	2.524(5)		
Angles (°)			
P3-P1-P2	59.6(2)	P5-P6-P7	101.5(1)
P1-P2-P3	60.2(2)	P6-P7-P8	100.1(9)
P2-P3-P1	60.2(6)	P1-Mo1-P3	50.2(2)
P14-P15-P16	60.2(4)	P1-Mo1-P2	50.1(6)
P15-P16-P14	59.8(1)	P2-Mo1-P3	50.2(7)
P16-P14-P15	60.0(5)	P1-Mo1-P4	80.3(6)
P7-P8-P9	96.9(4)	P4-Mo1-P11	79.6(7)
P9-P10-P11	95.5(5)	P8-Mo1-P10	78.4(7)
P10-P11-P12	101.4(8)	P7-Mo1-P8	50.8(9)
P11-P12-P13	100.7(1)	P10-Mo1-P11	50.9(9)
P12-P13-P4	96.5(4)	P5-Mo2-P13	78.8(2)
P5-P4-P13	89.9(2)	P6-Mo2-P9	78.6(2)
P8-P9-P10	89.7(3)	P5-Mo2-P6	50.3(2)
P4-P5-P6	94.8(7)	P12-Mo2-P13	50.6(5)

[a]Crystals of $[K(2,2,2\text{-crypt})]_4$[**5.1**]•0.5(en) were small, weakly reflecting (0.95 Å), and exhibited radiation damage during data collection (Advanced Photon Source). These factors collectively contributed to large ESDs in the bond distances and angles reported here.

5.2.2.2 Solid-State Structure of $[K(2,2,2\text{-crypt})]_3[Rh_3As(As_5)_3]\bullet 0.5(tol)$

The $[K(2,2,2\text{-crypt})]_3[Rh_3As(As_5)_3]\bullet 0.5(tol)$ salt is tetragonal, space group *I4₁cd*. The asymmetric unit contains the $[Rh_3As_{16}]^{3-}$ cluster, **5.2**, 3 $[K(2,2,2\text{-crypt})]^+$ cations, and 0.5 toluene solvate molecules. Disorder is present in two of the $[K(2,2,2\text{-crypt})]^+$ molecules over two orientations. The cluster $[Rh_3As(As_5)_3]^{3-}$ is also disordered, with two orientations observed in ratio of 82 : 18. While the major configuration is symmetric and ordered, the minor configuration contains disorder in one of the three As_5 rings. Only the major orientation is described here.

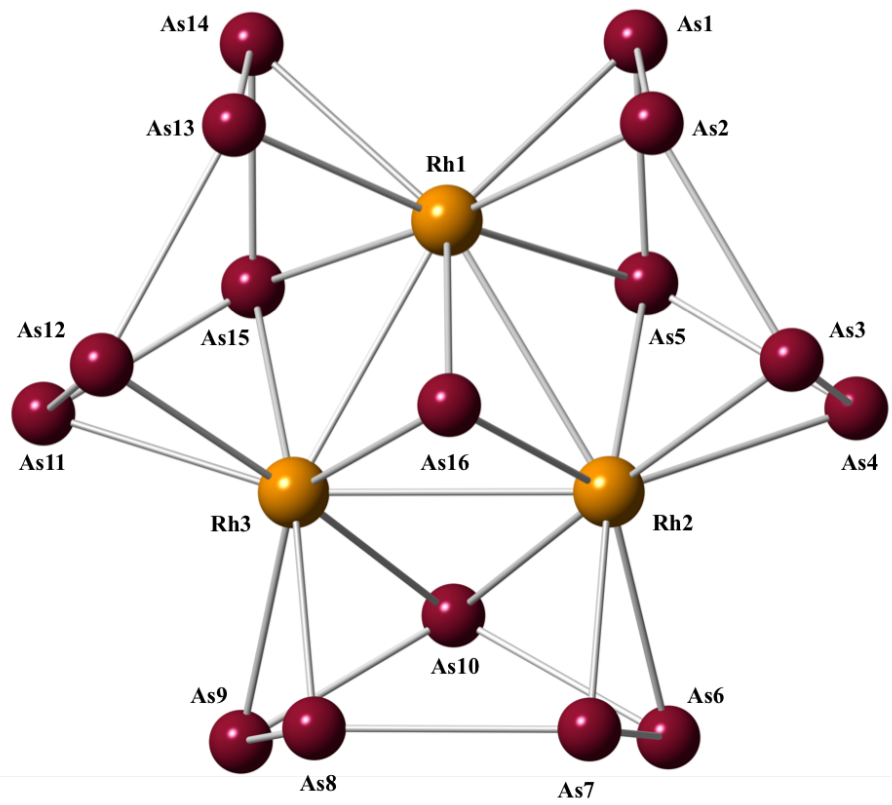

Figure 5.4: Ball and stick model of **5.2**. Rh = yellow, As = red-violet.

The cluster **5.2** has C_{3v} point symmetry, and is comprised of three near identical envelope configuration cyclo-pentaarsenide rings, As_5^{1-}, bound in a (μ_2:η^3:η^3) fashion to

Rh^{1+} metal centers (Figure 5.4). The Rh atoms form a regular *cyclo*-Rh_3 triangle. A lone As^{3-} ion bridges three rhodium centers in μ_3 fashion, located above the geometric center of the Rh_3 ring, to form a Rh_3As tetrahedron. Interatomic distances of 2.827(1) – 2.861(1) Å are within range for Rh-Rh bonding, and a narrow bond range is indicative of similar oxidation states for each Rh. The coordination environment of a single Rh is built from interactions with one μ_3-As^{3-}, two (μ_2-As) atoms and two η^2-As_2 contributions from the As_5^{1-} rings. Triangulo-Rh_3 cores are common, with products exhibiting Rh atoms in oxidation states varying from 1^+ to 3^+ reported. [151-153] Direct relationship between Rh-Rh interatomic distance and oxidation state are tenuous, as analysis of known structures indicates that interatomic distances in these complexes are influenced by size and steric constraints of the bridging ligands (μ_2 and μ_3). However, the range of bond distances and coordination environments of each Rh can be used to purport whether all Rh centers are in the same oxidation state (See Table 5.2).

Table 5.2: Rh-Rh and Rh-L interactions in 4.1 and similar species. Bond distances in [Å]. Refs [143-146].

	Rh-Rh	**Rh species**	**Rh-(μ_2-L)**	**Rh-(μ_3-L)**
$[Rh_3As_{16}]^{3-}$	2.835-2.851	Rh^I	2.608-2.665	2.429-2.447
$[Rh(\mu\text{-}^tBu_2P)_3CO]_3$	2.638 – 2.659	Rh^I	2.274 – 2.301	------
$[Rh_3(\mu_3\text{-}S)_2(CO)_6]^-$	3.00 – 3.08	Rh^I	------	2.351
$[Rh_3(\mu_3\text{-}Se)_2(CO)_6]^-$	3.08 – 3.16	Rh^I	------	2.458
$Rh_6(\mu_2\text{-}As(^tBu)_2)(\mu_4\text{-}As^tBu)(CO)_{11}$	2.72 – 2.93	Rh^I, Rh^{III}	2.363-2.430	------

The As_5 rings adopt an envelope conformation, containing bond distances ranging from 2.325(2) – 2.491(2) Å (Figure 5.5(a)). Three longer bonds and two shorter As-As

bonds suggest localized double bond character in each η^2 (As-As) feature (e.g. As1-As2, As3-As4). Additionally, endocyclic angles in the pentagonal plane around As1 and As4 are narrowed (97.3º). The As5 torsion angle, used to describe the deviation of this atom from a plane containing the other four As atoms in the ring, varies from 28.17º - 30.16º out of plane. This angle, coupled with the bond distances, is further indication that As5 is sp^3 hybridized, while As1, As2, As3, and As4 are sp^2-hybridized.

Through the Zintl-Klemm pseudoelement formalism, neutral As ≅ CH, while As^{1-} ≅ CH_2. Using this formalism, As atoms with three bonds are formally neutral, while those with two bonds are negatively charged. Assuming multiple bond character for [As1, As2, As3, As4] atoms imparts a neutral oxidation state. The two-coordinate As5 atom is given a formal charge of 1^-. Therefore, each As_5 ring carries an overall charge of 1^- and has an isolobal relationship to cyclopentadiene (C_5H_6). This is the first instance of a As_5^{1-} subunit isolated from Zintl reactions. A cyclo-As_5^{1-} subunit has been noted in the Zintl intermetallic clusters $[Pd_7As_{16}]^{4-}$, however, the cyclo-As_5^{1-} unit exhibits a planar geometry, yet are not structurally similar to the cyclopentadienide anion, and therefore indescribable via pseudoelement formalisms. [104] Other highly reduced forms of pentaarsenide rings, such as As_5^{5-} in the organo-substituted arsenomethane ($As_5(CH_3)_5$) and the ternary phase $RbBa_2As_5$ (Figure 5.5(b)), also adopt an envelope configuration. [154] In the latter, bond distances of the reported *cyclo*-As_5^{5-} are all within range of As-As single bonds, with no multiple bond character. The torsion angle of As5 from the plane containing other As atoms is smaller (19.73º – 28.91º) than that of cyclo-As_5^{1-} (28.17º - 30.16º), and endocyclic angles around each As atom are more consistent with expected values in a planar pentagonal ring (average 104.5º). [154]

While the configuration of As_5^{5-} is similar to the As_5^{1-} subunit in **5.2** in overall shape, the electronic structure, and therefore the geometry and charge on each As, is vastly different, and is more appropriately compared to other cyclic polyarsenides with high charge density, such as the *cyclo*-As_8^{8-} unit. [155,156]

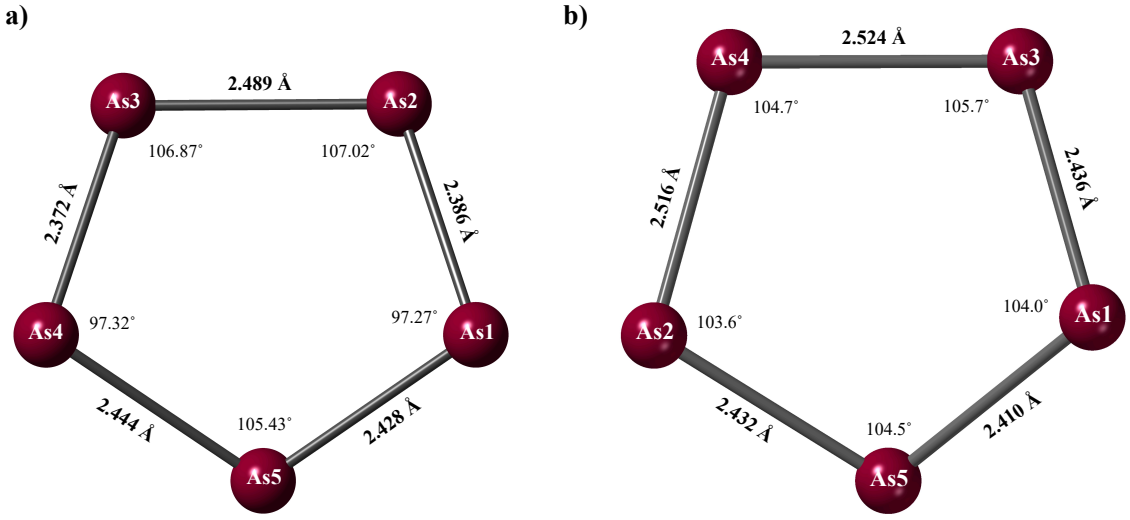

Figure 5.5: Comparisons of As_5 units found in the (a) $[Rh_3As_{16}]^{3-}$ anion and (b) the ternary phase $RbBa_2As_5$ through bond distances and endocyclic angles.

Table 5.3: Select Crystallographic, Data Collection, and Refinement Data for **5.1** and **5.2**.

	[K(2,2,2-crypt)]$_4$[**5.1**]•0.5en[a]	[K(2,2,2-crypt)]$_3$[**5.2**]•0.5tol[a]
Empirical formula	$C_{145}H_{292}K_8Mo_4N_{17}O_{48}$	$C_{57.5}H_{112}As_{16}K_3N_6O_{18}Rh_3$
Formula weight	1174.87	2800.27
Temperature/K	120(2)	120(2)
Crystal system	Monoclinic	Tetragonal
Space group	$P2_1/n$	$I4_1cd$
a/Å	14.6920(5)	33.916(2)
b/Å	24.1220(10)	33.916(2)
c/Å	30.5850(6)	32.442(2)
α/°	90	90
β/°	93.113(7)	90
γ/°	90	90
Volume/Å^3	10823(2)	37318(5)
Z	2	16
ρ_{cal} cg/cm^3	1.452	1.994
μ/mm-1	4.327	6.349
F(000)	1572.0	21808.0
Crystal size/mm^3	0.27 x 0.25 x 0.025	0.611 x 0.108 x 0.094
Radiation	sync (λ = 0.44310)	Mo Kα (λ = 0.71073)
2θ range for data collection/°	3.388 to 59.998	3.798 to 56
Index ranges	$-16 \leq h \leq 16$, $-30 \leq k \leq 30$, $-18 \leq l \leq 18$	$-44 \leq h \leq 44$, $-44 \leq k \leq 44$, $-42 \leq l \leq 42$
Reflections collected	44734	207936
Independent reflections	16887 [R_{int} = 0.0311, R_{sig} = 0.0421]	22501 [R_{int} = 0.0669, R_{sig} = 0.0428]
Data/restraints/parameters	16887/1/652	22501/1638/1241
Goodness-of-fit on F^2	1.000	1.260
R_1/wR_2 [$I>=2\sigma$ (I)]	0.0253, 0.0468	0.0491, 0.0958
R_1/wR_2 [all data]	0.0315, 0.0480	0.0708, 0.1032

[a]See the Crystallographic Studies Section for complete details on refinements.

Table 5.4: Selected bond lengths [Å] and angles (°) of $[Rh_3As_{16}]^{3-}$

Distance [Å]			
Rh1-Rh2	2.861(1)	As15-Rh3	2.623(2)
Rh1-Rh3	2.827(1)	As16-Rh1	2.429(2)
Rh2-Rh3	2.853(1)	As16-Rh2	2.446(2)
As1-Rh1	2.501(2)	As16-Rh3	2.442(2)
As2-Rh1	2.497(2)	As1-As2	2.386(2)
As3-Rh2	2.506(2)	As1-As5	2.428(2)
As4-Rh2	2.494(2)	As2-As3	2.489(2)
As6-Rh2	2.496(2)	As3-As4	2.372(2)
As7-Rh2	2.498(2)	As4-As5	2.443(2)
As8-Rh3	2.493(2)	As6-As7	2.373(2)
As9-Rh3	2.514(2)	As6-As10	2.431(2)
As11-Rh3	2.497(2)	As7-As8	2.491(2)
As12-Rh3	2.536(3)	As8-As9	2.380(2)
As13-Rh1	2.539(2)	As9-As10	2.422(2)
As14-Rh1	2.525(2)	As11-As12	2.325(3)
As5-Rh1	2.673(2)	As11-As15	2.446(2)
As5-Rh2	2.658(2)	As12-As13	2.479(3)
As10-Rh2	2.657(2)	As13-As14	2.375(3)
As10-Rh3	2.663(2)	As14-As15	2.429(3)
As15-Rh1	2.639(2)		
Angles (°)			
Rh1-Rh2-Rh3	59.3(3)	Rh2-As16-Rh3	71.4(4)
Rh1-Rh3-Rh2	60.5(3)	As1-Rh1-As2	57.1(5)
Rh2-Rh1-Rh3	60.2(3)	As1-Rh1-As5	55.9(5)
Rh1-As5-Rh2	64.9(4)	As16-Rh1-As5	111.1(6)
Rh2-As10-Rh3	64.9(4)	As3-As4-As5	97.3(7)
Rh1-As15-Rh3	65.0(5)	As1-As2-As3	107.0(7)
Rh1-As16-Rh2	71.9(5)	As1-As5-As4	105.4(7)
Rh1-As16-Rh3	70.9(4)	As2-As3-As4	106.9(7)

5.2.3 Mass Spectrometry Studies

Laser Desorption/Ionization time-of-flight mass spectra (LDI-TOF MS, Bruker Autoflex) were collected in negative ion mode with a nitrogen pulsed laser. The parent ion of **5.1** is observed as the potassium ion pair $[K_3Mo_2P_{16}]^{1-}$ at *m/z* = 804.28 amu (Figures 5.6, 5.7), and is considerably less intense than peaks for other gas phase species or fragments of the parent molecule. A large number of fragments and ion-pairs resulted in overlapping signals, making deconvolution of the entire spectrum difficult.

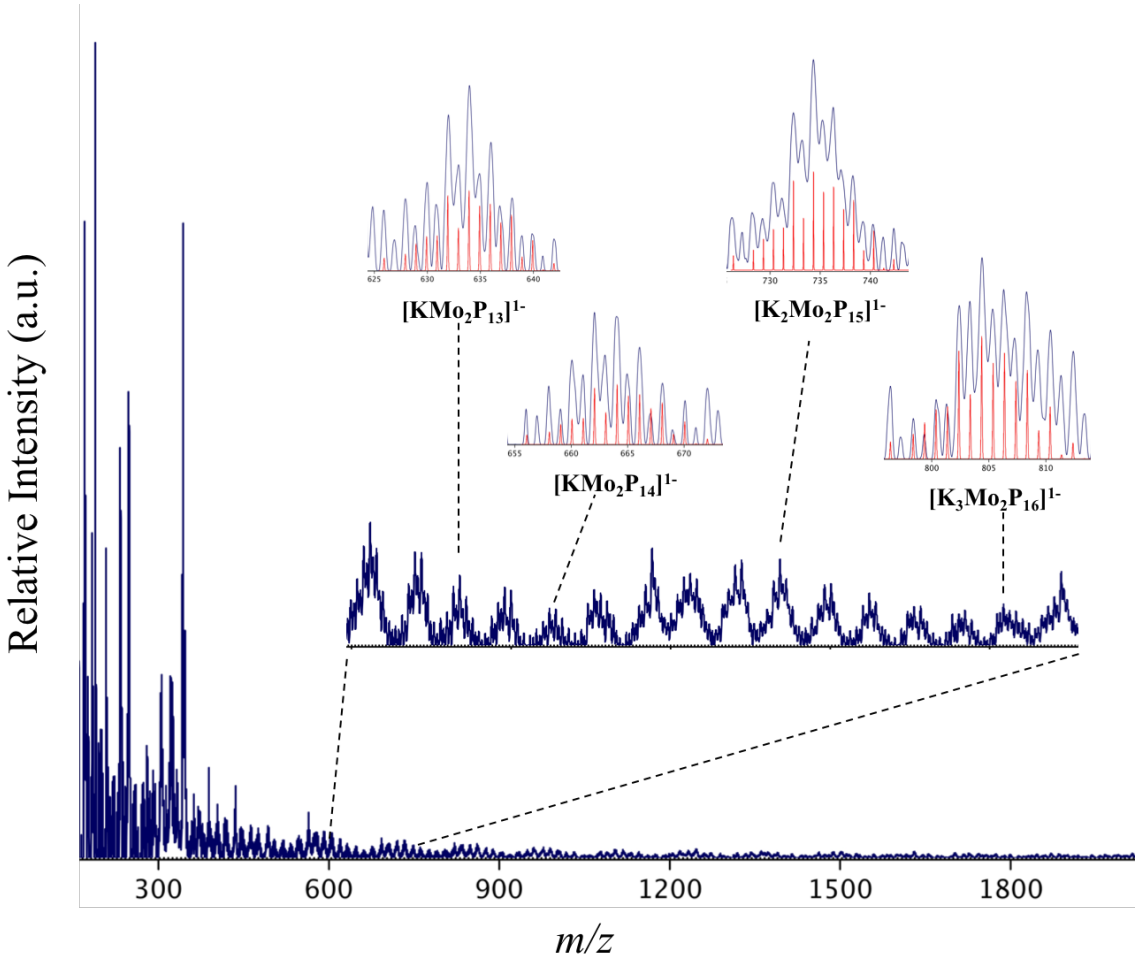

Figure 5.6: Selection of the negative-ion LDI of crystals of **5.1** (blue), focusing on the region between *m/z* = 600 - 850. Parent ion appears at *m/z* = 804.28 as a potassium ion pair as $[K_3Mo_2P_{16}]^-$. Simulated spectra in red (Mmass Software, version 3). Mass envelopes are also shown for potential fragments of the parent ion.

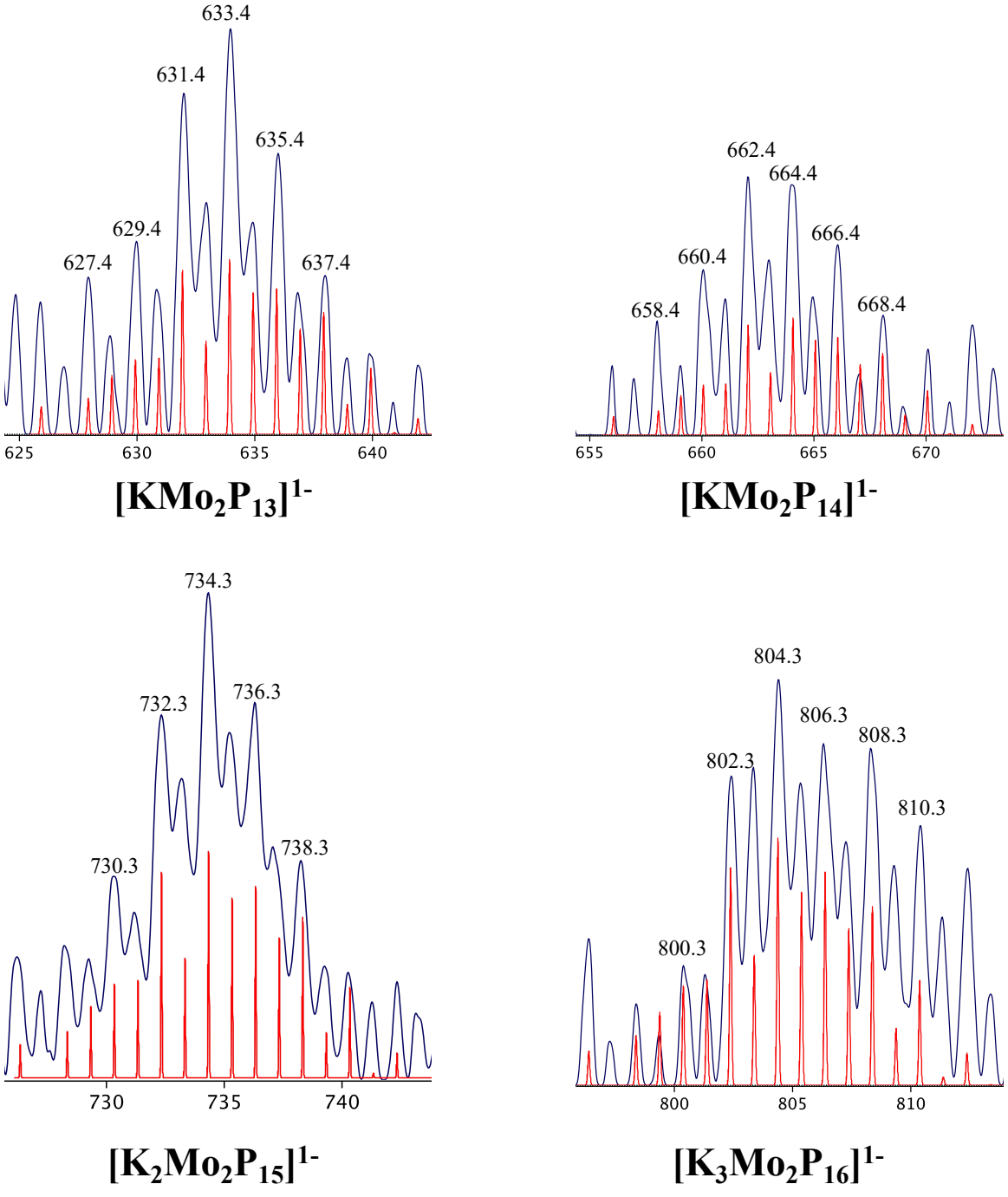

Figure 5.7: Expanded mass envelopes for fragments shown in Figure 5.6. Experimental spectra in blue, simulated spectra in red (Mmass Software, version 3).

The parent ion of cluster **5.2** is observed as $[Rh_3As_{16}]^{1-}$ at *m/z* = 1507.46 amu (Figure 5.8) and is considerably less intense than other fragments. Use of bis(1,8-dimethylamino)naphthalene in a CH_3CN:THF solution (75:25 v:v) as a matrix aided in increasing intensity of fragments, but also enhanced number and intensity of protonated species and ion-paired potassium salts observed, leading to a complex spectrum. Fragments of the parent ion, such as As_5^{1-} (374.61 *m/z*), $RhAs_5^{1-}$ (477.51 *m/z*), $KRh_2As_{10}^{1-}$ (993.99 *m/z*), and $Rh_3As_{12}^{1-}$ (1207.78 *m/z*) were prominent.

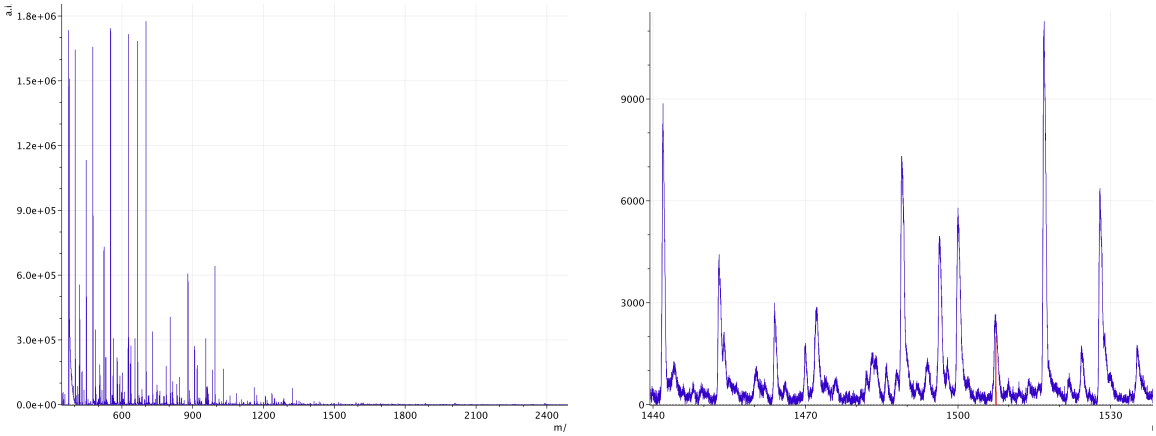

Figure 5.8: Selection of MALDI spectrum collected from crystals of **5.2** on carbon tape with an organic matrix. (a) Selection of spectrum, highlighting its complexity and the numerous gas phase species created during analysis. (b) The parent ion $[Rh_3As_{16}]^{1-}$ appears at *m/z* = 1507.46 as a single peak, as both Rh and As are monoisotopic. Simulated spectrum in red (Mmass Software, version 3).

5.2.4 Energy Dispersive X-Ray Spectroscopy (EDX)

EDX data for crystals containing **5.1** (Figure 5.9) do indicate the presence of desired elements K, P, and Mo, but the ratio of these elements [2.6: 3.8 : 1.0] is inconsistent with expected results (2.0: 8.0 : 1.0). The normalized atom percent of phosphorus, in particular, is quite low when compared to the expected value. Therefore, these results may be only used to validate that all three elements are present in the crystals, but do not confirm the molecular formula or charge on the anion.

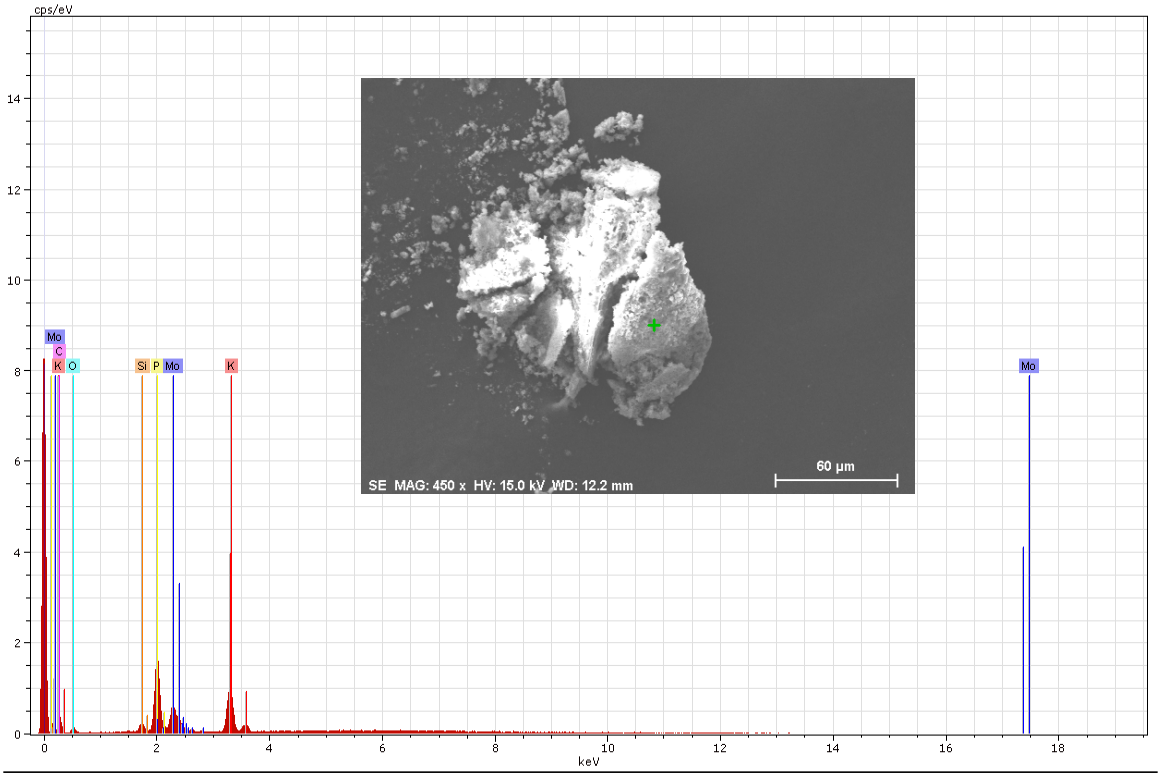

Element	AN	Series	[wt%]	[norm wt#]	[norm atom %]	Error [%]
P	15	K-series	14.95	19.85	14.14	0.6
K	19	K-series	13.10	17.40	9.82	0.4
Mo	42	L-series	12.17	16.16	3.72	0.4
Si	14	K-series	1.96	2.61	2.05	0.1
C	6	K-series	15.89	21.10	38.75	2.2
O	8	K-series	17.22	22.87	31.53	2.8
		Sum:	75.29	100.00	100.00	

Figure 5.9: EDX analysis of $[K(2,2,2\text{-crypt})]_4[Mo_2P_{16}]\bullet 0.5en$ on carbon tape. P:Mo:K = 3.8 : 1.0 : 2.6.

EDX analysis of crystals containing **5.2** (Figure 5.10) show the presence of desired elements As, Rh, and K, in a ratio (6.3: 1.0 : 1.9) close to expected (5.33: 1 : 1.0). Elemental scans of these crystals show that As, Rh, and K are homogeneously distributed throughout the remnants of the crystals (Figure 5.11)

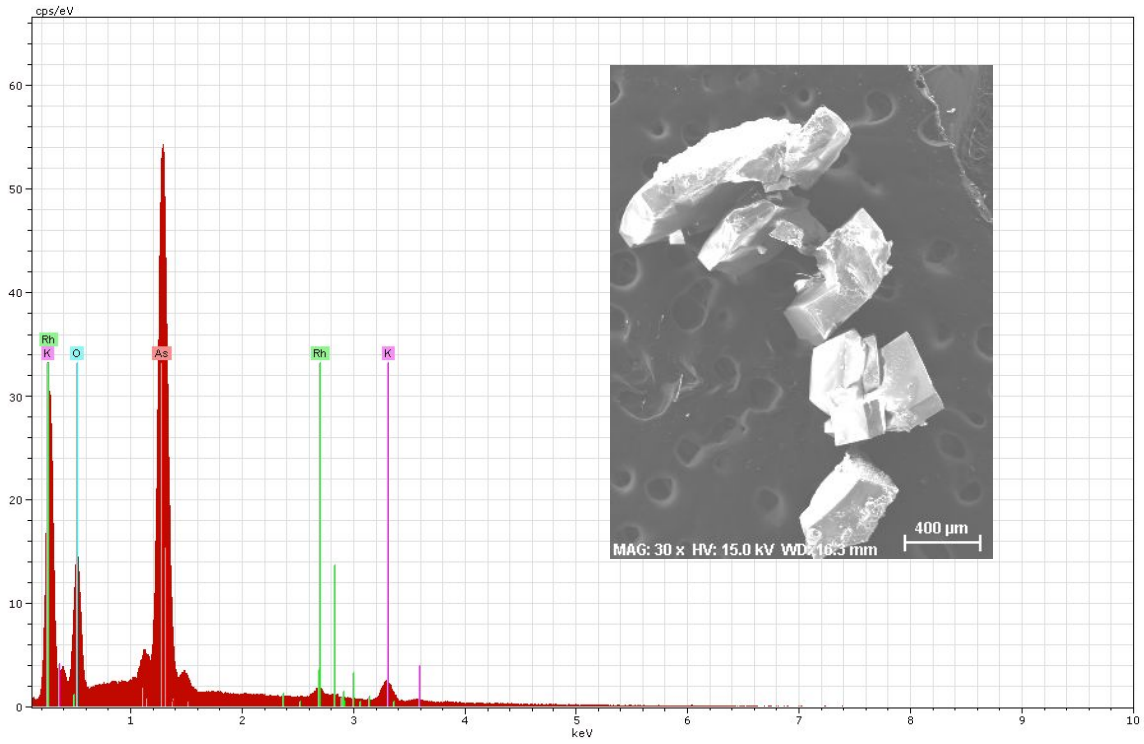

Element	AN	Series	[wt%]	[norm wt#]	[norm atom %]	Error [%]
As	33	L-series	23.29	43.95	19.24	1.2
Rh	45	L-series	5.09	9.61	3.06	0.2
O	8	K-series	16.95	31.98	65.58	1.8
K	19	K-series	7.66	14.45	12.12	0.2
		Sum:	52.99	100	100	

Figure 5.10: EDX analysis of $[K(2,2,2\text{-crypt})]_3[Rh_3As_{16}]$•0.5tol on carbon tape. As:Rh:K = 6.3 : 1.0 : 3.9.

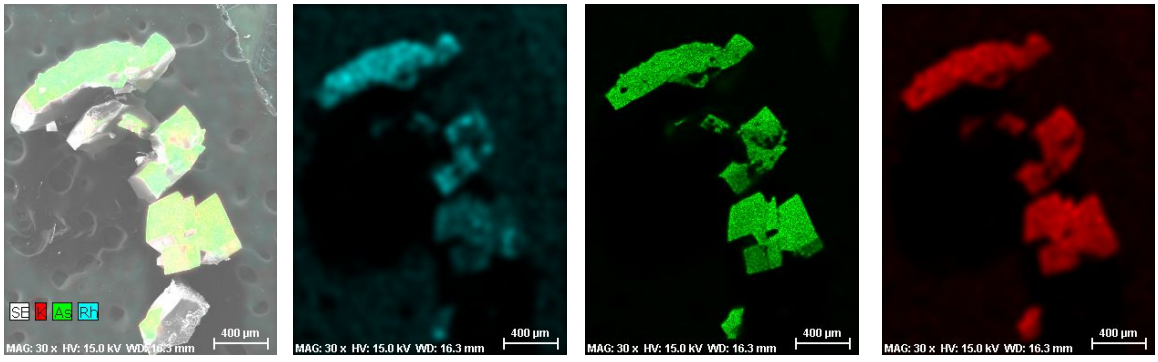

[K, As, Rh] [Rh] [As] [K]

Figure 5.11: Elemental scans of $[K(2,2,2\text{-crypt})]_3[Rh_3As_{16}]$•0.5tol crystals on carbon tape, showing homogeneity of the three desired elements throughout the crystals.

5.2.5 Molecular Orbital Calculations

Quantum calculations were performed on both **5.1** and **5.2** by Dr. Mark Palenik of the Naval Research Laboratory. Density functional theory (DFT) calculations were performed with a Def2-TZVP basis set in Gaussian 09, using the crystallographic structure as an initial model. Wiberg Bond Index (WBI) calculations were performed in Gaussian 09. Bader Charge Analysis Code from the Henkelman group was used to calculate atomic charges. The charge densities for this analysis were either generated in Gaussian 09 using a molecular calculation, or from Quantum Espresso using a periodic method that required Na^+ counterions.

5.2.5.1 Molecular Orbital Calculations on $[Mo_2P_{16}]^{4-}$

Cluster **5.1** has 96 valence electrons (including 5s electrons), and is predicted to be diamagnetic. The geometry was optimized in C_{2h} symmetry, using the coordinates of the solid-state structure as an initial model. Select molecular orbitals are shown in Figure 5.12, while WBI values, calculated bond distances, and Bader charges are given in Table 5.5.

The HOMO of **5.1** is mainly comprised of Mo-P interactions, including bonding between orthogonal p-orbital based lone pairs on P4 and P9 bridging both Mo centers (Figure 5.10).

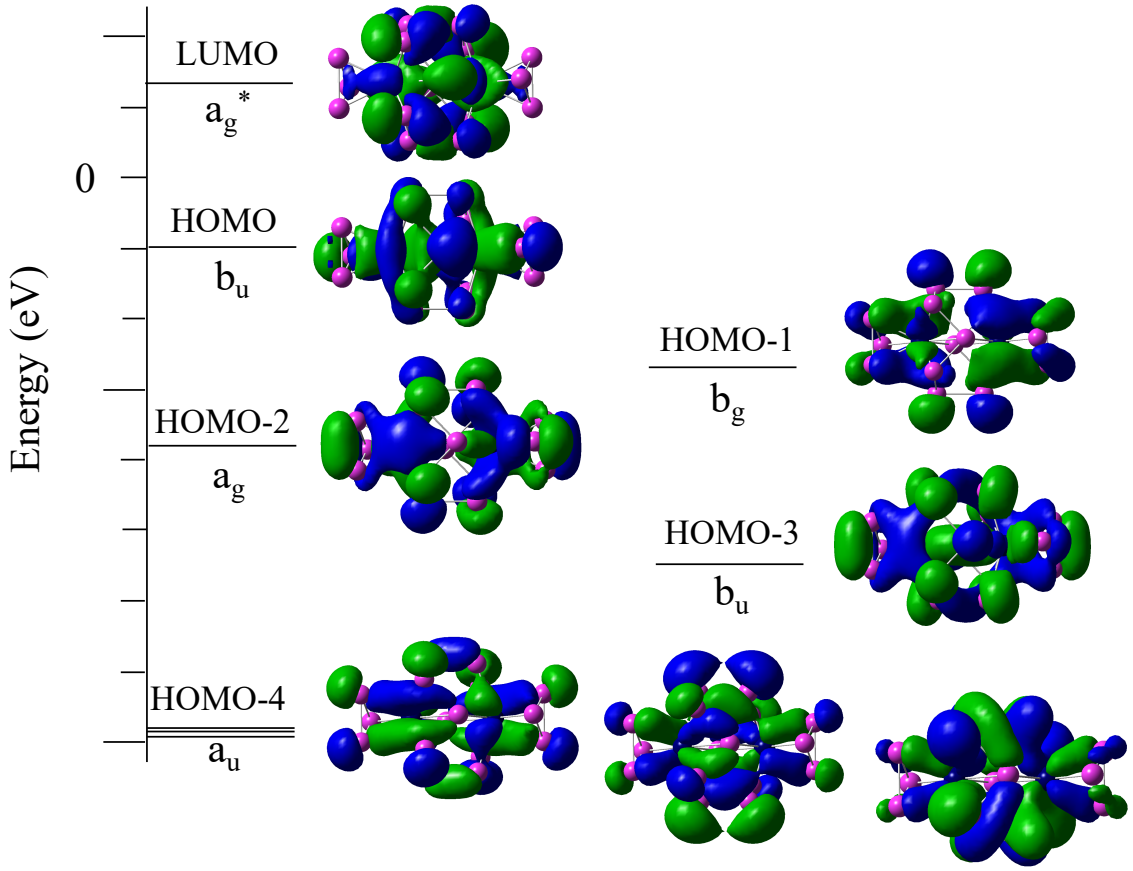

Figure 5.12: Representations of the frontier orbitals for **5.1**.

There is no overlap of orbitals between Mo atoms, as expected by the long interatomic bond distance. Delocalization between double bonded P atoms in the P_{10} ring is seen in the HOMO and lower lying orbitals. Molecular orbitals of the HOMO – HOMO-4 span the entire anion, indicating that Mo may be mediating interactions between the two cyclophophide units, which has been proposed in other transition-metal pnictide complexes. The LUMO is largely localized to the $[Mo_2P_{10}]^{2+}$ portion of the cluster.

Wiberg bond indices, which indicate the number of electron groups bound to a given atom, are consistent with the electronic description of bonding from both cyclo-P_n ligands to the Mo centers. Binding of formally negative P4 and P9 to each Mo in a μ_2 fashion is indicated through a larger bond order of 3.6 for these atoms, as compared to an

average of 3.14 for other P atoms, each of which is bound to three other groups. Calculated Mo-P bond distances are in excellent agreement with bond distances in the solid-state structure. Bader charges calculated through both molecular and periodic methodologies each give an expected total charge for the cluster (-4.0 for molecular, 0 for periodic), yet the individual charges differ significantly for P atoms. Typically, molecular methods for computing electron densities are more reliable than periodic charges, and will be further discussed.

Table 5.5: Results from Wiberg Bond Index calculations and Bader charge analyses on **5.1**. Bond Lengths in [Å].

Atom	Wiberg Index	Calculated d(Mo-P) [Å]	Measured d(Mo-P) [Å]	Bader Charge (Molecular)[a]	Bader Charge (Periodic)[b]
Mo1	7.2379	----	----	1.5868	1.53816
Mo2	7.2379	----	----	1.5877	1.54908
P1	3.1425	2.54	2.559(6)	-0.4642	-0.25022
P2	3.1425	2.54	2.526(5)	-0.4503	-0.30849
P3	3.1144	2.61	2.517(5)	-0.4205	-0.22426
P4	3.6008	2.60	2.554(5)	-0.4770	-0.40586
P5	3.1891	2.54	2.486(5)	-0.4443	-0.23115
P6	3.1440	2.50	2.560(5)	-0.4391	-0.21850
P7	3.1440	2.54	2.564(5)	-0.4380	-0.22044
P8	3.1891	2.54	2.460(5)	-0.4445	-0.23553
P9	3.6008	2.65	2.559(5)	-0.4787	-0.39996
P10	3.1891	2.54	2.492(5)	-0.4448	-0.24741
P11	3.1440	2.50	2.547(5)	-0.4451	-0.24807
P12	3.1440	2.54	2.557(5)	-0.4458	-0.24622
P13	3.1891	2.50	2.477(5)	-0.4517	-0.24173
P14	3.1425	2.54	2.565(5)	-0.4663	-0.25907
P15	3.1425	2.54	2.500(5)	-0.4497	-0.30849
P16	3.1144	2.61	2.524(5)	-0.4205	-0.22394
Na1	---	---	---	---	0.32452
Na2	---	---	---	---	0.32425
Na3	---	---	---	---	0.26640
Na4	---	---	---	---	0.26657
Total				-4.006	-0.00036

Charge densities for Bader Charge Analysis Code (Henkelman group) generated from [a] Molecular calculation in Gaussian and [b] Periodic calculation in Quantum Expresso using four Na^+ as counterions

Using the molecular method for calculating Bader charges, all P atoms have a formal charge around -0.5, differing from the assigned values of zero for P=P and 1^- for P4 and P9, but still in good agreement. Dual coordination to Mo centers, and therefore partial electron transfer, most likely decreases formal charge for P4 and P9. This is also reflected in the charge of Mo, which is reduced to +1.5 from the assigned +2.0.

5.2.5.2 Molecular Orbital Calculations on $[Rh_3As_{16}]^{3-}$

Density functional theory (DFT) calculations for **5.2** were performed with a Def2-TZVP basis set in Gaussian 09, using the crystallographic structure as an initial model. Wiberg Bond Index (WBI) calculations and charge density input for Bader Charge Analyses were performed in Gaussian 09. Results are shown in Figure 5.13 and Table 5.6.

Anion **5.2** has an electron count of 110 e^- per cluster, and is predicted to be diamagnetic. This ion is C_{3v}-symmetric in the solid-state, but distorts to C_1 symmetry when solvation is used in calculations. In a dielectric constant similar to ethylenediamine, HOMO-2 (e) and HOMO-3 (a_2) invert (Figure 5.11). The HOMO-LUMO gap is 1.30 eV. The doubly degenerate HOMO is comprised mainly of As-As and As-Rh σ bonding. Evidence of Rh-Rh bonding is shown in the a_1 HOMO-1. Indications of As-As π bonding is present in the lower energy orbitals.

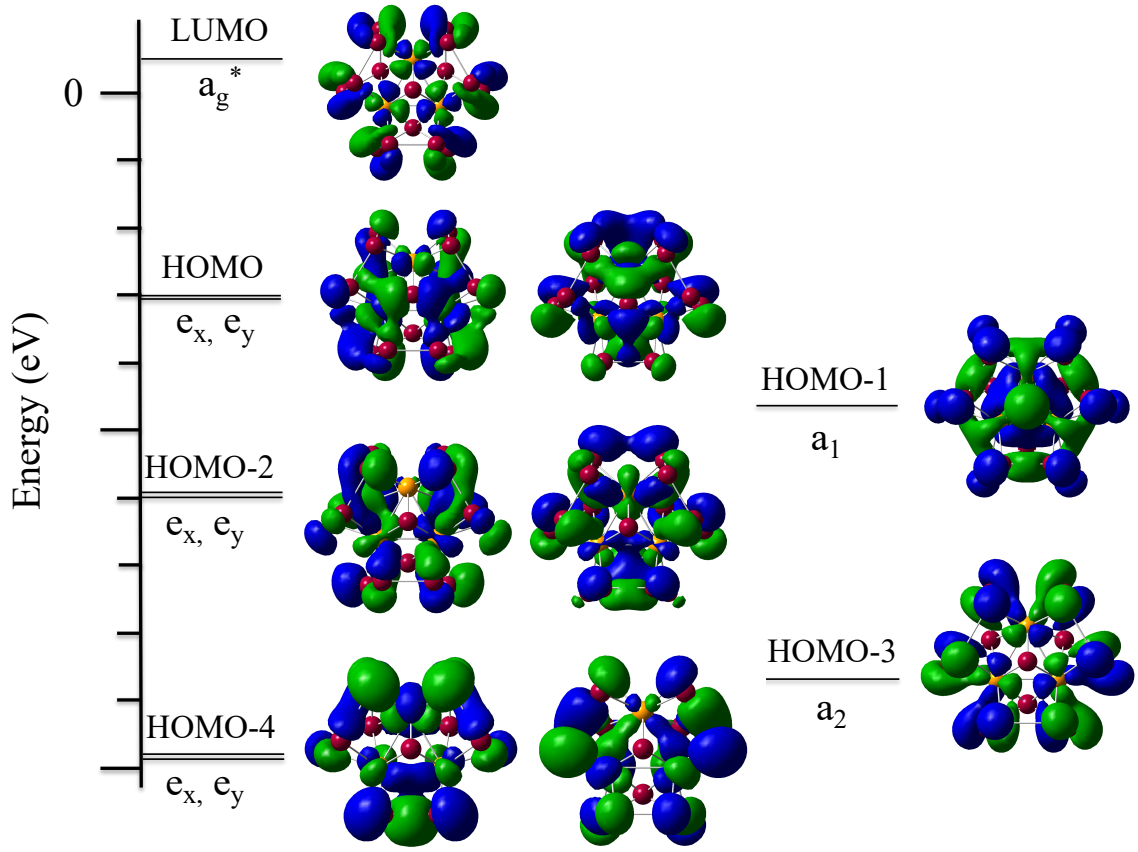

Figure 5.13: A simplified molecular orbital depiction of the frontier orbitals of **5.2**. Calculated energy values are shown for the LUMO ($3t_2^*$) down to HOMO -4, with a HOMO-LUMO gap of 1.30 eV.

Wiberg bond indices, similar to a calculation of bond order, and Bader partial charges are in excellent agreement with the description of bonding derived from the solid-state structure and isolobal analogies. Partial charges of all atoms are close to zero, with Rh partial charges being positive, and all As partial charges negative. These calculated partial charges may differ in magnitude from those described previously due to the small electronegativity difference between Rh (2.0) and As (2.2), implying that charges from the As atoms are assuaged by a positive charge on the Rh. The magnitude of these partial charges still support the overall bonding description using the Zintl-Klemm formalism.

Table 5.6: Results from Wiberg Bond Index calculations and Bader charge analyses on **5.2**. Bond Lengths in [Å].

Atom	Wiberg Index	Bader Partial Charges
Rh1	4.4547	0.02353
Rh2	4.4533	0.02832
Rh3	4.4533	0.02815
As1	3.1214	-0.21497
As2	3.1626	-0.19463
As3	3.1627	-0.19402
As4	3.1215	-0.21673
As5	3.1861	-0.15732
As6	3.1219	-0.22066
As7	3.1628	-0.21133
As8	3.1628	-0.17936
As9	3.1219	-0.21749
As10	3.1863	-0.15727
As11	3.1215	-0.21700
As12	3.1627	-0.19622
As13	3.1626	-0.19265
As14	3.1214	-0.21675
As15	3.1861	-0.15775
As16	3.1861	-0.12584
	Total	-2.98999

5.3 Discussion

The binary anion $[Mo_2P_{16}]^{4-}$, **5.1**, is the first highly ligand-free Mo polyphosphide. This cluster indicates that methodologies used to form binary anions of heavier Group 15 congeners As and Sb may also be viable methods for TM / phosphide anion syntheses. The subunits of **5.1** have been reported elsewhere from transition-metal mediated activation of P_4. Cyclo-P_3 – TM subunits were reported in the 1970's as products from reactions of white phosphorus with metal complexes, and have been well-studied, particularly for their use as phosphorus transfer reagents. [93,94,157] This is only the second instance of *cyclo*-P_3 formation from reactions of a $[P_7]^{3-}$ anion, and bond distances /

geometries are consistent with reported values. The cyclo-P_{10} ligand, previously reported in the organometallic structure $[(Cp^*Mo)_2((\mu_2,\eta^3{:}\eta^3\text{-}P_{10})]$, was characterized as a trace impurity in the crystal structure of the major product, $[(Cp^*Mo)_2(\mu_2,\eta^6{:}\eta^6\text{-}P_6)]$, formed from thermolysis of $[Cp^*Mo(CO)_{2/3}]_2$ with P_4. [158] This illustrates the ability of Zintl polyanions to undergo similar transformations leading to product types formerly only isolable through activation of P_4.

The anion **5.1** can be deconstructed to a $[Mo_2P_{10}]^{2+}$ unit bearing the same symmetry. Bonding between a single Mo and the cyclo-P_{10} ring bears some relationship to the $[MoPn_8]^{n-}$ (Pn = As, Sb ; n = 2, 3) structures, as shown in Figure 5.14. Each $[MoPn_8]^{n-}$ structure is described through Zintl formalisms as an Mo^{6+}/ Mo^{5+} encapsulated in a Pn_8^{8-} ring that is arranged in the configuration of S_8. Bond angles for the series are only similar at the negatively charged P4 and P9 (~89.7˚), which is comparable to the average angle for $[MoAs_8]^{2-}$ and $[MoSb_8]^{2-}$ (90.6˚ and 84.7˚, respectively). [73] Moreover, Mo-P distances (av. 2.521 Å) are consistent with expected values when compared to congeners Mo-As (av 2.566 Å) and Mo-Sb (2.826 Å). Several other species of $[MAs_8]^{3-}$ (Cr, Nb) and $[NbSb_8]^{3-}$ have been isolated, which show the ability of the Pn_8 rings to expand and contract as necessary to accommodate various metal centers. Limits to this expansion might dictate the existence of certain species, and explain why $[CrSb_8]^{n-}$ has yet to be isolated. These same principles may help rationalize why the analogous P_8^{8-} rings have not been characterized, as P-P single bonds (2.2 Å) may be too short to arrange in a cyclo-S_8 type structure while surrounding a transition metal.

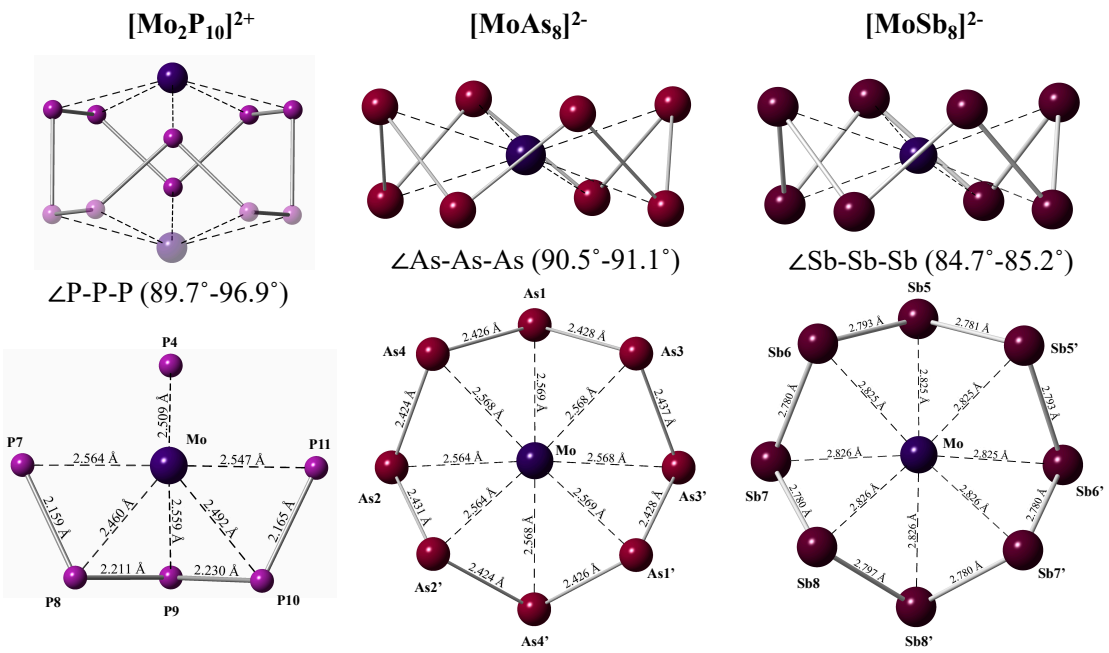

Figure 5.14: Comparisons of (a) $[Mo_2P_{10}]^{2+}$ unit and coordination of a single Mo center as $[MoP_6]^{n+}$ with the crown-like (b) $[MoAs_8]^{2-}$ and (c) $[MoSb_8]^{3-}$ anions.

The organization of $[K(2,2,2\text{-crypt})]^+$ and **5.1** in the solid state lattice is highly ordered (Figure 5.2), exhibiting hexagonal arrangements of the cations both above and below anionic clusters, similar to the ordering seen in other Zintl intermetalloid species such as $[Pt@Pb_{12}]^{2-}$.[159,160] These systems illustrate the ability to assemble naked binary anions into 3-dimensional ionic networks, garnering further interest in their potential use in assembled cluster materials.

Along with the clusters $[(\eta^4\text{-}As_7)Co(\eta^3\text{-}As_3]^{3-}$ (**3.1**), $[(\eta^4\text{-}As_7)Rh(COD)]^{2-}$ (**3.2**), $[(\eta^4\text{-}As_7)Ir(COD)]^{2-}$ (**3.3**), and binary intermetalloid $[Rh_3As_{16}]^{3-}$ (**5.2**) is a rare example of Group 9 / As systems, and, to our knowledge, is the first known Rh-As binary. The intermetalloid $[Rh_3As_{16}]^{3-}$ is unprecedented in its overall structure and the conformation of its subunits, particularly cyclo-As_5^{1-}. The monoanionic cyclopentapolyarsenide, As_5^{1-}, adopts an envelope configuration, and is relatable to CpH (C_5H_6) through isolobal analogy and the Zintl-Klemm formalism. This feature has only been reported in the

intermetalloid **5.2**, representing a new structural subunit possible for polyarsenic ligands. Highly charged *cyclo*-Pn_5^{5-} (Pn = P, As, Sb) also exhibiting a non-planar arrangement of Pn atoms have been characterized. [154,161] While the structures of *cyclo*-Pn_5^{5-} and *cyclo*-As_5^{1-} may initially appear similar, they are quite different in electronic structure. Pn_5^{5-}, bearing a high formal charge on each Pn atom, are more directly analogous to the crown-like Pn_8^{8-} units in $[MPn_8]^{n-}$ anions (M = Cr, Nb, Mo ; Pn = As ; n = 3, 2. M = Nb, Mo ; Pn = Sb, n = 3).

Triangulo-Rh cores with bridging ligands (both μ_2 coincident to the Rh-Rh-Rh plane and μ_3 coordination above and below the plane) are common, and this feature has been reported in structures $[Rh_3(\mu_2\text{-}P(^tBu)_2)_3(CO)_3]$, $[Rh_3(\mu_3\text{-}S)_2(CO)_6]^{1-}$, $[Rh_3(\mu_3\text{-}Se)_2(CO)_6]^{1-}$ (See Table 5.2).[151-153] These clusters, all containing Rh in a formal +1 oxidation state, exhibit Rh-Rh bond distances of 2.64 Å - 3.16 Å, demonstrate that the Rh-Rh interatomic distance is not solely determined by the metal oxidations state, but partially by size and steric impositions of the bridging ligands. Few examples have been reported with Rh coordination to As, with the exception of larger clusters, such as $Rh_6(\mu_2\text{-}As(^tBu)_2)(\mu_4\text{-}As^tBu)(CO)_{11}$. A greater number of Rh-As and Rh-L bonding environments, leading to a mixed-valent Rh system, is reflected in the range of Rh-Rh and Rh-L bond distances.

Comparisons of structural features of **5.2** with those of known intermetalloid species $[Ni_5Sb_{17}]^{4-}$, $[Pd_7As_{16}]^{4-}$, and the largest, most highly symmetric class of binary anion, $[E@M_{12}@E_{20}]^{n-}$ (E = As, Sb ; M = Ni, E = Sb, M = Pd) reveals some general similarities. Each cluster contains transition metals coordinated to at least five pnictogen elements, flanked by subunits resembling cyclo-E_5 in various configurations (Figure

5.15). Building to the $[E@M_{12}@E_{20}]^{n-}$ anion, the ratio of Pn:Tm decreases (5.33:1 Rh:As ; 4.25 Sb:Ni ; 2.28 As:Pd ; 1.75 Sb:Pd) and elongation / breaking of Pn-Pn bonds occurs.

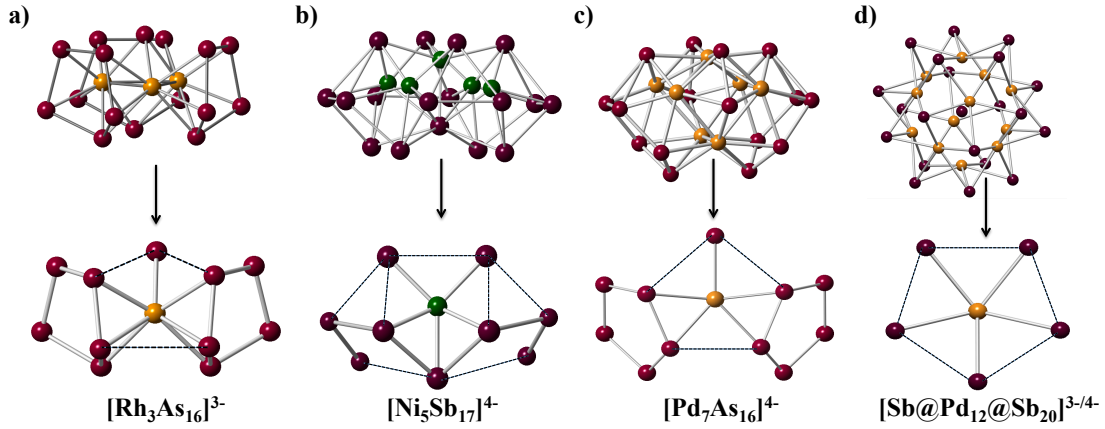

Figure 5.15: Structural comparisons of intermetalloids $[Rh_3As_{16}]^{3-}$, $[Ni_5Sb_{17}]^{4-}$, $[Pd_7As_{16}]^{4-}$, and $[Sb@Pd_{12}@Sb_{20}]^{3-/4-}$.

Heterometallic clusters **5.1** and **5.2** differ markedly not only in the arrangement of their 16 pnictide elements, but in electronic description when compared to $[Pd_7As_{16}]^{4-}$ and $[Ni_5Sb_{17}]^{4-}$ clusters. The Zintl-Klemm pseudoelement concept, while apt for describing bonding in the subunits of **5.1** and **5.2**, is difficult to implement for other intermetalloid species, such as those listed above, and a bond-valence formalism must be invoked to partially describe electron distribution and atom interactions / oxidation states. The Bader partial charges calculated for **5.1** and **5.2** are both in agreement with the charge models deduced from solid-state structures, but depict a more covalent bonding scheme, where large negative partial charges assigned to the main group element are alleviated by the positive charges on the transition metal. The overall description of bonding is still corroborated by quantum calculations.

Within clusters **5.1** and **5.2**, an analogy can be drawn between As_5^{1-} and P_{10}^{2-} subunits, where proposed rearrangement of P-P bonds leads to formation of two *cyclo*-P_5^{1-} moieties in envelope configurations, analogous to As_5^{1-}.

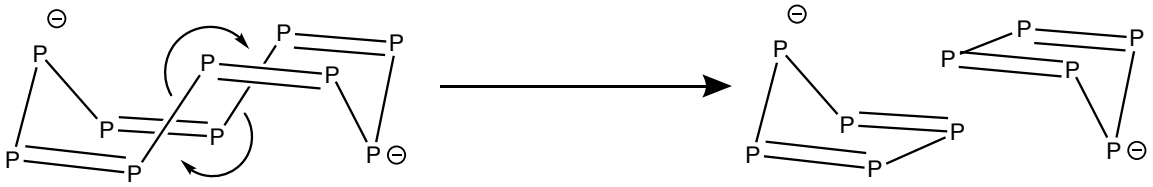

Scheme 5.1: Proposed interconversion between *cyclo*-$[P_{10}]^{2-}$ and *cyclo*-$[P_5]^{1-}$.

The clusters **5.1** and **5.2** are the first binaries of Mo/P and Rh/As pairs. The As_5^{1-} and P_{10}^{2-} moieties are novel features in intermetalloid clusters. Continued investigations on the behavior of these complexes will give further insight into descriptions of structure and bonding.

5.4 Experimental Section

5.4.1 General Considerations

Reactions were performed in a dedicated glovebox (Vacuum Atmospheres Co.) under an inert atmosphere of anhydrous dinitrogen / argon, or manipulated under an inert atmosphere using standard Schlenk techniques and glassware. Melts of nominal composition "K_3As_7" and "K_3P_7" were prepared via high-temperature fusion of the elements with an oxygen / natural gas flame in sealed, evacuated quartz tubes, which were kept under inert gas during fusion through a Schlenk line adapter. ***CAUTION****:* Formation of Zintl alloys is highly exothermic. Alkali polyphosphorus compounds are known to spontaneously detonate, even under rigorous anaerobic conditions. Quantities should be limited to under 500 mg at all times, with use of proper PPE and blast-proof barriers. Anhydrous ethylenediamine (en) (99.98%, Sigma Aldrich) was distilled twice from K_4Sn_9, purified via long-path distillation, and stored over 3 Å molecular sieves under anhydrous dinitrogen. Toluene and benzene were purified by distillation from sodium / benzophenone under a dinitrogen atmosphere and stored over 3 Å molecular

sieves in a dinitrogen atmosphere. $[Rh(COD)Cl]_2$ (98%, Strem Chemicals) was purchased as a microcrystalline powder and used as received. $Mo(naph)_2$ was synthesized according to literature procedure[162] from $MoCl_5$, and used within ten days of preparation. 4,7,13,16,21,24-hexaoxa-1,10-diazobicyclo[8.8.8]hexacosane (2,2,2-crypt, >98%, TCI America) was dried under dynamic vacuum for 24 hours prior to use. Unless noted otherwise, all solutions and reactions were stirred with ½" magnetic glass-covered stir bars (Pyrex, purchased from Amazon.com, cleaned in a KOH / isopropanol bath, followed by dilute HCl wash, then dried overnight at 150 °C prior to use).

5.4.2 Synthesis of $[K(2,2,2\text{-crypt})]_4[Mo_2P_{16}]\bullet 0.5(en)$

In a 10 mL glass scintillation vial, K_3P_7 (109 mg, 0.330 mmol) and 2,2,2-crypt (377 mg, 1.01 mmol) were dissolved in 5.0 mL of ethylenediamine and stirred for 10 min at 25 °C to yield a yellow-brown solution. In a separate vial, dark violet crystals of $Mo(naph)_2$ (232 mg, 0.660 mmol) were dissolved in 1.0 mL benzene and 2.0 mL toluene, and stirred for 5 min at 25 °C, yielding a mauve slurry. The slurry was added dropwise to the $[P_7]^{3-}$ solution with vigorous stirring, resulting in a color change from yellow-brown to black. The formation of fine particulates was evident by changing opacity of the reaction solution, coupled with solid adhering to the reaction vessel near the solvent line. After stirring for 4 hours at room temperature, the reaction was filtered through 1 cm tightly packed glass wool to remove the very fine particulates of dark brown precipitate. The solution was filtered a second time through 1 cm tightly packed glass wool directly into a clean test tube, then layered with ~ 2 mL dry benzene. After fourteen days, nearly all solution-phase ions had crystallized, as evidenced by a clear, colorless supernatant and fine dark brown – black needles. Upon further inspection, individual needles were aggregates comprised of hundreds of dark rhombohedral microcrystals of

$[K(2,2,2\text{-crypt})]_4[Mo_2P_{16}]\cdot 0.5(en)$. Due to the extremely small size of $[K(2,2,2\text{-crypt})]_4[Mo_2P_{16}]\cdot 0.5(en)$ crystals (largest dimension of a single crystal ≅ 0.1 μm), difficulties were encountered when harvesting and weighing the product. Therefore, yield was approximated at ≅ 130 mg, 38.2 % based on precursor K_3P_7 as a limiting reagent (Theoretical yield = 340 mg).

5.4.3 Synthesis of $[K(2,2,2\text{-crypt})]_3[Rh_3As(As_5)_3]\cdot 0.5(tol)$

In a 10 mL scintillation vial, K_3As_7 (130.2 mg, 0.203 mmol) and 2,2,2-crypt (231.1 mg, 0.615 mmol) were dissolved in 4 mL of ethylenediamine, producing a deep rust-colored solution. This solution was stirred for 10 min at 55 °C. In a separate vial, $[Rh(COD)Cl]_2$ (25.0 mg, 0.510 mmol) was dissolved in 1 mL toluene and stirred for 5 min at 55 °C to produce a vibrant orange solution. The $[Rh(COD)Cl]_2$ solution was added dropwise to the solution of $[As_7]^{3-}$. An immediate color change from deep red-orange to brown-black occurred, with a noticeable exotherm. An insoluble phase formed in the reaction mixture, which adhered to the vessel walls as a dark brown oil. The reaction was heated with vigorous stirring for 45 min at 55 °C, followed by 15 min at 80 °C, when noticeable darkening and homogenization of the solution occurred. The reaction was hot filtered through 1 cm tightly packed glass wool into a clean glass test tube. The $[K(2,2,2\text{-crypt})]^+$ salt of **5.2** formed from filtered reaction solutions that were layered with toluene (after 5 days) and non-layered solutions (7 days). The largest and highest quality crystals were isolated from untreated solutions that were slow-cooled to 25 °C following filtration of hot (80 °C) reaction solution, while maximum crystalline yield was obtained from reaction solutions layered with toluene. Product: $[K(2,2,2\text{-crypt})]_3[Rh_3As(As_5)_3]\cdot 0.5(tol)$. Yield = 116 mg, 47.2 % based on K_3As_7 as limiting reagent (Theoretical yield = 246 mg).

5.4.4 Crystallographic Studies

Single crystal data collections were performed at ChemMatCARS Sector 15-B of the Advanced Photon Source (APS) of Argonne National Laboratory (ANL) and in the X-Ray Crystallographic Center (XCC) at UMD. At APS, suitable single crystals of $C_{145}H_{292}K_8Mo_4N_{17}O_{48}$ (UMAPS-216-4-LS) and $C_{57.5}H_{112}As_{16}K_3N_6O_{18}Rh_3$ (UMAPS-216-3-LS) were analyzed using a Huber three-circle diffractometer (κ-angle offset of 60º) equipped with a Dectris PILATUS3X CdTe 1M detector. The crystals were kept at 150(2) K during data collection, and the distance between the crystal and detector was 130 mm. A custom-designed software was used for data collection, and frames were converted to Bruker-compatible format for data processing in *APEX II / APEX III*. At UMD, suitable single crystals of $C_{57.5}H_{112}As_{16}K_3N_6O_{18}Rh_3$ (UM3028) were selected and measured on a Bruker Smart Apex2 CCD diffractometer. The crystals were kept at 120(2) K during data collection.

In all cases, integral intensity data were corrected for absorption using the multi-scan method of SADABS software. Structures were solved with the ShelXT-2014 program and refined with the ShelXL-2015 program and least-square minimization using ShelX software package. Crystals of $C_{145}H_{292}K_8Mo_4N_{17}O_{48}$ were extremely small, and sustained radiation damage during the second scan of data collection in all attempts. This was accounted for during integration in SAINT, but both factors contributed to a high R-factor for this structure. Disorder was present in crystals of $C_{57.5}H_{112}As_{16}K_3N_6O_{18}Rh_3$, both in the cluster and in $[K(2,2,2\text{-crypt})]^+$ cations. All disorder was successfully modeled.

5.4.5 Laser Desorption / Ionization time-of-flight mass spectrometry

Laser Desorption / Ionization time-of-flight mass spectrometry (LDI-TOF MS) and Matrix-Assisted Laser Desorption/Ionization time-of-flight mass spectrometry (MALDI-TOF MS) analyses were performed on a Bruker Autoflex Speed in negative ion mode with a 2 KHz "Smart Beam II" nitrogen laser. The wavelength during analysis was 337 nm, with frequency of 10 Hz, and pulse power varying between 80 – 130 μJ. For LDI analyses, crystals of $[K(2,2,2\text{-crypt})]_4[Mo_2P_{16}]\cdot 0.5(en)$ and $[K(2,2,2\text{-crypt})]_3[Rh_3As_{16}]\cdot 0.5(tol)$ were loaded directly onto the target plate with carbon tape. Direct desorption from the crystalline samples at high laser pulse energies resulted in mass shifts of the ions to higher *m/z* due to distorted electric fields. Lowering the laser pulse energies decreased the mass shift, but subsequently decreased signal intensity for the entire spectrum. The parent ion was not observed from LDI-TOF MS analyses on crystals of $[K(2,2,2\text{-crypt})]_3[Rh_3As_{16}]\cdot 0.5(tol)$, though peaks attributed to fragmentation of the parent cluster were present. Using dry DMF as a matrix, the monoanionic parent ion, $[Rh_3As_{16}]^{1-}$ (*m/z* =1507.46 amu), and several higher mass fragments were observed. Using an organic matrix of naphthalene THF:Tol (50:50 v:v) or bis(1,8-dimethylamino)naphthalene in CH_3CN:THF (75:25 v:v) resulted in amplification of the signal by up to three orders of magnitude, with superior signal-to-noise ratios at higher mass ranges (*m/z* = 1500 – 3500 amu). Mass shifting at higher energies still persisted, and were corrected in the reported spectra. Mass envelopes were fit by using a quadratic peak fitting method to calibrate expected mass fragment values to observed values at six different positions at low (*m/z* = 400 – 600 amu), intermediate (*m/z* = 600 – 1500 amu), and high (*m/z* = 1500 – 3500 amu) mass ranges. The peak position and full width at half

maximum (FWHM) values were fixed before calibration, as calculated by Mmass Software Version 5.4.1 for Mac OSX.

5.4.6 Electron Dispersive X-Ray Spectroscopy (EDX) Analysis

Crude elemental analysis was performed for crystals of $[K(2,2,2\text{-crypt})]^+$ salts of **5.1** and **5.2** through point scan analysis at the center of air-oxidized target crystals via electron dispersive X-ray (EDX) spectroscopy. EDX analyses for all samples was performed on a Hitachi SU-70 SEM, operated at an acceleration voltage of 15 kV. Data acquisition was performed with accumulation intervals of 120 s. For cluster **5.2**, elemental mapping was performed to confirm that Rh, As, K were homogeneously distributed throughout remnants of the solid-state structure.

6.1 Appendix A – Group 15 Zintl Anions Isolated from Solution and Solid-State Methods

Table A1: Structurally characterized homoatomic chain, ring, and cage motifs for Polyanions of Group 15 Zintl Ions of P, As, Sb, Bi. Synthetic methods (solution-based [a] or solid-state [b]) are indicated.

Structure	Pnictide	Compound	Synthetic Method	Reference
$[Pn_2]^{2-}$	Bi	$[K(2,2,2\text{-crypt})]_2Bi_2$	a, b	163
		Cs_3Bi_2	b	164
$[Pn_3]^{3-}$	As	Cs_3As_3	b	165
$[Pn_3]^{4-}$	P	K_4P_3	b	166
$[Pn_3]^{5-}$	P	KBa_4P_5	b	167
$[Pn_4]^{2-}$	P	$Cs_2P_4 \cdot 2NH_3$	a	48,168
		$[K(18\text{-crown-6})]_2P_4 \cdot 8.5NH_3$	a	169
	As	$[Li(NH_3)_4]_2As_4$	a	170
		$[Na(NH_3)_5]_2As_4 \cdot 3NH_3$	a	170
		$[Cs_{0.35}Rb_{0.65}(2,2,2\text{-crypt})]_2As_4 \cdot 2NH_3$	a	170
	Sb	$[K(2,2,2\text{-crypt})]_2Sb_4$	a	171
	Bi	$[K(2,2,2\text{-crypt})]_2Bi_4$	a	53
		$[A(2,2,2\text{-crypt})]_2Bi_4$ (A = K, Rb)	a	172
$[Pn_4]^{4-}$	As	A_5As_4 (A = K, Rb, Cs)	b	173
	Sb	A_5Sb_4 (A = K, Rb, Cs)	b	174,175
	Bi	A_5Bi_4 (A = K, Rb, Cs)	b	176
$[Pn_4]^{6-}$	P	Ae_3P_4 (Ae = Ca, Sr, Ba)	b	177
	As	Ae_3As_4 (Ae = Ca, Sr, Ba)	b	178,179
	Bi	$K_6Bi_4 \cdot 8NH_3$	a	180
$[Pn_5]^{-}$	P	NaP_5 / THF solutions	a	58,181,182
$[Pn_5]^{5-}$	As	ABa_2As_5 (A = K, Rb)	b	183
	Sb	$[Li(NH_3)_4]_3[Li(NH_3)]_2Sb_5 \cdot 2NH_3$	a	184
$[Pn_6]^{4-}$	P	K_4P_6	b	185
		Rb_4P_6	b	186,187
		Cs_4P_6	b	187
	As	A_4As_6 (A = Rb, Cs)	b	188
		$[Rb(18\text{-crown-6})]_2Rb_2As_6 \cdot 6NH_3$	a,b	49
$[Pn_6]^{8-}$	Sb	Ae_2Sb_3 (Ae = Ba, Sr)	b	189
$[Pn_7]^{3-}$	P	Li_3P_7	b	190
		A_3P_7 (A = Na, K, Rb)	b	191
		Cs_3P_7	b	191,192
		Sr_3P_{14}	b	193
		Ba_3P_{14}	b	194
		$[Li(TMEDA)]_3P_7$	a,b	195
		$Cs_3P_7 \cdot 3NH_3$	a,b	196
		$Rb_3P_7 \cdot 7NH_3$	a,b	168
		$Ba_3(P_7)_2 \cdot 18NH_3$	a,b	197
		$[NEt_3Me]Cs_2P_7 \cdot NH_3$	a,b	198
		$[NEt_4]Cs_2P_7 \cdot 4NH_3$	a,b	198

Structure	Pnictide	Compound	Synthetic Method	Reference
		$[NEtMe_3]Cs_2P_7 \cdot 2NH_3$	a,b	199
		$[NMe_4]_2RbP_7 \cdot NH_3$	a,b	200
		$[Rb(18\text{-crown-}6)]_3P_7 \cdot 6NH_3$	a,b	169
		$K_3[K(18\text{-crown-}6)]_3P_{72} \cdot 10NH_3$	a,b	169
	As	Li_3As_7	b	201
		Na_3As_7	b	202
		K_3As_7	b	199
		Rb_3As_7	b	199,203
		Cs_3As_7	b	167
		Ba_3As_7	b	204
		$[Li(TMEDA)]_3As_7 \cdot 1.5tol$	a,b	205
		$[Li(NH_3)_4]_3As_7 \cdot NH_3$	a,b	206
		$Cs_3As_7 \cdot 6NH_3$	a,b	206
		$Cs_3As_7 \cdot NH_3$	a,b	207
		$[Li(TMEDA)]_3As_7 \cdot OEt_2$	a,b	208
		$[Li(DME)]_3As_7 \cdot OEt_2$	a,b	199
		$[NMe_4]_2RbAs_7 \cdot NH_3$	a,b	209
		$[Rb(18\text{-crown-}6)]_3As_7 \cdot 8NH_3$	a,b	206
		$[PPh_4]_2CsAs_7 \cdot 5NH_3$	a,b	206
		$[K(2,2,2\text{-crypt})]_3K_3As_{72}$	a,b	210
	Sb	Rb_3Sb_7	b	211
		Cs_3Sb_7	b	211,212
		$[Li(TMEDA)]_3Sb_7 \cdot tol$	a,b	213
		$[Na(2,2,2\text{-crypt})]_3Sb_7$	a,b	214
		$Na_3Sb_7 \cdot 4en$	a,b	215
		$[Na(TMEDA)]_3Sb_7 \cdot 3THF$	a,b	205
		$[Li(NHMe_2)_2]_3Sb_7$	a,b	213
		$[Li(TMEDA)]_3Sb_7 \cdot 3tol$	a,b	213
		$[K(2,2,2\text{-crypt})]_3Sb_7 \cdot 2en$	a,b	171
		$[Na(PMDETA)]_3Sb_7 \cdot tol$	a,b	216
		$[Rb(18\text{-crown-}6)]_3Sb_7 \cdot 4NH_3$	a,b	217
	Bi	$[K(2,2,2\text{-crypt})]_3Bi_7 \cdot 2py$	a	218
$[Pn_8]^{8-}$	Sb	$K_{17}(NH_2)(Sb_8)_2 \cdot 17.5NH_3$	a	219
$[Pn_8]^{10-}$	As	Ca_2As_3	b	199
$[Pn_9]^{10-}$	P	Ba_5P_9	b	199
$[Pn_{11}]^{3-}$	P	Na_3P_{11}	b	220
		A_3P_{11} (A = K, Rb, Cs)	b	221
		$[NEtMe_3]_4P_{11}$	a,b	222
		$Cs_3P_{11} \cdot 3NH_3$	a,b	199
		$BaCsP_{11} \cdot 11NH_3$	a,b	223
		$Cs[NEt_3Me]_2P_{11} \cdot 5NH_3$	a,b	224
		$[NEt_4]_3P_{11}$	a,b	225
		$[K(18\text{-crown-}6)]_3P_{11} \cdot 2en$	a,b	226
	As	K_3As_{11}	b	221

Structure	Pnictide	Compound	Synthetic Method	Reference
		A_3As_{11} (A = Rb, Cs)	b	165,221
		$[K(2,2,2\text{-crypt})]_3As_{11}$	a,b	51
		$[Cs(18\text{-crown-}6)]_2CsAs_{11}\cdot 8NH_3$	a,b	51
	Sb	$[Na(2,2,2\text{-crypt})]_3Sb_{11}$	a	57
		$[K(18\text{-crown-}6)(NH_3)_2]Sb_{11}\cdot 5.5NH_3$	a	51
		$[K(2,2,2\text{-crypt})]_3Sb_{11}$	a	199
		$[Li(12\text{-crown-}4)]_3Sb_{11}$	a	227
	Bi	$[K(2,2,2\text{-crypt})]_3Bi_{11}\cdot 2py\cdot tol$	a	228
$[Pn_{14}]^{4-}$	P	$Na_4(DME)_{7.5}P_{14}$	a	229
		$[Na(en)_{1.5}]_4P_{14}$	a	229
		$[Li(NH_3)_4]_4P_{14}\cdot NH_3$	a	169
	As	$[Rb(18\text{-crown-}6)]_4As_{14}\cdot 6NH_3$	a	169
$[Pn_{16}]^{2-}$	P	$[Na(18\text{-crown-}6)]_2P_{16}$	a	58
		$[PPh_4]_2P_{16}$	a	230
$[Pn_{19}]^{3-}$	P	Li, Na, K in DMF, THF or DME	a	231
$[Pn_{21}]^{3-}$	P	Li or Na solutions	a	232
		$[Li(12\text{-crown-}4)_2]_3P_{21}\cdot 2THF$	a	233
$[Pn_{22}]^{4-}$	P	$[NEtMe_3]_4P_{22}\cdot 2NH_3$	a	199
	As	$[Rb(2,2,2\text{-crypt})]_4As_{22}\cdot 4DMF$	a	234
$[Pn_{26}]^{4-}$	P	$Li_4P_{26}\cdot 16THF$	a	235

References

(1) Mittelbach, A.; Hoenle, W.; Schnering, Von, H. G.; Carlsen, J.; Janiak, R.; Quast, H. *Angew. Chem.* **1992**, *104* (12), 1681–1683. (See also *Angew. Chem., Int. Ed. Engl.*, **1992**, *31* (12), 1642–1643).

(2) Von Schnering, H. G.; Hoenle, W.; Mittelbach, A.; Carlsen, J.; Janiak, R.; Quast, H. Max-Planck-Gesellschaft zur Foerderung der Wissenschaften e.V., Germany. January 27, 1994, pg 13.

(3) Kellner, R.; Berger, N.; Stockle, R.; Vaas, K.; Soylemez, S.; Pfitzner, A.; Binder, H.; Hönle, W.; Grin, Y.; Burkhardt, A.; Schultheiss, M.; Wedig, U.; Nuss, J.; Schnering, Von, H. G.; Borrmann, H.; Simon, A. *Spec. Publ. - R. Soc. Chem.* **1997**, *201* (Advances in Boron Chemistry), 38–45.

(4) Wade, K. *Adv. Inorg. Chem. Radiochem.* **1976**, *18*, 1–66.

(5) Atwood, D. A.; Roesky, H. W. **2007**, 1–215.

(6) King, R.B.; Robinson, G.H. *J. Organomet. Chem.* **2000**, *597*, 54-60.

(7) Aldridge, S.; Downs, A. J. *The Group 13 Metals Aluminum, Gallium, Indium, and Thallium: Chemical Patterns and Peculiarities*; Aldridge, S., Downs, A. J., Eds.; 2011.

(8) Von Schnering, H. G. *Nova Acta Leopold.* **1985**, *59* (264), 165–182.

(9) Schaefer, H.; Eisenmann, B.; Mueller, W. *Angew. Chem.* **1973**, *85* (17), 742–760.

(10) Vidovic, D.; Aldridge, S. *Chem. Sci.* **2011**, *2* (4), 601–608.

(11) Minasian, S. G.; Krinsky, J. L.; Rinehart, J. D.; Copping, R.; Tyliszczak, T.; Janousch, M.; Shuh, D. K.; Arnold, J. *J. Am. Chem. Soc.* **2009**, *131* (38), 13767–13783.

(12) Minasian, S. G.; Krinsky, J. L.; Williams, V. A.; Arnold, J. *J. Am. Chem. Soc.* **2008**, *130* (31), 10086–10087.

(13) Roesky, P. W. *Dalton Trans.* **2009**, *28* (11), 1887–1888.

(14) Gemel, C.; Steinke, T.; Cokoja, M.; Kempter, A.; Fischer, R. A. *Eur. J. Inorg. Chem.* **2004**, *2004* (21), 4161–4176.

(15) Schnöckel, H. *Chem. Rev.* **2010**, *110* (7), 4125–4163.

(16) Schnepf, A.; Schnöckel, H. *Angew. Chem. Int. Ed.* **2002**, *41*, 3532–3552.

(17) Bassler, J. M.; Timms, P. L.; Margrave, J. L. *J. Chem. Phys.* **1966**, *45* (7), 2704–2706.

(18) Timms, P. *J. Am. Chem. Soc.* **1966**, *89* (7), 1629.

(19) Schiefer, M.; Reddy, N. D.; Roesky, H. W.; Vidovic, D. *Organometallics* **2003**, *22* (18), 3637–3638.

(20) Hardman, N. J.; Wright, R. J.; Phillips, A. D.; Power, P. P. *J. Am. Chem. Soc.* **2003**, *125* (9), 2667–2679.

(21) Asay, M.; Jones, C.; Driess, M. *Chem. Rev.* **2011**, *111* (2), 354–396.

(22) Jones, C. *Coordination Chemistry Reviews* **2010**, *254* (11-12), 1273–1289.

(23) Stender, M.; Eichler, B. E.; Hardman, N. J.; Power, P. P.; Prust, J.; Noltemeyer, M.; Roesky, H. W. *Inorg. Chem.* **2001**, *40* (12), 2794–2799.

(24) Schnitter, C.; Roesky, H. W.; Ropken, C.; Herbst-Irmer, R.; Schmidt, H.-G.; Noltemeyer, M. *Angew. Chem. Int. Ed.* **1998**, *37* (13), 1952–1955.

(25) Sitzmann, H.; Lappert, M.; Dohmeier, C.; Uffing, C.; Schnöckel, H. *Journal of Organometallic Chemistry* **1998**, *561*, 203–208.

(26) Uffing, C.; Baum, E.; Köppe, R.; Schnöckel, H. *Angew. Chem. Int. Ed.* **1998**, *37* (17), 2397–2400.

(27) Loos, D.; Baum, E.; Ecker, A.; Schnöckel, H.; Downs, A. J. *Angew. Chem. Int. Ed.* **1997**, *36* (8), 860–863.

(28) Uhl, W.; Hiller, W.; Layh, M.; Schwarz, A. D. *Angew. Chem. Int. Ed.* **1992**, *31*, 1364.

(29) Purath, A.; Köppe, R.; Schnöckel, H. *Angew. Chem. Int. Ed.* **1999**, *38* (19), 2926–2928.

(30) Purath, A.; Köppe, R.; Schnöckel, H. *Chem. Commun.* **1999**, *19*, 1933–1934.

(31) Köhnlein, H.; Purath, A.; Klemp, C.; Baum, E.; Krossing, I.; Stösser, G.; Schnöckel, H. *Inorg. Chem.* **2001**, *40* (19), 4830–4838.

(32) Köhnlein, H.; Stösser, G.; Baum, E.; Mollhausen, E.; Huniar, U.; Schnöckel, H. *Angew. Chem. Int. Ed.* **2000**, *39* (4), 799–801.

(33) Ecker, A.; Weckert, E.; Schnöckel, H. *Letters to Nature* **1997**, *387*, 1–3.

(34) Klemm, W.; Schnering, Von, H. G. *Z. Anorg. Allg. Chem.* **1982**, *491*, 9–26.

(35) Schnepf, A.; Stösser, G.; Schnöckel, H. *J. Am. Chem. Soc.* **2000**, *122* (38), 9178–9181.

(36) Schnepf, A.; Köppe, R.; Schnöckel, H. *Angew. Chem. Int. Ed.* **2001**, *40* (7), 1241–1243.

(37) Hartig, J.; Stößer, A.; Hauser, P.; Schnöckel, H. *Angew. Chem. Int. Ed.* **2007**, *46* (10), 1658–1662.

(38) Schnepf, A.; Stösser, G.; Schnöckel, H. *Angew. Chem. Int. Ed.* **2002**, *41* (11), 1882–1884.

(39) Vollet, J.; Burgert, R.; Schnöckel, H. *Angew. Chem. Int. Ed.* **2005**, *44* (42), 6956–6960.

(40) Schnepf, A.; Schnöckel, H. *Angew. Chem. Int. Ed.* **2001**, *40* (4), 711–715.

(41) Joannis, A. *Ann. Chim. Phys.* **1906**, *7* (viii), 5–118.

(42) Peck, E. B. *J. Am. Chem. Soc.* **1918**, *40* (2), 335–347.

(43) Fassler, T.; Miller, G. J. *Z. Anorg. Allg. Chem.* **2011**, *637* (13), 1935–1935.

(44) Scharfe, S.; Kraus, F.; Stegmaier, S.; Schier, A.; Fässler, T. F. *Angew. Chem. Int. Ed.* **2011**, *50* (16), 3630–3670.

(45) Eichhorn, B. *J. Am. Chem. Soc.* **1999**, *121* (22), 5352–5352.

(46) Fässler, T. F. In *Zintl Ions*; Structure and Bonding; Springer Berlin Heidelberg: Berlin, Heidelberg, 2011; Vol. 140, pp 91–131.

(47) Corbett, J. D.; Adolphson, D. G.; Merryman, D. J.; Edwards, P. A.; Armatis, F. J. *J. Am. Chem. Soc.* **1975**, *97* (21), 6267–6268.

(48) Kraus, F.; Aschenbrenner, J. C.; Korber, N. *Angew. Chem. Int. Ed.* **2003**, *42* (34), 4030–4033.

(49) Kraus, F.; Hanauer, T.; Korber, N. *Angew. Chem. Int. Ed.* **2005**, *44* (44), 7200–7204.

(50) Kraus, F.; Hanauer, T.; Korber, N. *Inorg. Chem.* **2006**, *45* (3), 1117–1123.

(51) Hanauer, T.; Korber, N. *Z. Anorg. Allg. Chem.* **2006**, *632* (7), 1135–1140.

(52) Critchlow, S. C.; Corbett, J. D. *Inorg. Chem.* **1985**, *24* (6), 979–981.

(53) Cisar, A.; Corbett, J. D. *Inorg. Chem.* **1977**, *16* (10), 2482–2487.

(54) Kuznetsov, A. N.; Fässler, T. F. *Z. Anorg. Allg. Chem.* **2002**, *628* (11), 2537–2541.

(55) Benda, C. B.; Köchner, T.; Schäper, R.; Schulz, S.; Fässler, T. F. *Angew. Chem. Int. Ed.* **2014**, *53* (34), 8944–8948.

(56) Reil, M.; Korber, N. *Z. Anorg. Allg. Chem.* **2007**, *633* (10), 1599–1602.

(57) Bolle, U.; Tremel, W. *J. Chem. Soc., Chem. Commun.* **1992**, *85* (2), 91–93.

(58) Baudler, M.; Duester, D.; Ouzounis, D. *Z. Anorg. Allg. Chem.* **1987**, *544*, 87–94.

(59) Sevov, S. C.; Goicoechea, J. M. *Organometallics* **2006**, *25* (24), 5678–5692.

(60) Turbervill, R. S. P.; Goicoechea, J. M. *Chem. Rev.* **2014**, *114* (21), 10807–10828.

(61) Turbervill, R. S. P.; Goicoechea, J. M. *Chem. Rev.* **2014**, *114* (21), 10807–10828.

(62) Wilson, R. J.; Weinert, B.; Dehnen, S. *Dalton Trans.* **2018**, *47* (42), 14861–14869.

(63) Eichhorn, B. W.; Haushalter, R. C.; Huffman, J. C. *Angew. Chem.* **1989**, *101* (8), 1081–1083.

(64) Charles, S.; Fettinger, J. C.; Bott, S. G.; Eichhorn, B. W. *J. Am. Chem. Soc.* **1996**, *118* (19), 4713–4714.

(65) Charles, S.; Eichhorn, B. W.; Rheingold, A. L.; Bott, S. G. *J. Am. Chem. Soc.* **1994**, *116* (18), 8077–8086.

(66) Charles, S.; Danis, J. A.; Mattamana, S. P.; Fettinger, J. C.; Eichhorn, B. W. *Z. Anorg. Allg. Chem.* **1998**, *624* (5), 823–829.

(67) Charles, S.; Danis, J. A.; Fettinger, J. C.; Eichhorn, B. W. *Inorg. Chem.* **1997**, *36* (17), 3772–3778.

(68) Charles, S.; Eichhorn, B. W.; Rheingold, A. L.; Bott, S. G. *J. Am. Chem. Soc.* **1994**, *116* (18), 8077–8086.

(69) Charles, S.; Fettinger, J. C.; Eichhorn, B. W. *Inorg. Chem.* **1996**, *35* (6), 1540–1548.

(70) Kesanli, B.; Mattamana, S. P.; Danis, J.; Eichhorn, B. *Inorganica Chimica Acta* **2005**, *358* (11), 3145–3151.

(71) Charles, S.; Fettinger, J. C.; Bott, S. G.; Eichhorn, B. W. *J. Am. Chem. Soc.* **1996**, *118* (19), 4713–4714.

(72) Charles, S.; Eichhorn, B. W.; Bott, S. G. *J. Am. Chem. Soc.* **1993**, *115* (13), 5837–5838.

(73) Kesanli, B.; Fettinger, J.; Eichhorn, B. *J. Am. Chem. Soc.* **2003**, *125* (24), 7367–7376.

(74) Kesanli, B.; Fettinger, J.; Scott, B.; Eichhorn, B. *Inorg. Chem.* **2004**, *43* (13), 3840–3846.

(75) Schnering, Von, H. G.; Wolf, J.; Weber, D.; Ramirez, R.; Meyer, T. *Angew. Chem.* **1986**, *98* (4), 372–373.

(76) Moses, M. J.; Fettinger, J. C.; Eichhorn, B. W. *Science* **2003**, 1–4.

(77) Wang, Y.; Moses-DeBusk, M.; Stevens, L.; Hu, J.; Zavalij, P.; Bowen, K.; Dunlap, B. I.; Glaser, E. R.; Eichhorn, B. *J. Am. Chem. Soc.* **2017**, *139* (2), 619–622.

(78) Moses, M. J.; Fettinger, J. C.; Eichhorn, B. W. *Inorg. Chem.* **2007**, *46* (4), 1036–1038.

(79) Moses, M. J.; Fettinger, J.; Eichhorn, B. *J. Am. Chem. Soc.* **2002**, *124* (21), 5944–5945.

(80) Charles, S.; Eichhorn, B. W.; Bott, S. G. *J. Am. Chem. Soc.* **1993**, *115* (13), 5837–5838.

(81) Wang, Y.; Zavalij, P.; Eichhorn, B. *Chem. Commun.* **2017**, *53* (84), 11600–11602.

(82) Eichhorn, B. W.; Mattamana, S. P.; Gardner, D. R.; Fettinger, J. C. *J. Am. Chem. Soc.* **1998**, *120* (37), 9708–9709.

(83) Kesanli, B.; Fettinger, J.; Eichhorn, B. *J. Am. Chem. Soc.* **2003**, *125* (24), 1–10.

(84) Hiller, W.; Klinkhammer, K-W.; Uhl, W.; Wagner, J. *Angew. Chem.* **1991**, *103*, 182-183.

(85) DeLisio, J. B.; Mayo, D. H.; Guerieri, P. M.; DeCarlo, S.; Ives, R.; Bowen, K.; Eichhorn, B. W.; Zachariah, M. R. *Chemical Physics Letters* **2016**, *661* (C), 168–172.

(86) Philip M Guerieri, DeCarlo, S.; Eichhorn, B.W.; Connell, T.; Yetter, R.A.; Tang, X.; Hicks, Z.; Bowen, K.H.; Zachariah, M.R. *J. Phys. Chem. A* **2015**, *119* (45), 1–10.

(87) Tang, X.; DeLisio, J. B.; Alnemrat, S.; Hicks, Z.; Stevens, L.; Stoltz, C. A.; Hooper, J. P.; Eichhorn, B. W.; Zachariah, M. R.; Bowen, K. H.; Mayo, D. H. *Inorg. Chem.* **2018**, *57* (14), 8181–8188.

(88) Ashby, E.C.; Goel, A.B. *Inorg. Chem.* **1981**, *20,* 1096-1101.

(89) Wright, R. J.; Brynda, M.; Power, P. P. *Angew. Chem. Int. Ed.* **2006**, *45* (36), 5953–5956.

(90) Krieck, S.; Görls, H.; Westerhausen, M. *Organometallics* **2008**, *27* (19), 5052–5057.

(91) Klemp, C.; Stober, G.; Krossing, I.; Schnöckel, H. *Angew. Chem. Int. Ed.* **2000**, *39* (20), 3691–3695.

(92) Baudler, M.; Glinka, K. *Chem. Rev.* **1993**, *93* (4), 1623–1667.

(93) Cossairt, B. M.; Piro, N. A.; Cummins, C. C. *Chem. Rev.* **2010**, *110* (7), 4164–4177.

(94) Scheer, M.; Balázs, G.; Seitz, A. *Chem. Rev.* **2010**, *110* (7), 4236–4256.

(95) Charles, S.; Eichhorn, B. W.; Rheingold, A. L.; Bott, S. G. *J. Am. Chem. Soc.* **1994**, *116* (18), 8077–8086.

(96) Charles, S.; Eichhorn, B. W.; Rheingold, A. L.; Bott, S. G. *J. Am. Chem. Soc.* **1994**, *116* (18), 8077–8086.

(97) Kesanli, B.; Eichhorn, B. *J. Am. Chem. Soc*, **2000**, *122* (45), 11101-11107.

(98) Knapp, C.; Zhou, B.; Denning, M. S.; Rees, N. H.; Goicoechea, J. M. *Dalton Trans.* **2010**, *39* (2), 426–436.

(99) Bolle, U.; Tremel, W. *J. Chem. Soc., Chem. Commun.* **1994**, *99* (2), 217–219.

(100) Knapp, C.; Zhou, B.; Denning, M. S.; Rees, N. H.; Goicoechea, J. M. *Dalton Trans.* **2010**, *39* (2), 426–436.

(101) Knapp, C. M.; Large, J. S.; Rees, N. H.; Goicoechea, J. M. *Dalton Trans.* **2011**, *40* (3), 735–745.

(102) Mandal, S.; Reber, A. C.; Qian, M.; Liu, R.; Saavedra, H. M.; Sen, S.; Weiss, P. S.; Khanna, S. N.; Sen, A. *Dalton Trans.* **2012**, *41* (40), 12365–12377.

(103) Mandal, S.; Reber, A. C.; Qian, M.; Liu, R.; Saavedra, H. M.; Sen, S.; Weiss, P. S.; Khanna, S. N.; Sen, A. *Dalton Trans.* **2012**, *41* (18), 5454–5457.

(104) Moses, M. J.; Fettinger, J.; Eichhorn, B. *J. Am. Chem. Soc.* **2002**, *124* (21), 5944–5945.

(105) Chaki, N. K.; Mandal, S.; Reber, A. C.; Qian, M.; Saavedra, H. M.; Weiss, P. S.; Khanna, S. N.; Sen, A. *ACS Nano* **2010**, *4* (10), 5813–5818.

(106) Downing, D. *Synthesis and Characterization of Bimetallic Zintl Clusters and Their Use in the Fabrication of Intermetallic Nanoparticles*. **2012**, 1–163. Accessed through lib.umd.edu

(107) Downing, D. O.; Zavalij, P.; Eichhorn, B. W. *Eur. J. Inorg. Chem.* **2010**, *2010* (6), 890–894.

(108) Wang, J.-Q.; Stegmaier, S.; Fässler, T. F. *Angew. Chem. Int. Ed.* **2009**, *48* (11), 1998–2002.

(109) Hlukhyy, V.; He, H.; Jantke, L.-A.; Fässler, T. F. *Chemistry - A European Journal* **2012**, *18* (38), 12000–12007.

(110) Wang, Y.; Wang, L.-L.; Ruan, H.-P.; Luo, B.-L.; Sang, R.-L.; Xu, L. *Chin. J. Struct. Chem.* **2015**, *34* (8), 1253–1258.

(111) Wang, J.-Q.; Stegmaier, S.; Wahl, B.; Fässler, T. F. *Chemistry - A European Journal* **2010**, *16* (6), 1793–1798.

(112) Bolle, U.; Tremel, W. *J. Chem. Soc., Chem. Commun.* **1994**, *99* (2), 217–219.

(113) Knapp, C. M.; Westcott, B. H.; Raybould, M. A. C.; McGrady, J. E.; Goicoechea, J. M. *Chem. Commun.* **2012**, *48* (100), 12183–12183.

(114) Scherer, O. J.; Blath, C.; Heckmann, G.; Wolmershaeuser, G. *Journal of Organometallic Chemistry* **1991**, *409* (3), C15–C18.

(115) Scherer, O. J.; Wiedemann, W.; Wolmershaeuser, G. *Chem. Ber.* **1990**, *123* (1), 3–6.

(116) Foust, A. S.; Foster, M. S.; Dahl, L. F. *J. Am. Chem. Soc.* **1969**, *91* (20), 5631–5633.

(117) Johnson, B. P.; Schiffer, M.; Scheer, M. *Organometallics* **2000**, *19* (17), 3404–3409.

(118) Schmidt, M.; Konieczny, D.; Peresypkina, E. V.; Virovets, A. V.; Balázs, G.; Bodensteiner, M.; Riedlberger, F.; Krauss, H.; Scheer, M. *Angew. Chem. Int. Ed.* **2017**, *56* (25), 7307–7311.

(119) Pan, F.-X.; Xu, C.-Q.; Li, L.-J.; Min, X.; Wang, J.-Q.; Li, J.; Zhai, H.-J.; Sun, Z.-M. *Dalton Trans.* **2016**, *45* (9), 3874–3879.

(120) Knapp, C. M.; Jackson, C. S.; Large, J. S.; Thompson, A. L.; Goicoechea, J. M. *Inorg. Chem.* **2011**, *50* (9), 4021–4028.

(121) Foust, A. S.; Foster, M. S.; Dahl, L. F. *J. Am. Chem. Soc.* **1969**, *91* (20), 5631–5633.

(122) Di Vaira, M.; Mani, F.; Moneti, S.; Peruzzini, M.; Sacconi, L.; Stoppioni, P. *Inorg. Chem.* **1984**, *24* (14), 2230-2236.

(123) Wang, J.-Q.; Stegmaier, S.; Wahl, B.; Fässler, T. F. *Chemistry - A European Journal* **2010**, *16* (6), 1793–1798.

(124) Bucher, U. E.; Currao, A.; Nesper, R.; Rueegger, H.; Venanzi, L. M.; Younger, E. *Inorg. Chem.* **1995**, *34* (1), 66–74.

(125) Xu, C.; Baum, T. H.; Rheingold, A. L. *Chem. Mater.* **1998**, *10* (9), 2329–2331.

(126) Downing, D. O.; Liu, Z.; Eichhorn, B. W. *Polyhedron* **2016**, *103* (Part_A), 66–70.

(127) Charles, S.; Eichhorn, B. W.; Rheingold, A. L.; Bott, S. G. *J. Am. Chem. Soc.* **1994**, *116* (18), 8077–8086.

(128) Charles, S.; Eichhorn, B. W.; Rheingold, A. L.; Bott, S. G. *J. Am. Chem. Soc.* **1994**, *116* (18), 8077–8086.

(129) Charles, S.; Danis, J. A.; Fettinger, J. C.; Eichhorn, B. W. *Inorg. Chem.* **1997**, *36* (17), 3772–3778.

(130) Charles, S.; Fettinger, J. C.; Eichhorn, B. W. *Inorg. Chem.* **1996**, *35* (6), 1540–1548.

(131) Charles, S.; Fettinger, J. C.; Eichhron, B. W. *J. Am. Chem. Soc.* **1995**, *117* (19), 5303–5311.

(132) Kesanli, B.; Mattamana, S. P.; Danis, J.; Eichhorn, B. *Inorganica Chimica Acta* **2005**, *358* (11), 3145–3151.

(133) Scharfe, S.; Kraus, F.; Stegmaier, S.; Schier, A.; Fässler, T. F. *Angew. Chem. Int. Ed.* **2011**, *50* (16), 3630–3670.

(134) Kesanli, B.; Fettinger, J.; Eichhorn, B. *J. Am. Chem. Soc.* **2003**, *125* (24), 7367–7376.

(135) Moses, M. J. *Science* **2003**, *300* (5620), 778–780.

(136) Esenturk, E.N.; Fettinger, J.C.; Eichhorn, B. *Chem. Commun.* **2005**, *2*, 247-249.

(137) Fässler, T. F.; Hoffmann, S. D. *Angew. Chem. Int. Ed.* **2004**, *43* (46), 6242–6247.

(138) Cossairt, B. M.; Cummins, C. C. *Angew. Chem. Int. Ed.* **2008**, *47* (1), 169–172.

(139) Cossairt, B. M.; Diawara, M. C.; Cummins, C. C. *Science* **2009**, *323* (5914), 602–602.

(140) Cossairt, B. M.; Piro, N. A.; Cummins, C. C. *Chem. Rev.* **2010**, *110* (7), 4164–4177.

(141) Piro, N. A.; Cummins, C. C. *J. Am. Chem. Soc.* **2008**, *130* (29), 9524–9535.

(142) Esenturk, E. N.; Fettinger, J.; Eichhorn, B. *J. Am. Chem. Soc.* **2006**, *128* (28), 9178–9186.

(143) Walker, W.E.; Pruett, R.L.; Schnoening, R.C.; Vidal, J.L. *Inorg. Chem.* **1979**, *18* (1), 128-136.

(144) Vidal, J.L.; Schoening, R.C.; Pruett, R.L.; Fiato, R.A. *Inorg. Chem.* **1979**, *18* (7), 1821-1823.

(145) Vidal, J. L. *Inorg. Chem.* **1981**, *20* (1), 243-249.

(146) Knapp, C.; Zhou, B.; Denning, M. S.; Rees, N. H.; Goicoechea, J. M. *Dalton Trans.* **2010**, *39* (2), 426–436.

(147) Cossairt, B. M.; Piro, N. A.; Cummins, C. C. *Chem. Rev.* **2010**, *110* (7), 4164–4177.

(148) Di Vaira, M.; Ghilardi, C. A.; Midollini, S.; Sacconi, L. *J. Am. Chem. Soc.* **1978**, *100* (8), 2550–2551.

(149) Tofan, D.; Cossairt, B. M.; Cummins, C. C. *Inorg. Chem.* **2011**, *50* (24), 12349–12358.

(150) Fleischmann, M.; Dielmann, F.; Gregoriades, L. J.; Peresypkina, E. V.; Virovets, A. V.; Huber, S.; Timoshkin, A. Y.; Balázs, G.; Scheer, M. *Angew. Chem. Int. Ed.* **2015**, *54* (44), 13110–13115.

(151) Atwood, J.L.; Hunter, W.E.; Jones, R.A.; Wright, T.C. *Inorg. Chem.* **1983**, *22* (6), 993-995.

(152) Galli, D.; Garlaschelli, L.; Ciani, G.; Fumagalli, A.; Martinengo, S.; Sironi, A. *J. Chem. Soc., Dalton Trans.* **1984**, *1*, 55–61.

(153) Jones, R.A.; Whittlesey, B.R. *J. Am. Chem. Soc.* **1985**, *107* (4), 1078-1079.

(154) Korber, N.; Schnering, H. G. V. *Z. Kristallogr. - New Cryst. Struct.* **1997**, *212*, 85–86.

(155) Eichhorn, B. W.; Mattamana, S. P.; Gardner, D. R.; Fettinger, J. C. *J. Am. Chem. Soc.* **1998**, *120* (37), 9708–9709.

(156) Kesanli, B.; Fettinger, J.; Eichhorn, B. *J. Am. Chem. Soc.* **2003**, *125* (24), 7367–7376.

(157) Di Vaira, M.; Ghilardi, C. A.; Midollini, S.; Sacconi, L. *J. Am. Chem. Soc.* **1978**, *100* (8), 2550–2551.

(158) Fleischmann, M.; Welsch, S.; Peresypkina, E. V.; Virovets, A. V.; Scheer, M. *Chemistry - A European Journal* **2015**, *21* (41), 14332–14336.

(159) Esenturk, E. N.; Fettinger, J.; Lam, Y.-F.; Eichhorn, B. *Angew. Chem. Int. Ed.* **2004**, *43* (16), 2132–2134.

(160) Esenturk, E. N.; Fettinger, J.; Eichhorn, B. *J. Am. Chem. Soc.* **2006**, *128* (28), 9178–9186.

(161) Mädl, E.; Butovskii, M. V.; Balázs, G.; Peresypkina, E. V.; Virovets, A. V.; Seidl, M.; Scheer, M. *Angew. Chem. Int. Ed.* **2014**, *53* (29), 7643–7646.

(162) Pomije, M.K.; Kurth, C.J.; Ellis, J.E.; Barybin, M.V. *Organometallics* **1997**, *16*, 3582-3587.

(163) Xu, L.; Bobev, S.; El-Bahraoui, J.; Sevov, S. C. *J. Am. Chem. Soc.* **2000**, *122* (8), 1838–1839.

(164) Gascoin, F.; Sevov, S. C. *J. Am. Chem. Soc.* **2000**, *122* (41), 10251–10252.

(165) Emmerling, F.; Rohr, C. *Z. Naturforsch., B: Chem. Sci.* **2002**, *57* (9), 963–975.

(166) Schnering, Von, H. G.; Hartweg, M.; Hartweg, U.; Hoenle, W. *Angew. Chem.* **1989**, *101* (1), 98–99.

(167) Derrien, G.; Tillard, M.; Manteghetti, A.; Belin, C. *Z. anorg. allg. Chem.* **2003**, *629* (9), 1601–1609.

(168) Kraus, F.; Korber, N. *Chemistry - A European Journal* **2005**, *11* (20), 5945–5959.

(169) Hanauer, T.; Aschenbrenner, J. C.; Korber, N. *Inorg. Chem.* **2006**, *45* (17), 6723–6727.

(170) Hanauer, T.; Kraus, F.; Reil, M.; Korber, N. *Monatsh. Chem.* **2006**, *137* (2), 147–156.

(171) Critchlow, S. C.; Corbett, J. D. *Inorg. Chem.* **1984**, *23* (6), 770–774.

(172) Kuznetsov, A. N.; Fässler, T. F. *Z. Anorg. Allg. Chem.* **2002**, *628* (11), 2537–2541.

(173) Gascoin, F.; Sevov, S. C. *Inorg. Chem.* **2001**, *40* (24), 6254–6257.

(174) Somer, M.; Hartweg, M.; Peters, K.; Schnering, Von, H. G. *Z. Kristallogr.* **1991**, *195* (1-2), 103–104.

(175) Gascoin, F.; Sevov, S. C. *Inorg. Chem.* **2001**, *40* (20), 5177–5181.

(176) von Schnering, H.G.; Hartweg, M.; Hartweg, U.; Hoenle, W *Angew. Chem. Int. Ed.* **1989**, *28*, 56-62.

(177) Schnering, Von, H. G.; Wittmann, M.; Sommer, D. *Z. Anorg. Allg. Chem.* **1984**, *510*, 61–71.

(178) Deller, K.; Eisenmann, B. *Z. Naturforsch., B: Anorg. Chem., Org. Chem.* **1976**, *31B* (8), 1023–1027.

(179) Deller, K.; Eisenmann, B. *Z. Naturforsch., B: Anorg. Chem., Org. Chem.* **1977**, *32B* (12), 1368–1370.

(180) Benda, C. B.; Fässler, T. F. *Z. Anorg. Allg. Chem.* **2013**, *640* (1), 40–45.

(181) Milyukov, V. A.; Kataev, A. V.; Sinyashin, O. G.; Hey-Hawkins, E. *Russ. Chem. Bull.* **2006**, *55* (7), 1297–1299.

(182) Baudler, M.; Akpapoglou, S.; Ouzounis, D.; Wasgestian, F.; Meinigke, B.; Budzikiewicz, H.; Münster, H. *Angew. Chem.* **1988**, *100* (2), 288–289.

(183) Emmerling, F.; Petri, D.; R hr, C. *Z. Anorg. Allg. Chem.* **2004**, *630* (13-14), 2490–2501.

(184) Korber, N.; Richter, F. *Angew. Chem., Int. Ed. Engl.* **1997**, *36* (1314), 1512–1514.

(185) Abicht, H. P.; Hoenle, W.; Schnering, Von, H. G. *Z. Anorg. Allg. Chem.* **1984**, *519*, 7–23.

(186) Von Schnering, H. G.; Meyer, T.; Hoenle, W.; Schmettow, W.; Hinze, U.; Bauhofer, W.; Kliche, G. *Z. Anorg. Allg. Chem.* **1987**, *553*, 261–279.

(187) Schmettow, W.; Lipka, A.; Schnering, Von, H. G. *Angew. Chem.* **1974**, *86* (10), 379–380.

(188) Hönle, W.; Krogull, G.; Peters, K.; Schnering, H. G. V. *Z. Kristallogr. - New Cryst. Struct.* **1999**, *214* (1), 17–18.

(189) Eisenmann, B.; Jordan, H.; Schaefer, H. *Z. Naturforsch., B: Anorg. Chem., Org. Chem.* **1985**, *40B* (12), 1603–1606.

(190) Manriquez, V.; Hoenle, W.; Schnering, Von, H. G. *Z. Anorg. Allg. Chem.* **1986**, *539*, 95–109.

(191) Santandrea, R. P.; Mensing, C.; Schnering, Von, H. G. *Thermochim. Acta* **1986**, *98*, 301–311.

(192) Meyer, T.; Hoenle, W.; von Schnering, H. G. *Z. Anorg. Allg. Chem.* **1987**, *552*, 69–80.

(193) Dahlmann, W.; von Schnering, H. G. *Naturwissenschaften* **1972**, *59* (9), 420.

(194) Dahlmann, W.; von Schnering, H. G. *Naturwissenschaften* **1973**, *60* (9), 429.

(195) Hoenle, W.; von Schnering, H. G.; Schmidpeter, A.; Burget, G. *Angew. Chem.* **1984**, *96* (10), 796–797.

(196) Korber, N.; Daniels, J. *Helv. Chim. Acta* **2004**, *79* (8), 2083–2087.

(197) Korber, N.; Daniels, J. *Z. anorg. allg. Chem.* **1999**, *625* (2), 189–191.

(198) Korber, N.; Daniels, J. *J. Chem. Soc., Dalton Trans.* **1996**, No. 8, 1653–1658.

(199) Goicoechea, J. M. In *Clusters – Contemporary Insight in Structure and Bonding*; Dehnen, S., Ed.; Clusters – Contemporary Insight in Structure and Bonding; Springer International Publishing: Cham, 2017; pp 63–97.

(200) Korber, N.; von Schnering, H. G. *Chem. Ber.* **1996**, *129* (2), 155–159.

(201) Hönle, W.; Buresch, J.; Peters, K.; Chang, J. H.; von Schnering, H. G. *Z. Kristallogr. - New Cryst. Struct.* **2002**, *217* (JG), 485–486.

(202) Hönle, W.; Buresch, J.; Peters, K.; Chang, J. H.; von Schnering, H. G. *Z. Kristallogr. - New Cryst. Struct.* **2002**, *217* (JG), 487–488.

(203) Hönle, W.; Buresch, J.; Wolf, J.; Peters, K.; Chang, J. H.; von Schnering, H. G. *Z. Kristallogr. - New Cryst. Struct.* **2002**, *217* (JG), 489–490.

(204) Schmettow, W.; Schnering, Von, H. G. *Angew. Chem.* **1977**, *89* (12), 895–895.

(205) Bashall, A.; Beswick, M. A.; Choi, N.; Hopkins, A. D.; Kidd, S. J.; Lawson, Y. G.; Mosquera, M. E. G.; McPartlin, M.; Raithby, P. R.; Wheatley, A. A.; Wood, J. A.; Wright, D. S. *Dalton* **2000**, *4*, 479–486.

(206) Hanauer, T.; Grothe, M.; Reil, M.; Korber, N. *Helv. Chim. Acta* **2005**, *88* (5), 950–961.

(207) Somer, M.; Hönle, W.; von Schnering, H. G. *Z. Naturforsch., B: Chem. Sci.* **1989**, *44* (3), 296–306.

(208) Driess, M.; Merz, K.; Pritzkow, H.; Janoschek, R. *Angew. Chem., Int. Ed. Engl.* **1996**, *35* (21), 2507–2510.

(209) Korber, N.; von Schnering, H. G. *Z. Kristallogr. - New Cryst. Struct.* **1997**, *212*, 85–86.

(210) Castleman, A. W.; Khanna, S. N.; Sen, A.; Reber, A. C.; Qian, M.; Davis, K. M.; Peppernick, S. J.; Ugrinov, A.; Merritt, M. D. *Nano Lett.* **2007**, *7* (9), 2734–2741.

(211) Dorn, F. W.; Klemm, W. *Z. Anorg. Allg. Chem.* **1961**, *309*, 189–203.

(212) Hirschle, C.; Rohr, C. *Z. Anorg. Allg. Chem.* **2000**, *626* (9), 1992–1998.

(213) Beswick, M. A. *Science* **1998**, *281* (5382), 1500–1501.

(214) Adolphson, D. G.; Corbett, J. D.; Merryman, D. J. *J. Am. Chem. Soc.* **1976**, *98* (23), 7234–7239.

(215) Diehl, L.; Khodadadeh, K.; Kummer, D.; Straehle, J. *Z. Naturforsch., B: Anorg. Chem., Org. Chem.* **1976**, *31B* (4), 522–524.

(216) Breunig, H. J.; Ghesner, M. E.; Lork, E. *Z. Anorg. Allg. Chem.* **2005**, *631* (5), 851–856.

(217) Mutzbauer, F.; Korber, N. *Acta Crystallogr., Sect. E: Struct. Rep. Online* **2011**, *67* (11), 1551.

(218) Perla, L. G.; Oliver, A. G.; Sevov, S. C. *Inorg. Chem.* **2014**, *54* (3), 872–875.

(219) Reil, M.; Korber, N. *Z. Anorg. Allg. Chem.* **2007**, *633* (10), 1599–1602.

(220) Wichelhaus, W.; Schnering, Von, H. G. *Naturwissenschaften* **1973**, *60* (2), 104.

(221) Schnering, Von, H. G.; Somer, M.; Kliche, G.; Hoenle, W.; Meyer, T.; Wolf, J.; Ohse, L.; Kempa, P. B. *Z. Anorg. Allg. Chem.* **1991**, *601*, 13–30.

(222) Korber, N.; Daniels, J.; von Schnering, H. G. *Angew. Chem., Int. Ed. Engl.* **1996**, *35* (10), 1107–1110.

(223) Korber, N.; Daniels, J. R. *Z. Anorg. Allg. Chem.* **1996**, *622* (11), 1833–1838.

(224) Korber, N.; Daniels, J. *Polyhedron* **1996**, *15* (16), 2681–2688.

(225) Korber, N.; von Schnering, H. G. *Chem. Ber.* **1996**, *129* (2), 155–159.

(226) Dai, F.-R.; Xu, L. *Chin. J. Struct. Chem.* **2007**, *26* (1), 45–48.

(227) Garcia, F.; Less, R. J.; Naseri, V.; McPartlin, M.; Rawson, J. M.; Sancho Tomas, M.; Wright, D. S. *Chem. Commun.* **2008**, *216* (7), 859–861.

(228) Weinert, B.; Eulenstein, A. R.; Ababei, R.; Dehnen, S. *Angew. Chem. Int. Ed.* **2014**, *53* (18), 4704–4708.

(229) Miluykov, V.; Kataev, A.; Sinyashin, O.; Lönnecke, P.; Hey-Hawkins, E. *Z. Anorg. Allg. Chem.* **2006**, *632* (10-11), 1728–1732.

(230) Von Schnering, H. G.; Manriquez, V.; Hoenle, W. *Angew. Chem.* **1981**, *93* (6-7), 606–607.

(231) Baudler, M.; Duester, D.; Germeshausen, J. *Z. Anorg. Allg. Chem.* **1986**, *534*, 19–26.

(232) Baudler, M.; Glinka, K. *Chem. Rev.* **1993**, *93*, 1623-1667.

(233) Fritz, G.; Schneider, H. W.; Hönle, W.; Schnering, H. G. V. *Z. Naturforsch., B: Chem. Sci.* **1988**, *43* (5), 561–566.

(234) Haushalter, R. C.; Eichhorn, B. W.; Rheingold, A. L.; Geib, S. J. *J. Chem. Soc., Chem. Commun.* **1988**, No. 15, 1027–1028.

(235) Baudler, M.; Heumueller, R.; Duester, D.; Germeshausen, J.; Hahn, J. *Z. Anorg. Allg. Chem.* **1984**, *518*, 7–13.